Analysing the thermal properties of borehole heat exchanger systems

Zur Erlangung des akademischen Grades einer

Doktorin der Naturwissenschaften (Dr. rer. nat.)

von der KIT Fakultät für
Bauingenieur-, Geo- und Umweltwissenschaften

des Karlsruher Instituts für Technologie (KIT)

genehmigte

DISSERTATION

von

M.Sc. Anna Albers

Tag der mündlichen Prüfung: 06. Mai 2025

Referent: Prof. Dr. Philipp Blum
Korreferent: Prof. Dr. Javier Urchueguía Schölzel

Karlsruhe 2025

“Let's do the things we are afraid of
Tell the stories we are made of
And maybe we'll find the place where we can stay
Stay as we are”

- Bukahara (“Grotta Delle Ninfe”)

To my friends and family.

Abstract

Ground source heat pump (GSHP) systems using borehole heat exchangers (BHE) can aid in decarbonising the heating and cooling sector. The sustainable and economically competitive design of these systems depends on understanding the thermal properties of the BHE system, including the subsurface and the grouting material. Therefore, this thesis aims to investigate and refine reliable methods for analysing the thermal properties of BHE systems in the laboratory and field by presenting the findings of four individual studies.

In Study 1, the enhanced thermal response test (ETRT) is critically evaluated for in-situ analysis of depth-specific effective thermal conductivities and Darcy velocities. Different approaches in determining the specific heat load of an ETRT are compared, and an improved evaluation procedure of the ETRT is introduced that adjusts the specific heat load over time and along the heating cable. The results demonstrate that the appropriate specific heat load is highly dependent on the heat transport properties of the study site. High Darcy velocities (> 0.6 m d^{-1}) may require a higher specific heat load to achieve an adequate temperature increase ($\Delta T > 0.6$ K), though overheating of the part of the cable installed outside of the BHE must be prevented. Thereby, helpful information and improvements for the planning and evaluation of ETRTs are provided.

In Study 2, as an alternative approach towards field experiments, thermal conductivity models are evaluated for their suitability and transferability by comparing estimated thermal conductivities to laboratory measurements and ETRT results. Effective thermal conductivities from the ETRT range between 2.3 and 6.1 W m^{-1} K^{-1} with an average of 4.7 W m^{-1} K^{-1}. By analysing 156 core samples, a group of theoretical models is identified as being capable of roughly estimating the thermal conductivities of Triassic sandstones at laboratory and field scale. The Voigt-Reuss-Hill model achieves the best agreement with an average thermal conductivity of 4.5 W m^{-1} K^{-1} ($T = 20$ °C). It is demonstrated that models which assume randomly distributed components (e.g., geometric mean, Voigt-Reuss-Hill model, statistical spatial distribution, Hashin-Shtrikman average) provide estimates with an accuracy of 0.7 – 0.8 W m^{-1} K^{-1}. The accuracy is limited by uncertainties in determining the matrix thermal conductivity, model assumptions, sample quantity, and study sites where groundwater flow is negligible.

The thermal properties of grouting materials are commonly analysed in the laboratory. Study 3 provides a comprehensive literature overview of the various methods currently used to determine the thermal conductivity and volumetric heat capacity of grouting materials. In extensive laboratory experiments, the influence of the measurement method and the sample preparation on the analysis of the thermal properties is compared, and a recommended standard procedure is established: mixing the grouting material at high mixing speed and curing the samples under water for 28 d at room temperature. This study further demonstrates the benefits of calculating the volumetric heat capacity using the specific heat capacities of dry samples measured by differential scanning calorimetry (DSC), water content and bulk density. The influence of the water-solid ratio (w/s) on the properties of grouting materials is examined and used to derive an empirical relationship for estimating the volumetric heat capacity of grouting materials with an

uncertainty of smaller than ± 5 %. Thereby, the consistency and comparability between laboratory studies on the thermal properties of grouting materials are improved.

Nevertheless, the thermal properties of grouting materials in the field can differ from those of laboratory samples. Hence, in Study 4, new insights into the properties of grouting materials in the field are provided from a large-scale field experiment, where grouted boreholes are excavated up to a depth of 15 m. Collected field samples show higher thermal conductivities by 13 % (w/s = 0.3) and 35 % (w/s = 0.8) than laboratory samples of the same material. These differences are mainly explained by filtration in the loess and weathered limestone during the curing process of the grouting materials. With a short-time enhanced thermal response test (ETRT), 17 % lower in-situ thermal conductivities are analysed than in comparison to the field samples. The deviations are attributed to the geometry of the borehole, the trajectory of the BHE and the heating cable. Thereby, this study demonstrates the limitations when transferring laboratory-derived properties of grouting materials to a field site and emphasises the importance of considering site conditions.

Summarising, this thesis provides recommendations for analysing the thermal properties of BHE systems. The findings contribute to understanding, improving and selecting the method to analyse the thermal properties. Moreover, further insights are provided into crucial factors and processes that influence thermal properties. Thus, this thesis improves the reliability of laboratory results and supports the interpretation of field experiments. Thereby, it contributes to the reliability of the simulation and design of GSHP systems, which can improve public acceptance of the technology.

Kurzfassung

Erdgekoppelte Wärmepumpenanlagen unter Nutzung von Erdwärmesonden (EWS) können zur Dekarbonisierung des Heiz- und Kühlsektors beitragen. Die nachhaltige und wettbewerbsfähige Auslegung dieser Systeme hängt vom Verständnis für die thermischen Eigenschaften des EWS-Systems ab, einschließlich des Untergrunds und des Verfüllmaterials. Ziel dieser Arbeit ist es daher, zuverlässige Methoden zur Analyse der thermischen Eigenschaften von EWS-Systemen im Labor und im Feld zu untersuchen und zu verfeinern. Hierfür werden die Ergebnisse von vier einzelnen Studien präsentiert.

In Studie 1 wird der Enhanced Thermal Response Test (ETRT) kritisch bewertet in Bezug auf die in-situ-Analyse der tiefenbezogenen effektiven Wärmeleitfähigkeiten und Darcy-Geschwindigkeiten. Es werden verschiedene Ansätze zur Bestimmung der spezifischen Heizleistung eines ETRT verglichen und ein verbessertes Auswertungsverfahren des ETRT eingeführt, welches die spezifische Heizleistung über die Zeit und entlang des Heizkabels anpasst. Die Ergebnisse zeigen, dass die angemessene spezifische Heizleistung stark von den Wärmetransporteigenschaften des Untersuchungsgebiets abhängt. Bei hohen Darcy-Geschwindigkeiten ($> 0{,}6$ m d^{-1}) kann eine höhere spezifische Heizleistung erforderlich sein, um eine ausreichende Temperaturerhöhung ($\Delta T > 0{,}6$ K) zu erreichen, wobei eine Überhitzung des außerhalb der EWS verlegten Kabels vermieden werden muss. Hierdurch werden hilfreiche Informationen und Verbesserungen für die Planung und Bewertung von ETRTs bereitgestellt.

In Studie 2 werden anschließend Wärmeleitfähigkeitsmodelle auf ihre Eignung und Übertragbarkeit als Alternative zu Feldexperimenten hin bewertet, indem geschätzte Wärmeleitfähigkeiten mit Labormessungen und ETRT-Ergebnissen verglichen werden. Die effektiven Wärmeleitfähigkeiten aus dem ETRT liegen zwischen 2,3 und 6,1 W m^{-1} K^{-1} mit einem Durchschnitt von 4,7 W m^{-1} K^{-1}. Durch die Analyse von 156 Kernproben wird eine Gruppe theoretischer Modelle identifiziert, die in der Lage sind, die Wärmeleitfähigkeiten von triassischen Sandsteinen im Labor- und Feldmaßstab grob zu schätzen. Die beste Übereinstimmung wird mit dem Voigt-Reuss-Hill-Modell mit einer durchschnittlichen Wärmeleitfähigkeit von 4,5 W m^{-1} K^{-1} ($T = 20$ °C) erzielt. Es wird gezeigt, dass Modelle, die von zufällig verteilten Komponenten ausgehen (z. B. geometrisches Mittel, Voigt-Reuss-Hill-Modell, statistische räumliche Verteilung, Hashin-Shtrikman-Mittelwert), Schätzungen mit einer Genauigkeit von $\geq 0{,}7$ W m^{-1} K^{-1} liefern. Die Genauigkeit wird durch Unsicherheiten bei der Bestimmung der Matrixwärmeleitfähigkeit, Modellannahmen, die Probenmenge und Untersuchungsstandorte mit vernachlässigbarer Grundwasserströmung eingeschränkt.

Die thermischen Eigenschaften von Verfüllmaterialien werden in der Regel im Labor untersucht. Studie 3 gibt einen umfassenden Literaturüberblick über die verschiedenen derzeit verwendeten Methoden zur Bestimmung der Wärmeleitfähigkeit und der volumetrischen Wärmekapazität von Verfüllmaterialien. In umfangreichen Laborexperimenten wird der Einfluss der Messmethode und der Probenvorbereitung auf die Analyse der thermischen Eigenschaften verglichen und ein empfohlenes Standardverfahren festgelegt: Mischen des Verfüllmaterials mit hoher Mischgeschwindigkeit und Aushärten der Proben unter Wasser für

28 Tage bei Raumtemperatur. Diese Studie zeigt die Vorteile der Berechnung der volumetrischen Wärmekapazität anhand der spezifischen Wärmekapazitäten trockener Proben, die mit Hilfe der Differential-Scanning-Kalorimetrie (DSC) gemessen wurden, des Wassergehalts und der Rohdichte. Der Einfluss des Wasser-Feststoff-Verhältnisses (w/f) auf die Eigenschaften von Verfüllmaterialien wird untersucht und zur Ableitung einer empirischen Beziehung zur Schätzung der volumetrischen Wärmekapazität von Verfüllmaterialien mit einer Unsicherheit von weniger als ± 5 % verwendet. Dadurch wird die Kohärenz und Vergleichbarkeit zwischen Laboruntersuchungen zu den thermischen Eigenschaften von Verfüllmaterialien verbessert.

Die thermischen Eigenschaften der Verfüllmaterialien im Feld können jedoch von den Eigenschaften der Laborproben abweichen. Ein groß angelegter Feldversuch, bei dem verfüllte Bohrlöcher bis zu einer Tiefe von 15 m ausgehoben werden, liefert daher in Studie 4 neue Erkenntnisse zu den Eigenschaften von Verfüllmaterialien im Feld. Die im Feld entnommenen Proben weisen um 13 % (w/f = 0,3) bzw. 35 % (w/f = 0,8) höhere Wärmeleitfähigkeiten auf als Laborproben desselben Materials. Diese Unterschiede sind hauptsächlich auf die Filtration im Löß und im verwitterten Kalkstein während des Aushärtungsprozesses der Verfüllmaterialien zurückzuführen. Mit einem Enhanced tThermal Response Test (ETRT) werden im Vergleich zu den Feldproben 17 % niedrigere in-situ-Wärmeleitfähigkeiten ermittelt. Die Abweichungen werden auf die Geometrie des Bohrlochs, den Verlauf der EWS und des Heizkabels zurückgeführt. Damit zeigt diese Studie die Grenzen bei der Übertragung von im Labor ermittelten Eigenschaften von Verfüllmaterialien auf das Gelände auf und unterstreicht, wie wichtig es ist, die Bedingungen vor Ort zu berücksichtigen.

Zusammenfassend gibt diese Arbeit Empfehlungen für die Analyse der thermischen Eigenschaften von EWS-Systemen. Die Ergebnisse tragen zum Verständnis, zur Verbesserung und zur Auswahl der Anlysemethode der thermischen Eigenschaften bei. Darüber hinaus werden weitere Erkentnisse zu entscheidenden Faktoren und Prozessen gewonnen, die die thermischen Eigenschaften beeinflussen. Somit verbessert diese Arbeit die Zuverlässigkeit von Laborergebnissen und unterstützt die Interpretation von Feldexperimenten. Damit trägt die Arbeit zur Zuverlässigkeit der Simulation und der Auslegung von erdgekoppelten Wärmepumpenanlagen bei, was die öffentliche Akzeptanz der Technologie verbessern kann.

Contents

Abstract ..... **i**

Kurzfassung ..... **iii**

Contents ..... **v**

List of figures ..... **ix**

List of tables ..... **xi**

Acronyms and symbols ..... **xiii**

1 Introduction **1**

1.1 Motivation 1
1.2 Thermal properties of BHE systems 2
1.3 Measurement methods 3
1.3.1 Laboratory methods 3
1.3.2 Thermal response test 4
1.4 Objectives 5
1.5 Outline 6

2 Evaluating an enhanced thermal response test (ETRT) with high groundwater flow **9**

Abstract 9
2.1 Introduction 9
2.2 Material and methods 12
2.2.1 Experimental 12
2.2.2 Evaluation 14
2.3 Results and discussion 17
2.3.1 Averaging the specific heat load 17
2.3.2 Spatial adjustment of the specific heat load 18
2.3.3 Depth-specific effective thermal conductivity evaluation 20
2.3.4 Discussion 21
2.4 Conclusion 26
2.5 Acknowledgements 27

3 Depth-specific thermal conductivities of Triassic sandstones **29**

Abstract 29
3.1 Introduction 29
3.2 Study site and geological background 31
3.3 Methods 32
3.3.1 Laboratory analysis 33
3.3.2 Theoretical estimation of thermal conductivity 34
3.3.3 Field measurements 36
3.4 Results and discussion 37

3.4.1 Laboratory results ... 37
3.4.2 Estimated thermal conductivity ... 39
3.4.3 Field results ... 42
3.5 Conclusion ... 46
3.6 Acknowledgements ... 46

4 Determination of thermal properties of grouting materials for borehole heat exchangers (BHE) ... 47

Abstract ... 47
4.1 Introduction ... 47
4.2 Material and methods ... 50
4.2.1 Material ... 51
4.2.2 Sample preparation ... 52
4.2.3 Suspension properties ... 53
4.2.4 Wet bulk density, water content, porosity and saturation ... 53
4.2.5 Thermal conductivity measurement ... 53
4.2.6 Specific heat capacity ... 54
4.2.7 Volumetric heat capacity ... 55
4.2.8 Measurement uncertainties ... 55
4.3 Results and discussion ... 56
4.3.1 Measurement method ... 56
4.3.2 Sample preparation ... 58
4.3.3 Influence of the water-solid-ratio (w/s) ... 62
4.3.4 Estimation of the volumetric heat capacity ... 63
4.4 Conclusion ... 66
4.5 Acknowledgements ... 67

5 In-situ thermal properties of grouting materials in borehole heat exchangers ... 69

Abstract ... 69
5.1 Introduction ... 69
5.2 Material and methods ... 71
5.2.1 Study site ... 71
5.2.2 Sampling ... 72
5.2.3 Laboratory analyses ... 73
5.2.4 In-situ experiment ... 74
5.3 Results and discussion ... 75
5.3.1 Laboratory and batch samples ... 75
5.3.2 Field samples ... 76
5.3.3 In-situ results ... 81
5.4 Conclusion ... 85
5.5 Acknowledgements ... 85

6 Synthesis ... 87

6.1 Summary ... 87
6.2 Perspectives and Outlook ... 90

Appendices ... 93

Appendix Study 1 93
Appendix Study 2 108
Appendix Study 3 111

References 117

Acknowledgements 133

Declaration of authorship 135

List of figures

Figure 1-1: Graphical overview of this thesis 6
Figure 2-1: Site location in Biberach an der Riß 13
Figure 2-2: Average cable temperatures and specific heat load during the heating time 17
Figure 2-3: Adjusted specific heat loads about the cable length 19
Figure 2-4: Depth-specific results 21
Figure 2-5: Evaluation of the effective thermal conductivities 22
Figure 2-6: Darcy velocities and corresponding effective thermal conductivities from studies evaluating groundwater-influenced TRTs 24
Figure 3-1: Overview of the study site in Neuweiler 32
Figure 3-2: Petrophysical properties of the Triassic sandstones 38
Figure 3-3: Thermal conductivities derived using various theoretical models 39
Figure 3-4: Exemplary polarisation microscopy images from thin sections 40
Figure 3-5: Comparison of the different methods to determine the thermal conductivities 43
Figure 4-1: Workflow for the determination of thermal conductivity and volumetric heat capacity of grouting materials 51
Figure 4-2: Comparison of measurement methods 56
Figure 4-3: Comparison of thermal conductivities and volumetric heat capacities with varying mixing speed. 59
Figure 4-4: Comparison of water contents, thermal conductivities and volumetric heat capacities for varying curing conditions 60
Figure 4-5: Thermal conductivity, specific heat capacity, wet bulk density and water content with increasing hydration times. 61
Figure 4-6: Influence of the water-solid-ratio 64
Figure 4-7: Correlation between the wet bulk density and the suspension density. 65
Figure 4-8: Comparison of the measured and the estimated volumetric heat capacities 66
Figure 5-1: Location of the field site 72
Figure 5-2: Material properties of the grouting materials 77
Figure 5-3: Pore size distribution of the two grouting materials 78
Figure 5-4: Pore size distribution and particle size distribution 80
Figure 5-5: Depth-specific thermal conductivities 81
Figure 5-6: Evaluation of the short-time ETRT for stacked data 83
Figure 5-7: Position of the BHE pipes and the hybrid cables within borehole B1 84
Figure 6-1: Analysing the thermal properties of BHE systems 88

List of tables

Table 2-1: Thermal conductivities of bucket samples 12
Table 2-2: Specific heat load, effective thermal conductivity, Darcy velocity and hydraulic conductivity....17
Table 3-1: Petrophysical, mineralogical and structural analysis methods 34
Table 3-2: Theoretical models to estimate thermal conductivities....35
Table 3-3: Thermal conductivity values of the mineral components and their estimated weighing factors. 36
Table 4-1: Overview of the analysed grouting materials 52
Table 4-2: Suspension properties and porosity of the grouting materials at varying mixing speed....59
Table 5-1: Borehole geometry, specifications of the BHE and grouting materials. 73
Table 5-2: Samples and methods applied in this study 73
Table 5-3: Material properties of the laboratory, batch and field samples....76
Table 5-4: Material properties of the soil samples. 79

Acronyms and symbols

A	Cross sectional area [m^2]
A_{pore}	Average inner pore surface [m^2 g^{-1}]
A-DTS	Active distributed temperature sensing
ATRT	Actively heated fibre optic thermal response test
bgl	Below ground level
BHE	Borehole heat exchanger
C	Empirically derived coefficient
Cl	Clay content [%]
CLSM	Controlled low strength material
CO_2	Carbon dioxide
CO_3	Carbonate content [%]
c_p	Specific heat capacity [kJ kg^{-1} K^{-1}]
$c_{p,d}$	Specific heat capacity of the dry sample [kJ kg^{-1} K^{-1}]
$c_{p,f}$	Specific heat capacity at original water content [kJ kg^{-1} K^{-1}]
$c_{p,g}$	Specific heat capacity of the grouting material [kJ kg^{-1} K^{-1}]
$c_{p,s}$	Specific heat capacity of the subsurface [kJ kg^{-1} K^{-1}]
$c_{p,w}$	Specific heat capacity of water [kJ kg^{-1} K^{-1}]
d_b	Borehole diameter [m]
D_{15}	Particle diameter of the loess with 15 % smaller particles [µm]
d_{85}	Particle diameter of the grouting material with 85 % smaller particles [µm]
DIN	Deutsches Institut für Normung (German Institute for Standardisation)
d_{po}	Outer pipe diameter [m]
d_{pore}	Pore diameter [µm]
DSC	Differential scanning calorimetry

DTRT	Distributed thermal response test
DTS	Distributed temperature sensing
EGRT	Enhanced geothermal response test
E_i	Exponential integral
ETRT	Enhanced thermal response test
f	Rock-specific empirical f-constant [-]
Fsp	Feldspar content [%]
g_i	Geometrical shape factor [-]
GSHP	Ground source heat pump
i	Hydraulic gradient [-]
I	Current [A]
ICS	Infinite cylindrical source
ILS	Infinite line source
k	Hydraulic conductivity [m s^{-1}]
K	Permeability [mD]
l	Cable length [m]
l_c	Characteristic length [m]
m	Slope [K $ln(s)^{-1}$]
m_d	Mass of the dried sample [g]
m_f	Mass of the wet sample [g]
m_h	Mass under buoyancy [g]
MILS	Moving infinite line source
n	Number of measurements
N	Filter criterion by Terzaghi [-]
n_c	Rock-specific empirical n-constant [-]
NMR	Nuclear magnetic resonance
Pe	Péclet number

PE	Polyethylene
P_{el}	Electrical power [W]
PVC	Polyvinyl chloride
Q	Heat load [W]
q	Specific heat load [W m^{-1}]
q_{adj}	Adjusted specific heat load [W m^{-1}]
q_{ave}	Average specific heat load [W m^{-1}]
$q_{R=fix}$	Specific heat load assuming constant electrical resistance [W m^{-1}]
RH	Relative humidity
Qz	Quartz content [%]
r	Pearson coefficient
R	Electrical resistance [Ω]
R^2	Degree of determination
r_b	Borehole radius [m]
$R_{b,eff}$	Effective borehole thermal resistance
r_{cable}	Radius of the hybrid cable [m]
r_H	Distance from the heat source [m]
RMSE	Root mean square error
r_{pi}	Inner pipe radius [m]
r_{po}	Outer pipe radius [m]
Rock	Lithic fragment content [%]
R_T	Electrical resistance at a defined temperature [Ω]
R_{T20}	Reference electrical resistance [Ω]
R_{th}	Thermal borehole resistance [m K W^{-1}]
s	Standard deviation
SO_2	Sulphur dioxide
S_r	Saturation [-] or [%]

t	Time [s]
T	Temperature [°C]
T_0	Undisturbed subsurface temperature [°C]
TCR	Temperature coefficient of resistance
THW	Transient hot wire
TPS	Transient plane source
TRT	Thermal response test
T_{sub}	Subsurface temperature [°C]
T_{sur}	Surface temperature [°C]
t_{start}	Theoretical starting time criterion [s]
u	Integration variable
U	Voltage [V]
UN	United Nations
u_s	Standard uncertainty
VDI	Verein Deutscher Ingenieure (Association of German engineers)
v_f	Darcy velocity [m d^{-1}]
v_{th}	Effective heat transport velocity [m s^{-1}]
w	Water content [-] or [%]
w/s	Water-solid-ratio [-]
x_i	Measurement value
$\bar{x}$	Arithmetic mean of all measurement values
z	Depth [m]
α	Thermal diffusivity [m^2 s^{-1}]
α_{T20}	Temperature coefficient of resistance [K^{-1}]
γ	Euler's constant
ϑ	Angle to the groundwater flow direction
λ	Thermal conductivity [W m^{-1} K^{-1}]

λ_{ari}	Thermal conductivity calculated with the arithmetic mean [W m^{-1} K^{-1}]
λ_{ave}	Thermal conductivity calculated with the Hashin-Shtrikman average [W m^{-1} K^{-1}]
λ_{dry}	Laboratory-measured thermal conductivity of a dry sample [W m^{-1} K^{-1}]
λ_{eff}	Effective thermal conductivity [W m^{-1} K^{-1}]
λ_{est}	Estimated thermal conductivity [W m^{-1} K^{-1}]
λ_{f}	Thermal conductivity of the pore fluid [W m^{-1} K^{-1}]
λ_{g}	Thermal conductivity of the grouting material [W m^{-1} K^{-1}]
λ_{geo}	Thermal conductivity from geometric mean [W m^{-1} K^{-1}]
λ_{har}	Thermal conductivity from harmonic mean [W m^{-1} K^{-1}]
λ_{l}	Thermal conductivity from the Hashin-Shtrikman lower bound [W m^{-1} K^{-1}]
λ_{m}	Thermal conductivity of the solid matrix [W m^{-1} K^{-1}]
λ_{p}	Thermal conductivity of the BHE pipe [W m^{-1} K^{-1}]
λ_{s}	Thermal conductivity of the subsurface [W m^{-1} K^{-1}]
λ_{sat}	Laboratory-measured thermal conductivity of a saturated sample [W m^{-1} K^{-1}]
λ_{SSD}	Thermal conductivity from the statistical spatial distribution mean [W m^{-1} K^{-1}]
λ_{u}	Thermal conductivity from the Hashin-Shtrikman upper bound [W m^{-1} K^{-1}]
λ_{VRH}	Thermal conductivity from the Voigt-Reuss-Hill model [W m^{-1} K^{-1}]
λ_{Vries}	Thermal conductivity from the de Vries model [W m^{-1} K^{-1}]
ρ_{b}	Wet bulk density [g cm^{-3}]
ρ_{d}	Dry bulk density [g cm^{-3}]
ρ_{s}	Solid density [g cm^{-3}]
ρ_{sus}	Suspension density [g cm^{-3}]
ρ_{w}	Density of water [g cm^{-3}]
ρc_{p}	Volumetric heat capacity [MJ m^{-3} K^{-1}]
$\rho c_{p,d}$	Volumetric heat capacity of the dry sample [MJ m^{-3} K^{-1}]
$\rho c_{p,f}$	Volumetric heat capacity at original water content [MJ m^{-3} K^{-1}]
$\rho c_{p,g}$	Volumetric heat capacity of the grout [MJ m^{-3} K^{-1}]

$\rho c_{p,s}$	Volumetric heat capacity of the subsurface [MJ m^{-3} K^{-1}]
ρc_w	Volumetric heat capacity of water [MJ m^{-3} K^{-1}]
ρ_{T20}	Reference resistivity [Ω mm^2 m^{-1}]
ϕ	Total porosity [-]
ϕ_{open}	Open porosity [%]
ϕ_W	Water filled pore space [-]

1 Introduction

1.1 Motivation

Amidst the accomplishment of the climate goals (United Nations, 2015), the heating and cooling sector has to transition to renewables. Heating and cooling account for over 50 % of the primary energy consumption in Germany, while only 18.8 % of the total energy consumption for heating and cooling is provided by renewable energy sources (AGEB, 2024). The German Climate Protection Law (*Bundes-Klimaschutzgesetz (KSG)*, 2019) strives for a reduction of 65 % of greenhouse gas emissions by 2030. In the building sector, a decrease of 43 % is planned. Furthermore, the German Heat Planning Act (*Wärmeplanungsgesetz*, 2023) defines a percentage of 50 % renewables and anavoidable waste heat for grid-bound heating supply until 2030.

Heat pumps are accepted as one key technology to achieve these targets (Greif, 2023). The two most common heat pump systems are the air source heat pump (ASHP) and the ground source heat pump (GSHP). GSHP systems have several advantages against ASHP systems. Since GSHP systems use the subsurface as a heat source, they can achieve higher efficiencies, have lower energy consumption, a higher seasonal stability of the heat source and, thereby, support a higher electrical grid stability (Rashid et al., 2023). Moreover, the ground can serve as a heat sink for cooling demands. GSHP systems were increasingly adopted worldwide (Adebayo et al., 2024). As of 2019, GSHP systems are installed worldwide, with a capacity of 77.5 GW_t, with 4.4 GW_t being installed in Germany (Lund and Toth, 2021). The increase of heat pumps continues in general, but the rise of GSHP systems in Germany stagnates (Bundesverband Deutsche Wärmepumpe, 2023). Reasons for this trend are the high initial costs of installing the GSHP system (Maghrabie et al., 2023) and the public awareness and acceptance of the technology due to past damage events (Fleuchaus and Blum, 2017).

Generally, GSHP systems can be divided into open and closed systems. While open systems use directly pumped groundwater as a heat source, closed systems use a secondary cycle, where a heat transfer fluid is pumped through heat exchanger pipes (Stauffer et al., 2014). Closed systems can be installed vertically, e.g., in the form of a borehole heat exchanger (BHE), or horizontally (Rashid et al., 2023). This thesis explicitly focuses on the BHE, as BHEs are the primary installed GSHP systems (Acuña and Palm, 2010; Bayer et al., 2012). They require limited land usage and are independent of seasonal fluctuations of the ground temperature (Maghrabie et al., 2023; Yang et al., 2010).

To promote GSHP systems, the systems have to be safe and economically viable. Thus, they have to be planned efficiently and sustainably by knowing the effective heat transfer capacity of the BHE and, thus, by understanding the thermal properties of the BHE system.

1.2 Thermal properties of BHE systems

The BHE system is thermally described by the conditions of the study site and the borehole. The study site is characterised by its geological and hydrogeological specifications, which can be heterogeneous and variable. The borehole includes the backfill material, the heat exchanger pipes and the heat transfer fluid. Technical adjustments to the borehole, i.e., the choice of materials, configurations and operational parameters, can improve the performance of the GSHP system. In many countries, the backfill material consists of a grouting material, i.e., a cement-based backfill material (IEA ECES, 2020; Stober and Bucher, 2020). The grouting material stabilises the borehole, hinders vertical groundwater flow at the borehole and enables the heat transfer from the subsurface to the heat exchanger pipes (Allan and Kavanaugh, 1999; IEA ECES, 2020; Javadi et al., 2018). Hence, grouting materials are often thermally enhanced (Javadi et al., 2018; Mahmoud et al., 2021). Overviews of grouting materials for BHEs can be found, e.g., in Javadi et al. (2018), Liang et al. (2022) or Wang et al. (2024).

The primary heat transport mechanisms at a BHE are heat conduction and advection. Conduction is defined by the thermal conductivity λ_s and volumetric heat capacity $\rho c_{p,s}$ of the subsurface. Advection is defined by the hydraulic conductivity k of the subsurface, the hydraulic gradient i and the corresponding Darcy velocity v_f. The thermal conductivity of the subsurface is a crucial design property for GSHP systems and focus of many studies (Galgaro et al., 2021; Han and Yu, 2016; Rashid et al., 2023; Spitler and Gehlin, 2015). The volumetric heat capacity of the subsurface was identified to have a lower influence on the efficiency of the GSHP system with only a limited value range in geologic media (Giordano et al., 2021; Wagner and Clauser, 2005). In contrast, groundwater flow can significantly improve heat transport and, therefore, the efficiency of BHEs (Han and Yu, 2016; Jia et al., 2022; Liang et al., 2022; Stauffer et al., 2014).

The heat transfer from the subsurface to the heat exchanger pipes is influenced by heat conduction through the grouting material, defined by the thermal conductivity λ_g and the volumetric heat capacity $\rho c_{p,g}$ of the grouting material. A high thermal conductivity of the grout improves the heat transfer from the ground to the heat transfer fluid (Allan and Kavanaugh, 1999; Delaleux et al., 2012; Desmedt et al., 2012; Lee et al., 2012; Verdoya et al., 2018; Viccaro, 2018). However, the appropriate grout thermal conductivity depends also on the subsurface thermal properties (Liu et al., 2024). The grout volumetric heat capacity is an important property, especially for the short-term temperature response and the operation of the GSHP system in intermittent mode (Han and Yu, 2016; Li et al., 2019; Nian and Cheng, 2018; Wang et al., 2022).

Thus, knowledge of the thermal properties of the BHE system is crucial to reducing the BHE length and to planning cost-efficient and sustainable GSHP systems (Zhang et al., 2014). Hence, careful determination of the properties is vital.

1.3 Measurement methods

The following paragraph summarises the common methods described in the literature to analyse the thermal properties of the BHE system (Liang et al., 2022; Luo et al., 2016; Stauffer et al., 2014).

1.3.1 Laboratory methods

Thermal properties of the subsurface material, i.e., rock and soil, are measured from core samples or cuttings. The sampling of representative aliquots and the sample preparation are crucial parts of the laboratory analysis (Popov et al., 2016). Grout thermal properties are analysed from samples manufactured in the laboratory. The manufacture procedures vary between studies from different laboratories (e.g., Erol and François, 2014; Kim and Oh, 2020; Song et al., 2019; Zhao et al., 2024).

Thermal conductivity is measured with steady-state or transient measurement methods (Clauser and Huenges, 1995; Liang et al., 2022). Steady-state methods establish a constant temperature gradient within the sample. Thermal conductivity is calculated by applying Fourier's Law, in one-dimensional form expressed as

$$q_x = -\lambda \frac{\partial T}{\partial x} \tag{1-1}$$

with q_x [W m^{-2}] being the specific heat flow density, λ [W m^{-1} K^{-1}] the thermal conductivity and $\partial T / \partial x$ [K m^{-1}] the temperature gradient. One common steady-state method is the divided bar method (Clauser and Huenges, 1995; Popov et al., 2016; Schön, 2011). Transient methods evaluate the time-dependent temperature response of the sample due to a defined heat load by applying analytical models derived from the differential equation for heat conduction (e.g., Hellström, 1991):

$$\nabla^2 T = \frac{1}{\alpha} \frac{\partial T}{\partial t} \tag{1-2}$$

with t [s] being the time and α [m^2 s^{-1}] thermal diffusivity. Commonly applied transient methods are the transient hot wire (THW) method as a full space line source (needle probe) (ASTM International, 2023) or as a half space line source (surface probe), the transient plane source (TPS) method (Gustafsson, 1991), and the contactless optical scanning (OS) method (Popov et al., 1983). While the steady-state methods generally produce more accurate results, the transient methods have the advantage of shorter measurement times (Zhao et al., 2016). Moreover, moisture migration and sample drying can be an issue when using steady state methods on (partly) saturated samples (Vieira et al., 2017). Overviews of the different measurement techniques can be found, e.g., in Popov (2016) or Zhao et al. (2016). A summary of the limitations and advantages of different measurement techniques can be found in Viera et al. (2017). An overview of grout investigations for GSHP systems can be found in Liang et al. (2022). However, a comprehensive method review for grouting materials is currently lacking.

The volumetric heat capacity of rocks is typically derived from specific heat capacity values analysed with calorimetric methods (Clauser, 2006; Popov et al., 2016). Measurement principles

depend on the relationship between the temperature change in a sample and the amount of injected or extracted heat (Stober and Bucher, 2020). One common method is the differential scanning calorimetry (DSC), which evaluates the difference in heat flow between the sample material and a reference material as a function of temperature (Höhne et al., 2003; Popov et al., 2016). Only a few studies analysed the heat capacity of grouting materials. Calorimetric methods were applied (Extremera-Jiménez et al., 2021), as well as deriving the volumetric heat capacity from transient thermal conductivity measurements (e.g., Frąc et al., 2021; Kim and Oh, 2019).

Additionally, for small systems or in the early stages of planning, reported laboratory data is often used to estimate thermal conductivity and volumetric heat capacity of the subsurface from lithological data (Galgaro et al., 2021; Sakata et al., 2020). Estimates are based on lithology or known material properties, e.g., mineralogy and porosity, in combination with thermal conductivity models (Abdulagatova et al., 2009; Clauser, 2006; Jia et al., 2019). The quality of the estimate depends on the quality of the database, the borehole profile, and the heterogeneity of the subsurface (Galgaro et al., 2021).

1.3.2 Thermal response test

Laboratory-derived thermal conductivities may not be representative for field conditions due to, e.g., variations in temperature and pressure, fractures or groundwater flow. Thermal response tests (TRT) are established field tests to determine the thermal properties of the subsurface in situ (Spitler and Gehlin, 2015; Zhang et al., 2014). Based on the operation of a GSHP, a fluid is circulated through the BHE with a defined heat load. The temperature response to the heat load is logged at the inlet and outlet of the BHE (Gehlin, 2002; Raymond et al., 2011). Evaluation of the TRT is based on the differential equation for heat conduction. Several analytical solutions solve this equation about effective thermal conductivity λ_{eff} and effective borehole thermal resistance $R_{b,eff}$ under the assumption of several boundary conditions (Li and Lai, 2015; Yang et al., 2010). The effective borehole thermal resistance summarises the heat transfer processes within the borehole, from the subsurface to the heat transfer fluid (Hellström, 1991). The most common solutions are the infinite line source (ILS) model and the infinite cylindrical source (ICS) model (Carslaw and Jaeger, 1959; Ingersoll and Plass, 1948). To account for advective heat transport, other analytical models like the moving infinite line source (MILS) model can be applied (Diao et al., 2004; Wagner et al., 2013). However, model assumptions, such as homogeneous flow conditions, limit the application of these models (Jia et al., 2022). Numerical models are applied to better describe the BHE system as a composite system (Rainieri et al., 2011; Zhang et al., 2024). Long computational times are a drawback and a hindrance to applying numerical models in practice (Jia et al., 2019).

The volumetric heat capacity of the subsurface cannot reliably be determined with a TRT. Even though in some TRT studies, parameter estimation approaches were used to estimate volumetric heat capacity from a TRT (Zhang et al., 2019), the sensitivity of the temperature response to the volumetric heat capacity is low, and therefore, the uncertainty of the estimation is very high (Pasquier, 2015; Raymond et al., 2015, 2011; Wagner and Clauser, 2005). Thus, volumetric

heat capacity is commonly derived from lithological data rather than field studies (Raymond et al., 2015; Wagner and Clauser, 2005).

The conventional TRT analysis provides one effective value for thermal conductivity and borehole thermal resistance for the entire borehole. However, in a heterogeneous subsurface, the thermal properties of the subsurface can highly vary, and depth-specific information is desirable to improve the BHE design (Bertermann and Suft, 2024; Luo et al., 2016, 2014; Ma et al., 2022; Wilke et al., 2020). Further enhancement of the TRT technique to additionally derive depth-specific information of the subsurface was achieved using fibre optic cables and distributed temperature sensing (DTS) (Wilke et al., 2020). DTS is based on Raman scattering using the temperature-dependent ratio between anti-Stokes and Stokes signals (Hartog and Gamble, 1991; Selker et al., 2006). A laser emits a short optical pulse into an optical fibre. The photon backscatter is measured as a function of time to derive the temperature at different positions along the optical fibre. Fibre optic cables are used passively as a distributed thermal response test (DTRT), where the heat load is applied by a circulated fluid (Acuña, 2013; Fujii et al., 2006). Moreover, they are used actively with a heating cable as an enhanced thermal response test (ETRT) (Heidinger et al., 2004; Zhang et al., 2020). With less metrological effort, heating cables can apply a more controlled heat load to the subsurface (Raymond et al., 2010). Still, only a few studies on ETRT are available, especially about validation with high-resolution borehole data (e.g., Ma et al., 2022) or application of the ETRT for depth-distributed groundwater flow determination (e.g., Lehr and Sass, 2014).

To analyse the thermal properties of grouting materials in situ, some studies suggested evaluating the thermal response time-dependently, where the early-time data describes the thermal properties of the grout and the late-time data describes the ground thermal properties (Bozzoli et al., 2011; Li et al., 2019; Riegger et al., 2012; Zhang et al., 2020). The early response was evaluated from conventional TRT by applying the concept of equivalent diameter or numerical models (Lamarche and Beauchamp, 2007; Shirazi and Bernier, 2013). Moreover, Riegger et al. (2012) proposed the evaluation with the ILS model from ETRT. However, validation of the method with field data is challenging.

1.4 Objectives

As demonstrated, several methods exist to determine the thermal properties of BHE systems. Most of these methods focus on the thermal conductivity of the subsurface. Further research is still needed regarding the analysis of grouting materials. Thus, to improve the knowledge of the thermal properties of the entire BHE system, the central objective of this thesis is to investigate and improve the methods to analyse the thermal properties of the subsurface and the grout. Accordingly, four specific research questions are derived that are focussed on in four individual studies. These four studies discuss and compare various analysis methods on different scales, from the laboratory to the field. Figure 1-1 graphically summarises the objectives of this thesis by highlighting the focus of the four studies.

- **Study 1** aims to understand the limitations of the ETRT and improve the measurement setup, the evaluation method and the interpretation of the results.

- **Study 2** aims to understand the suitability of theoretical models to estimate rock thermal conductivity in the laboratory and field.
- **Study 3** aims to improve the comparability between measurement data for the determination of the thermal properties of grouting materials in the laboratory by establishing a standardised method.
- **Study 4** aims to investigate the thermal properties of grouting materials in the field.

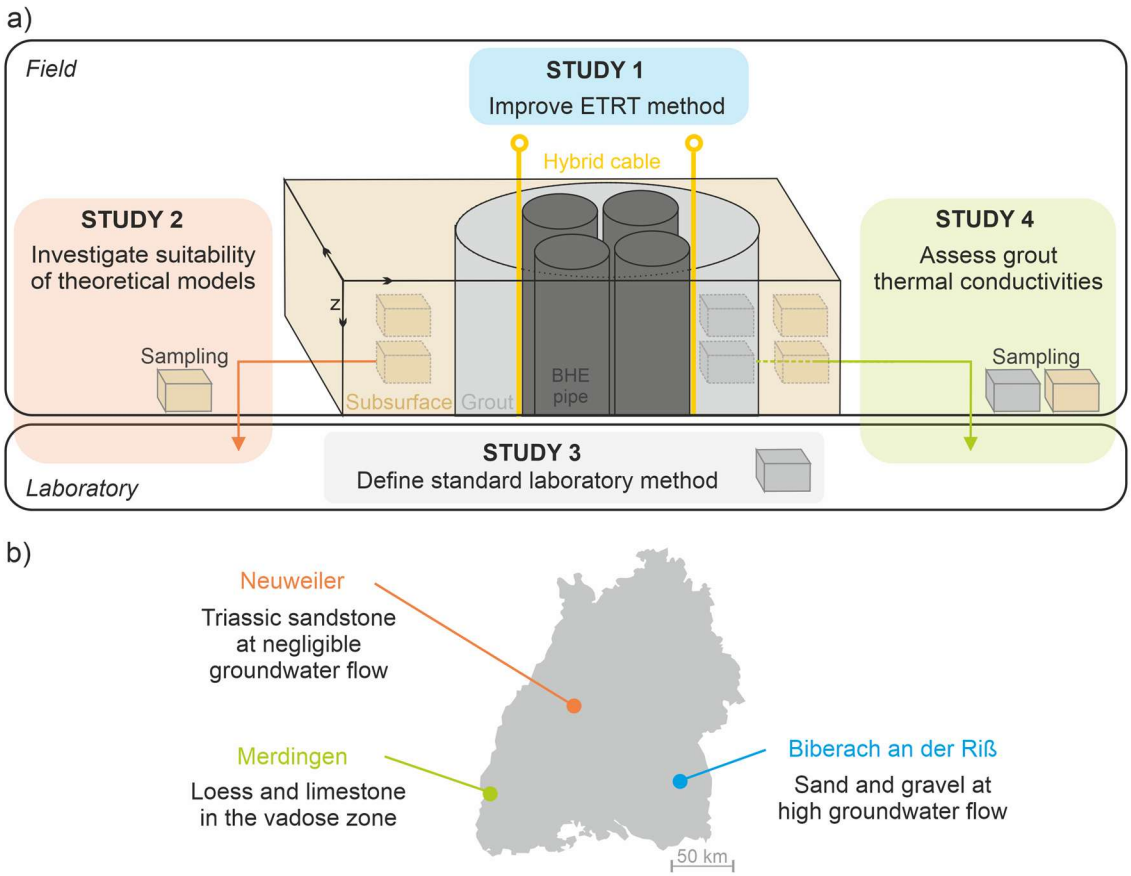

Figure 1-1: Graphical overview of this thesis, a) highlighting the focus of the different studies on analysing the thermal properties of BHE systems, b) location of the three investigated study sites and their (hydro-)geological conditions in the state of Baden-Württemberg, Germany.

1.5 Outline

This cumulative thesis presents four individual studies from Chapters 2 to 5. All studies were submitted to international peer-reviewed journals. Studies 1 and 3 are already published. Studies 2 and 4 are currently under review. The thesis is structured as follows:

- **Study 1** on "*Evaluating an enhanced thermal response test (ETRT) with high groundwater flow*" presents a field study. The ETRT is applied at a study site with high groundwater flow and critically evaluated. Darcy velocities are determined using the ILS model and Péclet number analysis and compared to the results from evaluation with the MILS model and from a pumping test. Additionally, different approaches for

calculating the specific heat load of the ETRT are examined. Improvements in the measurement setup, the evaluation method and the interpretation of the results are given.

- **Study 2** on "*Depth-specific thermal conductivities of Triassic sandstones*" is a combined laboratory and field study. Thermal conductivities of Triassic sandstones are analysed and related to their material properties. Existing theoretical models are examined for suitability and transferability to the field by verifying estimated thermal conductivities with laboratory measurements and comparing them to ETRT results.
- **Study 3** focuses on the "*Determination of thermal properties of grouting materials for borehole heat exchangers (BHE)*". First, a comprehensive overview of the analysis methods for the thermal properties of grouting materials is provided. Then, in an extensive laboratory study, different procedures for analysing thermal conductivity and volumetric heat capacity of grouting materials are examined by systematically comparing the influence of the measurement method and the sample preparation on the resulting thermal properties for seven dissimilar grouting materials with varying water-solid ratios (w/s) and compositions. From the findings, recommendations for the analysis procedure to determine thermal properties in the laboratory are derived.
- **Study 4** on "*In-situ thermal properties of grouting materials in borehole heat exchangers*" combines a laboratory and a large-scale field experiment for determining the thermal properties of grouting materials in the field. BHEs with two different grouting materials are constructed within unsaturated loess and limestone. After conducting field experiments, the boreholes are excavated up to a depth of 15 m. Field samples of the grouting materials are collected, and their thermal properties are characterised by extensive laboratory experiments. The results are compared with grouting samples manufactured in the laboratory and discussed about filtration. Moreover, they are compared with in-situ thermal conductivities determined with the short-time ETRT.

The thesis concludes with a synthesis in Chapter 6. The main findings of the different studies are discussed in relation to the main objective. Recommendations for a "best practice" approach for the analysis of the thermal properties of BHE systems are derived. Finally, an outlook proposing ideas for future research is provided.

2 Evaluating an enhanced thermal response test (ETRT) with high groundwater flow

Reproduced from Albers, A., Steger, H., Zorn, R., Blum, P., 2024. Evaluating an enhanced thermal response test (ETRT) with high groundwater flow. Geothermal Energy 12:1. https://doi.org/10.1186/s40517-023-00278-y

Abstract

Enhanced thermal response tests (ETRT) enable the evaluation of depth-specific effective thermal conductivities. Groundwater flow can significantly influence the interpretation of ETRT results. Hence, this study aims to critically evaluate an ETRT with high groundwater flow (> 0.2 m d^{-1}). Different approaches in determining the specific heat load of an ETRT are compared. The results show that assuming constant electrical resistance of the heating cable with time can account for an inaccuracy of 12 % in the determination of effective thermal conductivities. Adjusting the specific heat loads along the borehole heat exchanger (BHE) depth, the specific heat loads vary within 3 %. Applying the infinite line source model (ILS) and Péclet number analysis, a depth-average hydraulic conductivity is estimated to be 3.1×10^{-3} m s^{-1}, thereby, confirming the results of a pumping test of a previous study. For high Darcy velocities (> 0.6 m d^{-1}), the uncertainty is higher due to experimental limitations in ensuring a sufficient temperature increase for the evaluation ($\Delta T > 0.6$ K). In these depths, the convergence criterion of $\Delta\lambda_{eff}/\lambda_{eff} < 0.05$ / 20 h for the ILS sequential forward evaluation cannot be achieved. Thus, it can be concluded that time-averaging of the heat load by monitoring voltage and current during ETRT is essential. Therefore, the specific heat load adjustment along the heating cable is recommended. To improve the estimation of depth-specific effective conductivities with high groundwater flow and to reduce the sensitivity towards temperature fluctuations ($\Delta T \sim 0.1$ K), measures for applying higher specific heat loads during the ETRT are essential, such as actions against overheating of the cable outside the BHE.

2.1 Introduction

For the dimensioning of ground source heat pump (GSHP) systems, knowledge of the thermal properties of the subsurface is crucial. Not only the effective thermal conductivity λ_{eff} of the subsurface but also the consideration of groundwater flow is important since advection can significantly improve the heat transport and, therefore, the efficiency of borehole heat exchangers (BHE) (Stauffer et al., 2014). The thermal response test (TRT) is an established method to determine in-situ effective thermal conductivities (Spitler and Gehlin, 2015). In a conventional TRT, a defined heat load is injected into or extracted from the ground by circulating the heat

transfer fluid of the BHE, and the temperature development is measured at the inlet and outlet of the pipes with temperature probes (Verein Deutscher Ingenieure, 2020). Using analytical solutions of the heat source equation, e.g., the infinite line source model (ILS), an integral value of the effective thermal conductivity can be derived (Carslaw and Jaeger, 1959; Gehlin, 2002; Verein Deutscher Ingenieure, 2020). Elevated groundwater flow (> 0.1 m d^{-1}) can influence the interpretation of TRT results (Chiasson et al., 2000; Signorelli et al., 2007). The system adjusts fast to the applied heat disturbance when advection is present and significant. If the ILS is applied, higher values of the effective thermal conductivity λ_{eff} will be evaluated due to the groundwater flow and the results will show sensitivity towards evaluation time (Angelotti et al., 2018; Katsura et al., 2006; Sanner et al., 2005). Other evaluation models such as the moving infinite line source model (MILS) are therefore recommended if groundwater flow is present (Diao et al., 2004; Molina-Giraldo et al., 2011; Wagner et al., 2013).

In the last years, the TRT setup was further developed (Wilke et al., 2020; Zhang et al., 2021). One development was the application of optic fibre distributed temperature sensing (DTS) for quasi-continuous temperature profile measurement, the so-called distributed TRT (DTRT) with the advantage of determining depth-specific effective thermal conductivities (Acuña, 2013; Fujii et al., 2006). Another development was the use of heating cables as a heat source. With heating cables, a more controlled heat load can be applied to the subsurface with less metrological effort (Raymond et al., 2010). With an enhanced TRT (ETRT) (Wilke et al., 2020), also described as actively heated fibre optic TRT (ATRT) (Zhang et al., 2020), fibre optic cables are used along with heating cables. Thus, the advantages of both implementations are combined. Most ETRT studies were conducted with a hybrid cable, a composite cable of fibre optic and heating cables (Dalla Santa et al., 2022; Galgaro et al., 2018; Hakala et al., 2022; Huber, 2013; Lehr and Sass, 2014; Maldaner et al., 2019; Simon and Bour, 2022; Vieira et al., 2017). Hence, temperature measurement and heating were located at the same location. However, some studies used separate heating cable and fibre optic cable in different shanks of the BHE pipe (Vélez Márquez et al., 2018). Thereby, adding the distance between both cables as an additional parameter of uncertainty. Hakala et al. (2022) used an additional reference fibre optic cable to measure the temperature in the subsurface apart from the elevated temperature at the heating cable.

Applying a TRT, the correct determination of the effective thermal conductivity is proportionally linked to the correct calculation of the applied heat load Q. In an ETRT, the heat load is induced by an electrical shortcut of the conductor material of the heating cable. The electrical resistance of the conductor material depends on temperature (Hacker and Sumereder, 2020). During an ETRT, the cable temperature increases when the cable is heated. Thereby, its electrical resistance also changes. If the heat load is calculated with a resistance value that is determined before or at the start of an ETRT, the temperature dependence of the resistance is not considered (Luo et al., 2015). In contrast, other studies accounted for this by logging not only the voltage but also the current during the ETRT and then calculating the average heat load for the entire heating time (Dalla Santa et al., 2022; Huber, 2013; Vélez Márquez et al., 2018). Raymond et al. (2010) addressed the problem of temperature-dependent resistance by calibrating their heating cable in a circulation bath under varying temperatures before use. In some studies, the use of a power controller was recommended ensuring a constant heat load over time (Hakala et al., 2022; Lehr and Sass, 2014). For several studies, the determination approach for

the heat load was not mentioned specifically (Bussmann et al., 2015; Freifeld et al., 2008; Galgaro et al., 2018; Heske et al., 2011; Riegger et al., 2012; Vieira et al., 2017; Zhang et al., 2020). Summarising, no distinction between the different ways to calculate the specific heat load is currently made in the ETRT literature. The overall assumption is that the specific heat load does not vary along the length of the heating cable (Dalla Santa et al., 2022; Hakala et al., 2022; Lehr and Sass, 2014; Maldaner et al., 2019). However, as implied by Wilke et al. (2020), during an ETRT the temperature increase in the cable varies along the depth depending on the contact material of the cable (air, unsaturated soil, saturated soil, groundwater influence) and therefore its electrical resistance. For the application of soil water content determination, Sayde et al. (2014) addressed this by performing an adjustment of the electrical resistance along the cable length using fibre optic temperature measurements.

Of the TRT studies applying heating cables, only a limited amount is conducted in environments with enhanced groundwater flow. For example, Lehr and Sass (2014) analysed ETRT data from a study site with groundwater velocities of > 0.4 m d^{-1} in various depths. They used Péclet number analysis to derive Darcy velocities from ILS results. Antelmi et al. (2020) applied the MILS to evaluate temperature data (from wireless probes) at a study site with depth-specific groundwater velocities ranging between 0.001 m d^{-1} and 0.26 m d^{-1}. However, the principle of ETRT is analogously applied in hydrogeology as active distributed temperature sensing (A-DTS) focusing mainly on the determination of groundwater flow velocity (Banks et al., 2014; Bense et al., 2016; Coleman et al., 2015; Read et al., 2014). Instead of a hybrid cable, most often the steel case of the fibre optic cable is used as the heating element (Ciocca et al., 2012; Del Val et al., 2021; Read et al., 2014; Sayde et al., 2014; Simon and Bour, 2022). Des Tombe et al (2019) and Bakker et al (2015) applied the MILS to evaluate groundwater velocity from their A-DTS results. Del Val et al. (2021) placed the fibre optic cable between the well casing and the aquifer. They analysed the temperature data regarding groundwater flow by separating it into different heating phases. The application of ETRT for the identification of depths with enhanced groundwater flow is promising. However, due to the limited amount of studies, further experience and understanding regarding the experimental issues of ETRT are necessary.

The objective of this study is to critically evaluate an ETRT with high groundwater flow. Hence, the results of a case study in Biberach an der Riß (Germany) are presented. The evaluation of depth-specific effective thermal conductivities is conducted by applying the ILS with iterative forward modelling. Furthermore, the hydraulic conductivity is evaluated with Péclet number analysis and compared to the results applying the MILS as well as to the results of a pumping test. In addition, different methods for specific heat load calculations, which are used in the literature, are compared. Thus, for the first time, the specific heat load during the ETRT is adjusted along the heating cable using the theory of temperature-dependent resistances. The models are critically discussed and their suitability is evaluated. Finally, lessons learned are presented from applying an ETRT with high groundwater flow. Although mainly site-specific results are discussed, this study provides useful information for the planning and evaluation of future ETRT.

2.2 Material and methods

2.2.1 Experimental

2.2.1.1 Study site

The study site is located at the University of Applied Sciences in Biberach an der Riß, Germany (Figure 2-1a). This area is part of the Molasse basin. The borehole has a depth of 24 m below ground level (bgl) and penetrates the entire upper quaternary aquifer, which is characterised by alternating gravel and sand layers (Figure 2-1). The thermal conductivities were measured in the laboratory from bucket samples collected during drilling (Reuß et al., 2012). They were measured with the hot wire method (Isomet 2104, Applied Precision Ltd.) and range between 1.5 – 2.8 W m^{-1} K^{-1} (Reuß et al., 2012).

Table 2-1 gives a summary of the thermal conductivity values. In a previous study, the unconfined groundwater level was identified at a depth of about 5.6 m bgl (Reuß et al., 2012). The hydraulic gradient was measured to be $i = 0.002$ (Reuß et al., 2012). The mean hydraulic conductivity of the aquifer was measured by a pumping test to be $k = 3.1 \times 10^{-3}$ m s^{-1} (Reuß et al., 2012). From 23.4 m bgl, the aquifer is limited by tertiary sediments of the Upper Freshwater Molasse, predominantly marlstones.

Table 2-1: Thermal conductivities λ of bucket samples from the drilling at the study site in Biberach an der Riß.

Sampling depth z [m bgl]	Thermal conductivity λ [W m^{-1} K^{-1}]	Sampling depth z [m bgl]	Thermal conductivity λ [W m^{-1} K^{-1}]
0.54 – 1.57	1.9 ± 0.2	11.00 – 11.48	2.8 ± 0.1
1.57 – 2.74	1.5 ± 0.1	11.48 – 13.00	2.7 ± 0.1
2.74 – 3.00	2.2 ± 0.1	13.00 – 13.75	2.8 ± 0.1
3.00 – 3.40	2.4 ± 0.1	13.75 – 15.00	2.8 ± 0.1
3.40 – 4.61	2.5 ± 0.1	15.00 – 15.41	2.6 ± 0.1
4.61 – 5.33	2.1 ± 0.1	15.41 – 15.78	2.3 ± 0.1
4.61 – 5.33	2.7 ± 0.1	15.78 – 17.63	2.7 ± 0.1
5.33 – 6.62	2.7 ± 0.1	17.63 – 19.00	2.4 ± 0.1
6.62 – 7.56	2.5 ± 0.1	19.00 – 19.43	2.5 ± 0.1
7.56 – 8.00	2.3 ± 0.1	19.43 – 19.64	2.5 ± 0.1
8.00 – 8.60	2.6 ± 0.1	19.64 – 21.00	2.6 ± 0.1
8.60 – 9.64	2.9 ± 0.1	21.00 – 23.43	2.6 ± 0.1
9.64 – 10.91	2.5 ± 0.1	**Average**	**2.5 ± 0.4**

2.2.1.2 Material

Figure 2-1b and 1c present the experimental setup. The BHE consists of a double U-pipe with a pipe diameter of 0.025 m. The borehole has a radius of 0.089 m and is grouted with an enhanced backfill material (ThermoCem® PLUS, HeidelbergCement, $\lambda_g = 2.0$ W m^{-1} K^{-1}). In addition to 21 resistance temperature sensors (Pt100), the BHE is equipped with a hybrid cable (Figure 2-1d) with an optic fibre for temperature measurements and three copper conductors as heating element (Helukom® A-DSQ(ZN)B2Y, 1 × 4 G 50/125 + Cu 3 × 0.5 mm², length = 69.1 m). The measuring technique was pre-assembled at the outside of one U-pipe.

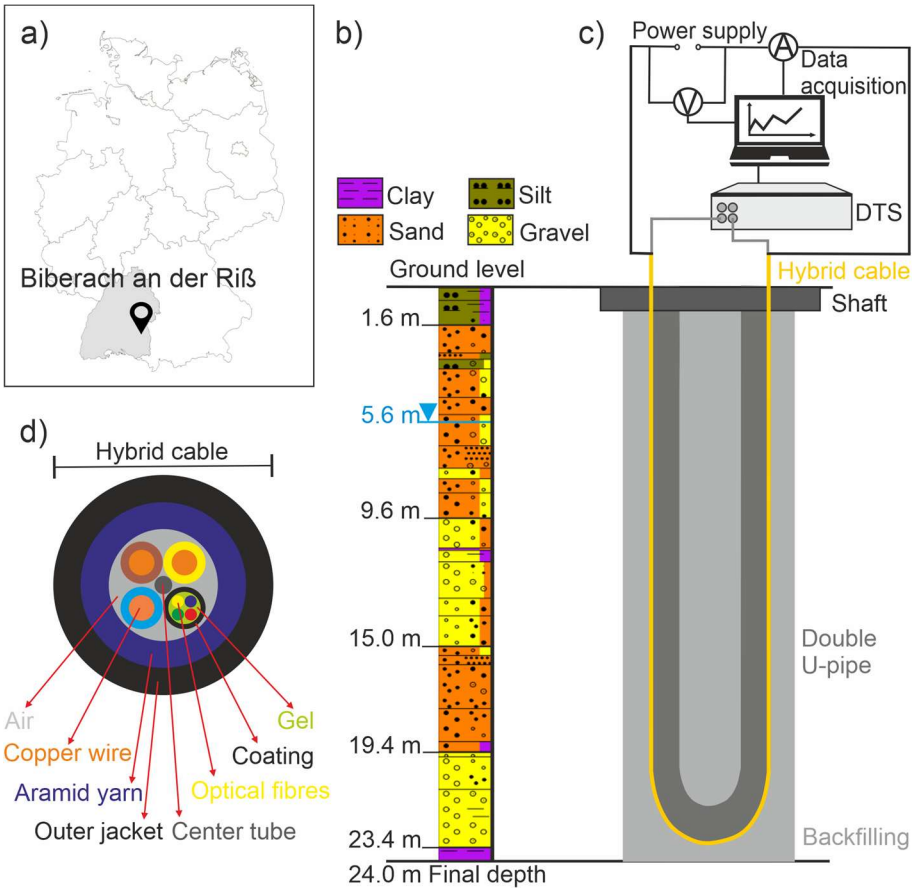

Figure 2-1: a) Site location in Biberach an der Riß (Germany), b) geological profile, c) setup of the enhanced thermal response test (ETRT) and d) cross-section of the hybrid cable.

2.2.1.3 Enhanced thermal response test (ETRT)

The ETRT started on 28th June 2021. The heating time was about 170 h. A constant voltage of about 75 V was applied to the heating cable with a DC-power supply (Power Ten Inc., R86 D-200100; 200V/100A). The voltage and the resulting current were logged for the entire heating time. The voltage was measured with a multimeter (Ahlborn, ALMEMO® 2590, measurement uncertainty ± 0.4 V). The current was indirectly measured by measuring the voltage at a shunt (Ahlborn, ALMEMO® 2590, measurement uncertainty ± 0.5 mV). The temperature was measured using DTS (Agilent, AP Sensing, N4386B, dual end measurement, measurement uncertainty manufacturer value ± 0.2 K). The temperature was measured every 60 s over the entire length of the hybrid cable with a spatial resolution of 0.5 m and a measurement interval of 1 m. The calibration of the DTS measurement was conducted by adjusting the offset to the resistance thermometers when determining the undisturbed ground temperature T_0. At the beginning, from minute 19 – 46, there was a break in heating. For the effective thermal conductivity evaluation using the ILS model, this is not expected to influence since the first hours of temperature data are excluded from the analysis.

2.2.2 Evaluation

2.2.2.1 Calculation of the specific heat load

For the calculation of the heat load, the electrical power $P_{el.}$ [W] is assumed to be equal to the heat load Q [W]:

$$P_{el.} = Q \quad \textbf{(2-1)}$$

With Joule's Law, the heat load is calculated as the product of voltage U [V] and current I [A] (Meschede, 2015):

$$Q = U\,I \quad \textbf{(2-2)}$$

The specific heat load q [W m^{-1}] is then the heat load per meter length l of the heating cable:

$$q = Q\,l^{-1} \quad \textbf{(2-3)}$$

To compare different approaches applied in ETRT studies, Equations 2 and 3 are calculated with a single measurement at the beginning of the ETRT, therefore, assuming a constant electrical resistance of the heating cable by time. This value is further referred to as $q_{R=fix}$. Additionally, the arithmetic mean of the specific heat load over the entire heating time is calculated to an average specific heat load q_{ave}.

2.2.2.2 Spatial adjustment of the specific heat load

According to Ohm's Law, the measured current is related to the electrical resistance R [Ω] of the cable. Electrical resistance is dependent on temperature, as stated in Equation 4 (Meschede, 2015). The resistance at a defined temperature R_T is calculated using the temperature difference to a reference temperature T_{20} and the material-specific temperature coefficient of the resistance (TCR) α_{T20}.

$$R_T = R_{T_{20}}(1 + \alpha_{T20}\,(T - T_{20})) \quad \textbf{(2-4)}$$

The reference resistance R_{T20} is calculated using the literature value of the resistivity ρ_{T20} and the length l and cross-section A of the heating cable (Meschede, 2015):

$$R_T = \rho_{T20}\,l\,A^{-1} \quad \textbf{(2-5)}$$

Values for α_{T20} and ρ_{T20} are taken from Kuchling (2014). Applying Ohm's law, the specific heat load can be calculated using Equation 6:

$$q = I^2\,R_{T_{20}}\big(1 + \alpha_T\,(T - T_{20})\big)\,l^{-1} \quad \textbf{(2-6)}$$

The optic fibre provides temperature values averaged over the measuring time of 60 s for every 0.5 m. Considering the heating cable as a serial connection of resistances, it applies $R_{total} = \sum R_i$ and $I_{total} = I_i$. Thus, the specific heat load can be individually determined for every length interval of the hybrid cable. The depth-specific heat load is the sum of the specific heat loads applied to both shanks of the U-pipe. Hence, applying the principle of temperature-dependent resistances using the depth-differentiated temperature measurement of the DTS, the specific heat load is spatially adjusted along the heating cable. This value is further referred to as the adjusted specific heat load q_{adj}.

2.2.2.3 Evaluation of depth-specific effective thermal conductivities

As the hybrid cable is installed in a loop next to an U-pipe of the BHE (Figure 2-1d), the temperature data of two corresponding length intervals of the DTS cable are averaged for each depth interval. In a preliminary data processing step, a moving average of every 20 measurement values of the fibre optic data is applied to reduce the noise. Then, the effective thermal conductivity λ_{eff} is evaluated using the ILS model as given in Equations 7 and 8 (Carslaw and Jaeger, 1959; Gehlin, 2002).

$$T(r_H, t) - T_0 = \frac{q}{4\,\pi\,\lambda_{eff}} E_i \left[\frac{{r_b}^2}{4\,\alpha\,t}\right] + q\,R_{th} \approx \frac{q}{4\,\pi\,\lambda_{eff}} \left(ln\left(\frac{4\,\alpha\,t}{{r_b}^2}\right) - \gamma\right) + q\,R_{th} \quad \textbf{(2-7)}$$

$$\lambda_{eff} = \frac{q}{4\,\pi\,m}\,; m = \frac{\Delta T}{\Delta ln(t)} \quad \textbf{(2-8)}$$

$T(r_H,t)$ is the temperature at a defined distance r from the heat source and a specific time t. T_0 is the undisturbed subsurface temperature at time $t = 0$. E_i is the exponential integral, α is the thermal diffusivity calculated

$$\alpha = \frac{\lambda_{eff}}{\rho c_p} \quad \textbf{(2-9)}$$

and assuming a volumetric heat capacity of the subsurface ρc_p of 2.5 MJ m^{-3} K^{-1} (Verein Deutscher Ingenieure, 2010), r_b is the borehole radius, R_{th} is the thermal borehole resistance, γ is Euler's constant and m is the slope of the linear regression line. The evaluation time is determined by applying the following theoretical starting criterion (Gehlin, 2002):

$$t_{start} = \frac{P\,{r_b}^2}{\alpha} \quad \textbf{(2-10)}$$

A model error of 5 % is accepted by setting $P = 10$. Based on the German technical guideline VDI 4640-5 (Verein Deutscher Ingenieure, 2020), the data is evaluated iteratively with the sequential forward evaluation. The convergence criterion for an effective thermal conductivity constancy of $\Delta\lambda_{eff}/\lambda_{eff} < 0.05$ / 20 h is applied. For q, the values for the different specific heat load calculations are inserted into Equation 8 (see Chapters 2.2.2.1 and 2.2.2.2). The ILS is only valid for transient heat transport. For the ideal case of constant unique groundwater flow with equal groundwater temperatures, the temperature approaches a constant value at steady-state conditions. If advection is present and significant, these conditions can occur during a TRT. Thus, for the evaluation of effective thermal conductivities, the data is evaluated up to the time when the temperature increase starts to stagnate. Thus, the point, when the effective thermal conductivity starts to approach infinity, is identified. The degree of determination R^2 and the convergence criterion are additionally considered. Measurement uncertainties of the results are considered according to the study by Witte (2013).

2.2.2.4 Evaluation of hydraulic conductivities with Péclet number analysis

As a simple way to estimate Darcy velocities from TRT results, some studies applied the Péclet analysis (Lehr and Sass, 2014; Pambou et al., 2019). This method assumes a simple linear relationship between the advective heat flow component and the difference between effective thermal conductivity λ_{eff} and thermal conductivity by conduction only λ, as stated in Equations

11 and 12. Péclet number analysis is applied for depth intervals below the groundwater level of 5.6 m.

$$Pe = \frac{\lambda_{eff}}{\lambda} - 1 \quad \textbf{(2-11)}$$

The thermal conductivity λ is taken from laboratory measurements (Chapter 2.2.1.1). To attribute the laboratory values to the depth intervals evaluated with DTS, weighted arithmetic mean values of corresponding thermal conductivities are calculated.

$$v_f = \frac{\lambda_{eff} - \lambda}{l_c \, \rho c_{p,w}} \quad \textbf{(2-12)}$$

v_f is the Darcy velocity, $l_c = r_b$ is the characteristic length based on similar studies (Ferguson, 2015) and $\rho c_{p,w}$ is the volumetric heat capacity of water.

Assuming a constant hydraulic gradient of $i = 0.002$ (see Chapter 2.2.1.1), a value for the hydraulic conductivity k can be derived:

$$k = \frac{v_f}{i} \quad \textbf{(2-13)}$$

2.2.2.5 Evaluation of hydraulic conductivities with the MILS

With significant groundwater flow, the evaluation of TRT with the MILS is recommended (Diao et al., 2004; Molina-Giraldo et al., 2011; Wagner et al., 2013). Hence, the dataset is additionally evaluated by applying the following MILS (Equation 14):

$$T_r(r_H, \vartheta, t) - T_0 = \frac{q}{4\,\pi\,\lambda}\, exp\left[\frac{v_{th}\, r_H\, cos(\vartheta)}{2\alpha}\right] \times \int_{\frac{r_H{}^2}{4\,\alpha\,t}}^{\infty} exp\left[-\frac{v_{th}{}^2\, r_H{}^2}{16\,\alpha^2\, u} - u\right]\frac{du}{u} + q\, R_{th} \quad \textbf{(2-14)}$$

ϑ is the angle to the groundwater flow direction. Considering the observation point r_H as the borehole radius r_b, the average temperature at the borehole wall is calculated as the integral average in all spatial directions (Diao et al., 2004), which can be approximated at $\vartheta = \pi/2$. The variable v_{th} is the effective heat transport velocity and u is the integration variable. The thermal conductivity λ is taken from laboratory measurements (see Chapter 2.2.1.1). Since the MILS also applies for steady-state conditions, in contrast to the ILS the later time data can be also evaluated. The parameter estimation problem is solved by minimising the root mean squared error (RMSE) by fitting R_{th} and v_{th} with the Nelder-Mead algorithm.

The Darcy velocity v_f can be calculated using the effective heat transport velocity (v_{th}) as follows (Diao et al., 2004; Zubair and Chaudhry, 1996):

$$v_f = \frac{v_{th}\, \rho c_{p,s}}{\rho c_{p,w}} \quad \textbf{(2-15)}$$

$\rho c_{p,s}$ is the volumetric heat capacity of the soil.

2.3 Results and discussion

2.3.1 Averaging the specific heat load

The specific heat load, calculated using Equation 3, is plotted in Figure 2-2 about the heating time.

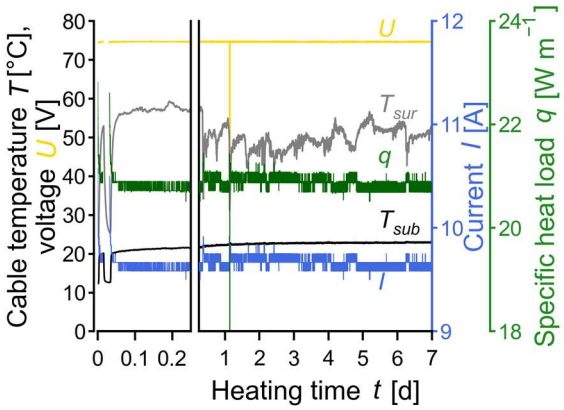

Figure 2-2: Average cable temperatures at the surface (T_{sur}) and subsurface (T_{sub}), voltage (U), current (I) and specific heat load (q) during the heating time (t).

At the start of the heating, the specific heat load equals 22.8 W m^{-1}. This value is representative of the specific heat load assuming constant electrical resistance of the heating cable with time $q_{R=fix}$ (Table 2-2). Within the first minutes of heating, the specific heat load shows a strong decrease of nearly 10 %. Then, the specific heat load varies between 20.5 W m^{-1} and 21.4 W m^{-1} with a time-averaged specific heat load of q_{ave} = 20.8 W m^{-1} (Table 2-2). Hence, the results show that although a constant voltage is applied to the heating cables, the specific heat load shows some variations during the ETRT, which are most significant at the start of the test. Thus, assuming constant electrical resistance can account for an inaccuracy in the determination of the specific heat load. An average specific heat load is more representative of the heat load applied during the ETRT.

Table 2-2: Specific heat load (q), effective thermal conductivity (λ_{eff}), Darcy velocity (v_f) and hydraulic conductivity (k) for the different approaches of heat load determination: $q_{R=fix}$ assuming constant electrical resistance, average q_{ave} and adjusted q_{adj}. Measurement uncertainties are provided in brackets. The averages of depth-specific values are calculated by applying the arithmetic mean.

Specific heat load	q [W m^{-1}]	λ_{eff} [W m^{-1} K^{-1}]	v_f [m d^{-1}] [a]	$k \times 10^{-3}$ [m s^{-1}] [b]
$q_{R=fix}$	22.8 ± 0.8	5.1 ± 0.2	0.68 ± 0.18	3.9 ± 1.0
q_{ave}	20.9 ± 0.8	4.6 ± 0.2	0.57 ± 0.16	3.2 ± 0.9
q_{adj}	20.2 ± 1.1	4.5 ± 0.2	0.53 ± 0.15	3.1 ± 0.9

[a] from Péclet number analysis
[b] from v_f assuming a constant hydraulic gradient of i = 0.002

The change in the specific heat load during the ETRT can be explained by a change in the electrical resistance of the heating cable. The electrical current is a direct indicator of the electrical resistance as an integral value for the total cable length (Figure 2-2). The change in the electrical resistance is a consequence of the change in the cable temperature. In Figure 2-2 the average subsurface temperature T_{sub} and the average surface temperature T_{sur} are plotted complementary by calculating the arithmetic mean of the respective cable lengths. The temperature change and thus the change of the specific heat load is most distinct within the first minutes of the ETRT. The temperatures increase by around 11 K in the subsurface and by around 28 K at the surface. This first heating phase is attributed to the cable material, mainly the cable isolation (Figure 2-1d). The variation of the specific heat load for the rest of the heating time can be attributed mainly to the part of the cable outside the borehole. At the surface, high diurnal temperature variations can be observed during the test. In the subsurface, these variations are considerably smaller. Hence, a depth-specific assessment of the specific heat load is suggested (Chapter 2.3.2).

Summarised, the assumption of constant electrical resistance is inappropriate for the calculation of the specific heat load. Prior knowledge of the cable's electrical resistance is insufficient to derive the heat load from the applied voltage. Further measurements of the heat load during the experiment are therefore necessary. Then, an average value can be calculated for the entire heating time. At the same time, the model assumption of constant heat load during the ETRT for effective thermal conductivity estimation can be confirmed. The average specific heat load is more representative of the heat load applied during the ETRT.

2.3.2 Spatial adjustment of the specific heat load

The theory of temperature-dependent resistances for adjusting the specific heat load along the depth of the BHE (Equation 6) is applied. The results are plotted in Figure 2-3. The specific heat loads along the entire length of the heating cable range between 20.2 W m^{-1} and 23.0 W m^{-1} (Figure 2-3b). Higher specific heat loads can be found at the surface, whereas lower specific heat loads are calculated for the installed cable in the ground. According to the theory (Equation 6), these differences are associated with the differences in the temperature increase along the cable. The different temperature increases along the cable are associated with varying heat transport along the length of the cable.

Along the heating cable, three representative areas are identified: (1) The upper part of the heating cable is installed above the surface. Here, heat transfer is mainly characterised by the surrounding air and is expected to be low. Thus, the cable significantly heats up. Due to the diurnal temperature changes, high variations of the specific heat load during the heating time can be observed (Figure 2-3a), which can also be seen in Figure 2-2. (2) The lower part of the heating cable is installed below the groundwater level. Here, the heat transfer is characterised by conductive and convective transport and is expected to be quite good. Hence, the cable shows a low-temperature increase only due to the applied heat load. Compared to the upper part of the heating cable, only a marginal time dependency of the specific heat load is apparent. (3) Above the groundwater level, the heating cable is installed some meters in the vadose zone. Heat transfer is predominantly characterised by conduction. Moisture content and seepage can have

an influence. Effectively, only the part of the heating cable installed inside the BHE can inject heat into the subsurface. Along the length of the heating cable inside the BHE, the heat load only varies within 3 % between 20.2 and 20.6 W m^{-1}. Calculating the average of the adjusted specific heat loads for this part provides an average adjusted specific heat load of 20.2 W m^{-1} (Table 2-2). Figure 2-3b compares this value with the other approaches for heat load calculation (see Chapter 2.3.1: $q_{R=fix}$ and $q_{adj,ave}$). The deviations between $q_{R=fix}$ and $q_{adj,ave}$ is 12 % and only 3 % between q_{ave} and $q_{adj,ave}$.

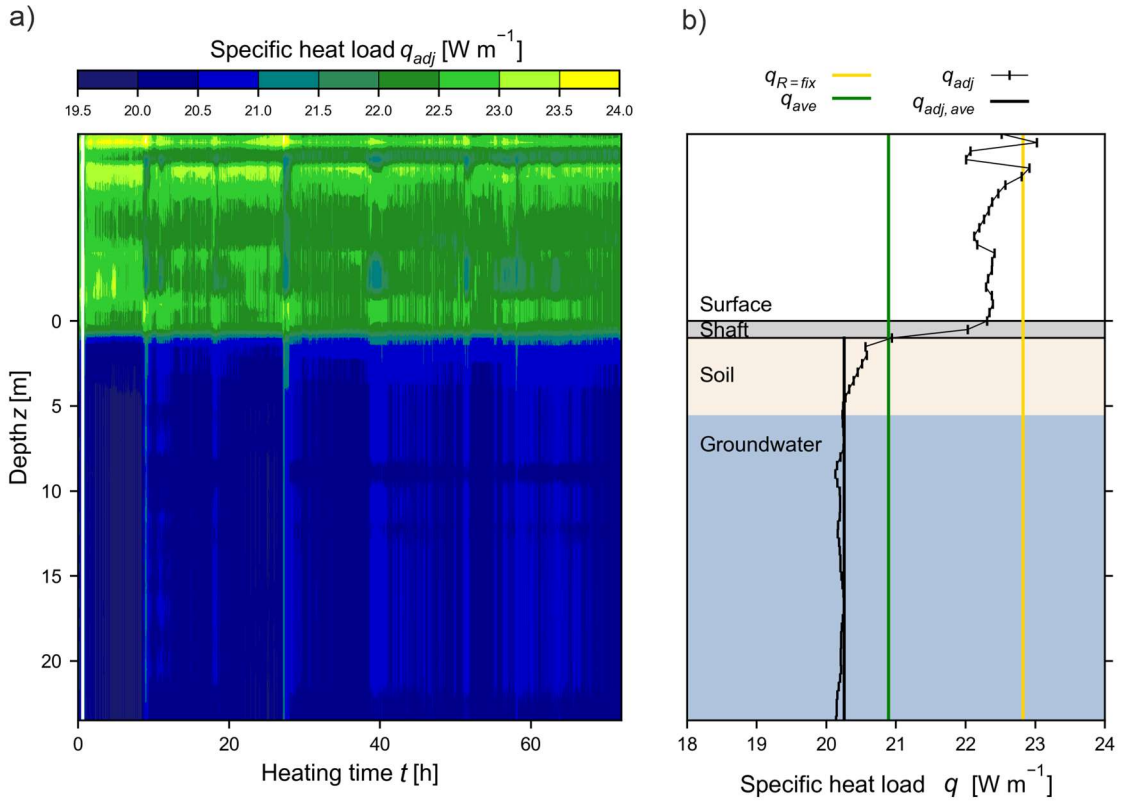

Figure 2-3: Adjusted specific heat loads (q_{adj}) about the cable length: a) plotted for the first 72 h of the ETRT, b) averaged for the entire heating time in comparison with the specific heat load assuming constant electrical resistance ($q_{R=fix}$), the average specific heat load (q_{ave}) and the adjusted specific heat load averaged over depth ($q_{adj,ave}$).

In this study, the variations along the depth of the BHE are minor. Overall, the variations of the specific heat along the cable length mainly depend on the following aspects: (1) It is influenced by the material of the heating cable. The dependence of the electrical resistance and, therefore, of the specific heat load on the temperature is proportional to the temperature coefficient of resistance (TCR) of the material (Equation 4). (2) The influence of the surface depends on the ambient conditions as well as the percentage of the heating cable above the surface, which is most often determined by the site-specific conditions. In this study, the ETRT was conducted in summertime with ambient temperatures above 28 °C during the day. The hybrid cable was exposed to the subsurface with a length of 24 m, which corresponds to 35 % of the total cable length. (3) The heat transport in the subsurface determines the variation of the specific heat load

along the depth of the BHE. When the thermal properties of the subsurface are very different along the depth, e.g., at a study site, where alternating layers of aquifers and aquitards are present, the temperature increase during the ETRT can vary considerably (> 30 K) with depth. This can account for a significant difference (> 8 %) in the heat load at the different depths. Further information on the thermal properties of the subsurface in this study can be found in the following chapter.

Figure 2-3b emphasises that by adjusting the heat loads with the DTS measurements, the variation of the specific heat loads along the heating cable can be calculated. This method can be easily integrated into the evaluation procedure and is, therefore, highly recommended for the evaluation of future ETRTs. However, the application of this adjustment is limited to ETRT using hybrid cables or cables, where the fibre optic is in direct contact with the heating cable. Only then, the DTS temperature measurements can be used representatively for the temperature of the heating cable.

2.3.3 Depth-specific effective thermal conductivity evaluation

Table 2-2 summarises the depth-averaged results for the effective thermal conductivities, Darcy velocities and hydraulic conductivities applying different specific heat loads. The deviation in the effective thermal conductivity is proportional to the deviation in the specific heat load (Equation 8). Thus, the errors of 3 % and 12 %, respectively, can also be found in this comparison. Referring to the results of Chapters 2.3.1 and 2.3.2, the further discussion of the results focuses solely on the evaluation of applying the adjusted specific heat load.

With the ILS, the depth-averaged effective thermal conductivity is evaluated to 4.5 W m^{-1} K^{-1}. With Péclet number analysis, an average Darcy velocity of 0.53 m d^{-1} is evaluated. Applying a hydraulic gradient of $i = 0.002$, an average hydraulic conductivity of 3.1×10^{-3} m s^{-1} is calculated. With the MILS an average Darcy velocity of 0.23 m d^{-1} is evaluated. The average hydraulic conductivity value analysed with the MILS is estimated to be 1.4×10^{-3} m s^{-1}. Thereby, both hydraulic conductivity values are within the same order of magnitude as derived with the pumping test (k_{pt}) with 3.1×10^{-3} m s^{-1} (Reuß et al., 2012). Thus, the comparison between the different methods indicates that the evaluation of the ETRT regarding average Darcy velocity and hydraulic conductivity is successfully conducted (Table 2-2).

Over the entire depth of the BHE, heterogeneous thermal properties of the subsurface can be observed (Figure 2-4). The effective thermal conductivities vary between 1.9 and 9.3 W m^{-1} K^{-1} (Figure 2-4b). Lower effective thermal conductivities are evaluated for the upper part of the borehole and between 15.5 and 18 m. High effective thermal conductivities with values above 6 W m^{-1} K^{-1} are evaluated for depths around 9.5, 12.5 and 22 m. According to the results of the Péclet number analysis, these high effective thermal conductivities can be attributed to high Darcy velocities in the order of about > 0.6 m d^{-1} and therefore to high hydraulic conductivities. The MILS results confirm areas of higher Darcy velocity (Figure 2-4c), however also indicate that high Darcy velocities are slightly overestimated with Péclet number analysis. Comparing the results with the borehole profile (Figure 2-4d), elevated effective thermal conductivities and Darcy velocities correlate with zones of coarser sediments. Additionally, the evaluated hydrau-

lic conductivities are between 1.1×10^{-4} and 8.8×10^{-3} m s^{-1}, which are in the range of typical sand and gravel aquifers (Domenico and Schwartz, 1990).

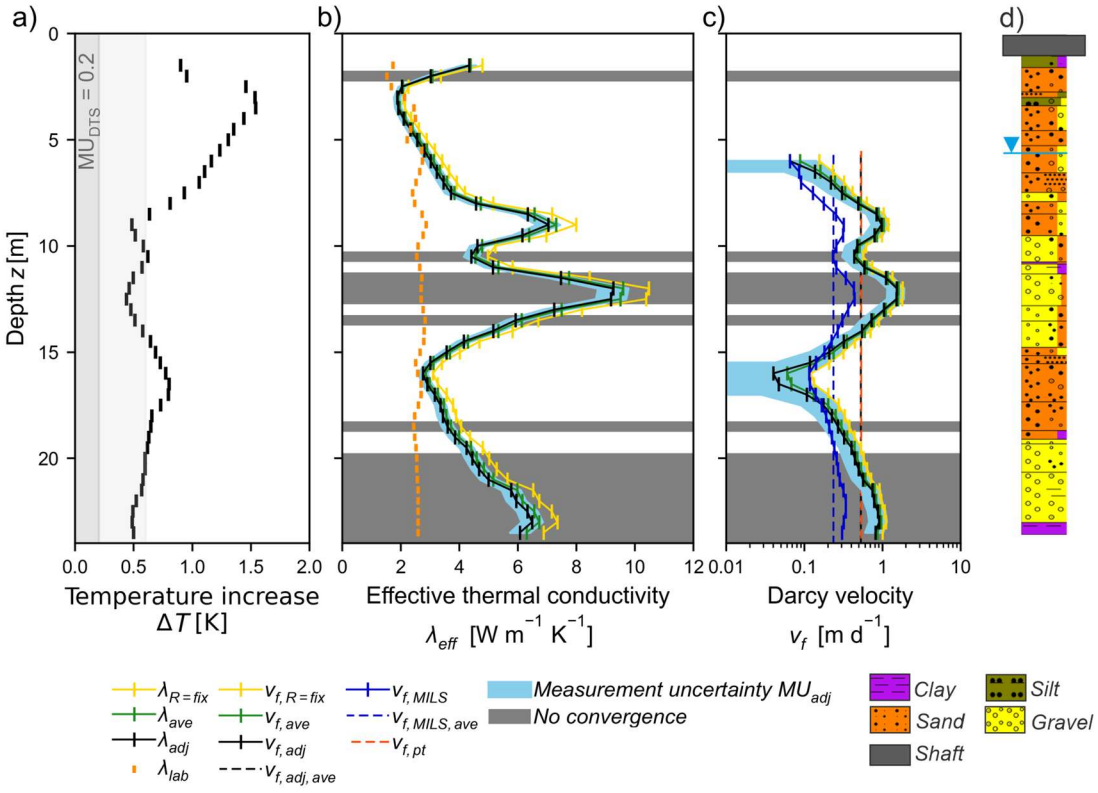

Figure 2-4: Depth-specific results for a) the representative transient temperature increase (ΔT), b) the effective thermal conductivity (λ_{eff}) and c) Darcy velocity (v_f) from the Péclet number analysis applying the different specific heat loads, and d) the borehole profile. Darcy velocities are compared with results from the MILS analyses ($v_{f,MILS}$) and the pumping test (v_{pt}) by Reuß et al. (2012). Depth intervals where no convergence criterion ($\Delta\lambda_{eff}/\lambda_{eff}$ < 0.05 / 20 h) are obtained are highlighted in grey (i.e., no convergence).

2.3.4 Discussion

In the following paragraph limitations of this study are discussed. Figure 2-5 shows the evaluation procedure for effective thermal conductivity for two representative depth intervals (5 m and 12.5 m). Complementary, the evaluation of all 45 analysed depth intervals can be found in Appendix Study 1(Figure A1- 1 to Figure A1- 45).

The depth interval at 5 m represents a conduction-dominated depth interval. The entire time data shows a transient temperature increase. Applying forward modelling, the effective thermal conductivity results converge to a stable value within the convergence criterion of $\Delta\lambda_{eff}/\lambda_{eff}$ < 0.05 within 20 h. Contrary, the depth interval at 12.5 m is advection-dominated. The iterative evaluation indicates strong groundwater influences showing an increase in effective thermal conductivities with evaluation time. The later temperature-time data approaches a steady state value and is not evaluated with ILS. Hence, no convergence is obtained. In Figure 2-4, the areas

where convergence of the effective thermal conductivity result cannot be achieved are highlighted. Convergence cannot be achieved for 33 % of the evaluated depth intervals, which are associated with high advective heat transport. In depth intervals with high groundwater flow, the system quickly approaches steady-state conditions, which reduces the evaluation time. For these depth intervals, near-steady-state conditions are achieved within 2 – 3 days. Hence, fewer data points can be used for linear regression. The degree of determination R^2 is lower (< 0.85, for z = 12 m and 12.5 m < 0.7). Summarised, even though the ILS evaluation is conducted for all depth intervals, the assumptions of the ILS are invalid for some areas of high Darcy velocities. This is indicated by the convergence criterion and the overestimation of the Darcy velocities in comparison to the MILS.

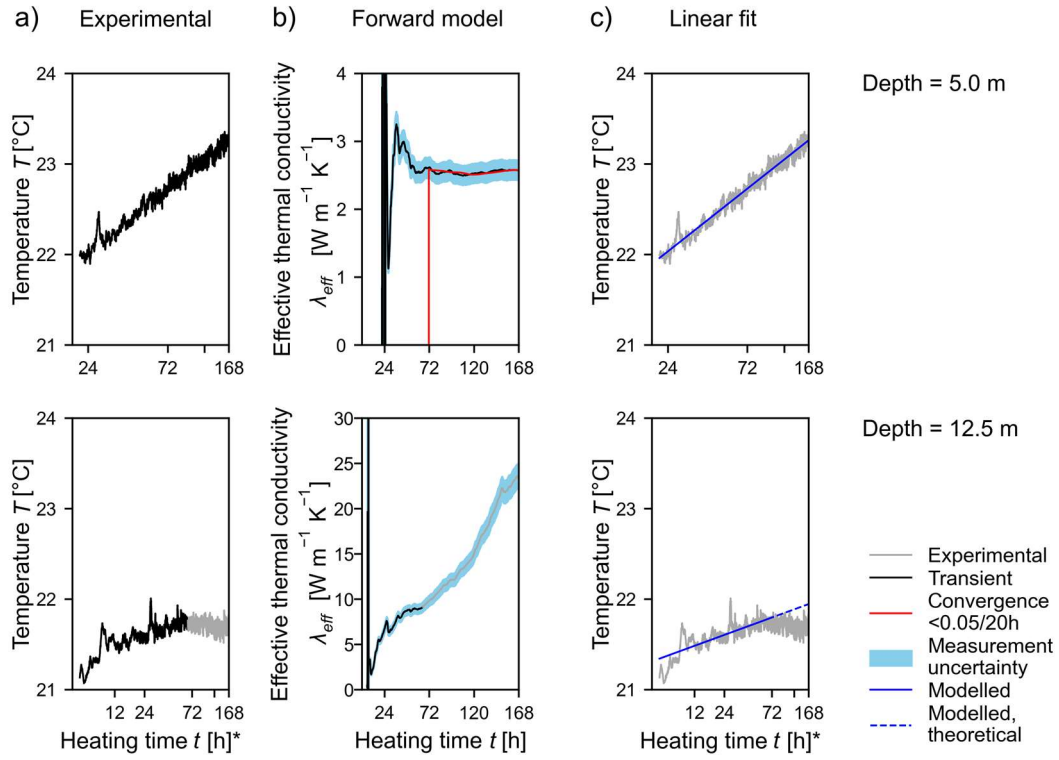

Figure 2-5: Evaluation of the effective thermal conductivities (λ_{eff}) for two representative depths of 5.0 m and 12.5 m, respectively: a) Identifying the transient temperature increase from the experimental data, b) applying sequential forward evaluation with the ILS and testing for convergence of the result, c) deriving parameters for linear fit. *Please note that the axes are scaled to the natural logarithm.

In addition, the Péclet number analysis to estimate Darcy velocities from ILS results has to be examined critically. Applying the Péclet number analysis, several assumptions are made that contribute to the uncertainty of the estimate. (1) The method defines the advective heat flow component by the difference between effective thermal conductivity λ_{eff} and thermal conductivity by conduction only λ. However, whereas thermal conductivity λ increases linearly with the specific heat load (Equation 7), the effective thermal conductivity at groundwater-influenced conditions increases non-linearly (Equation 14). (2) The characteristic length is an ambiguous number. It depends on the experiment time and the heat transfer properties of the medium. By defining the characteristic length as a fixed value equal to the borehole radius, the estimated

Darcy velocities are assumed to be defined mainly by the properties of the borehole. Thereby, a conservative calculation approach is chosen, which can result in an overestimation of higher Darcy velocities. Instead of the borehole radius, the radius of temperature influence would be a more suitable value. However, the determination of this value is challenging. (3) Thermal conductivity values of the subsurface have to be known. In this study, thermal conductivities from laboratory measurements of disturbed samples are used. Thus, there are uncertainties, e.g., whether the depth-specific laboratory values actually represent the thermal conductivities at in-situ conditions or whether these values represent the considered soil volume influenced by the TRT. Alternatively, thermal conductivities can be defined from ETRT results influenced by conduction only, thereby, defining one single value of thermal conductivity for the entire depth of the BHE. As indicated in Figure 2-4b, average deviations of 14 % between the thermal conductivities from laboratory measurements and ETRT results can be observed (depth interval 2.5 to 5.5 m). Regarding these uncertainties, the Péclet analysis can only be used to give a rough estimate. For a more precise determination of Darcy velocities from ETRT results the MILS has to be applied. Nevertheless, with the ILS, valid estimates of the average values and qualitative identification of areas of enhanced heat transport are analysed. Despite a higher uncertainty of the results, the lower computational effort justifies the application of the ILS.

In depth intervals with high groundwater flow, the heat is transported fast away from the BHE. Thus, the temperature increase, that can be used for evaluation, is low (< 0.6 K, Figure 2-4a). Overall, temperature fluctuations within the DTS data in the order of $\Delta T \sim 0.1$ K are observed. Thus, for depth intervals with a low-temperature increase, the uncertainty of the calculation increases, too. The applied specific heat load of 20 W m^{-1} for this highly advective aquifer does not generate a sufficient temperature increase to evaluate for all depths (Figure 2-4a), however is in the typical range of specific heat loads applied in TRT studies using heating cables between 6.1 to 48 W m^{-1} with an average of about 25 W m^{-1} (Antelmi et al., 2020; Dalla Santa et al., 2022; Freifeld et al., 2008; Galgaro et al., 2018; Giordano et al., 2021; Hakala et al., 2022; Huber, 2013; Lehr and Sass, 2014; Maldaner et al., 2019; Minchio et al., 2020; Raymond et al., 2010; Simon and Bour, 2022; Vélez Márquez et al., 2018; Vieira et al., 2017; Zhang et al., 2020).

The duration of the ETRT within this study was about 170 h, which is quite long for a TRT. Concerning the evaluation of a TRT, the longer the testing time, the bigger the sample volume of the subsurface. Hence, the effect of the grouting material decreases with time, as well as the influence of inhomogeneity of the subsurface. Thus, a more representative evaluation of the subsurface conditions can be conducted, especially by combining it with the sequential forward modelling (Chapter 2.2.2.3). However, regarding the practical application of ETRT, a shorter test duration is required. From Figure A1- 1 to A1- 45, a testing time of about 80 – 90 h can be recommended that allows for a clear identification of the turning point, when effective thermal conductivity values start to increase and, therefore, to evaluate the groundwater effect. Nevertheless, the required testing time depends on site-specific conditions like the subsurface conditions, the grouting material and the borehole radius.

Figure 2-6 shows the relation between Darcy velocities and effective thermal conductivities as evaluated in this study and compared to reported values from other studies dealing with the determination of groundwater flow velocities from TRT data.

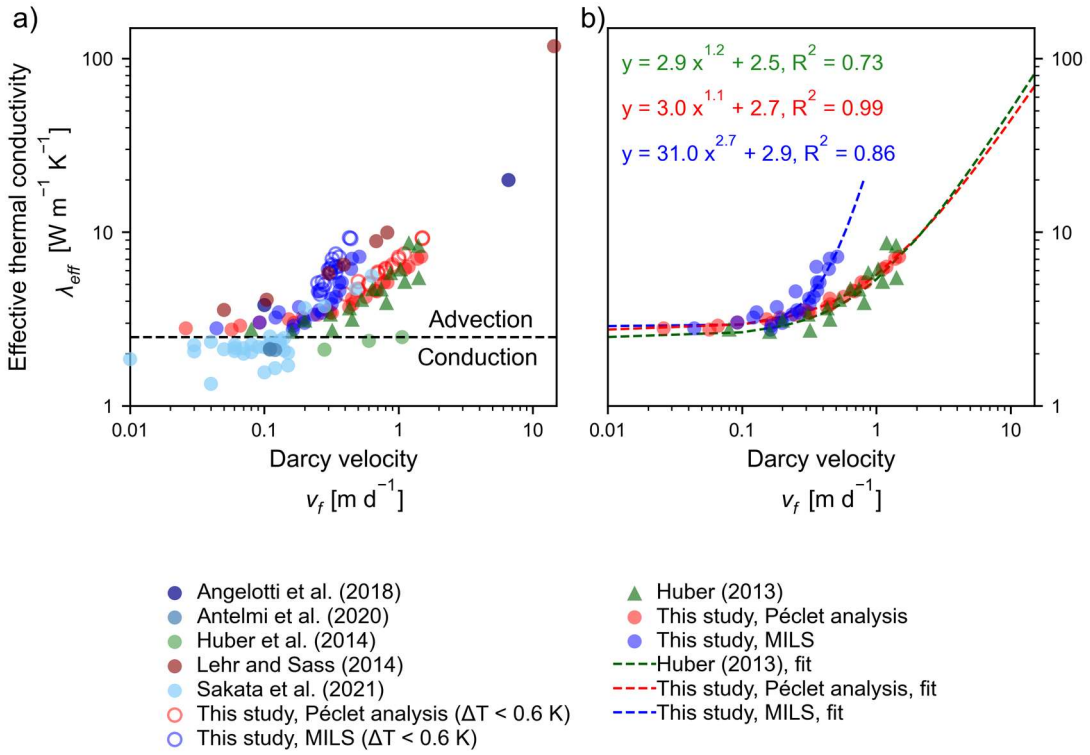

Figure 2-6: Darcy velocities (v_f) and corresponding effective thermal conductivities (λ_{eff}) from studies evaluating groundwater-influenced TRTs, a) all datasets, b) datasets used for curve fitting. The colour code indicates the applied evaluation method (blue = MLS, red = Péclet number analysis, green = experimentally set Darcy velocity). The symbol code indicates the test method (circle = field study, triangle = sandbox experiment).

It contains data from different aquifer types with varying properties. In addition, different TRT methods and evaluation procedures were applied. The data collection highlights that with increasing Darcy velocities, effective thermal conductivities also increase. In Figure 2-6b the correlation between these two properties is separately fitted for three distinct datasets, including the two datasets from this study and the dataset from Huber (2013), where Darcy velocities were experimentally set in sandbox experiments. The power function in the form of $y = a\,x^b + c$ is fitted to the data. If the exponent b becomes 1.0 the power function will take the form of a linear equation. Thus, comparison of linear and exponentiating relationship between the Darcy velocity and effective thermal conductivities is made easier. The parameter c corresponds to the thermal conductivity λ without groundwater flow. Thus, it depends highly on the geologic conditions of the study site. The average thermal conductivity of this study determined in the laboratory is 2.5 W m^{-1} K^{-1}. The deviations of c from this value also indicate the difficulty in distinguishing between the heat transport mechanism of conduction and advection at low flow conditions. The relationship in Figure 2-6b shows that effective thermal conductivity is not significantly affected by groundwater flow up to a Darcy flow of about 0.2 to 0.3 m d^{-1}. With increasing Darcy velocities, the effective thermal conductivity increases significantly. The highest degree of determination is achieved for the results of the Péclet number analysis. This is expected, as the Darcy velocities are directly derived from the effective thermal conductivities based on a linear relationship (Equation 12). The deviation from the perfect correlation is mainly due to the variance in thermal conductivity derived from laboratory measurements. However,

the assumptions made for the evaluation with the Péclet number analysis result in high uncertainties in the estimation of Darcy velocities with this method, as discussed before in detail. The dataset with the lowest degree of determination is the dataset from Huber (2013), which can be easily explained. On one hand, different measurement methods were applied. The effective thermal conductivities are evaluated from temperature-time data, whereas the Darcy velocities are measured with flowmeters. On the other hand, results from several tests are combined in one dataset. The fit calculated for the dataset by Huber (2013) agrees well with the fit for the Péclet number analysis, which supports the assumptions made for the Péclet number analysis. However, it does not prove that the Péclet number analysis is the recommended analysis method for this specific case study.

The MILS fit significantly deviates from the best fit of the other two datasets. The plotted MILS dataset includes the results of both evaluation methods (ILS and MILS) based on the same experimental data (Figure 2-6). Although, the chosen convergence criterion was acceptable for evaluation using the ILS. The latter is not the recommended model for the evaluation of groundwater-influenced TRT. However, uncertainties therefore still remain, which could result in an overestimation of the derived effective thermal conductivities especially for higher Darcy velocities. To address these uncertainties during the evaluation of ETRTs, we recommend performing field experiments under controlled groundwater flow velocities combined with numerical heat transport models.

For the conduct of future ETRTs with high groundwater influence, the knowledge derived from this study can provide valuable insights. Ensuring a sufficient temperature increase for the evaluation of all depth intervals is crucial for the reliable determination of effective thermal conductivities and groundwater velocities. This could reduce the sensitivity of the data towards temperature noise and at the same time improve the estimation of the regression (Figure 2-6) and therefore of the depth-specific effective thermal conductivities. Nevertheless, increasing the specific heat load for ETRT is not trivial. Depending on the experimental setup and conduct, different aspects have to be considered. In principle, it applies, that the higher the heat load, the higher the temperature increase. However, the highest possible heat load is defined by cable specifications. Typically, the maximum temperature allowed for such cables is 60 to 80 °C. Especially in the upper part of the heating cable, when the cable is in contact with air, there is a high risk of overheating at high specific heat loads (Figure 2-2). Hence, to increase the heat load during the ETRT, the heat transfer in the surface area has to be improved. Thus, actions against overheating are necessary, e.g., burying the cable or placing water-filled tubes on it. In the study by Hakala et al. (2022), they used an air fan to cool the cable. However, practical issues and site characteristics such as the duration of the experiment, the available space to bury the cable, and the necessary length of the cable above the surface have to be considered. Apart from that, improvements in the material of the heating cable towards the application at elevated temperatures are desirable. A compromise between decreasing the thermal resistance of the heating cable, and at the same time maintaining sufficient electrical isolation when working with current in a wet environment have to be made. In addition, the fibre optics have to be protected against moisture. Otherwise, the temperature measurement becomes inaccurate. Further issues applying a higher heat load have to be considered. For ETRTs in open boreholes or with the heating cable installed inside the heat exchanger pipe induced convection can occur. Regarding this, Hakala et

al. (2022) recommended a maximum specific heat load of 20 W m^{-1}. However, a grouted cable is used in this study indicating a minor influence. There are only a few studies, which compare the influence of the heat load on the results of TRTs. Huber (2013), for example, compared in his ETRT study different specific heat loads at the same BHE ranging from 6 – 46 W m^{-1}. He observed that less variation in depth-specific thermal conductivities was resolved by applying a higher specific heat load. Partly, this could be explained by a lower influence on the accuracy of the temperature measurement due to a higher temperature increase. Additionally to increasing the heat load, the uncertainty of the slope can be reduced using temperature measurements with better accuracy than DTS. This includes placing additional punctual temperature sensors or combining DTS data with temperature profiles from wireless measurement tools (Schüppler et al., 2021).

2.4 Conclusion

In this study, an ETRT is evaluated with significant groundwater flow (> 0.2 m d^{-1}). Different approaches for the determination of the specific heat load of the ETRT are discussed. Evaluations of effective thermal conductivities and Darcy velocities are conducted by applying the ILS combined with the Péclet number analysis and the MILS. Depth-averaged effective thermal conductivity and hydraulic conductivity are evaluated to be 4.5 W m^{-1} K^{-1} and 3.1 × 10^{-3} m s^{-1}, respectively. Considering the results of this study, the following conclusions can be made:

(1) Assuming constant electrical resistance of the heating cable can account for an inaccuracy of 12 % in the determination of depth-specific effective thermal conductivities. Thus, this method is inappropriate for the calculation of the specific heat load. Hence, time-averaging of the heat load by logging voltage and current during the ETRT is recommended.

(2) Applying the theory of temperature-dependent resistances, the variation of the specific heat loads along the length of the heating cable can be adjusted. In this study, variations within 3 % were observed along the BHE. For hydrogeological conditions with varying groundwater flow (i.e., at a study site with alternating layers of aquifers and aquitards), the variations are expected to be more significant. The adjustment of the specific heat loads can be easily integrated into the evaluation procedure and is therefore also recommended.

(3) For high Darcy velocities, experimental issues ensuring a sufficient temperature increase ($\Delta T > 0.6$ K) are shown to increase the uncertainty of the evaluation. To reduce the sensitivity towards temperature fluctuations, measures applying a higher specific heat load are desirable. This includes actions against overheating of the cable outside the borehole heat exchanger and improvements of the material of the heating cable towards the application at elevated temperatures (> 60 °C). In 33 % of the analysed depth intervals, due to a fast adjustment of the system to the applied heat load, the convergence criterion of $\Delta\lambda_{eff}/\lambda_{eff} < 0.05$ / 20 h of the ILS sequential forward evaluation cannot be achieved. Temperature measurements with better accuracy (adding punctual sensors, in combination with profiles from wireless measurement tools) are expected to also improve the evaluation of ETRT.

Finally, to address the uncertainties during the evaluation of ETRTs with high groundwater flow, we recommend performing field experiments under controlled groundwater flow velocities combined with numerical heat transport models.

2.5 Acknowledgements

The authors would like to thank Andreas Köhler of the University of Applied Sciences Biberach for his help with the ETRT measurements and provision of the Pt100 temperature data. The helpful comments of the two reviewers are also gratefully acknowledged.

3 Depth-specific thermal conductivities of Triassic sandstones

Reproduced from Albers, A., Glatting, F., Menberg, K., Steger, H., Fliegauf, C., Schindler, L., Wilke, S., Zorn, R., Blum, P. Depth-specific thermal conductivities of Triassic sandstones. (*submitted to Geothermal Energy, July 2024*)

Abstract

Triassic sandstones of the Middle and Upper Buntsandstein are highly suitable for ground source heat pump (GSHP) systems. Thus, knowledge of their thermal properties, which can be measured or estimated by theoretical models, is crucial. However, the transferability of estimated thermal conductivities to the field scale has not been thoroughly examined yet. In this study, the thermal and lithological properties of 156 core samples from a borehole in the Buntsandstein are therefore analysed in the laboratory. Various theoretical models are applied and compared to laboratory-derived thermal conductivities. The best agreement is achieved with the Voigt-Reuss-Hill model with an average thermal conductivity of 4.5 W m^{-1} K^{-1} and an RMSE of 0.7 W m^{-1} K^{-1} (T = 20 °C). The results of this model are compared to depth-specific, effective thermal conductivities from an enhanced thermal response test (ETRT). These effective thermal conductivities range between 2.3 and 6.1 W m^{-1} K^{-1} with an average of 4.7 W m^{-1} K^{-1}. We demonstrate that some theoretical models can provide an initial estimation of the effective thermal conductivity of sandstones when groundwater flow is negligible. However, the accuracy of the estimation is limited by sample quantity and model assumptions.

3.1 Introduction

Using shallow geothermal energy, carbon dioxide emissions from heating-related energy consumption can be reduced significantly (Blum et al., 2010). Ground source heat pump (GSHP) systems using borehole heat exchangers (BHE) are the most popular shallow geothermal installations (Acuña and Palm, 2010; Bayer et al., 2012). To efficiently size GSHP systems and ensure sustainable long-term operation, knowledge of the subsurface thermal properties at the system's site is crucial, with the thermal conductivity of the ground being the critical design property (Spitler and Gehlin, 2015).

The Buntsandstein in the Central European Basin represents a significant geological formation from the early Triassic (Soyk, 2015). Due to its typically high thermal conductivity (Franz and Schulze, 2016; Haffen et al., 2017; Kämmlein and Stollhofen, 2019), the Buntsandstein is a favourable host rock for shallow geothermal applications. Buntsandstein rocks were formed

through diverse sedimentary environments and diagenetic processes, resulting in heterogeneous properties (Soyk, 2015). The reported thermal conductivity of saturated laboratory samples varied significantly between 1.7 and 5.8 W m^{-1} K^{-1} at room temperature (Franz and Schulze, 2016; Haffen et al., 2017; Kämmlein and Stollhofen, 2019).

The standard method for determining thermal conductivity in the context of GSHP systems is the thermal response test (TRT) (Spitler and Gehlin, 2015), which produces estimates of effective thermal conductivities (λ_{eff}) of the subsurface at in-situ conditions. Further enhancement of the TRT using fibre optic cables enables determining depth-specific effective thermal conductivity (Wilke et al., 2020). The so-called distributed thermal response tests (DTRT) use distributed temperature sensing (DTS) in combination with a circulating heat transfer fluid, whereas enhanced thermal response tests (ETRT) combine DTS with a heating cable (Wilke et al., 2020).

The main disadvantage of in-situ TRTs is that they are expensive and time-consuming (Abuel-Naga et al., 2009). A cost-effective alternative is to measure thermal conductivity in the laboratory. The transient half-space probe line source method (e.g., Jorand et al., 2015; Kämmlein and Stollhofen, 2019) and the optical scanning method (e.g., Franz and Schulze, 2016; Popov et al., 1983) are most often applied to measure the thermal conductivity of sandstones. Still, only a few studies (e.g., Ma et al., 2022) compare ETRT results with high-resolution borehole data from laboratory measurements.

Alternatively, various theoretical models were suggested to estimate the thermal conductivities based on petrophysical properties, such as porosity and density, and mineralogy (see, e.g., Clauser, 2006; Fuchs et al., 2013; Pauselli et al., 2021 and references therein). An extensive overview of different models can be found in Abdulagatova et al. (2009). Commonly, these models are classified into mixing models, that are solely based on geometrical considerations, and empirical models. The arithmetic, harmonic and geometric mean are the most widely-used models among the theoretical models. These models use thermal conductivity values of the individual rock components and their corresponding volume fraction as input parameters. They differ in the assumption of the spatial distribution of the solid components and the pore space including the pore fluid. The arithmetic mean assumes components arranged in parallel, with heat flow aligned parallel to them. In contrast, the harmonic mean assumes heat flow perpendicular to the arrangement, whereas the geometric mean model assumes a random distribution of components without a preferential alignment. Some theoretical models include an additional uncertainty factor related to pore and particle structure expressed by an empirically derived constant. For example, de Vries (1963) developed a semi-empirical model for unconsolidated materials based on the Maxwell equation, which includes a shape factor g for oblate ellipsoids of rotation. Pichugin et al. (2022) reviewed several studies that derive correction factors for the geometric mean model. They obtained average correction factors f for different rock types and pore fluids. Sugawara and Yoshizawa (1961) empirically derived an equation for estimating bulk thermal conductivity from controlled laboratory measurements of thermal conductivity using materials with defined geometry. Finally, they introduced an empirical constant n that depends on pore geometry and tested it on sandstones.

Further studies focused on developing empirical models for site-specific sandstones (e.g., El Sayed, 2011; Nabawy and Géraud, 2016). From laboratory analyses of specific sandstones, linear or log-linear relationships between thermal conductivities and materials properties were established by correlating petrophysical properties, such as porosity and density, and mineral contents with measured thermal conductivities. For example, El Sayed (2011) evaluated 35 samples of non-homogeneous, fine-grained sandstones from the Bahariya formation (Egypt) to develop an empirical model based on porosity, bulk density and permeability. Nabawy and Géraud (2016) evaluated 19 samples of the Nubia sandstones (Egypt), which are characterised by high porosities (~ 25 to 39 %), to build an empirical model based on the mineral content (clay and quartz) and porosity.

The ability of mathematical models to accurately estimate thermal conductivities is usually evaluated by comparing the estimated values against laboratory measurements. However, estimated thermal conductivities have yet to be compared against field measurements from depth-resolved TRT. Menberg et al. (2013) compared estimated thermal conductivities from mathematical models (i.e. arithmetic, harmonic and geometric mean; de Vries, 1963) against depth-averaged effective thermal conductivity determined with a conventional TRT. The best fit for the analysed unconsolidated sediments was obtained with the geometric mean model.

This study focuses on the thermal conductivity analysis of Triassic Buntsandstein sandstones. We identify theoretical models that can be used to determine the thermal conductivity of the sandstones and yield comparable results to laboratory and field tests. First, the material properties, mineralogy and thermal conductivity of core samples from Triassic sandstones were measured in the laboratory. Known theoretical models were then applied to estimate the thermal conductivities of the core samples and verified against laboratory measurements. Finally, the estimated and measured thermal conductivities were compared to depth-resolved, effective thermal conductivities obtained with an ETRT. Thus, challenges in comparing laboratory and in-situ thermal conductivities are identified and discussed.

3.2 Study site and geological background

The study site is located in Neuweiler in the northern Black Forest, Germany (Figure 3-1a), where a borehole with a borehole radius of 0.089 m was drilled in sedimentary rocks of the Lower Triassic. Stratigraphically, the rocks likely span from the Olenekium, (251 – 247.5 Ma) to the Anisium (247.5 – 241 million years). They were encountered in the locally mappable formation of the Upper to Middle Buntsandstein (Figure 3-1c). From 0 – 35.3 m bgl, the "Plattensandstein" formation (Anisium) was encountered, including two weathering horizons between 11.5 and 19.2 m bgl, and one paleosol between 23.4 and 25.6 m bgl. At 35.4 – 39.1 m bgl another weathering horizon marks the transition zone to the underlying "Kristallsandstein" sub-formation (Olenekium). The "Kristallsandstein" formation extends up to a depth of 50.9 m bgl, where another weathering horizon initiates the "Geröllsandstein" sub-formation (Olenekium), which is encountered up to the final borehole depth. Generally, the upper layers are predominately characterised by fine sandstones with a high occurrence of mudstones in the first ten meters. From about 42.2 m bgl, alternating strata of fine and medium sandstones are found. The underlying layers are mainly characterised by medium sandstones. These sandstones are strong-

ly silicified within the “Kristallsandstein” formation (Günther, 2010). The unconfined groundwater level was measured at a depth of 28.5 m bgl. In total 169 samples were collected from the drill cores (Figure 3-1d), representing homogeneous sections of the borehole profile. Since some samples were in poor conditions, the laboratory analyses were feasible only on 156 samples.

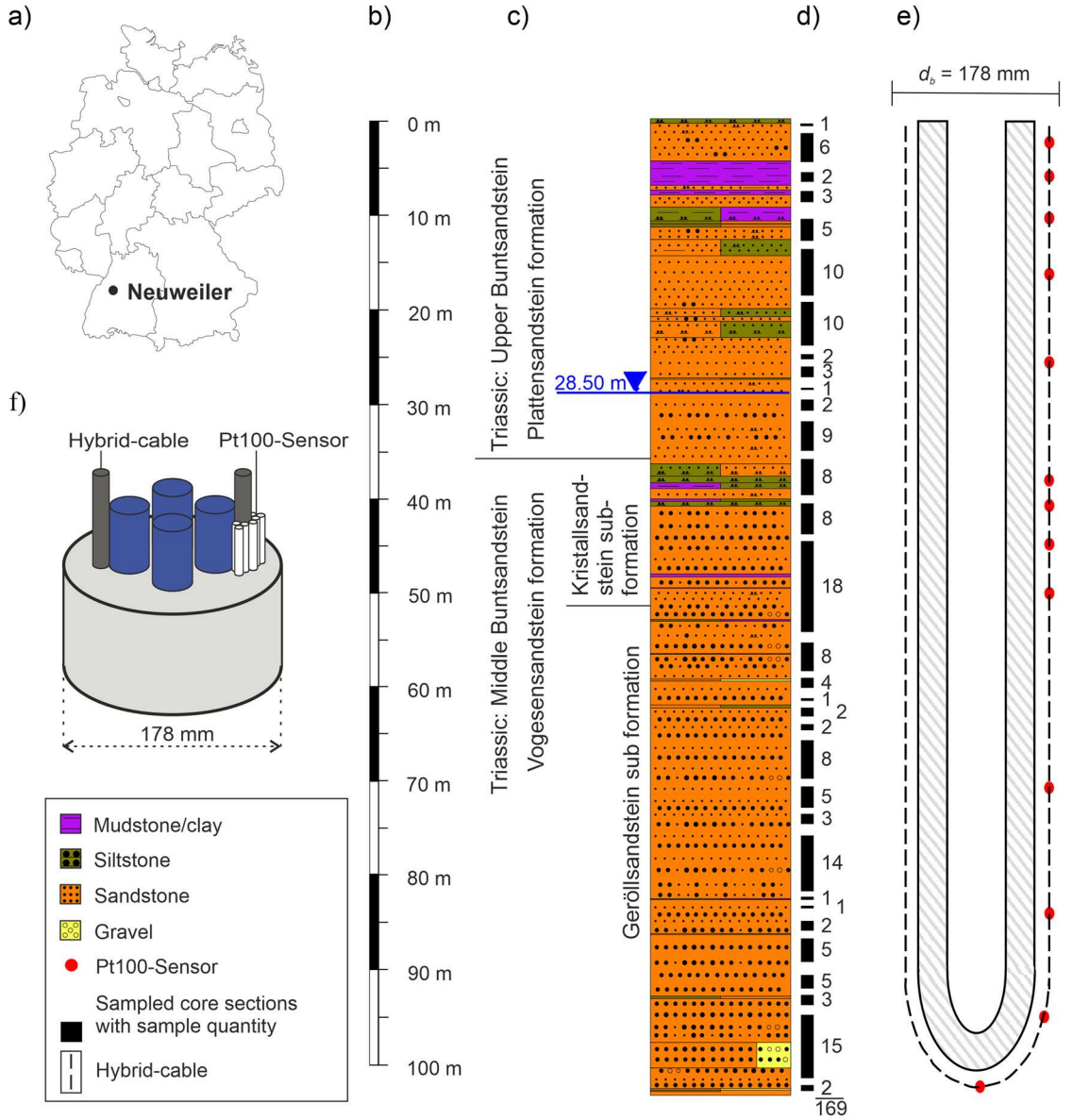

Figure 3-1: Overview of the study site in Neuweiler, Germany: a) location, b) borehole depth, c) stratigraphy with geological profile including, d) number of samples, e) arrangement of the hybrid cable and temperature probes (Pt100) and f) schematic setup.

3.3 Methods

The thermal conductivities of the Triassic sandstones were evaluated with several methods. First, the thermal conductivities of the samples were measured in the laboratory (λ_{sat}). In addi-

tion, petrophysical, mineralogical and structural properties of the samples, such as porosity and bulk density, were determined. Then, the thermal conductivities (λ_{est}) were estimated with theoretical models and compared with the laboratory measurements. Finally, effective thermal conductivities (λ_{eff}) were determined with an ETRT. The methods are described in detail in the following paragraphs.

3.3.1 Laboratory analysis

Thermal conductivities are measured of samples at dry (oven drying at 105 °C) and at saturated conditions. The samples' minimum length was from 50 – 200 mm. They were cut and polished to have three flat sides. To saturate the samples, the dry samples were placed in a desiccator and vacuumed for 4 h. Afterwards, the degassed samples were immersed in degassed tap water for at least 12 h to fully saturate.

Thermal conductivity was measured with the transient hot wire method as half space line source using surface probes (ISOMET 2104, Applied Precision Ltd., Slovakia, measurement accuracy provided by the manufacturer is 10 %). During measurement, heat from the probe propagates in all spatial directions within the sample. Four measurements were repeated on each of the three flat sample surfaces, resulting in $n = 12$ measurements. Measurement uncertainties were calculated according to the Guide to the expression of uncertainty in measurements (ISO IEC 98-3, 2008) with a 10 % accuracy of the measurement device, standard deviation and student-t-distribution and was between 10 and 11 %. Table 3-1 summarises the determined material properties and the corresponding measurement methods. All measurements were carried out in accordance with the German Institute of Standardization (DIN). The mineralogy of ten samples was determined by modal analysis using a polarisation microscope (AXIO Scope.A1, Carl Zeiss Microscopy GmbH, Germany). The mineral content was quantified by manual point counting.

The water content is analysed for the re-saturated samples. Based on the results of the laboratory measurements, the open porosity ϕ_{open} is determined from the evaporable water content w at saturated conditions (DIN EN 1936, Deutsche Norm, 2007) as follows:

$$\phi_{open} = \frac{w\,\rho_d}{\rho_w} \tag{3-1}$$

with ρ_d being the dry bulk density and ρ_w being the density of water at a defined temperature. Moreover, total porosity ϕ is determined from the solid density ρ_s and applying the following equation:

$$\phi = 1 - \left(\frac{\rho_d}{\rho_s}\right) \tag{3-2}$$

Table 3-1: Petrophysical, mineralogical and structural analysis methods used on the Triassic sandstone samples.

	Parameter	Method	Measurement uncertainty
Petrophysical analysis	Water content w	Oven drying (DIN EN ISO 17892-1, Deutsche Norm 2015)	± 0.002 g accuracy of the scale and 1 % handling error, n = 1
	Bulk densities ρ_d, ρ_b	Immersion weighing (DIN EN 1936, Deutsche Norm 2007)	± 0.002 g accuracy of the scale and 1 % handling error, n = 1
	Solid density ρ_s	Capillary pycnometer (DIN EN 1936, Deutsche Norm 2007)	± 0.0005 g accuracy of the scale and 1 % handling error, n = 2
	Permeability K	TinyPerm 3	Standard deviation from 10 measurements at different positions on the 1 – 6 sample surfaces (n = 20 – 60)
Mineralogical analysis	Carbonate content CO_3	Gasometrical determination (DIN 18129, Deutsche Norm, 2011)	± 0.0005 g accuracy of the scale, ± 0.1 mL accuracy of gas volume, n = 2 – 4
	Mineral components (quantitative)	Polarisation microscopy	Assuming a 10 % error, n = 2
Structural analysis	Average pore diameter d_{pore}	Mercury porosimetry (DIN ISO 15901-1, Deutsche Norm 2019)	Assuming a 15 % error (based on the deviation between matrix densities from MIP and solid density), n = 1
	Average inner pore surface A_{pore}		
	Texture	Polarisation microscopy	
	Grain size		
	Grain contacts		
	Degree of sorting and roundness		
	Porosity and pore filling		

n = number of measurements

3.3.2 Theoretical estimation of thermal conductivity

The theoretical models used to estimate thermal conductivity are summarised in Table 3-2. They are commonly used in literature, and require a limited number of material properties.

The mixing models assume fully water-saturated samples, with the thermal conductivity of the pore fluid (λ_f) equal to that of water (λ_w = 0.598 W m^{-1} K^{-1} at T = 20 °C). The thermal conductivity of the solid matrix λ_m was calculated with the geometric mean using the thermal conductivities of the minerals λ_i provided in Table 3-3. The thermal conductivity of the lithic fragments was calculated estimating a composition of 80 % quartzite, 15 % mica and 5 % claystone from polarisation microscopy. The mineral composition was analysed in only ten samples representing homogeneous lithological zones. The average matrix thermal conductivity of these ten samples was then adopted for the model evaluation of the remaining 131 samples.

Table 3-2: Theoretical models to estimate thermal conductivities.

Type	Model name	Equation		Assumptions and reference
Mixing models	Arithmetic mean	$\lambda_{ari} = \phi\,\lambda_f + (1-\phi)\,\lambda_m$	(3-3)	Theoretical maximum, heat flow parallel to a layered material
	Harmonic mean	$\frac{1}{\lambda_{har}} = \frac{\phi}{\lambda_f} + \frac{1-\phi}{\lambda_m}$	(3-4)	Theoretical minimum, heat flow perpendicular to a layered material
	Geometric mean	$\lambda_{geo} = {\lambda_f}^{\phi}\,{\lambda_m}^{(1-\phi)}$	(3-5)	Mean constrained within the bounds of the theoretical minimum and maximum
	Voigt-Reuss-Hill average	$\lambda_{VRH} = 0.5\,(\lambda_{arit} + \lambda_{har})$	(3-6)	Mean of theoretical maximum and minimum, Hill (1952)
	Statistical spatial distribution mean	$\lambda_{SSD} = \sqrt{\lambda_{ari}\,\lambda_{har}}$	(3-7)	Assuming layered arrangement of mineral components, Pribnow and Umsonst (1993)
	Hashin-Shtrikman upper bound	$\lambda_u = \lambda_m + \phi\left(\frac{1}{\lambda_f - \lambda_m} + \frac{1-\phi}{3\lambda_m}\right)^{-1}$	(3-8)	Narrower bounds, derived for effective elastic moduli of a multiphase material of arbitrary phase geometry, Hashin and Shtrikman (1963)
	Hashin-Shtrikman lower bound	$\lambda_l = \lambda_f + (1-\phi)\left(\frac{1}{\lambda_m - \lambda_f} + \frac{\phi}{3\lambda_f}\right)^{-1}$	(3-9)	
	Hashin-Shtrikman average	$\lambda_{ave} = 0.5\,(\lambda_u + \lambda_l)$	(3-10)	
(Semi-)empirical, considering pore geometry	de Vries	$\lambda_{Vries} = \frac{\phi\,\lambda_f + (1-\phi)\,F_1\,\lambda_m}{\phi + (1-\phi)\,F_1}$ $F_1 = \frac{1}{3}\sum_{i=1}^{3}\left[1 + \left(\frac{\lambda_m}{\lambda_f} - 1\right)g_i\right]^{-1}$	(3-11)	Based on the Maxwell-Eucken equation, including a geometrical shape factor g_i of the solid particles, in de Vries (1963)
	Weighted geometric mean	$\lambda_{est} = {\lambda_f}^{f\phi}\,{\lambda_m}^{(1-f\phi)}$	(3-12)	Based on the geometric mean, including a rock-specific empirical *f*-constant, Pichugin et al. (2022)
	Sugawara and Yoshizawa	$\lambda_{est} = (1-A)\,\lambda_m + A\,\lambda_f$ $A = \left[\frac{2^{n_c}}{2^{n_c}-1}\right]\{1 - [1/(1+\phi)^{n_c}]\}$	(3-13)	Empirically derived model, including a rock-specific empirical *n*-constant, Sugawara and Yoshizawa (1961)
Empirical	El Sayed	$\lambda_{est} = 3.003 + 0.533\,\phi + 0.044\,\rho_b - 0.091\,logK$	(3-14)	Derived from 35 samples, El Sayed (2011)
	Nabawy and Géraud	$\lambda_{est} = 0.022\,Qz - 0.0456\,Cl - 0.069\,\phi_W + 3.18$	(3-15)	Derived from 19 samples, Nabawy and Géraud (2016)

Thermal conductivity of the pore fluid (λ_f), thermal conductivity of the solid matrix (λ_m), quartz content (Qz), clay content (Cl), porosity (ϕ), porosity measured with water injection (ϕ_w), permeability (K), bulk density (ρ_b)

The semi-empirical models were evaluated by assuming empirical parameters using the information available from the different studies. For the de Vries (1963) model, the shape factors g_i = {0.75, 0.125, 0.125} are applied (De Vries, 1963; Woodside and Messmer, 1961). In accordance with Pichugin et al. (2022), the correction factor f = 0.65 was applied to the weighted geometric mean model assuming monomictic and saturated sandstones. Sugawara and Yoshizawa (1961, 1962) derived two empirical constants n_c for their model, which correspond to two different sets of sandstones, n_c = 2.5 and n_c = 2, and were both adopted in this study.

Two empirical models developed for different sandstones were evaluated. To apply the model by El Sayed (2011), porosity, bulk density and permeability were determined according to the methods described in Table 3-1. Since the model by Nabawy and Géraud (2016) is based on quartz and clay content, the model was only applied to the ten samples with evaluated mineralogy.

Table 3-3: Thermal conductivity values of the mineral components used for the calculation of matrix thermal conductivities based on Schön (2011) and their estimated weighing factors.

Mineral	Thermal conductivity λ_i [W m^{-1} K^{-1}]	Weighing factor [-]
Quartz	7.7	mineral content from polarisation microscopy
Feldspar (Microcline)	2.5	mineral content from polarisation microscopy
Lithic fragments, including:		mineral content from polarisation microscopy
Quartzite	5.1	0.8
Mica [a]	2.3	0.15
Claystone	2.0	0.05

[a] Value for muscovite

3.3.3 Field measurements

A double U-pipe BHE with an outer pipe diameter of 0.032 m was installed in the borehole, which was grouted afterwards with a backfill material (Füllbinder H-hs PLUS, Schwenk Zement GbH &Co. KG, $\lambda_g \geq 1.0$ W m^{-1} K^{-1}). The BHE is equipped with a hybrid cable, four optic fibres for temperature measurements and four copper conductors as heating elements (Helukom® A-DSQ(ZN)B2Y, 1 × 4 G 50/125 + Cu 4 × 1.5 mm², length = 234 m), at the outside of one U-pipe (experimental setup see Figure 3-1e, f). The ETRT is conducted over the duration of about 186 h by applying an average specific heat load of 32 W m^{-1} (PowerTen Power Ten Inc. R66E-60220 DC Power Supply, data logger ALMEMO 2590, AHLBORN). The specific heat load was determined from voltage (accuracy ± 0.1 % of the full-scale value of 200 V + 2 digits + 0.03 % of the measurement value + 2 digits) and current (accuracy ± 0.1 % of the full-scale value of 200 mV + 2 digits + 0.03 % of the measurement value + 2 digits + 0.5 % uncertainty of the shunt). The temperature was measured at 60 s intervals using DTS with a measurement interval of 1 m (Agilent, AP Sensing, N4386B, dual ended measurement, measurement uncertainty provided by the manufacturer is ± 0.2 K).

As the hybrid cable is installed in a loop, the temperature data of two corresponding length intervals of the optic fibre are averaged for each depth interval. The effective thermal conductivity (λ_{eff}) is evaluated using the infinite line source (ILS) model as given in Equations 16 and 17 (Carslaw and Jaeger 1959; Gehlin 2002):

$$T(r_H, t) - T_0 \approx \frac{q}{4\,\pi\,\lambda_{eff}}\left(\ln\left(\frac{4\,\alpha\,t}{{r_b}^2}\right) - \gamma\right) + q\,R_{th} \quad (3\text{-}16)$$

$$\lambda_{eff} = \frac{q}{4\,\pi\,m}\,; m = \frac{\Delta T}{\Delta \ln(t)} \quad (3\text{-}17)$$

$T(r_H,t)$ is the temperature at a defined distance r_H from the heat source and a specific time t. T_0 is the undisturbed subsurface temperature at time t=0, and α is the thermal diffusivity calculated as:

$$\alpha = \frac{\lambda_{eff}}{\rho c_p} \quad (3\text{-}18)$$

assuming a volumetric heat capacity of the subsurface ρc_p of 2.3 MJ m^{-3} K^{-1} (Verein Deutscher Ingenieure, 2010). r_b is the borehole radius, R_{th} is the thermal borehole resistance, γ is Euler's constant and m is the slope of the linear regression line. The starting evaluation time is defined by applying the theoretical criterion:

$$t_{start} = \frac{P\,{r_b}^2}{\alpha} \quad (3\text{-}19)$$

where P = 10 (Gehlin, 2002). In accordance with the German technical guideline VDI 4640-5 (Verein Deutscher Ingenieure, 2020), the data was evaluated with the sequential forward evaluation by iteratively increasing the evaluated datapoints. The resulting thermal conductivities were checked for independence of the test time by applying the convergence criterion $\Delta\lambda_{eff}/\lambda_{eff}$ < 0.05 / 20 h. The uncertainty of the effective thermal conductivity from ETRT was calculated based on Witte (2013) from the uncertainty of the specific heat load and standard uncertainty of the slope, adding a 5 % model error, and was about 9 %.

3.4 Results and discussion

3.4.1 Laboratory results

The laboratory results are summarised in Figure 3-2. A table including the values is also provided in Appendix Study 2 (Table A2- 1). The results indicate a large variability of thermal properties of the Triassic sandstones (Figure 3-2a), as also reported in literature (Franz and Schulze, 2016; Kämmlein and Stollhofen, 2019). The average thermal conductivity of saturated core samples is 4.6 W m^{-1} K^{-1} with values ranging between 2.7 ± 0.28 and 6.4 ± 0.6 W m^{-1} K^{-1}.

Porosities range between 5.6 ± 0.1 and 23.6 ± 0.4 % (Figure 3-2b). They are very strongly negatively correlated with the dry bulk densities (Pearson correlation coefficient r = 0.96), as higher bulk densities are related to a denser packaging of the particles. Assessment of the pore geometry shows average pore diameters ranging between 0.010 ± 0.001 and 1.04 ± 0.16 µm with an average value of 0.14 µm (Figure 3-2e). The average inner pore surface is 2.75 m² g^{-1} covering a wide range of values from 0.06 ± 0.01 to 8.5 ± 1.3 m² g^{-1} (Figure 3-2f). Correlation with the laboratory-derived thermal conductivity of saturated samples indicates decreasing thermal conductivities with increasing inner pore surface (r = 0.63).

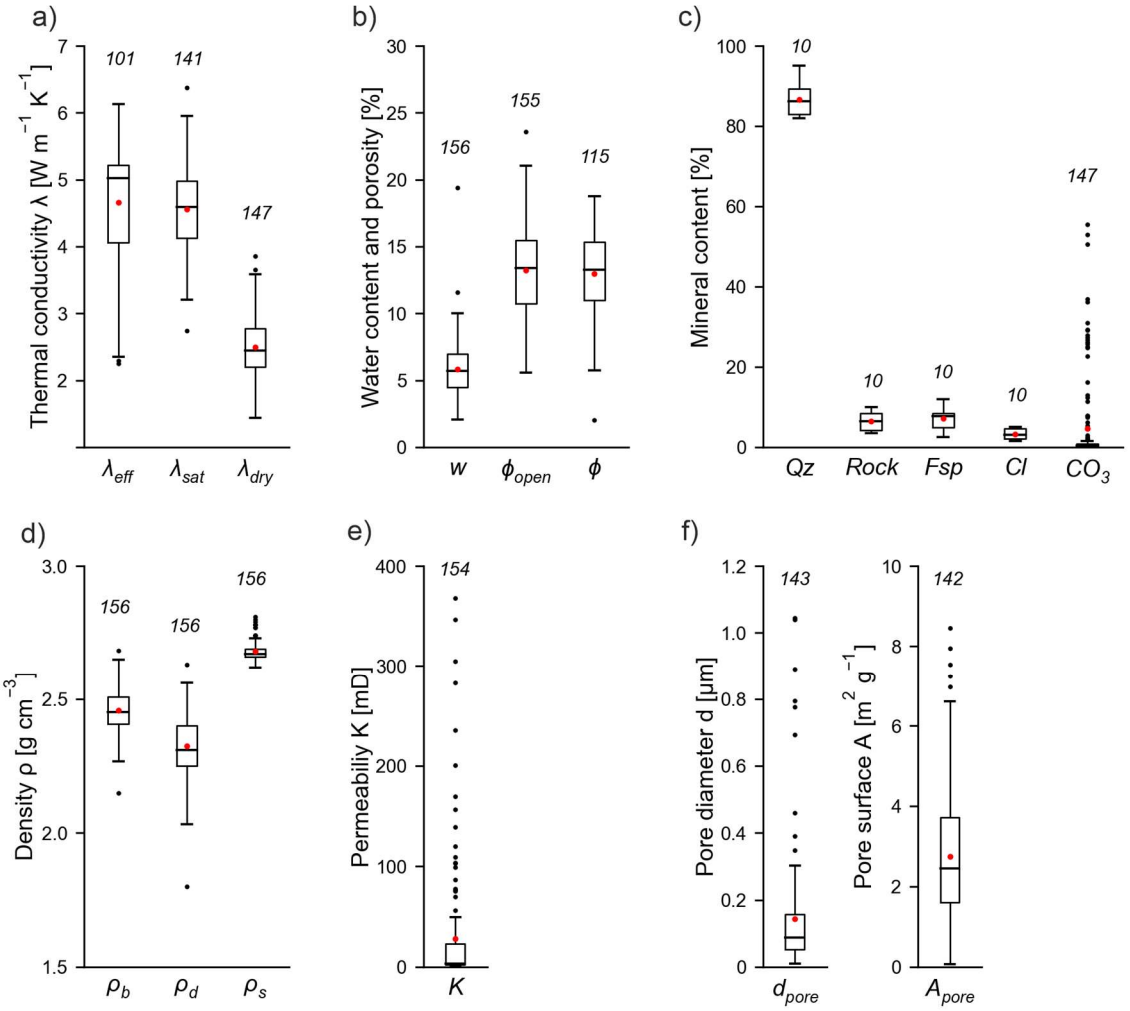

Figure 3-2: Petrophysical properties of the Triassic sandstones. Number of samples in italics and mean values in red: a) thermal conductivities, b) water content and porosities, c) mineral contents, d) densities, e) permeability, f) pore diameter and inner pore surface from mercury intrusion porosimetry.

The mineral contents of the ten representative samples vary only slightly Figure 3-2b). The samples predominantly consist of quartz (82 ± 8 to 95 ± 10 %), feldspar (especially microcline, 3 ± 1 to 12 ± 6 %), clay (1.5 ± 0.9 to 5.0 ± 0.5 %), carbonate (0.06 ± 0.03 % to 55 ± 5) and lithic fragments (4 ± 1 % to 10 ± 1 %). The hematite was found with contents < 1 %. As quartz has a high thermal conductivity (7.7 W m^{-1} K^{-1} in Schön, 2011), higher quartz contents result in higher matrix thermal conductivities and, therefore, in higher bulk thermal conductivities. A correlation coefficient of r = 0.80 (10 samples) can be determined by correlating quartz content with saturated thermal conductivities. The repeated analysis shows a higher uncertainty due to the heterogeneous distribution of the minerals in the optically homogeneous impression of the sample.

The permeability of the Triassic sandstones (Figure 3-2d) shows a large variation with values ranging between 1.2 ± 1.4 and 368 ± 213 mD and a mean value of 28.0 mD. The high measurement uncertainties result from measurement at different positions on the sample surfaces. A

corresponding median of 3.2 ± 2.7 mD indicates a strong skewness in the distribution towards low permeabilities.

3.4.2 Estimated thermal conductivity

The estimated thermal conductivities from the different theoretical models are illustrated in Figure 3-3 and summarised in the Appendix Study 2 (Table A2- 2). The model performance is evaluated by comparing the estimated thermal conductivities and the laboratory results.

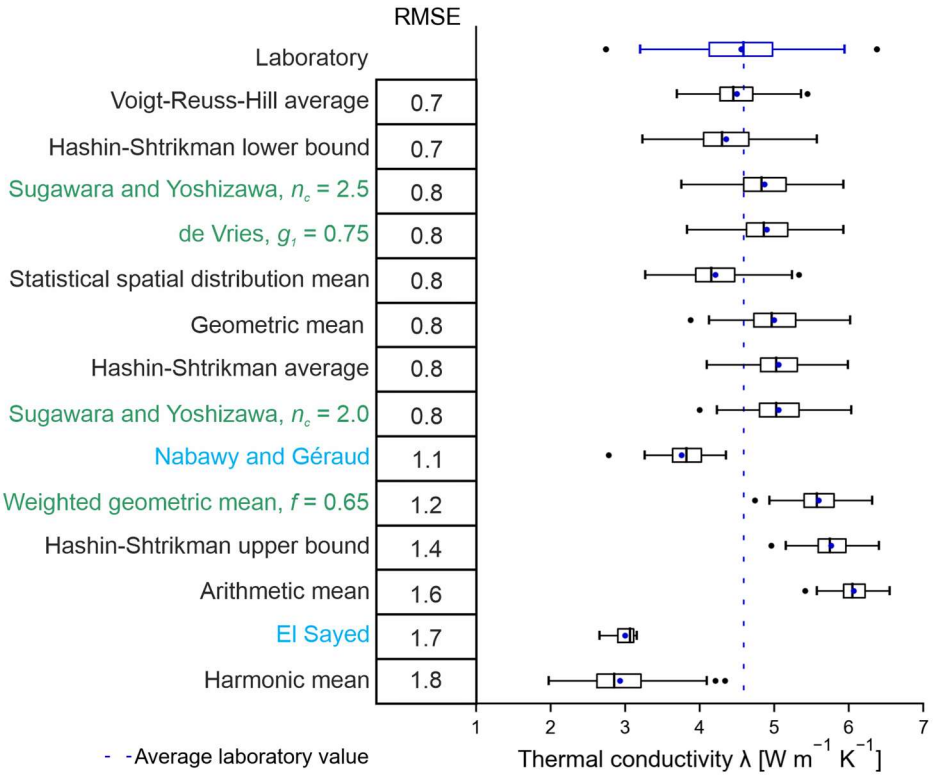

Figure 3-3: Thermal conductivities derived using various theoretical models sorted according to the root mean square error (RMSE). The models are classified into mixing models (black), semi-empirical (green) and empirical models (blue).

The average root mean square error (RMSE) of all applied models is 1.0 W m^{-1} K^{-1}. The best agreement is achieved with the Voigt-Reuss-Hill model with an average estimated thermal conductivity of 4.6 W m^{-1} K^{-1} and an RMSE of 0.7 W m^{-1} K^{-1}, which corresponds to 15 % of the mean thermal conductivity measured on the samples. However, several models have acceptable RMSE ≤ 0.8 W m^{-1} K^{-1}, which accounts for ≤ 18 % of the average thermal conductivity (Figure 3-3). Among them are the statistical spatial distribution mean, the model by Sugawara and Yoshizawa, the de Vries model, the geometric mean model and the Hashin-Shtrikman average.

3.4.2.1 Mixing models

Figure 3-3 shows that models assuming randomly distributed components (geometric mean, Voigt-Reuss-Hill average, statistical spatial distribution mean, average Hashin-Shtrikman mean) are in good agreement with the average thermal conductivity of the Triassic sandstone samples

at saturated conditions. Porosity is an important influencing parameter in all theoretical models. However, the porosity value only provides one bulk value of the percentage of the pore space, and does not take into account the topology (connectivity), the geometry of the pores and the inhomogeneity of the pore space. However, the characteristics of the pore space were shown to influence heat conduction (e.g., Albert et al., 2017; Midttomme and Roaldset, 1998).

To further investigate this influence for the ten selected samples, polarisation microscopy was used to qualitatively assess pore geometry and the matrix distribution (Figure 3-4).

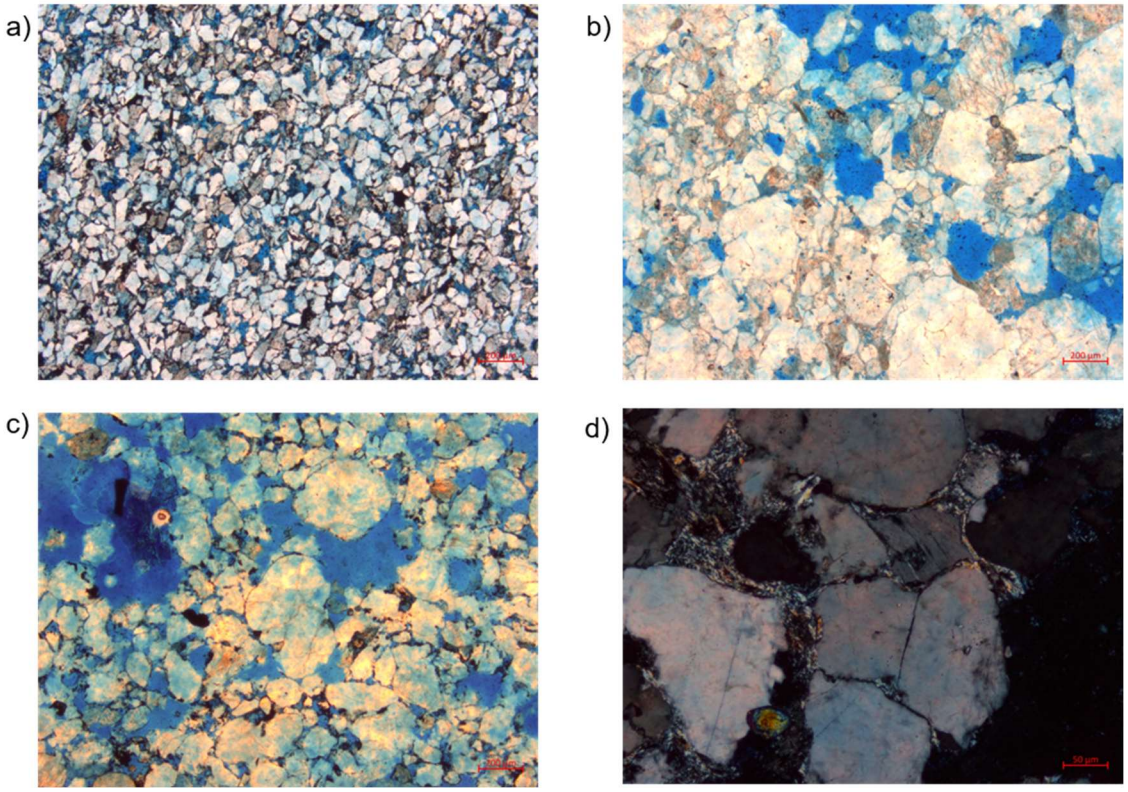

Figure 3-4: Exemplary polarisation microscopy images from thin sections, a) arrangement of particles (bright field, sample at 58.1 m), b) inhomogeneity of pore size (bright field, sample at 100.1 m), c) varying degrees of roundness (bright field, sample at 61.2 m), d) varying pore filling (crossed polarisers, sample at 95.6 m).

Figure 3-4a exemplary shows the arrangement of silt particles building the rock matrix. Most samples showed an irregular distribution of the pore space and local accumulation of smaller or larger grains (Figure 3-4b). The degree of roundness and the number and kind of grain contacts vary widely (Figure 3-4c and d). In theory, more contacts and a higher contact surface result in higher thermal conductivities. Hence, in addition to absolute porosity values, material properties such as grain size, pore size and particle contact area are expected to be relevant input parameters for theoretical models. However, quantifying such relationships using qualitative data from thin section analysis is challenging due to the heterogeneity of the microstructure.

Previous studies also tried to quantify the effect of pore connectivity on thermal conductivity. For example, a stronger effect of the pore shape on the thermal conductivity was shown for samples with generally higher porosities (Ordonez-Miranda and Alvarado-Gil, 2012). Moreover, Shen et al. (2021) tried to define pore connectivity through the ratio of effective porosity

(determined with mercury intrusion porosimetry) and total porosity. They proposed a new model to estimate thermal conductivities based on this relationship that could improve their estimation results (mean deviation < 10 % for saturated samples). These models could potentially estimate thermal conductivities more accurately, but require further laboratory measurements such as mercury intrusion porosimetry, polarisation microscopy etc.

3.4.2.2 Semi-empirical models

The semi-empirical models intend to overcome the lack of knowledge on pore geometry by deriving empirical parameters. By applying fitting parameters reported in different studies (De Vries, 1963; Pichugin et al., 2022; Sugawara and Yoshizawa, 1962, 1961), thermal conductivities were estimated with varying success (Figure 3-3). The de Vries (1963) model results in acceptable estimates with an RMSE of 0.8 W m^{-1} K^{-1}, although thermal conductivities are generally overestimated.

The correction of the geometric mean as suggested by Pichugin et al. (2022) gives a worse fit than the original geometric mean model (RMSE of 1.2 W m^{-1} K^{-1} compared to 0.9 W m^{-1} K^{-1}). With a fitting parameter of $f < 1$ Pichugin et al. (2022) aim at compensating an underestimation of thermal conductivities with the geometric mean model. However, the results of this study show a minor overestimation of thermal conductivities (with an estimated average of 5.0 W m^{-1} K^{-1}), indicating that a fitting parameter $f > 1$ would improve the estimation.

The model of Sugawara and Yoshizawa (1961, 1962) is applied with two different fitting parameters, derived for two different sets of sandstones. Using a fitting parameter of $n_c = 2.5$, the average thermal conductivity of 4.9 W m^{-1} K^{-1} is closer to the laboratory-derived thermal conductivity, than with 5.1 W m^{-1} K^{-1} for $n_c = 2.0$. However, the RMSE is 0.8 W m^{-1} K^{-1} for both fitting parameters.

3.4.2.3 Empirical models

The two selected empirical models assume linear or log-linear relationships between material properties and thermal conductivities. Both show a large error for the estimated thermal conductivities (Figure 3-3). The model by El Sayed (2011) significantly underestimates the thermal conductivities with an average value of 3.0 W m^{-1} K^{-1} and an RMSE of 1.7 W m^{-1} K^{-1}. This model is based on porosity and dry bulk density, and therefore on two significantly correlated properties (Chapter 3.4.1). Furthermore, the model is based on the decadic logarithm of permeability, which only weakly correlates with thermal conductivity ($r = 0.43$). Accordingly, the permeability does not significantly impact the thermal conductivities of the Triassic sandstones evaluated in this study. As thermal conductivity describes the ability of a material to conduct heat and permeability describes the ability of a material to transport fluids, both properties define the heat transport properties of a medium. However, they have no clear physical correlation, even if they both can be interconnected to each other through porosity.

The model by Nabawy and Géraud (2016) also underestimates the thermal conductivities with an average value of 3.8 W m^{-1} K^{-1}. As this model considers the quartz and clay content, it was only applied to the ten samples with quantified mineralogy, which reduces the statistical significance of the results. Moreover, in the selected samples clay does not occur in the form of dis-

tinct particles but rather in the form of the matrix, which increases the uncertainty of the mineral content.

In addition to the aforementioned limitations for applying the empirical models to the samples of this study, our findings also suggest that empirical models derived for a specific set of sandstone samples, cannot be easily transferred to other study sites and sandstones. Due to the varying sedimentation and consolidation processes, the composition and properties of sandstones are very diverse, which hinders the transferability of empirically derived constants and relationships. In contrast, models based on theoretical considerations, for example, of spatial particle distribution can be applied to different rock types or different study sites in order to estimate thermal conductivities at a laboratory scale within an uncertainty range of 15 – 20 % (Figure 3-3).

The limited samples analysed about mineralogy is one major limitation of comparing modelled thermal conductivities. Estimated thermal conductivities were calculated with an average matrix thermal conductivity when applying the mixing models and semi-empirical models. The average matrix thermal conductivity was determined based on the mineral content analysed for ten representative samples. The average matrix thermal conductivity is 6.9 W m^{-1} K^{-1} with values ranging between 6.5 ± 1.4 and 7.3 ± 1.4 W m^{-1} K^{-1}. Hence, the range in matrix thermal conductivities is lower than the uncertainties in their determination. In the Appendix Study 2, estimated thermal conductivities calculated with an average matrix thermal conductivity are compared with those calculated from sample-specific matrix thermal conductivities (Figure A2- 1 and Table A2- 3). The comparison demonstrates that the simplified assumption does not affect the conclusions drawn from it.

3.4.3 Field results

The estimated thermal conductivities were compared to effective thermal conductivities measured in the field (Figure 3-5). The average effective thermal conductivity evaluated with the ETRT was 4.7 W m^{-1} K^{-1} with values ranging between 2.3 ± 0.2 and 6.1 ± 0.4 W m^{-1} K^{-1} (Figure 3-2a). Effective thermal conductivities are compared with laboratory values by individually attributing each laboratory value to the corresponding fibre optic depth interval. The difference in the average values of the effective thermal conductivities and the laboratory measurements is only 0.1 W m^{-1} K^{-1}. In Figure 3-5a, the laboratory-derived thermal conductivities are plotted against the effective thermal conductivities.

Both field and laboratory methods result in similar value ranges with an RMSE of 0.7 W m^{-1} K^{-1}. Only a few samples have an error > 20 % (Figure 3-5a). The frequency distribution of the values is complementary shown as marginal distribution. The marginal distribution of the laboratory values is narrower than the field values, which can also be expressed with a lower standard deviation (0.6 W m^{-1} K^{-1}) than that of the ETRT data (0.9 W m^{-1} K^{-1}). This can partly be explained by the different conditions in the laboratory compared to the field (defined measurement temperature, defined evaluated sample material, solely conduction). However, the results also indicate that the laboratory measurements can be used as representative of the effective thermal conductivities of the study site (Figure 3-5a).

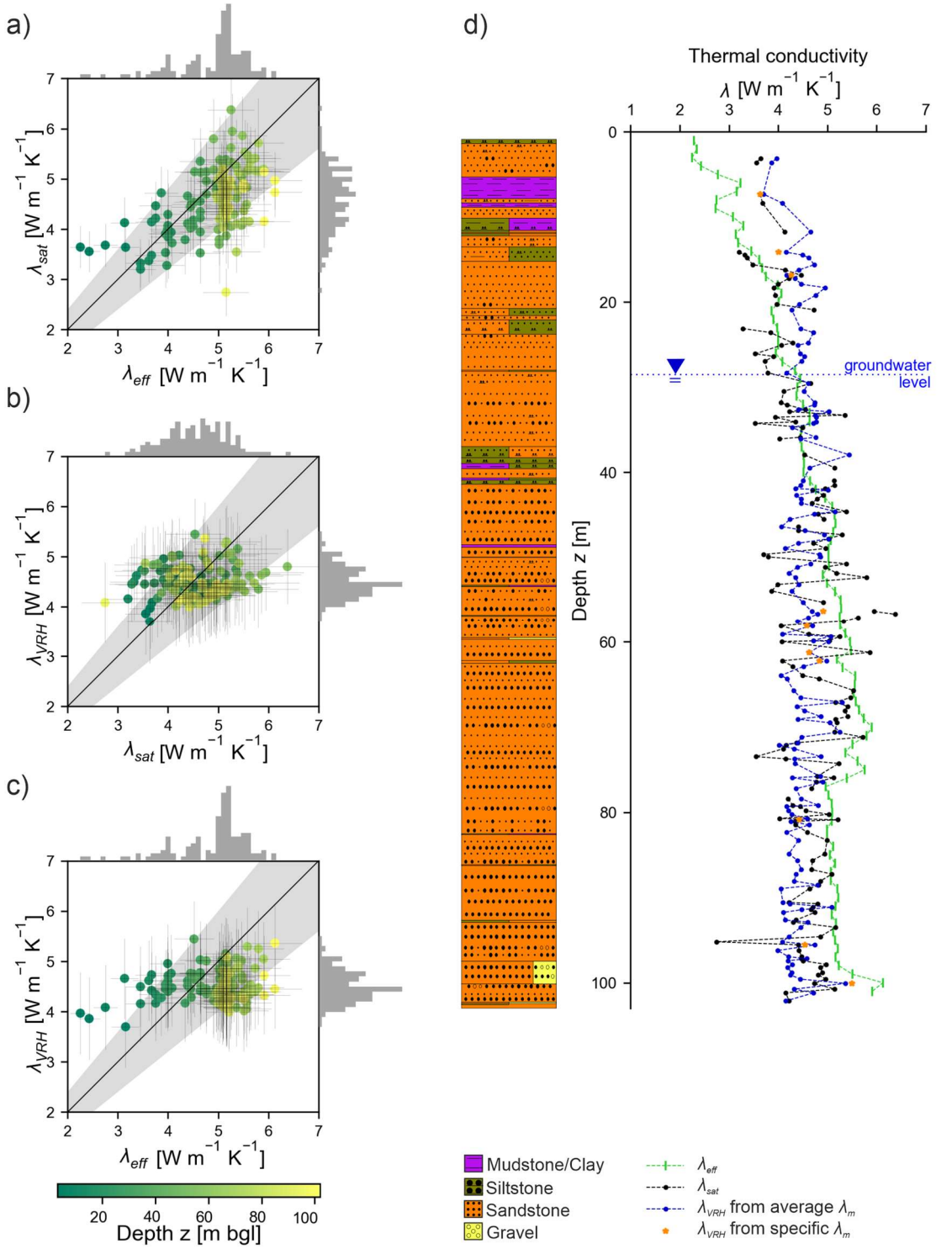

Figure 3-5: Comparison of the different methods to determine the thermal conductivities: a) laboratory (λ_{sat}) and field values (λ_{eff}), b) laboratory and estimated thermal conductivities applying the Voigt-Reuss-Hill average (λ_{VRH}), c) estimated and field values (the grey area indicates an error of 20 %, the grey lines indicate measurement uncertainties), d) depth-specific results.

However, the marginal distribution of the estimated values using the Voigt-Reuss-Hill model (λ_{VRH}) is significantly narrower than the measured values (Figure 3-5b and c) and the standard

deviation of the estimated thermal conductivities is low, with 0.3 W m^{-1} K^{-1}. About 18 % of the samples show an error > 20 %. Explanations can be found in the assumptions made when applying the Voigt-Reuss-Hill model. Matrix thermal conductivities of the samples are expressed by an average value of ten representative samples. Thus, thermal conductivities are mainly dependent on the porosity of the samples. Hence, other possible influencing parameters or conditions are neglected. Plotting the estimated thermal conductivities for the ten samples with known matrix thermal conductivities reveals that the uncertainty of the assumption is smaller than the observed variability in thermal conductivity (Figure 3-5d).

Moreover, Figure 3-5c suggests a relation between the thermal conductivities and the borehole depth which cannot be clearly observed in (Figure 3-5b and c). The thermal conductivity variation obtained with the three different methods (Figure 3-5d) confirms the larger deviations from the effective thermal conductivities in the deepest section of the borehole. This can be related to the fact that towards the bottom of the borehole, the assumption of an infinite line source is flawed. Here, heat can propagate not only horizontally but also in vertical (i.e. downward) direction. This results in an overestimation of the effective thermal conductivity. Moreover, larger deviations near the surface of the BHE can be explained by high temperature differences within the first meters of the fibre optic cable and due to surface effects (e.g. Galgaro et al., 2018).

Above the groundwater table, thermal conductivities are overestimated with the laboratory measurements and the Voigt-Reuss-Hill model (Figure 3-5d). This can be explained by different water saturations in situ compared to laboratory measurements and the assumed conditions in the theoretical models. Laboratory measurements are conducted on fully water-saturated samples, and for the theoretical models also full saturation of the pore space is assumed. In theory, partial saturation could be considered in the mathematical models. However, measuring the in-situ water saturation of core rock samples is experimentally challenging (Dalla Santa et al., 2022). By using the laboratory-derived thermal conductivities of dry and saturated samples, however, a range can be defined for the thermal conductivity of partially saturated samples.

Below the groundwater table (> 28.5 m bgl), especially at depths > 60 m, effective thermal conductivities tend to be higher than laboratory-derived thermal conductivities (Figure 3-5d). This is likely related to groundwater flow which can enhance the effective thermal conductivities in the field. Previous studies showed that groundwater flow can also impede evaluation of the TRT as obtained results from the ILS approach shown an increased sensitivity to the chosen evaluation time step (see, e.g., Albers et al., 2024b; Angelotti et al., 2018; Katsura et al., 2006; Sanner et al., 2005; Verdoya et al., 2018). However, in this study, a valid evaluation with the ILS is obtained with values converging towards a stable value for all depths below the groundwater level. Hence, the higher values cannot clearly be attributed to groundwater flow. Furthermore, it should be noted that the estimation of effective thermal conductivities from laboratory measurements is limited to study sites with negligible groundwater flow velocities as advective heat transport can significantly increase the effective thermal conductivities determined with an ETRT (Albers et al., 2024b; Dalla Santa et al., 2022; Luo et al., 2015).

Figure 3-5a and c show a cluster of effective thermal conductivities at around 5.1 W m^{-1} K^{-1}, which is not reflected in laboratory-measured and estimated thermal conductivities. An explana-

tion for this observation can be found in the measurement principles and the varying sample sizes. Laboratory measurements (and estimation using mathematical models) are point measurements, whereas with the ETRT average values for 1 m depth intervals are determined. Hence, small-scale changes in lithology and therefore thermal conductivities, which are represented only by thin layers, cannot be properly resolved with the DTS. This also leads to a smoother depth-profile for effective thermal (Figure 3-5d). The comparison between laboratory and field measurements is further limited, as laboratory samples represent the lithology at the borehole, while the ETRT analyses the rock volume outside of the borehole. The sample dimensions are significantly different, with a few centimetres in the laboratory and a penetration depth of the heat signal of about 1.7 m during the ETRT, as estimated with the ILS model. Especially for sandstones, properties can be horizontally and vertically heterogeneous due to the variability in the sedimentation conditions and diagenetic processes.

One major limitation of this study is that the anisotropy of thermal conductivity is not considered. Mixing models, such as the Voigt-Reuss-Hill model, assume isotropic properties. Moreover, the surface probe used for thermal conductivity measurement captures a mixed signal from heat flow in all spatial directions, yielding averaged thermal conductivities. By measuring thermal conductivity at three perpendicular sample surfaces, the heterogeneity of the sample is measured rather than anisotropy in thermal conductivity is measured. In contrast, effective thermal conductivities from ETRT are evaluated assuming radial heat flow and, thus, represent horizontal thermal conductivities, which may result in higher values due to horizontal layering effects.

The method comparison shows that laboratory-measured as well as estimated thermal conductivities of saturated core samples can represent the effective thermal conductivities of the Triassic sandstones at the study site within an uncertainty of about 15-20 %. No model is really satisfying. The “best” model shows an error > 20 % for 18 % of the analysed samples. The quality of determination of the average thermal conductivity for the study site depends on the number of samples. Even though the lithology is dominated by sandstones, the obtained thermal conductivities range between 2.7 ± 0.3 and 6.4 ± 0.6 W m^{-1} K^{-1}. With 156 core samples from one borehole, this study has an exceptionally high depth resolution. Another limitation is the high uncertainty in the mineral content, based on the analysis of two aliquots for only ten samples, which impacts the thermal conductivity estimates. Additional mineral analyses could reduce this uncertainty and strengthen the interpretations and comparisons.

The thermal conductivity values are generally within but slightly higher than those values reported in the literature, which vary between 1.7 and 5.8 W m^{-1} K^{-1} (Franz and Schulze, 2016; Haffen et al., 2017; Kämmlein and Stollhofen, 2019). The German industrial guideline VDI 4640, part 1 provides thermal conductivities for sandstones between 1.9 and 4.6 W m^{-1} K^{-1}. Our study shows that, for the Buntsandstein site, the upper bound of this values range serves as a good initial estimate.

3.5 Conclusion

The aim of this study is the determination of depth-specific thermal conductivities of Triassic Buntsandstein sandstones. Hence, we obtained thermal conductivities from laboratory analyses, theoretical models and ETRT, and compared the various approaches. From this study, the following conclusions can be made:

(1) Effective thermal conductivities range between 2.3 and 6.1 W m^{-1} K^{-1} with an average of 4.7 W m^{-1} K^{-1}, which makes the Triassic Buntsandstein highly suitable for shallow geothermal systems, such as GSHP systems. The observed heterogeneity highlights the importance of in-situ thermal conductivity determination for shallow geothermal applications.
(2) None of the applied theoretical models achieved satisfying results. The Voigt-Reuss-Hill model, however, achieved the best agreement with an RMSE of 0.7 W m^{-1} K^{-1}. Other theoretical models that assume randomly distributed components (e.g., geometric mean, statistical spatial distribution, Hashin-Shtrikman average) estimated thermal conductivities with similar errors. This can partly be explained by the uncertainties in mineral composition and determining the matrix thermal conductivity. Hence, only an initial estimation of thermal conductivities of studied Triassic sandstones is possible with theoretical models.
(3) Laboratory measurements and theoretical models achieved only a specific level of accuracy with an RMSE of ≥ 0.7 W m^{-1} K^{-1}, comparing them to effective thermal conductivities from ETRT. The challenges of this comparison are demonstrated, including the difference in sampling and measurement principles, the limited sample quantity, varying saturation and the possible influence of groundwater flow.

Finally, the findings of this study highlight the importance of choosing an appropriate method for evaluating the thermal conductivities of Triassic sandstones. Laboratory measurements and theoretical models were shown to be no reliable alternative to in-situ field measurements, such as the ETRT. Nevertheless, considering various methods improved our understanding of the parameters and processes influencing the thermal conductivity of sandstones.

3.6 Acknowledgements

The authors would like to thank Dr. PD Kirsten Drüppel, Kristian Nikoloski and Beate Oetzel for their help in preparing, analysing and evaluating the thin sections with polarisation microscopy and XRD analyses. Further, they would like to thank Dr. Petra Huttenloch, Joshua Schnurr and Felix Voss for their help with the laboratory analyses. The helpful comments of the two reviewers are also gratefully acknowledged.

4 Determination of thermal properties of grouting materials for borehole heat exchangers (BHE)

Reproduced from Albers, A., Huttenloch, P., Zorn, R., Steger, H., Blum, P., 2024. Determination of thermal properties of grouting materials for borehole heat exchangers (BHE). Geothermal Energy 12:36. https://doi.org/10.1186/s40517-024-00316-3

Abstract

Thermal properties of grouting materials for borehole heat exchangers (BHE) are currently analysed with varying measurement methods and analysis procedures, resulting in difficulties when comparing values of different studies. This study therefore provides the first comprehensive investigation of different analysis procedures by systematically comparing the influence of the measurement method and the sample preparation on the determination of the thermal conductivity and the volumetric heat capacity. Seven dissimilar grouting materials with varying water-solid ratios (w/s) and compositions are analysed. The thermal conductivities of the materials range between 0.9 and 1.8 W m^{-1} K^{-1} (transient plane source method, TPS). The volumetric heat capacities range between 3.01 and 3.63 MJ m^{-3} K^{-1} (differential scanning calorimetry, DSC). From the findings of this study, a standardised analysis of grouting materials is provided which suggests mixing of the grouting material at a high mixing speed and sample curing under water for 28 d at room temperature. The benefits of calculating the volumetric heat capacities of grouting materials from the specific heat capacities of dry samples measured with the DSC, the water content and the bulk density are demonstrated. Furthermore, an estimation procedure of volumetric heat capacity from the w/s and suspension density with an uncertainty of smaller ± 5 % is provided. Finally, this study contributes to consistency and comparability between existing and future studies on the thermal properties of grouting materials.

4.1 Introduction

For the planning and design of ground source heat pump (GSHP) systems, knowledge of the thermal properties of the borehole heat exchanger (BHE) system is essential. This includes not only the thermal properties of the ground but also of the backfill material. A large number of boreholes are backfilled with grouting material (IEA ECES, 2020). Reviews of grouting materials and their influence on the performance of GSHP systems are provided by Javadi et al. (2018) and Mahmoud et al. (2021). For an efficient GSHP system, high thermal conductivities λ

[W m^{-1} K^{-1}] and high volumetric heat capacities ρc_p [MJ m^{-3} K^{-1}] of the ground and backfill material are desirable. A high thermal conductivity of the grouting material decreases the thermal borehole resistance and ensures an efficient heat transfer from the ground to the heat transfer fluid (Allan and Kavanaugh, 1999; Delaleux et al., 2012; Viccaro, 2018). The knowledge of the volumetric heat capacity is essential for estimating the radius of the temperature disturbance during operation and, thus, evaluating the interactions with neighboured BHE (Zhou et al., 2018). Commercially available grouting materials for BHE are typically specified with a value for thermal conductivity, however, information on the volumetric heat capacity of grouting materials is often not provided. Commonly, the volumetric heat capacity is not specifically considered, as the thermal conductivity has a higher influence on the efficiency of the BHE. Although, the volumetric heat capacity is especially relevant at the start of the operation or when operating the BHE in intermittent mode (Li et al., 2019; Nian and Cheng, 2018; Wang et al., 2022).

Albeit with the ASTM D5334-22a (ASTM International, 2023) and the ASTM D4611 (ASTM International, 2016) there are some standards for the measurement of thermal conductivities and specific heat capacities of soils and rocks, there is yet no standard for the analysis of the thermal properties of grouting materials. Hence, for the determination of the thermal conductivity of grouting materials, various measurement methods were applied in the literature (Delaleux et al., 2012, p. e.g.,; Erol and François, 2014; Song et al., 2019). In Appendix Study 3, a comprehensive overview of applied measurement methods is provided (Table A3- 1). Although some authors applied steady-state methods, where a constant temperature gradient within the sample is established (e.g., Song et al., 2019), transient methods were applied more often. The transient hot wire method (THW) was applied using a needle probe (e.g., Blázquez et al., 2017; Erol and François, 2014; Kim and Oh, 2020). The needle probe was inserted into the sample via holes, which can cause an underestimation of the thermal conductivity due to insufficient thermal contact between the probe and the sample (Kim and Oh, 2020). Others used a surface probe, where the needle was pressed against the surface of the sample (e.g., Allan, 1997; Frąc et al., 2021; Kim and Oh, 2020; Viccaro, 2018). In some studies, the transient plane source method (TPS) was applied (e.g., Delaleux et al., 2012; Dong et al., 2022; Zhao et al., 2024). While the steady-state methods generally produce more accurate results, the transient methods have the advantage of shorter measurement times (Zhao et al., 2016). This reduces the errors due to evaporation or convection when measuring grouting materials at saturated or partly saturated conditions. Rarely, different measurement methods were compared with each other (Kim and Oh, 2020). Thermal conductivity measurements were usually conducted at room temperature at about 20 °C.

Compared to the number of studies on the determination of thermal conductivity of grouting materials, there are only a few studies on the determination of volumetric heat capacity (Appendix Study 3, Table A3- 2). Some studies used the volumetric heat capacity values derived from transient thermal conductivity measurements (e.g., Frąc et al., 2021; Kim and Oh, 2019). Extremera-Jiménez et al. (2021) determined the specific heat capacity by applying the calorimetry method. The differential scanning calorimetry (DSC) method was applied to measure the specific heat capacity of dry cementitious materials based on the DIN EN ISO 11357-4 (Deutsche

Norm, 2021) for plastics (Schutter and Taerwe, 1995; Shafigh et al., 2020). Specific heat capacity values were typically provided for 20 °C, i.e., room temperature.

However, the measurement of the thermal parameters is only the last step in the analysis of grouting materials. Beforehand, the sample has to be manufactured and prepared for the measurement. Sample preparation procedures can significantly influence the results of a measurement. Sample preparation procedures of grouting materials, especially regarding the mixing and storing conditions, vary immensely between the different studies (Appendix Study 3, Table A3-3). The German standard DIN EN 196-1 (Deutsche Norm, 2016a) establishes the sample preparation method of cements and mortars for the analysis of the strength of cement. In some of the studies on grouting materials, these were also adapted (Frąc et al., 2021; Mascarin et al., 2022; Viccaro, 2018). In analysing grouting materials, the samples have to be first manufactured by mixing the powdery raw material with a defined amount of water. The mixing procedure (including the size of the mixing vessel and the suspension volume) differed between the different studies as well as the used mixing device, which varied from disperser or mortar mixer to colloidal mixer (e.g., Allan, 1997; Mascarin et al., 2022; Pascual-Muñoz et al., 2018; Viccaro, 2018). After mixing, the suspension is filled in moulds and stored for curing until the measurement. Here, the specific material properties of cementitious materials have to be considered, as cementitious samples change their structure and mineralogical composition during ageing in the process of hydration (e.g., Kurdowski, 2014). The samples were predominantly cured at room temperature (about 20 °C) under water (e.g., Allan, 1997; Dong et al., 2022; Frąc et al., 2021) or under air-moist conditions with varying relative humidity from 45 % – 100 % (e.g., Erol and François, 2014; Viccaro, 2018; Zhao et al., 2024). In contrast, Kim and Oh (2019) cured their samples at ambient conditions, drying them in the oven and re-saturating them by placing them in water for 2 – 5 d. Song et al. (2019) used a consistometer to cure the samples at elevated temperatures (60 °C) and pressure (20 MPa). Due to the ongoing hydration process, the time when the measurement is conducted after the manufacturing can become relevant. In the different studies, various hydration times were chosen ranging from measurement at 7 (Berktas et al., 2020) – 30 d (Erol and François, 2014). Some studies evaluated the influence of the hydration time on the thermal properties by measurement at different hydration times up to 30 d (Bentz, 2007; Erol and François, 2014; Park et al., 2011), finding that after the first days, no significant changes in the thermal parameters occurred.

To understand how different measurement methods and sample preparation methods can influence thermal properties, it is therefore essential to understand the material properties that influence thermal properties. Grouting samples are porous samples. Thus, the properties of the sample depend on the properties of the solid part (i.e., mineralogy, grain contact, arrangement) and of the pores (i.e., pore size, pore distribution, pore filling). As the enhancement of thermal conductivity is the main focus of most of the studies, the influence of additives is well-studied in the literature (e.g., Allan, 1997; Erol and François, 2014; Viccaro, 2018). The most common additives are silica sand and graphite. While silica sand increases the thermal conductivity, it has a decreasing effect on the specific heat capacity of the grouting material (Allan, 1997; Kim and Oh, 2019; Kim et al., 2017). Although small amounts of graphite increase the thermal conductivity of the grout, it also can have a negative effect on the porosity and the workability of the material (Erol and François, 2014; Pascual-Muñoz et al., 2018; Song et al., 2019; Vicca-

ro, 2018). The porosity of the grouting material is highly dependent on the water-solid ratio (w/s), the ratio of water and the raw material used for manufacturing (Dong et al., 2022; Lafhaj et al., 2006; Stark and Wicht, 2013). More importantly, the pore size distribution is also dependent on the w/s, which has a significant impact on the hydraulic conductivity of the system (Stark and Wicht, 2013). Most material properties are negatively influenced by a high w/s. As the pore fluids have a lower thermal conductivity than the solid material, increasing w/s decreases the thermal conductivity of the grouting material (Allan, 1997). Park et al. (2011) showed for their studied materials a decrease in the thermal conductivity by 0.01 to 0.07 $W\ m^{-1}\ K^{-1}$ when increasing the w/s by 0.1. Air as a pore fluid has a significantly lower thermal conductivity than water. Hence, thermal conductivity increases with increasing saturation (Delaleux et al., 2012). At the same time, specific heat capacity increases with increasing water content (Kim and Oh, 2019; Kim et al., 2017).

As highlighted before, in the literature on grouting materials, the main focus is on the determination and improvement of thermal conductivity. Most often, the volumetric heat capacity is neglected. Yet, there is no standard measurement procedure for the determination of the thermal properties of grouting materials. Hence, various laboratories worldwide have developed their own procedure. Rarely, comparisons between different measurement methods or different sample preparation procedures are conducted apart from the studies by Kim and Oh (2020) and Do et al. (2017).

Hence, the objective of this study is the comprehensive comparison of analysis methods to determine the thermal conductivity and the volumetric heat capacity of grouting materials for BHE. This study does not aim to develop a new procedure, instead it highlights the weaknesses and strengths of the different existing methods and provides recommendations for the analysis procedure based on the findings of this study. This is the first study that provides a comprehensive overview of the analysis methods for the thermal properties of grouting materials. For the first time, the influence of not only the measurement method, but also the sample preparation procedure on the determination of the thermal properties is thoroughly evaluated. In extensive laboratory experiments, different measurement methods are applied and sample preparation procedures are systematically varied and evaluated about the mixing speed, curing conditions and hydration time. An estimation procedure for volumetric heat capacity is also derived. Thereby, this study contributes to the consistency and comparability between studies on the thermal properties of grouting materials. The findings of this study help to interpret the results of different studies with regard to the analysis methods. Furthermore, they offer a guideline to decide, which method should be applied to analyse the thermal properties of grouting materials, which therefore is a first step for a standardised approach.

4.2 Material and methods

The general workflow of the analysis of grouting materials is presented in Figure 4-1. Further information can be found in the respective chapters. The influencing parameters of the measurement method and the sample preparation on the analysis of thermal conductivity and volumetric heat capacity of grouting materials are systematically evaluated. As common for method development, first, the measurement method is optimised, representing a good controllable

system. Afterwards, the sample preparation method is also evaluated. Thermal conductivity is analysed with two different transient measurement methods, which also determine volumetric heat capacity. The volumetric heat capacity results from these transient methods are compared to volumetric heat capacities calculated from DSC results. Finally, using the relationships between material properties, volumetric heat capacities are estimated from w/s and suspension properties.

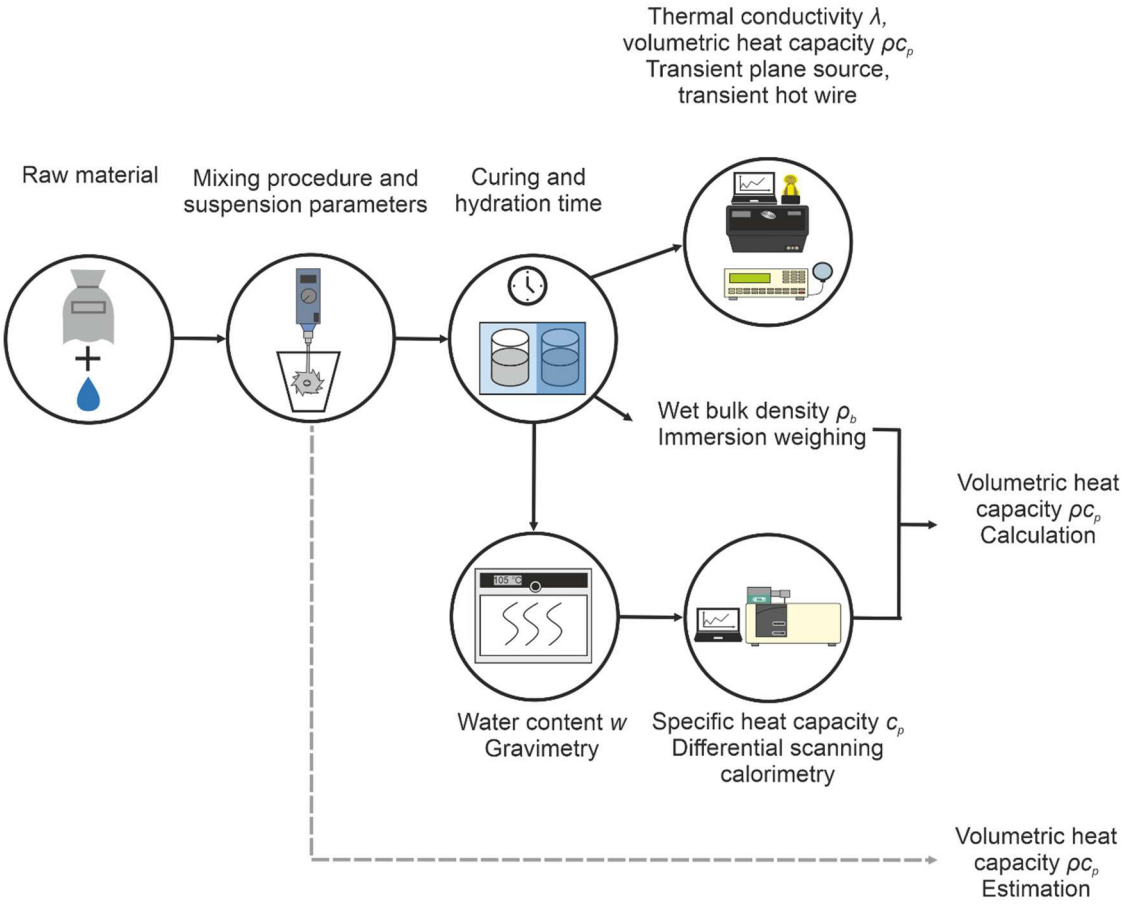

Figure 4-1: Workflow for the determination of thermal conductivity λ and volumetric heat capacity ρc_p of grouting materials applying different methods.

4.2.1 Material

A range of commercially available materials is analysed. This includes seven different grouting materials from five manufacturers with varying material properties. The materials vary in their mineralogy and chemistry (main components, additives), the w/s, the suspension density and, therefore, their thermal properties. The variety of materials allows generalisations of outcomes of this study about grouting materials. Table 4-1 provides an overview of the materials and the investigation program applied to the different materials. A detailed list of the applied methods and the corresponding sample conditions can also be found in Appendix Study 3 (Table A3- 4).

Table 4-1: Overview of the analysed grouting materials (M1 – M7), their properties and the applied investigation program.

Properties	M1	M2	M3	M4	M5	M6	M7
Water-solid ratio w/s [-]	0.80	0.80	0.30	0.60	0.38	0.57	0.45
Suspension density ρ_{sus} [g cm^{-3}] [a]	1.48	1.55	1.94	1.6	1.9	1.7	1.80
Composition	cement based	cement based	cement based	cement based	cement based	cement based	cement, bentonite, clay and stone powders
Thermally enhanced	no	graphite	quartz	no information	additives, fine aggregates	additives	aggregates
Investigation program	**M1**	**M2**	**M3**	**M4**	**M5**	**M6**	**M7**
Measurement method	×	×	×	×	×	×	×
Mixing speed	×	×	×	–	×	–	–
Curing conditions	×	×	×	–	×	–	–
Hydration time	×	×	×	×	–	–	–
Variation of w/s	×	–	–	–	–	×	×

[a] Manufacturer value

4.2.2 Sample preparation

The grouting samples are manufactured based on the specifications of the manufacturers. From a homogenised sample, the raw material is weighed for the manufacturing of a defined suspension volume of 2.5 L (scale accuracy 0.1 g). A defined mixing bucket (Carl Roth GmbH + Co. KG, volume 5 L, top diameter = 180 mm, bottom diameter = 160 mm, height = 270 mm) is filled with tap water according to the provided w/s. An overhead stirrer is used as a mixing device (IKA Eurostar 60 digital, dissolver stirrer R1300, diameter = 80 mm). The dissolver is positioned in a way that the vertical distance between the bottom of the vessel and the centre of the dissolver corresponds to the radius of the dissolver. The dissolver is aligned horizontally in the centre of the measuring beaker. The mixing speed is set to a defined rotation velocity (650 rpm and 2000 rpm, respectively). The grouting material is added evenly and quickly using a laboratory shovel. The suspension is stirred for 5 min.

The suspension properties are determined according to the following chapter. The suspension is filled in moulds with a defined geometry. For thermal conductivity measurements, the suspension is filled in cylinders (plexiglass, 10 cm diameter, about 5 cm height), which are fixed to a planar polyvinyl chloride (PVC) plate, taking care of an even and smooth surface of the sample. For the other analyses, the suspension is filled in three separate silicon cubes (5 cm in length). The moulds are cured under defined conditions (at room temperature 20 ± 2 °C; under deionised water and air-moist 85 ± 5 % relative humidity). Analyses of the hydrated samples are conducted at defined hydration times (from 7 up to 365 d).

4.2.3 Suspension properties

Suspension properties are analysed based on the recommendations of the Association of German Engineers VDI 4640-2 (Verein Deutscher Ingenieure, 2019). Suspension stability is determined for the time of 3 h in a cylinder (volume 250 mL). The suspension density ρ_{sus} [g cm^{-3}] is analysed with a mud balance. The workability is analysed with the Marsh funnel based on German Industrial Standard DIN 4127 (Deutsche Norm, 2014).

4.2.4 Wet bulk density, water content, porosity and saturation

Wet bulk density ρ_b [g cm^{-3}] is analysed using immersion weighing according to German Industrial Standard DIN 17892-2 (Deutsche Norm, 2015). Water content w [-] is determined by oven drying (at 105 °C) based on German Industrial Standard DIN EN ISO 17892-1 (Deutsche Norm, 2022a). From dried and ground samples, solid density ρ_s [g cm^{-3}] is analysed with the pycnometer method according to German Industrial Standard DIN ISO 17892-3 (Deutsche Norm, 2016b). Applying the following equations (4-1) to (4-3), dry bulk density ρ_d [g cm^{-3}], porosity ϕ [-] and saturation S_r [-] are calculated (Prinz and Strauß, 2018):

$$\rho_d = \frac{\rho_b}{1 + w} \tag{4-1}$$

$$\phi = 1 - (\rho_d / \rho_s) \tag{4-2}$$

$$S_r = \frac{\phi_w}{\phi} = \frac{w\,(\rho_d / \rho_w)}{\phi} \tag{4-3}$$

ϕ_w [-] is the water-filled pore space and ρ_w [g cm^{-3}] is the density of water.

4.2.5 Thermal conductivity measurement

The thermal conductivity of the hydrated samples is measured with two different measurement methods: (1) transient hotwire (THW) method and (2) transient plane source (TPS) method. Thermal conductivity is measured by evaluating the temperature response due to a defined heat load. Both methods applied in this study use a transient measurement principle. The THW method using needle probes is based on the standard ASTM D5334-22a (ASTM International, 2023). The heat load is applied to the sample using an electrical resistor. The temperature is recorded with time directly at the heat source. Under the assumption of an infinite medium, the temperature increase is evaluated based on the infinite line source method. The method is modified for surface probes under the assumption that the heat propagates in half-space direction through the specimen. The THW method is applied using a stiff, half-space surface probe (ISOMET 2104, Applied Precision Ltd., Slovakia) that is placed on the surface of the sample. The measurement probe is calibrated for thermal conductivities from 0.3 – 3.0 W m^{-1} K^{-1}. Two cylindrical samples are separately analysed and the mean value is calculated.

The TPS method is described in Gustafsson (1991) and in German Industrial Standard DIN EN ISO 22007-1 (Deutsche Norm, 2022b) in detail. The measurement probe is shaped in form of a nickel-metal double spiral. The user-defined heat load is induced by applying an electrical voltage. The temperature response of the sample is derived from the change of electrical re-

sistance. Evaluation of the temperature increase is based on the solution of the heat transport equation under the assumption of a defined number of concentric ring heat sources. The TPS method is applied with a full space probe (HotDisk TPS1500, C3 Prozess- und Analysentechnik, Germany) by placing a flexible probe between two sample cylinders of the same material. For the TPS method, the data acquisition is conducted with the software *Hot Disk Thermal Constants Analyser* (Version 7.4.17). The software enables control of the quality of the measurements by direct interpretation of the raw data and model fit.

The samples are measured at room temperature (20 ± 2 °C) and original water content. Thermal conductivity measurements with the THW are carried out at the conditions the samples were cured at, i.e., under water or air-moist. The measurements are carried out in a closed, thermally insulated container that is protected from sunlight. The samples are conditioned to the respective temperature before measurement. In between repeated measurements, the samples are always stored at the cured conditions. The same specimens are used for both, THW and TPS, measurements to enable valid comparison of the methods.

4.2.6 Specific heat capacity

Calorimetry is used to determine the amount of heat that must be applied or is generated during a physical or chemical transformation of a material, which results in a change of the internal energy of the material, referred to as the enthalpy H at constant pressure (Haines, 2002). Differential scanning calorimetry is based on the difference of the heat flow between a material and a reference sample as a function of temperature. The heat flows are derived from the continuously measured temperatures of the material and the reference. By integrating the peak area of the difference signal, the change in enthalpy is calculated. One frequently applied reference material is sapphire. Further information on the measurement principle can be found, e.g., in Höhne et al. (2003).

In this study, the specific heat capacity of the grouting materials is measured with a differential scanning calorimeter (DSC, No. 204 F1 Phönix, Netzsch, Germany) applying the sapphire comparison method according to German Industrial Standard DIN EN ISO 11357-4 (Deutsche Norm, 2021). The DSC is equipped with a cooling unit (IntraCooler IC85, Netzsch, Germany). For samples containing water, the enthalpy peaks of the water would superimpose the specific heat capacity signal of the grout. Thus, DSC measurements are conducted on ground, dried samples (oven dried at 105 °C). The material is weighed into crucibles (aluminium, 40 µL, Netzsch) using a microfine scale (Cubis II MCE 125P, accuracy ± 0.01 mg). The measurements are carried out in a nitrogen atmosphere (flow rate: 20 mL h^{-1}). The temperature range is -16 to 45 °C with a heating rate of 10 K min^{-1}. Data acquisition and analysis are performed using associated *Proteus*® software. The specific heat capacity is an additive quantity (Bentz, 2007). Thus, the specific heat capacity at original water content $c_{p,f}$ [kJ kg^{-1} K^{-1}] is the weighted arithmetic mean of the specific heat capacities of the components:

$$c_{p,f} = \frac{w}{1+w}\, c_{p,w} + \left(1 - \frac{w}{1+w}\right) c_{p,d} \quad \textbf{(4-4)}$$

$c_{p,d}$ [kJ kg^{-1} K^{-1}] is the specific heat capacity of the dried sample. The specific heat capacity of water $c_{p,w}$ [kJ kg^{-1} K^{-1}] is determined beforehand in the investigated temperature range and compared to literature data.

4.2.7 Volumetric heat capacity

The volumetric heat capacity is analysed with three different methods. It is (1) calculated from DSC measurements for dried and saturated samples ($\rho c_{p,d}$ and $\rho c_{p,f}$ [MJ kg^{-1} K^{-1}]), respectively:

$$\rho c_{p,d} = \rho_d \times c_{p,d} \quad \textbf{(4-5)}$$

$$\rho c_{p,f} = \rho_b \times c_{p,f} \quad \textbf{(4-6)}$$

In addition, measurements of the volumetric heat capacity of the samples at the original water content are conducted during the measurement of thermal conductivity with (2) the THW as well as with (3) the TPS (Chapter 4.2.5). The THW method uses the temperature change with time to derive the thermal diffusivity α. Applying the TPS method, thermal diffusivity is derived through parameter fit. Volumetric heat capacity is calculated applying:

$$\rho c_p = \frac{\lambda}{\alpha} \quad \textbf{(4-7)}$$

4.2.8 Measurement uncertainties

Measurement uncertainties of the analysed properties are calculated based on the *Guide to the Expression of Uncertainty in Measurement* (ISO IEC 98-3, 2008). For repetitive measurements the standard deviation s is determined according to the following equation:

$$s = \sqrt{\frac{1}{n-1}\sum_{i=1}^{n}(x_i - \bar{x})^2} \quad \textbf{(4-8)}$$

n is the number of measurements, x_i is the measurement value and $\bar{x}$ is the arithmetic mean of all measurement values. With the student t-distribution the standard uncertainty u_s with a confidence interval of 0.68 is calculated.

$$u_s = t\,\frac{s}{\sqrt{n}} \quad \textbf{(4-9)}$$

Combined measurement uncertainties are calculated from the propagation of uncertainties. In Appendix Study 3 (Table A3- 5) the measurement uncertainties for the different parameters are summarised.

4.3 Results and discussion

First, the measurement methods for the determination of thermal conductivity and volumetric heat capacity are evaluated. Then, the sample preparation is evaluated regarding (1) mixing speed, (2) curing conditions and (3) hydration time. In the third step, the influence of the w/s on the thermal properties is discussed. The results of this study are additionally used to derive an estimation procedure of the volumetric heat capacity from the w/s and the suspension density ρ_{sus}.

4.3.1 Measurement method

4.3.1.1 Thermal conductivity

The thermal conductivities of the analysed samples range between 0.9 and 1.8 W m^{-1} K^{-1}. Figure 4-2a shows the thermal conductivity results of the different measurement methods.

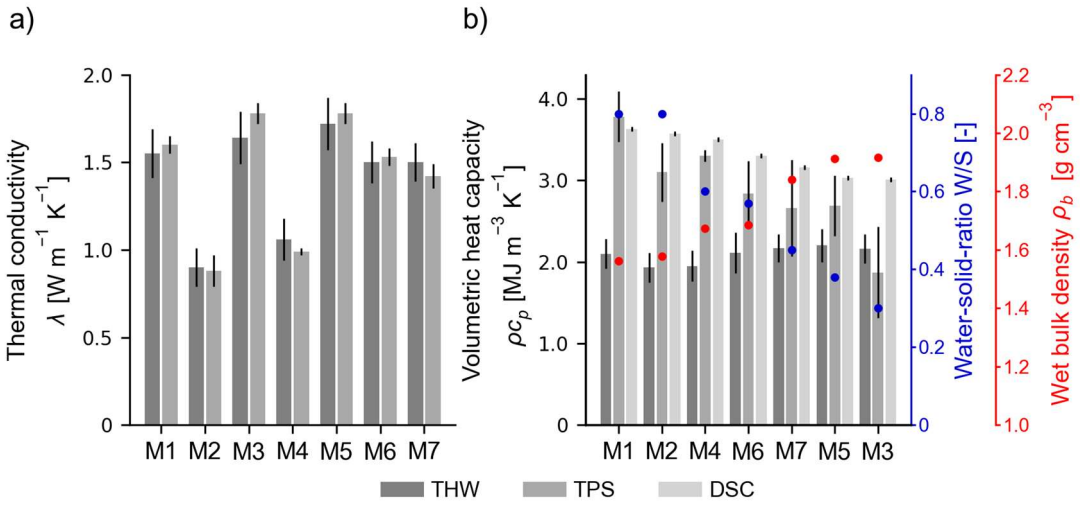

Figure 4-2: Comparison of measurement methods for the analysis of a) thermal conductivity and b) volumetric heat capacity. The black lines indicate standard uncertainties (Chapter 4.2.8). Samples preparation: Mixed at 2000 rpm, cured under water, hydration time 28 d and measured at 20 °C.

The thermal conductivity is measured with two transient measurement methods, the transient hotwire (THW) and the transient plane source (TPS) method. Both methods lead to comparable results. The mean deviation between both methods is only 4.5 %. The maximum deviation is 8 % for the material M3, and thereby still below the 10 % measurement uncertainty stated by the manufacturer.

The accuracy of the thermal conductivity measurement is highly influenced by the quality of the thermal contact between the measurement probe and the sample or sample surface. The manufacture of the sample with a smooth and plane surface is crucial. The measurement probes of the THW and the TPS have different specifications. The THW probe is stiffwe, which is accounted for by the manufacturer of the device during the calibration of the probe. The TPS probe is more flexible, which can partly compensate irregularities in the sample surface. The results show that both methods are suitable for the measurement of thermal conductivities of grouting materials.

It should be noted that the recommendations on the measurement method of thermal properties refer especially to grouting materials. The thermal conductivity measurement with surface probes (THW, TPS) is recommended for solid samples with smooth surfaces, such as grouting materials or rocks, as surface probes ensure a good thermal contact. Regarding the measurement of unconsolidated material such as soils and sands, a needle probe can be the better choice. However, this comparison is not considered in this study. Concerning validation of the results, measuring with two measurement methods is recommended when available and feasible. However, for the sake of clarity, further results for thermal conductivity are presented for TPS measurements only.

4.3.1.2 Volumetric heat capacity

The determined values for the volumetric heat capacity of the grouting samples at saturated conditions range between 1.9 and 3.8 MJ m^{-3} K^{-1} (Figure 4-2b). The deviation between the different measurement methods is rather high. For nearly all materials, the lowest values are measured with the THW and the highest values are determined with the DSC. On average, the volumetric heat capacity measured with the THW is 36 % below that of the DSC, and the volumetric heat capacity measured with TPS is 13 % below that of the DSC. Values are compared at room temperature. With the DSC, specific heat capacities are always analysed above a temperature range. In Appendix Study 3 (Figure A3- 1) the specific heat capacities are complementary shown for the entire analysed temperature range (-10 to 40 °C) with only a minor increase in the specific heat capacities to a maximum of 0.05 kJ kg^{-1} K^{-1} in the range of 5 to 40 °C. Investigating the plausibility of the measured volumetric heat capacities for the different materials, higher volumetric heat capacities should be evaluated for materials with higher w/s. The volumetric heat capacity of water predominately influences the volumetric heat capacity of the water-saturated grouting material (Table 4-1, Equation 6). The values derived with the THW method show no correlation between higher w/s and higher volumetric heat capacities. By comparing the values for M2 and M3, the materials with the highest and lowest w/s, respectively, even higher values are measured for the material M3 with the lower w/s. The TPS results are more consistent, however not for all samples. By comparing the values of M7 and M5 (w/s = 0.45 and 0.38), the volumetric heat capacity of M7 is lower than that of M5. Only the DSC values are plausible considering the relationship between the density and the composition of the sample (w/s). A detailed discussion on the relationship between the w/s and the properties of the grouting materials (water content, density, specific heat capacity) is included in Chapter 4.3.3.

The standard uncertainties are also rather high for the transient measurement methods and the repeatability is low as indicated by the error bars (Figure 4-2b). Average relative uncertainties for the THW and the TPS are 9 % and 15 %, respectively. In contrast, the standard uncertainty of the volumetric heat capacity determination with DSC is only ± 0.03 MJ kg^{-1} K^{-1}, which accounts for a relative error of 1 %.

The high variation of volumetric heat capacity between the three measurement methods can be explained with the difference in the measurement methods. The samples for the transient methods (THW, TPS) are measured at the original water content and as a bulk. The measurement probes are placed at the surface of the sample and only a specific sample volume is analysed. Thus, inhomogeneity, surface and structure effects add to the uncertainty of the measurement. In

contrast, the samples for measurement with the DSC are dried and ground resulting in very homogeneous samples. Repeated measurements on different aliquots prove the repeatability of the measurements. Volumetric heat capacity as a composite parameter is calculated with the water content and the bulk density determined on bulk samples. Hence, uncertainties increase due to the necessity of conducting three different analyses.

In addition, determination of the volumetric heat capacity from the transient measurements is based on curve fitting of the temperature change due to a defined heat input (Chapter 4.2.7). Hence, the fit is based on model assumptions. Furthermore, contact thermal resistance can influence the results of the fit. As natural samples typically have rougher surfaces compared to ideal flat surfaces, there is always a higher error due to the irregular contact between the probe and the sample surface. DSC, on the other hand, is a very accurate method to measure the specific heat capacity of dry grouting materials, rocks or unconsolidated materials as the specific heat capacity is directly derived from the heat flow. In conclusion, measuring the volumetric heat capacity with transient measurement methods such as THW and TPS can only provide first and rough estimates with high uncertainty. Hence, the DSC is our recommended method for the determination of the volumetric heat capacity of grouting materials. Accordingly, further results for the specific heat capacity and volumetric heat capacity, respectively, are only presented for the DSC method.

4.3.2 Sample preparation

The sample preparation is crucial for the quality of an analysis. Following, the influence of the sample preparation on the thermal conductivity and volumetric heat capacity is evaluated.

4.3.2.1 Mixing speed

The mixing procedure of the grouting material is essential to ensure a good blend of the raw material and the mixing water and, therefore, manufacture a homogeneous material. In this study, two different mixing velocities (650 and 2000 rpm) and their effect on the thermal properties are compared (Figure 4-3).

The results of the studied materials show almost no measurable influence of the mixing speed on the thermal conductivity and the volumetric heat capacity. This applies to grouting materials with high w/s (M1, M2) as well as to grouting materials with low w/s (M3). However, the mixing speed influences the suspension parameters and the structure of the sample (Table 4-2).

The suspensions mixed at lower mixing speed indicate inhomogeneity and the formation of lumps. Furthermore, they show a quality loss in the flow parameters. For example, material M2 has a higher suspension stability at a lower mixing speed. Significantly lower Marsh funnel flow times (15 – 50 %) are observed for the materials M2, M3 and M5. The porosity of all materials increases slightly for mixing at 650 rpm compared to 2000 rpm. Thus, between the two mixing speeds a clear recommendation for 2000 rpm can be made. However, the influence of the mixing method on the properties of cementitious material is complex (e.g., Dils et al., 2012). It depends not only on the mixing speed but also on the type of mixer and the mixing procedure, including, for example, the amount of material and the mixing time. Hence, the recommended

mixing speed is not transferable to other mixing devices. However, it is highlighted to always use a mixing speed that ensures a homogeneous mixture during the manufacturing of grouting materials.

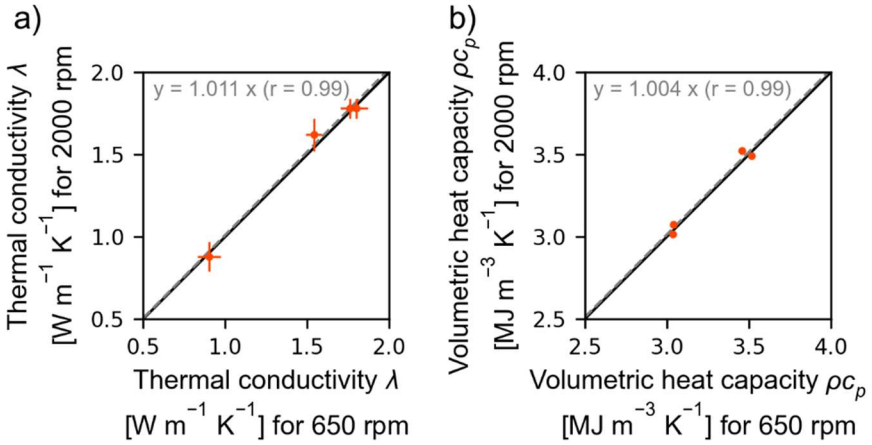

Figure 4-3: Comparison of a) thermal conductivities and b) volumetric heat capacities with varying mixing speed. Sample preparation: cured under water, hydration time 28 d and measured at room temperature (20 °C)

Table 4-2: Suspension properties and porosity of the grouting materials at varying mixing speed (650 rpm and 2000 rpm)..

Sample	M1		M2		M3		M5	
Mixing speed [rpm]	650	2000	650	2000	650	2000	650	2000
Suspension stability [%]	0.8	0.8	1.6	0.8	0.4	0.4	1.6	1.6
Workability (1 L) [s]	43	48	42	62	68	94	93	181
Suspension density ρ_{sus} [g cm^{-3}]	1.53	1.54	1.54	1.55	1.93	1.92	1.85	1.87
Porosity ϕ [%]	65.1	63.9	65.5	64.9	44.2	43.3	46.2	45.4

4.3.2.2 Curing conditions

To analyse the influence of the curing conditions during hydration, the grouting samples are cured under two different conditions: submerged under water and air-moist (85 ± 5 % relative humidity) conditions (Figure 4-4).

Curing conditions are expected to influence the water content due to evaporation processes. Figure 4-4a shows slightly lower water content under air-moist curing for all samples. On average, the water content is 4 % lower for air-moist cured grouting samples, with a maximum of 9 % for material M3. Thus, the total saturation of S_r = 1.0 as achieved with the samples cured under water is not always achieved. A decrease in thermal conductivities due to the lower water content is not measured (Figure 4-4). This could be explained by the evaporation process. Water evaporates from the sample at the surface, resulting in an inhomogeneous water distribution inside the grouting sample. Thus, the major part of the grouting sample is not affected by the curing conditions during the observed hydration time of 28 d. Figure 4-4a shows that the decrease in water content due to evaporation is minor, which is related to a low water vapour pressure at a relative humidity (RH) of about 85 %. However, Do et al. (2017) showed a de-

crease in thermal conductivities, when storing samples under air-moist conditions instead of under water. Do et al. (2017) compared the curing under water, the curing in a wet chamber at 100 % RH and a wet chamber at 50 % RH. For controlled low strength materials (CLSM) with cementless binders, they evaluated a decrease in thermal conductivities of > 50 % at 50 % RH and about 36 % at 100 % RH.

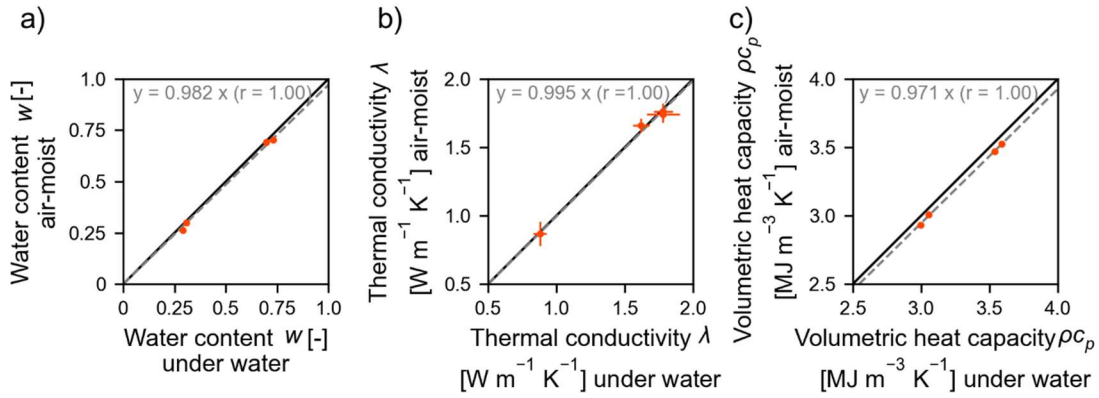

Figure 4-4: Comparison of a) water contents, b) thermal conductivities and c) volumetric heat capacities for varying curing conditions. Sample preparation: mixed at 2000 rpm, hydration time 28 d and measured at room temperature (20 °C).

The specific heat capacity of dry samples is not affected by the curing conditions. However, since the water content is used for the calculation of volumetric heat capacity at original water content (Equation (4-4)), lower water contents result in lower volumetric heat capacities (Figure 4-4c). For material M1 the values are lower by 0.04 MJ m^{-3} K^{-1}, for M2 the values are lower by 0.02 MJ m^{-3} K^{-1}. For material M3, the values are lower by 0.05 MJ m^{-3} K^{-1}. The influence of the curing conditions could also be shown by Bentz (2007) who evaluated higher specific heat capacity for samples cured under water than cured under air-moist conditions. From the results, under-water curing of the grouting samples can be recommended as in this way complete saturation of the samples can be achieved. Furthermore, easily controllable curing conditions can be maintained. Carbonation reactions with the CO_2 of the air can change the composition of the material surface (Verein Deutscher Zementwerke e.V., 2002). Thus, by curing the sample under water, carbonation processes at the surface of the samples can be hindered. However, the curing in deionised water can cause leaching of the sample.

4.3.2.3 Hydration time

The hydration of cementitious material is a continuous process (e.g., Aïtcin, 2016; Bullard et al., 2011). Thus, the age of the grouting samples has to be considered for the analyses of thermal properties. Hence, thermal conductivity and specific heat capacity are measured dependent on the hydration time (Figure 4-5). The samples are cured under water and measured at specific measurement days up to a hydration time of a year, to gain representative measurement values for the long-time development. Since the volumetric heat capacity of water-saturated samples is calculated with the wet bulk density and the water content, Figure 4-5c and d complementary show these values about the hydration time. Volumetric heat capacity is not shown, as wet bulk density is not evaluated for the entire hydration time.

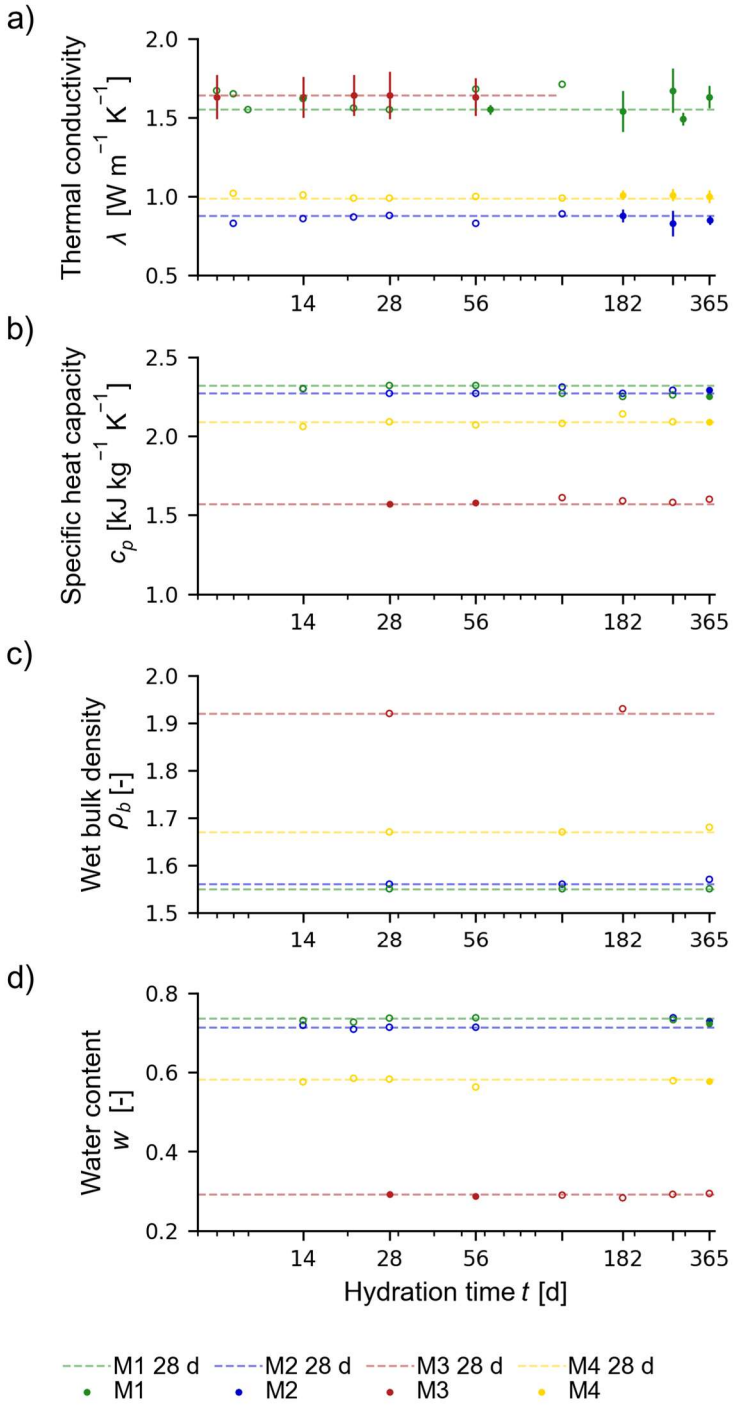

Figure 4-5: Thermal conductivity a), specific heat capacity b), wet bulk density c) and water content d) with increasing hydration times. Measurement uncertainties of the specific heat capacity below 0.01 kJ kg^{-1} K^{-1} are not shown. Values from single measurements are marked as open circles. The dashed line represents the reference value at 28 d. Sample preparation: mixed at 2000 rpm, cured under water and measured at room temperature (20 °C).

Regardless of the material composition, from 7 and 14 d, respectively, no significant influence of the hydration time on the thermal conductivity and the specific heat capacity is observed. The variations of the values lie within the range of the measurement error. Changes caused by the

ongoing hydration process cannot be resolved by the measurements. By comparing the specific heat capacities (Figure 4-5b) and the water contents (Figure 4-5c), higher values in the water content directly result in higher values of the specific heat capacity, e.g., for material M4 at 182 d. The wet bulk density of the samples shows little change during the analysed hydration time, indicating that the volumetric heat capacity does not change with later hydration times as well.

The results of this study follow the findings of other studies conducted about thermal conductivity (Bentz, 2007). Most reaction processes, where free water is chemically bound into silicate hydrate phases, take place within the first hours and days (Stark and Wicht, 2013). From there on, only marginal changes in the chemistry of the materials are expected. Regarding the specific heat capacity of concrete, Schutter and Taerwe (1995) studied the early hydration stage (1 – 7 d). They showed a decrease in the specific heat capacity with an increasing degree of hydration in the order of magnitude of about 13 %. Comparable results with cement paste were obtained by Bentz (2007). They showed that during the early hydration stage (< 7 d), the specific heat capacity decreased significantly before it reached an almost constant value. Measurement of the samples < 7 d is therefore not conducted during this study. At earlier time data, the strength of the sample is low. Handling of the sample is difficult. To maintain the integrity of the sample, only > 7 d measurements are conducted. However, for shallow geothermal energy systems, the comparison of this study aims to identify a value that is representative of the material during the application (>> 7 d). In some standards, the measurement of material properties at 28 d of hydration time is stated (Deutsche Norm, 2016a; Verein Deutscher Ingenieure, 2019). Figure 4-5 highlights that this value can be used representatively for more mature samples.

4.3.3 Influence of the water-solid-ratio (w/s)

The w/s of the studied materials ranges between 0.3 and 0.8. Furthermore, variation (± 5 % and ± 10 %) of the water content of the value recommended by the manufacturer is analysed for materials M1 (w/s = 0.8), M6 (w/s = 0.57) and M7 (w/s = 0.45) to extend the data. Figure 4-6 shows how the water content, wet bulk density and porosity as well as the thermal properties of saturated samples depend on the w/s. The calculated correlations are based on values from varying grouting materials. Regarding this, the correlations do not represent definite physical or chemical relationships, however, highlight to what extent the w/s influences the properties of the grouting materials. There is a clear linear relationship between the w/s and the corresponding water content for the materials analysed in this study (Figure 4-6a). The w/s is the ratio of the water mixed with the raw grouting material (powder). During the hydration of a cement, free water is chemically bound into silicate hydrate phases (Schutter and Taerwe, 1995; Stark and Wicht, 2013). Thus, water in hardened cement can be present as free water, physically bound water or chemically bound water. Experimentally, it cannot easily be distinguished between the three different types of water. However, the evaporable water, as determined with the water content, includes mainly the free water, the physically bound water and part of the chemically bound water (Adam, 2006). In a closed system (curing under water), the amount of water cannot be reduced. Thus, the decrease of the water content as compared to the w/s describes the amount of water that is no longer accessible as evaporable water. The amount of chemically bound water depends mainly on the cement content, the clay content and other additives (e.g., plasti-

cisers, liquifiers) of the raw material. Following the relationship between w/s and the water content, Figure 4-6a shows with a degree of determination of 0.97 that about 10 % of the added water is bound chemically for the analysed materials.

There is a nearly linear relation between the w/s and the wet bulk density (Figure 4-6b) for the analysed w/s range of 0.3 to 0.8. Higher w/s result in lower densities. The varying amounts of different additives (e.g., quartz, graphite) are leading to deviations from the linear correlation. Accordingly, higher w/s result in higher porosities (Figure 4-6c). Porosities are analysed in the range of 0.43 to 0.66. With higher porosities lower thermal conductivities are expected. However, Figure 4-6d shows that between the w/s and the thermal conductivities measured in this study, no general relationship can be established.

The thermal conductivities of the analysed samples range between 0.9 and 1.8 W m^{-1} K^{-1}. The grouting materials have varying amounts of different additives (e.g., silica sand, graphite). This effect superimposes the effect of the w/s. However, for the same material at varying w/s lower thermal conductivities with higher w/s are evaluated. In contrast, the specific heat capacities of saturated samples show a strong dependence on the w/s (Figure 4-6d). This relation is not surprising, as the specific heat capacity of a composite is the weighted arithmetic mean of the specific heat capacity of the components (Equation (4-4)). The specific heat capacities of the dry samples (at 20 °C) show only minor variations between 0.76 to 0.92 kJ kg^{-1} K^{-1}, with an average value of 0.83 kJ kg^{-1} K^{-1}. The specific heat capacity of water is higher than that of one of the mineral components ($c_{p,w}$ = 4.18 kJ kg^{-1} K^{-1} at 20 °C). Hence, the specific heat capacities of the saturated samples mainly depend on the water content, which also depends on the porosity. Higher specific heat capacity of water-saturated samples with higher w/s were also shown by other studies (Bentz, 2007; Kim and Oh, 2019; Marshall, 1972). Concerning the volumetric heat capacity, the decreasing effect of the w/s on the wet bulk density and the increasing effect of the w/s on the specific heat capacity of the saturated samples superimpose each other. However, the increasing effect of the specific heat capacity of the water is stronger than the decreasing effect of the density.

4.3.4 Estimation of the volumetric heat capacity

The w/s values as analysed in this study range from 0.3 – 0.8, which is common for commercially available grouting materials in Germany. Here, an estimation of the volumetric heat capacity of saturated grouting materials is proposed.

Based on the results of this study, the following assumptions are made:

(1) The specific heat capacities of dried grouting materials can be estimated with an average value of 0.83 ± 0.05 kJ kg^{-1} K^{-1} at 20 °C based on the measurements of the specific heat capacity of the grouting materials in this study.

(2) An empirical relationship between the w/s and the water content of grouting materials can be determined (Figure 4-6a).

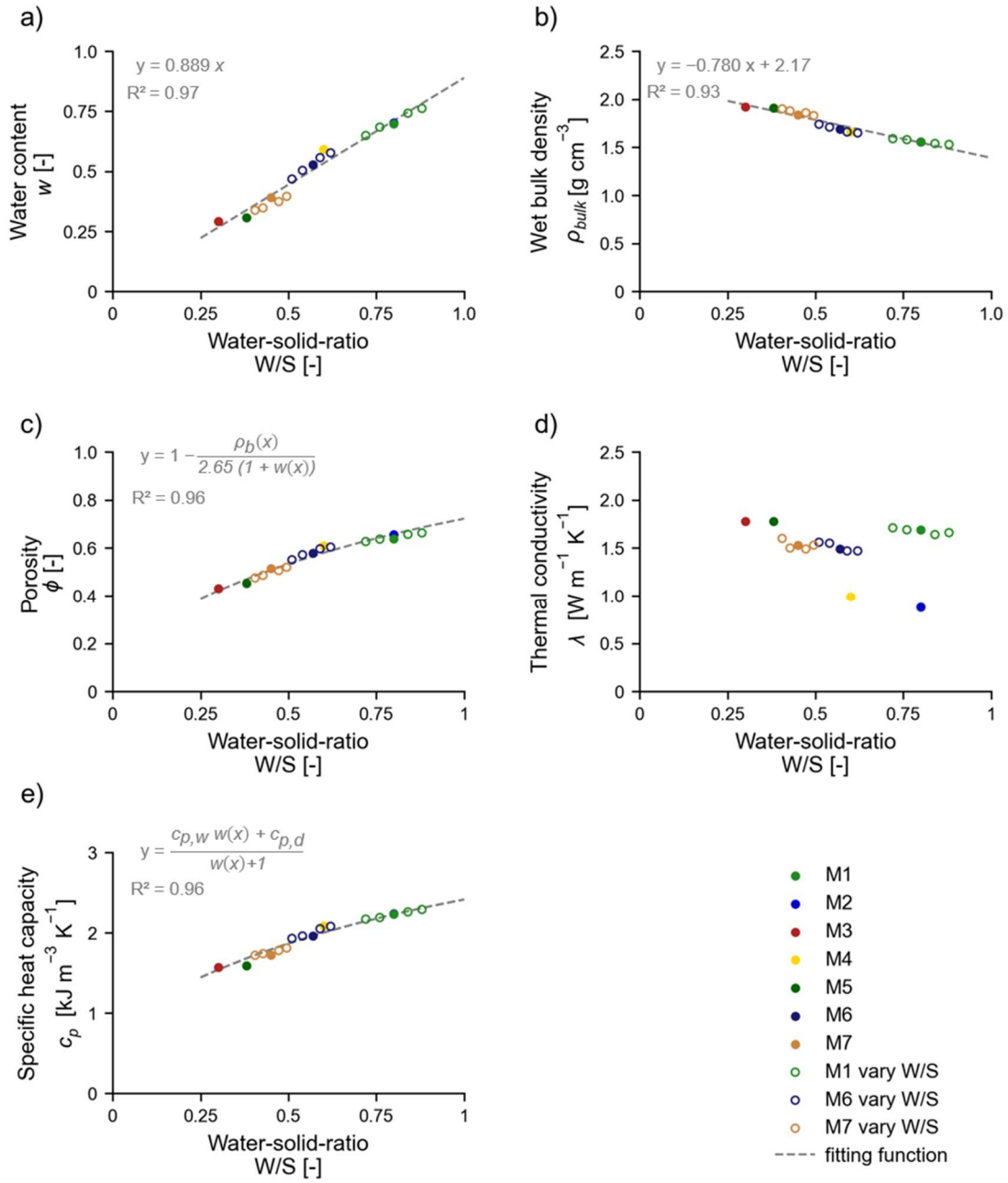

Figure 4-6: Influence of the water-solid-ratio on a) water content, b) wet bulk density, c) porosity, d) thermal conductivity and e) specific heat capacity. Sample preparation: mixed at 2000 rpm, cured under water, hydration time 28 d and measured at room temperature (20 °C). Including additional values varying the w/s for materials M1, M6 and M7 to increase the database. Fitting functions for c) and e) based on Equations 4 and 6.

(3) The wet bulk density can be estimated with the suspension density. Figure 4-7 shows, that wet bulk density is close to the density of the suspension. The maximum difference for the evaluated materials is only 2.7 %, which is expected in a closed system like the laboratory. Apparently, diffusion and exchange processes occur only to an insignificant extent.

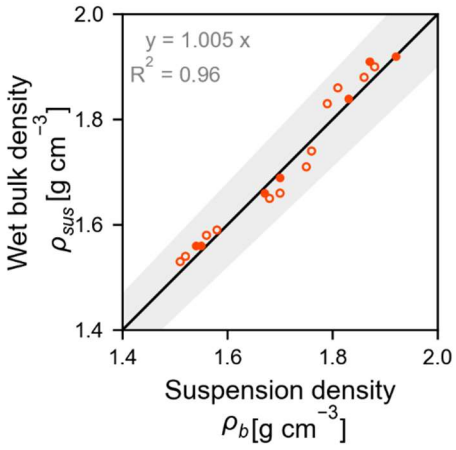

Figure 4-7: Correlation between the wet bulk density of the hydrated grouting samples and the suspension density. Sample preparation: mixed at 2000 rpm, cured under water, hydration time 28 d. Including additional values varying the w/s for materials M1, M6 and M7 to increase the database (open circles). The shaded area represents an error range of ± 5 %.

With these assumptions, a relationship is derived to estimate the volumetric heat capacity of grouting materials that can be applied only with the information available at a construction site, namely the measured suspension density and the w/s given by the manufacturer. The following equation summarises the calculation of the estimated volumetric heat capacity $\rho c_{p,est}$ [MJ kg^{-1} K^{-1}] at 20 °C:

$$\rho c_{p,est} = \rho_{sus}\left(C \times w/s \times c_{p,w} + (1 - C \times w/s) \times c_{p,d}\right) \quad \textbf{(4-10)}$$
$$= \rho_{sus}\,(0.89\; w/s \times 4.18\ \text{MJ m}^{-3}\ \text{K}^{-1} + 0.11\; w/s \times 0.83\ \text{MJ m}^{-3}\ \text{K}^{-1})$$

The coefficient C is empirically derived from the correlation between w/s and the water content (Figure 4-6a). Figure 4-8 demonstrates that a feasible estimate can be obtained.

All estimated values are in the error range of ± 5 %. The average difference between estimate and measurement value is only 1.7 %. Thus, the estimated values are more accurate than values analysed with THW and TPS methods, which have a measurement accuracy of about 5 – 10 %. Deviations can be explained by the composition of the materials and by the uncertainty of the combined measurement value of the volumetric heat capacity, which is calculated from three independent measurements. For planners of shallow geothermal energy systems, this estimation can provide valuable information. However, for this estimation, the mineralogical and chemical composition of the grouting sample is assumed to have a negligible influence compared to the w/s. This can result in a higher uncertainty of the estimate for materials with significantly different compositions. In addition, it has to be emphasised that this relationship is only valid for the comparisons conducted in this laboratory study. Further information on the behaviour and the properties of grouting materials at field conditions is therefore needed to validate our assumptions also for field sites.

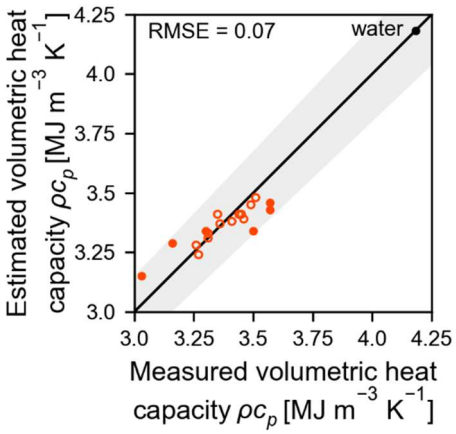

Figure 4-8: Comparison of the measured and the estimated volumetric heat capacities ρc_p. Sample preparation: mixed at 2000 rpm, cured under water, hydration time 28 d, measured at room temperature (20 °C). Including additional values varying the w/s for materials M1, M6 and M7 to increase the database (open circles). The shaded area represents the error range of ± 5 %.

4.4 Conclusion

In this study, analytical procedures for the determination of the thermal properties of grouting materials are evaluated. The influence of the measurement method and the sample preparation procedure on thermal conductivity and volumetric heat capacity is comprehensively investigated. Seven different grouting materials with varying water-solid ratios (w/s) and compositions are analysed. From the results of this study, we conclude the following:

(1) Several evaluated factors have only a minor influence on determining the thermal properties, such as mixing speed, curing conditions and hydration time. Furthermore, the transient methods applied to measure thermal conductivity provide consistent results.
(2) The results indicate that thermal conductivity values from different studies using various analysis procedures are quite comparable.
(3) For determining the volumetric heat capacity, the measurement method is shown to have a major influence on the results. The DSC method is the most precise method with measurement uncertainties of ≤ 1 %. An alternative estimation procedure based on the relation between w/s, water content and volumetric heat capacity achieved better estimation of the volumetric heat capacity of the grouting materials than measurement with the transient methods (< ± 5 %). Hence, the results from the transient methods should be used with caution regarding grouting materials.

Based on our findings, recommendations for standardised analysis of thermal conductivity and volumetric heat capacity of grouting materials are made:

(1) Mixing of the raw material at a high mixing speed (for the dissolver used in this study 2000 rpm).

(2) Curing the samples under water for 28 d at room temperature.
(3) Measuring thermal conductivity with transient measurement methods using surface probes at the original sample condition.
(4) Analysing the water content and wet bulk density. Using dried, ground samples for measurement of the specific heat capacity with differential scanning calorimetry (DSC). Subsequently, calculating the volumetric heat capacity.

In addition, an estimation procedure of volumetric heat capacity is introduced, that can be applied with the information available at a construction site. The estimation is based on the data of this study including materials with varying compositions and w/s. The verification of the estimation method with other materials is planned.

Future studies should focus on the validation of the developed methods in this study. A comparison of laboratory results and field studies is therefore necessary to investigate the suitability of the proposed laboratory methods for determining effective in-situ thermal properties of grouting materials. The analysis of grouting samples at saturated conditions represents an optimal case for the grouting material. In the field, the saturation however can vary from this assumption due to grouting in the vadose zone under seasonal changes and varying heat loads of the shallow geothermal system.

4.5 Acknowledgements

The authors would like to thank Madeline Dantin, Lucas Homann and Felix Voss for their help with the laboratory experiments. The authors would also like to thank the manufacturers for providing the grouting material. The helpful comments of the two reviewers are also gratefully acknowledged.

5 In-situ thermal properties of grouting materials in borehole heat exchangers

Reproduced from Albers, A., Huttenloch, P., Reduth, Y., Zorn, R., Steger, H., Blum, P. In-situ thermal properties of grouting materials in borehole heat exchangers (s*ubmitted to Geothermal Energy, November 2024*)

Abstract

The thermal properties of grouting materials characterise the heat transfer around borehole heat exchangers (BHE). However, these properties are typically determined in the laboratory. Thus, this study aims to assess the properties of grouting materials in the field. Two BHE grouted with two different grouting materials within unsaturated loess and limestone were excavated up to a depth of 15 m. Collected field samples show higher thermal conductivities by 13 % (w/s = 0.3) and 35 % (w/s = 0.8) than laboratory samples of the same material. These differences in thermal properties are mainly related to the filtration of the grouting suspension. In addition, with a short-time enhanced thermal response test (ETRT), 17 % lower in-situ thermal conductivities are determined than in comparison to the field samples. The deviations are attributed to the geometry of the borehole, the trajectory of the BHE and the heating cable. Thereby, this study shows the limitations when transferring laboratory-derived properties to a field site and emphasises the importance of considering site conditions, such as geology and hydrogeology.

5.1 Introduction

Ground source heat pump (GSHP) systems using borehole heat exchangers (BHE) present a sustainable technology to meet the heating and cooling demands of residential and office buildings (Bayer et al., 2012; Blum et al., 2010). The boreholes are often backfilled with grouting materials to stabilise the borehole and hinder vertical groundwater flow (IEA ECES, 2020; Javadi et al., 2018) avoiding major damages (Fleuchaus and Blum, 2017). Additionally, the grouting materials must ensure efficient heat transfer from the subsurface to the BHE (Allan and Kavanaugh, 1999). Thus, knowledge of the thermal properties of the grouting materials is crucial for an optimal design of GSHP systems.

The thermal response test (TRT) is a standard method to evaluate the thermal properties of the subsurface in situ (Spitler and Gehlin, 2015). Hence, a few studies used TRT to investigate the grout's thermal properties. By evaluating the thermal response time-dependently, the early-time data can represent the grout thermal properties (Bozzoli et al., 2011; Li et al., 2019). However, the early response is also influenced by the fluid-to-pipe and pipe-to-grout heat transfer process-

es. The concept of equivalent diameter was introduced to provide an analytical solution for this problem (Lamarche and Beauchamp, 2007; Shirazi and Bernier, 2013). Nevertheless, conventional TRTs can only provide one value for the entire borehole. One advancement of the conventional TRT is the enhanced TRT (ETRT), also described as enhanced geothermal response test (EGRT), where the defined heat load is applied by a heating cable and the temperature response is measured depth-specifically at a fibre optic cable (Wilke et al., 2020). This setup offers the advantage of early-time data evaluation since the cables are directly placed within the grout. Riegger et al. (2012) introduced the short-time enhanced thermal response test (ETRT) for detecting grouting defects defined by a distinct difference in the thermal conductivity between the fluid-filled void and the grouting material. By defining characteristic periods of the heating and recovery phase of an ETRT, thermal conductivities can be attributed to the different materials of the BHE system. (1) In the first period of a few seconds (Riegger et al., 2012) to a few minutes (Zhang et al., 2020), the temperature increase can be attributed to the heating cable or hybrid cable itself. (2) In the second period of several minutes, the temperature increase is predominately influenced by the borehole including the BHE pipes and the grouting material. (3) In the third period, with increasing test time the evaluated thermal conductivities approach a stable value that can be attributed to the ground thermal conductivity. By plotting the temperature increase about the heating time in a semi-logarithmic plot, these three periods can be distinguished via break points showing material changes. Riegger et al. (2012) applied the short-time ETRT in a field experiment and demonstrated the principle with a numerical model. Moreover, Heidinger and Fabritius (2017) successfully applied the short-time ETRT at a different study site with a heating time of 1.5 h. Zhang et al. (2020) also conducted a short-time ETRT experiment at a BHE that was backfilled with medium-sized sand. They attributed the duration between 5 min and about 14 min heating time to the borehole properties. However, no information was given on the borehole diameter.

Aside from in-situ experiments, Javadi et al. (2022) investigated varying grouting materials in sandbox experiments. For these, they manufactured columns of different grouting materials by curing the materials in moulds of 1 m height. Then, they placed the cured materials in silica sand and conducted thermal tests, evaluating the influence of defects on the results. Furthermore, they developed a numerical model that was validated with the results from the sandbox experiments as the experiments were conducted under the defined conditions. However, therefore, the curing conditions did not represent conditions as they would occur in a sandy subsurface. In this regard, Colombero et al. (2016) and Bucci et al. (2018) conducted an interesting field experiment by constructing a 7 m deep, grouted BHE in a quarry. The geology was characterised by gravel and sand. After 1.5 months, they excavated the grouted borehole and visually examined the grout integrity. They demonstrated defects and voids, especially at interfaces where the geology changed. However, the grouting materials were not analysed in terms of their material properties.

To summarise, with the short-time ETRT, a method was introduced that can be applied to evaluate the thermal conductivity of grouting materials in situ. However, validation of the method is difficult as more information is needed on the thermal properties of the grouting materials in the field. Commonly, the thermal properties of grouting materials are analysed at laboratory conditions from samples manufactured in the laboratory (Albers et al., 2024a).

Commercially available grouting materials are specified with the properties determined in the laboratory. However, these properties can differ in the field. Several studies showed that curing grouting materials in a natural geology can include filtration processes (Domes, 2015; Domes and Benz, 2015; Eklund and Stille, 2008; McKinley and Bolton, 1999). Filtration describes the removal of water from the cement suspension, where the suspended particle size is smaller than the pore size of the natural filter (Domes, 2015; McKinley and Bolton, 1999). The particle concentration in the suspension increases, and a filter cake is formed. The filtration of cement suspensions is studied mainly in geotechnical engineering, e.g., regarding the grouting of anchors (Domes and Benz, 2015) or tunnels (Eklund and Stille, 2008). Moreover, Theophil et al. (2023) recently demonstrated that the same processes are relevant for the grouting of BHE.

Thus, the objective of this study is to examine the in-situ thermal properties of grouting materials in BHEs. Grouted BHEs with two different grouting materials are therefore constructed in a large-scale field experiment. After conducting field experiments, the boreholes are excavated up to a depth of 15 m. Field samples of the grouting materials are collected, and their thermal properties are characterised by extensive laboratory experiments. The results are compared with grouting samples manufactured in the laboratory and discussed about filtration. Moreover, they are used for comparison with in-situ thermal conductivities determined with the short-time ETRT at one BHE. This study, therefore, provides new insights into the properties of grouting materials in the field from a unique study site. Our findings improve the reliability of material specifications and support the interpretation of field experiments.

5.2 Material and methods

5.2.1 Study site

The study site is situated in Merdingen, southwest Germany (Figure 5-1a). The geology is characterised by loess in the upper 14.5 m (Figure 5-1b). Below, weathered limestone is encountered, followed by solid limestone from about 21 m below ground level (bgl). The entire borehole is within the vadose zone. Eight boreholes are drilled on the edge of a quarry using a down-the-hole hammer, from which two boreholes (B1 and B2) are discussed within this study (Figure 5-1b).

The geometry and specifications of the boreholes are summarised in Table 5-1. Double U-pipe BHEs are installed in the boreholes (Table 5-1). Borehole B1 is equipped with a hybrid cable, containing fibre optic and heating cables (HELUKOM A-DSQ(ZN)B2Y; 1 × 4 G 50/125 + Cu 4 × 0.5 mm²; total cable length = 69.8 m), on the outside of one of the U-pipes. The grouting materials are mixed on the construction site with a colloidal mixer (GERTEC, IS-33-E) and filled into the borehole (Table 5-1).

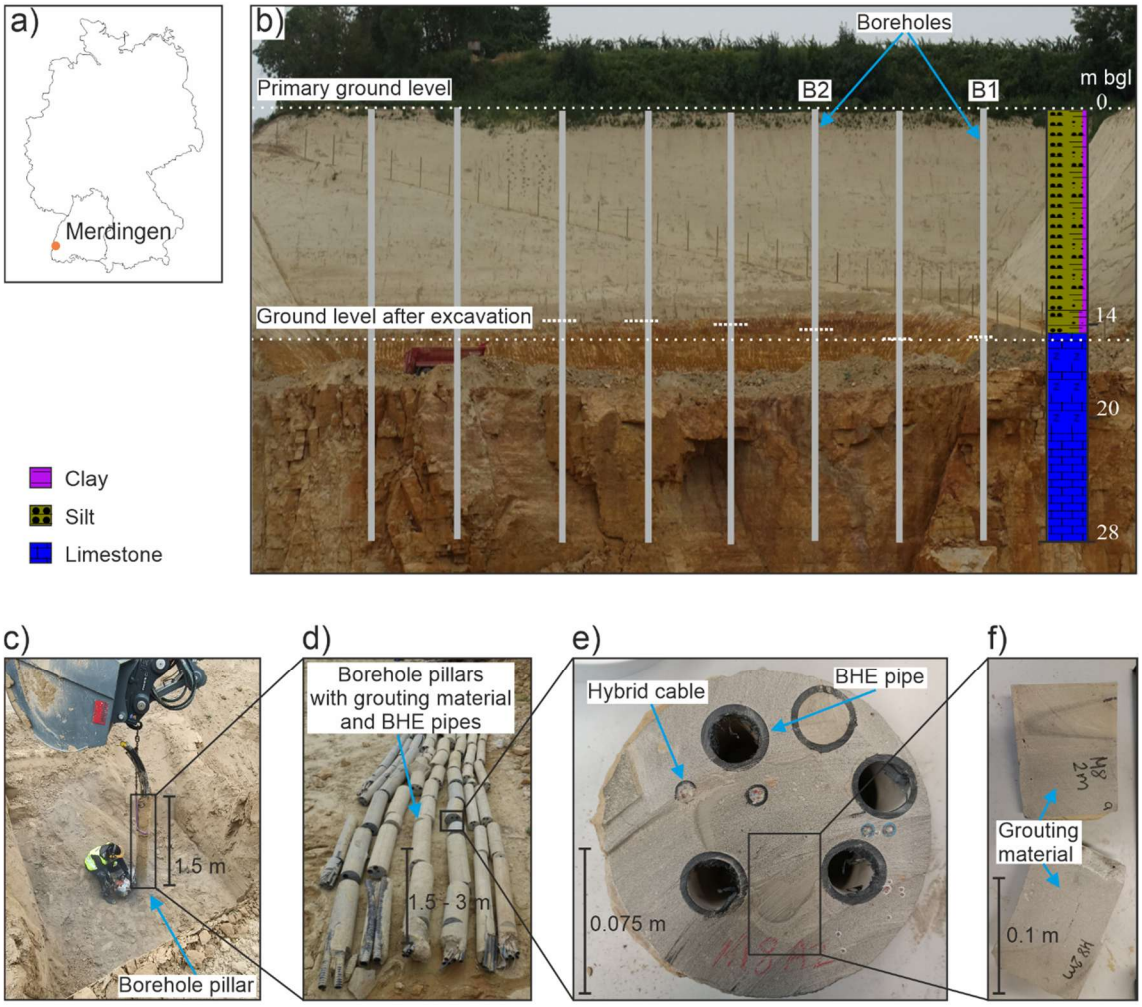

Figure 5-1: a) Location of the field site, b) geology, the position of the boreholes B1 and B2 before the deconstruction and the study site after the excavation, c) – f) sampling and sample preparation for the laboratory analyses.

5.2.2 Sampling

During the construction of the BHEs, material from the grouting suspension is sampled on-site and cured in the laboratory as *batch* sample (Chapter 5.2.3.1). About 10 to 11 months after the construction, the boreholes are deconstructed with an excavator up to a depth of about 15 m (Figure 5-1b,c). During excavation, the grouted boreholes, including the BHE pipes and the installed measurement technique, are sampled in pillars with lengths between 1.5 and 3 m (Figure 5-1c,d). At least every 2 m along these pillars, grouting samples are taken (Figure 5-1e). These *field* samples are further cut to prepare them for laboratory analyses (Figure 5-1e, Chapter 5.2.3). Moreover, eight core samples are taken from the soil surrounding B1 at several depths (1.5, 4.0, 5.2, 6.0, 8.0, 11.0, 13.2 and 14.5 m).

Table 5-1: Borehole geometry, specifications of the BHE and grouting materials.

Borehole	**B1**	**B2**
Borehole depth z [m]	28	26
Base of loess [m]	14.5	13
Base of weathering zone [m]	23	18.3
Borehole diameter d_b [mm]	150/132	219/190
Borehole casing [m]	19.5	4
Borehole heat exchanger (BHE)		
Type	Double U-pipe, PE100 RC	
Manufacturer	STÜWA Konrad Stükerjürgen GmbH	
Outer radius r_{po} [m]	0.016	
Inner radius r_{pi} [m]	0.013	
Thermal conductivity λ_p [W m^{-1} K^{-1}]	0.42	
Grouting material	**M1**	**M2**
Manufacturer	Schwenk Zement KG	Hans G. Hauri KG
Material	Füllbinder EWMplus	Zeotherm2.0
Batch	13.05.2022	2022-KW45
Water-solid ratio	0.3	0.8
Thermal conductivity λ [W m^{-1} K^{-1}] [1]	> 2.0	2.0
Suspension density ρ_{sus} [g cm^{-3}] [1]	1.94	1.48

[1] Manufacturer Value

5.2.3 Laboratory analyses

5.2.3.1 Sample preparation

A *laboratory* sample of the grouting material is manufactured based on the procedure recommended by Albers et al. (2024a). The grouting material is mixed in the laboratory with a dissolver (IKA Eurostar 60 digital, dissolver stirrer R1300, diameter = 80 mm) at a mixing speed of 2000 rpm for 5 min. The laboratory and the batch samples are cured in the laboratory for 28 d. For this purpose, the suspension is filled in moulds with a defined geometry (Albers et al., 2024a). The moulds are stored under deionised water at room conditions (20 ± 2 °C).

An overview of the different samples and methods is presented in Table 5-2. For the sake of clarity, the methods are referred to with the assigned names during the entire manuscript.

Table 5-2: Samples and methods applied in this study to analyse the thermal conductivity (λ_g) and specific heat capacity ($c_{p,g}$) of the grouting materials.

Sample	**Material**	**Manufacturing**	**Curing**	**Analyses**	**Thermal properties**
Laboratory	M1, M2	in the laboratory	laboratory for 28 d	TPS [a], DSC [b]	λ_g, $c_{p,g}$
Batch	M1, M2	in the field using a colloidal mixer			
Field	M1, M2		in situ for 11 months		
In-situ	M1		in situ for 1 – 3 months	ETRT	λ_g

[a] Transient Plane Source (TPS) method; [b] Differential Scanning Calorimetry (DSC).

5.2.3.2 Material properties

The material properties are determined in accordance with the German Industrial Standards (DIN). Water content w [-] is determined by oven drying at 105 °C according to DIN EN ISO 17892-1 (Deutsche Norm, 2022a). Wet bulk density ρ_b [g cm^{-3}] is analysed using immersion

weighing according to DIN EN ISO 17892-2 (Deutsche Norm, 2015). From dried and ground samples, solid density ρ_s [g cm^{-3}] is analysed with the pycnometer method according to DIN ISO 17892-3 (Deutsche Norm, 2016b). Dry bulk density ρ_d [g cm^{-3}], porosity ϕ [-] and saturation S_r [-] are calculated (Prinz and Strauß 2018).

Particle size analysis is conducted with a laser particle analyser (PSA 1190 L/D, *Anton-Paar*, accuracy ± 3 %) in accordance with DIN ISO 13320 (Deutsche Norm, 2022c). The grain size of the samples is < 250 mm. Before the measurement, soil samples are mixed with 0.2 % sodium pyrophosphate solution; grout samples are measured in ethanol. The samples are dispersed with ultrasound (50 W) for 1 min. For soil samples, ultrasound is used during the 1-min measurement. Grout samples are measured without ultrasonic at defined mixing (350 rpm) and pumping speed (300 rpm). The data is analysed using Kalliope software (*Anton-Paar*) according to the Fraunhofer model.

The pore size distribution is analysed using a mercury porosimeter (Autopore III Analyzer, *Micromeritics Instruments Corporation*) in accordance with DIN ISO 15901-1 (Deutsche Norm, 2019). For this purpose, the samples are cut into cubes with an edge length of approximately 5 mm. The materials are oven-dried at 105 °C.

Thermal conductivity is measured with the transient plane source method (HotDisk TPS1500, *C3 Prozess- und Analysentechnik*, Germany; measurement uncertainty ± 2 %). The samples are measured at room temperature (20 ± 2 °C) in a closed, thermally insulated container that is protected from sunlight. The specific heat capacity of the grouting materials is measured with a differential scanning calorimeter (DSC, No. 204 F1 Phönix, *Netzsch*, Germany) applying the sapphire comparison method according to DIN EN ISO 11357-4 (Deutsche Norm, 2021) and described in Albers et al. (2024a) in detail. DSC measurements are conducted on ground, dry samples (oven-dried at 105 °C). The specific heat capacity at original water content $c_{p,f}$ [kJ kg^{-1} K^{-1}] is the weighted arithmetic mean of the specific heat capacities of the components. Volumetric heat capacity $\rho c_{p,f}$ [MJ kg^{-1} K^{-1}] is calculated with the bulk density.

5.2.4 In-situ experiment

5.2.4.1 Enhanced thermal response test (ETRT)

A short-time ETRT is conducted about one month after the construction of the BHEs at B1, when the undisturbed subsurface temperature has been reached again. An average specific heat load of 22.1 W m^{-1} is applied for 13 h using a DC-power supply (Power Ten Inc., R86 D-200100; 200V/100A). Current and voltage are logged during the entire heating time (ALMEMO 2890-9, *Ahlborn*; uncertainty of the current ± 0.1 % of the full-scale value of 200 V + 2 digits + 0.03 % of the measurement value + 2 digits + 0.5 % uncertainty of the shunt; uncertainty of the voltage ± 0.1 % of the full-scale value of 200 V + 2 digits + 0.03 % of the measurement value + 2 digits). The temperature is measured at 240 s intervals using distributed temperature sensing (DTS) with a measurement interval of 1 m (N4386B, *Agilent*, *AP Sensing*, dual-ended measurement, measurement uncertainty provided by the manufacturer is ± 0.2 K).

5.2.4.2 Evaluation

The short time ETRT is evaluated about depth-specific thermal conductivities of the grouting material (λ_g) and of the subsurface (λ_{eff}) by applying the infinite line source (ILS) model (Carslaw and Jaeger, 1959) with a parameter estimation approach:

$$T(r_H, t) - T_0 = \frac{q}{4\,\pi\,\lambda_{eff}} E_i \left[\frac{{r_H}^2}{4\,\alpha\,t}\right] + q\,R_{th} \quad \textbf{(5-1)}$$

with $T(r_H,t)$ being the temperature at a defined distance r_H from the heat source and a specific time t, T_0 being the undisturbed subsurface temperature at time $t = 0$, q being the specific heat load calculated according to Albers et al. (2024b), E_i being the potential integral, r_H being the radius of the hybrid cable (r_{cable} = 0.006 m) and α being the thermal diffusivity calculated as:

$$\alpha = \frac{\lambda_{eff}}{\rho c_p} \quad \textbf{(5-2)}$$

by assuming volumetric heat capacities of $\rho c_{p,g}$ = 2.71 MJ m^{-3} K^{-1} for the grouting material and $\rho c_{p,s}$ = 1.92 MJ m^{-3} K^{-1} for the subsurface. As the hybrid cable is installed in a loop parallel to the BHE pipes, both shanks of the cable are evaluated separately, resulting in two values for each depth interval.

The temperature data is evaluated for different evaluation times. The later temperature increase is expected to be mainly influenced by the thermal conductivity of the subsurface (Riegger et al., 2012). To derive grout thermal conductivities, only the early time data is characteristic. Using the equation for the penetration depth of the heat signal

$$r_H = \sqrt{\frac{4}{e^{\gamma}}\,\alpha\,t} \quad \textbf{(5-3)}$$

the theoretical time when the heat signal reaches the borehole wall is calculated. The heating cables are assumed to be positioned in the centre of the borehole. The distance r_H is set to $r_H = r_b - r_{cable.}$ The calculated time is then used as a criterion until when the temperature increase can be attributed to the borehole.

5.3 Results and discussion

5.3.1 Laboratory and batch samples

The influence of the manufacturing process on the material properties is investigated by comparing the material properties of the grouting samples manufactured in the laboratory (laboratory sample) and on-site (batch sample). Differences are observed in the water content (Table 5-3). Material M1 has a 17 % lower water content comparing the batch to the laboratory sample, whereas M2 has a 6 % higher water content. However, the other properties show no significant differences (Table 5-3). This indicates that the dissolver used in the laboratory ensures a sufficient mixing of the components. Hence, the mixing procedure in the laboratory is comparable to that in the field. Differences between laboratory and field samples (Chapter 5.2.3.1) are, there-

fore, not attributed to the mixing procedure. However, it is to be expected that inhomogeneities and inconsistencies occur more easily when mixing on-site with a colloidal mixer. Thus, the quality of the grouting material may vary between different mixed batches.

Table 5-3: Material properties of the laboratory, batch and field samples of the grouting materials M1 and M2.

Material		**M1**	
Sample	***Laboratory***	***Batch***	***Field*** mean of n = 9 [min; max]
Water content w [%]	27.7 ± 0.2	23.1 ± 0.3	12.6 [11.6 ± 1.0; 14.1 ± 1.9]
Bulk density ρ_b [g cm^{-3}]	1.96 ± 0.02	2.03 ± 0.02	2.19 [2.13 ± 0.06; 2.22 ± 0.02]
Porosity ϕ [%]	42.2 ± 1.7	38.6 ± 1.8	27.5 [25.7 ± 1.9; 30.0 ± 3.2]
Saturation S_r [%]	101 ± 6	99 ± 7	89 [85 ± 16; 93 ± 12]
Thermal conductivity λ_g [W m^{-1} K^{-1}]	1.98 ± 0.06	1.99 ± 0.06	2.3 [1.85 ± 0.05; 2.45 ± 0.05]
Volumetric heat capacity $\rho c_{p,g}$ [MJ m^{-3} K^{-1}]	3.02 ± 0.07	2.92 ± 0.07	2.61 [2.50 ± 0.10; 2.74 ± 0.16]
Material		**M2**	
Sample	***Laboratory***	***Batch***	***Field*** mean of n = 6 [min; max]
Water content w [%]	71.1 ± 0.1	75.5 ± 0.3	35.6 [31.8 ± 0.5; 42.5 [a]]
Bulk density ρ_b [g cm^{-3}]	1.57 ± 0.02	1.55 ± 0.02	1.82 [1.73 ± 0.06; 1.87 ± 0.02]
Porosity ϕ [%]	65.2 ± 1.7	66.7 ± 1.6	48.8 [46.5 ± 1.7; 53.5 ± 2.9]
Saturation S_r [%]	100 ± 4	100 ± 4	98 [97 ± 8;100 ± 9]
Thermal conductivity λ_g [W m^{-1} K^{-1}]	1.72 ± 0.04	1.68 ± 0.08	2.29 [2.19 ± 0.06; 2.40 ± 0.05]
Volumetric heat capacity $\rho c_{p,g}$ [MJ m^{-3} K^{-1}]	3.48 ± 0.06	3.58 ± 0.07	3.16 [3.09 ± 0.09; 3.22 ± 0.14]

[a] single measurement

5.3.2 Field samples

5.3.2.1 Grouting materials

Depth-specific results of the field samples are shown for the upper 15 m bgl in Figure 5-2. The comparison of laboratory and field samples shows significant changes in the properties of the grouting materials.

The thermal conductivities of material M1 range between 1.85 ± 0.05 and 2.45 ± 0.05 W m^{-1} K^{-1} (Figure 5-2a). The average thermal conductivity is 2.26 W m^{-1} K^{-1}. The thermal conductivities of M2 range between 2.19 ± 0.06 and 2.40 ± 0.05 W m^{-1} K^{-1}. The average thermal conductivity is 2.29 W m^{-1} K^{-1}. The average thermal conductivity significantly increased for both grouting materials compared to the laboratory sample. For M1, an increase of 13 % is observed; for M2, an increase of 35 % is analysed. These higher thermal conductivities represent improved thermal properties in the field regarding the heat transfer of the subsurface to the BHE pipe. The average volumetric heat capacities vary between 2.50 ± 0.10 and 2.74 ± 0.16 MJ m^{-3} K^{-1} for M1, and between 3.09 ± 0.09 and 3.22 ± 0.14 MJ m^{-3} K^{-1} for M2 (Figure 5-2b). Hence, consequently lower values are analysed than those of the laboratory sample.

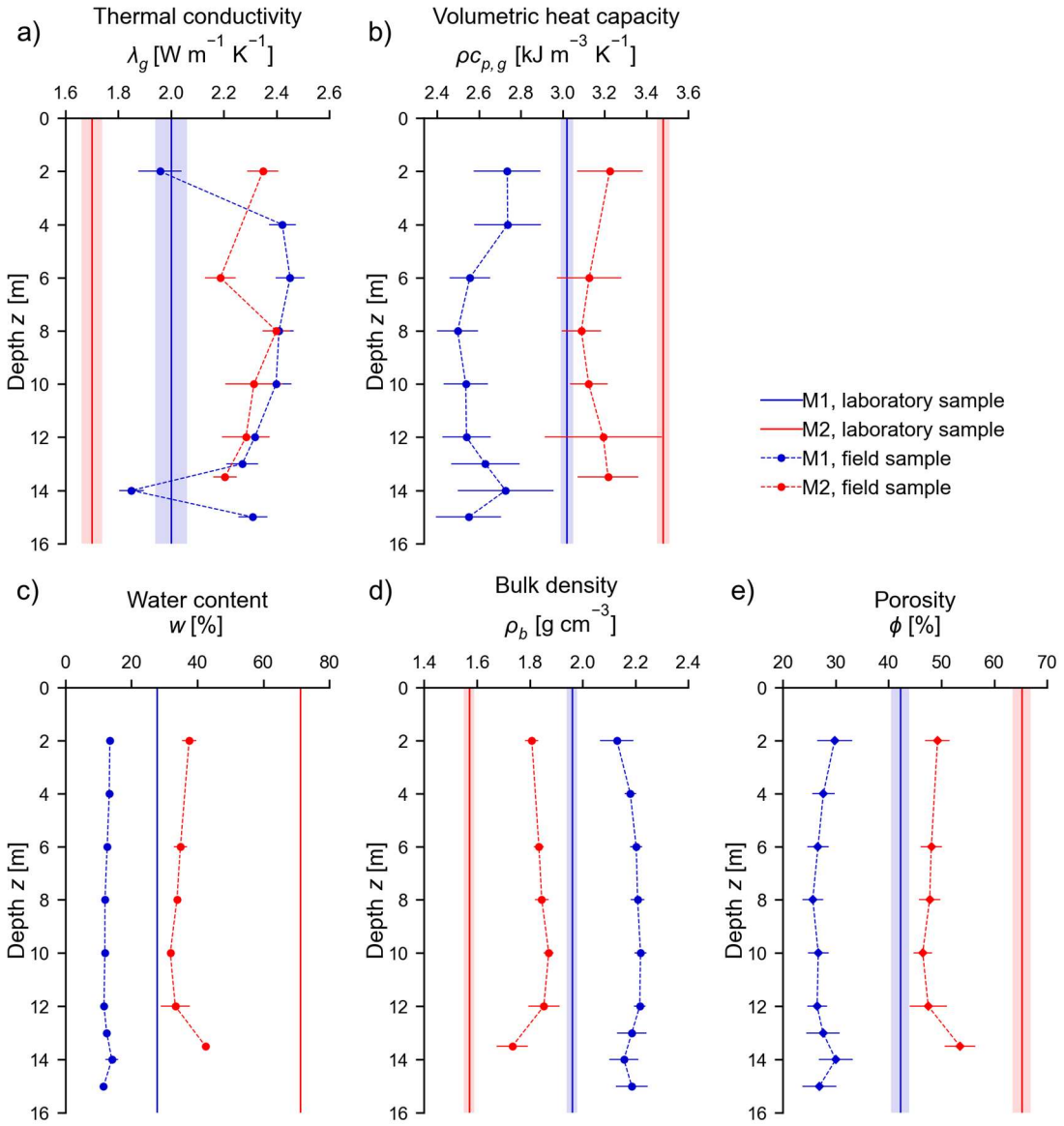

Figure 5-2: Material properties a) thermal conductivity λ_g, b) volumetric heat capacity ρc_p, c) water content w, d) bulk density ρ_b and e) porosity ϕ of the grouting materials M1 and M2 from field samples compared to the laboratory samples.

The differences in the material properties can explain the differences in the thermal properties. Volumetric heat capacity is a combined parameter of the specific heat capacity of dry samples, the water content and the bulk density (Chapter 5.2.3.2). The water content of the field samples is lower by 55 % for M1 and 50 % for M2 (Figure 5-2c). Laboratory samples are manufactured so that complete saturation of the samples is obtained. In contrast, the saturation of the field samples is reduced. Material M1 shows saturation of only 85 to 95 %. The reduction is not that significant for M2, with saturation of 97 to 100 %. Furthermore, the field samples have a higher bulk density than the laboratory samples, with 2.19 g cm^{-3} instead of 1.96 g cm^{-3} for M1, and 1.82 g cm^{-3} instead of 1.57 g cm^{-3} for M2 (Figure 5-2d). The lower water contents of the field samples have a higher impact on the volumetric heat capacity than the higher bulk density.

Higher thermal conductivities of grouting materials are related to lower porosities since the solid matrix of the sample usually has a higher thermal conductivity than the pore fluid (Allan, 1997). The porosity of all field samples is significantly reduced compared to the laboratory samples (Figure 5-2e). A clear correlation, however, cannot be established within the values. However, for material M1, the two field samples with the highest porosities (at depth z = 2 m and 14 m) have the lowest thermal conductivities (Figure 5-2a,e).

Not only the porosity but also the average pore throat diameters of the field samples are lower than those of the laboratory samples (Figure 5-3). Material M1 has an average pore diameter of 0.017 µm instead of 0.021 µm (laboratory). M2 has an average pore diameter of 0.024 µm instead of 0.055 µm (laboratory). Especially for material M2, the laboratory sample shows a peak at a diameter of about 1.5 µm, which shifts towards 0.1 µm for the field sample (Figure 5-3b). M1 also shows a shift towards lower pore diameters. Here, a bimodal pore size distribution evolves within the field sample. Thus, the decrease in the pore volume can mainly be attributed to the reduction of the bigger pores. However, all samples show pore sizes below the hydraulically effective pore diameter (Busch and Luckner, 1973). Thus, the grouting materials are appropriate materials to hinder fluid flow.

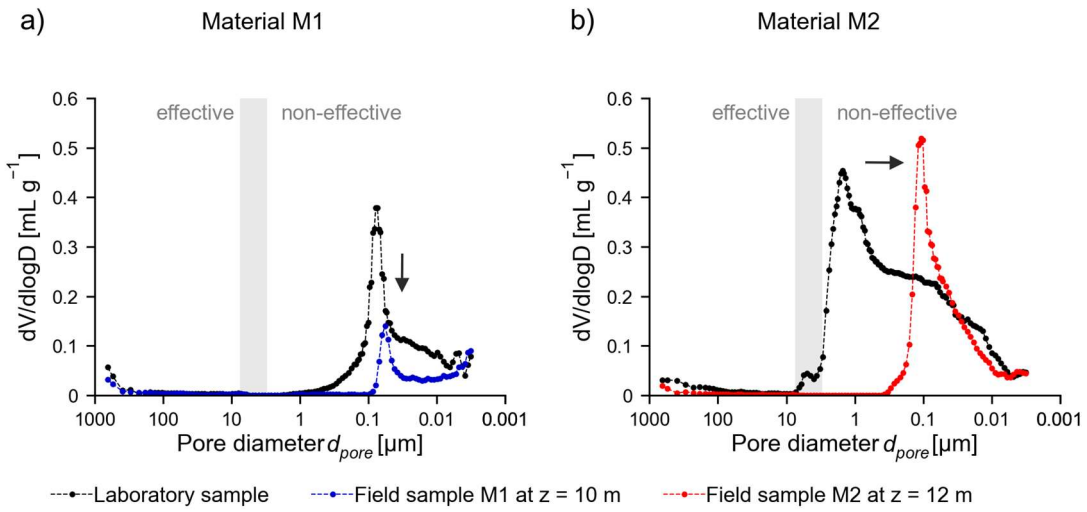

Figure 5-3: Pore size distribution from mercury intrusion porosimetry of the two grouting materials a) M1 and b) M2, highlighting the differences between the laboratory samples and the field samples at two specific depths *z*. The value ranges of hydraulically effective and non-effective pore diameters are indicated.

Summarising, the higher bulk densities, the reduction of the pore space and the decrease of the water content indicate agglomeration of the solid material within the field samples. The differences between laboratory and field samples are more profound for material M2 than for M1. Some sample-specific observations limit the interpretations of the material properties. A closer look at the sample at 2 m bgl (M1) reveals a material change within the sample (Figure 5-1f), which could indicate a flow channel. This demonstrates that the grouting material within the borehole does not necessarily represent one homogeneous material. However, due to the necessary sample size for thermal conductivity analysis, no separate analysis of the two different materials could be conducted.

5.3.2.2 Soil properties

The differences in the material properties between laboratory and field samples can be explained by the difference in the backfilling process and the hydration conditions. In the laboratory, the samples are cured in moulds stored under water, ensuring controlled conditions and complete saturation. In contrast, in the field, the samples are in direct contact with the natural subsurface. Thus, the properties of the subsurface can have a relevant influence on the properties of the grouting materials. Several studies show that filtration processes can influence the curing of grouting materials in a natural geology (Domes, 2015; Domes and Benz, 2015; Eklund and Stille, 2008; McKinley and Bolton, 1999). Hence, the properties of the subsurface as a filter medium for the grouting suspension are described. Table 5-4 summarises the properties determined for the subsurface.

Table 5-4: Material properties of the soil samples.

Material (Depth and number of samples *n*)	**Loess** (1.5 to 13.2 m) Mean of $n = 7$ [min; max] [a]	**Weathered limestone** (14.5 m) $n = 1$ [a]
Water content w [%]	11.6 [7.9; 18.7]	13.7
Bulk density ρ_b [g cm^{-3}]	1.56 [1.46 ± 0.06; 1.77 ± 0.02]	2.01 ± 0.11
Porosity ϕ [%]	47.9 [44.8; 51.0]	36.5
Saturation S_r [%]	34 [24; 62]	66.5
Thermal conductivity λ_g [W m^{-1} K^{-1}]	1.09 [0.91 ± 0.03; 1.39 ± 0.08]	1.07 ± 0.06
Volumetric heat capacity $\rho c_{p,g}$ [MJ m^{-3} K^{-1}]	1.83 [1.68; 2.10]	2.58

[a] single measurements without measurement uncertainty

In this study, grouting is only conducted in the vadose zone. The upper meters (ground level to 11 m bgl) are unsaturated loess with water contents of about 10 % and saturations between 24 to 36 %. Bulk densities are determined at about 1.5 g cm^{-3}. Below 11 m bgl, water contents increase up to 65 %. The base of the excavated zone is defined by a strongly weathered limestone (Figure 5-1b). A core sample of the weathered material and a grouting sample at the same depth is ensured to be collected. However, further excavation below this zone is not possible due to the increasing strength of the subsurface. Thus, the investigation within this study focuses on the accessible 15 m of the study site (Figure 5-1b). The particle size distribution presented in Figure 5-4 illustrates the loess material as a well-sorted silt. The raw materials of M1 and M2 can be defined as widely distributed silt, with a bigger particle size for M2. The filter criterion by Terzaghi can be applied (Terzaghi et al., 1996):

$$N = \frac{D_{15}}{d_{85}} \tag{5-4}$$

with D_{15} being the 15 % particle diameter of the filter (soil) and d_{85} being the 85 % particle diameter of the filtrate (grouting material). Values of N = 0.4 (M1) and N = 0.1 (M2) are calculated, which characterise the loess as an efficient filter for the two grouting materials (N < 4, Terzaghi et al. 1996).

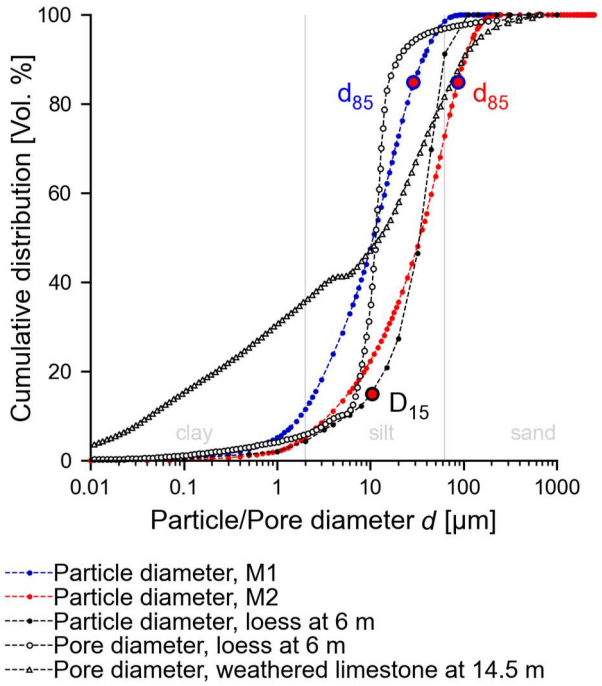

Figure 5-4: Pore size distribution of the loess (depth z = 6 m) and the weathered limestone (z = 14.5 m), and particle size distribution of the loess and the grouting materials (raw material before hydration) with the significant particle diameters d_{85} and D_{15} for applying the filter criterion by Terzaghi et al. (1996), demonstrating that the soil effectively filters the grouting particles.

Water can be transported within the soil through Darcy or capillary flow. Darcy flow can be defined through hydraulic conductivity. The hydraulic conductivity of the loess (at 8 m bgl) is evaluated to 3×10^{-7} to 1×10^{-6} m s^{-1} (± 4.8 %, T = 10 °C) and, therefore, can be relevant for flow transport processes. The ability for capillary flow can be estimated through pore size distribution. The average pore diameter is evaluated between 0.28 and 0.84 µm, corresponding to a capillary height of 8.9 to 27.0 m. The weathered limestone has a significantly higher average pore diameter of 42.2 µm, corresponding only to a capillary height of 0.2 m.

Besides the soil properties, the pressure difference and the properties of the grouting suspension also have to be considered for the filtration process. The pressure difference between the borehole and the surrounding ground is defined by the pressure of the suspension column, which also depends on the density of the grouting material. Thus, higher depths experience a higher pressure, which could result in stronger filtration in these areas. The suspension density of the grouting materials is analysed to 1.96 g cm^{-3} at 29.5 °C (M1) and 1.53 g cm^{-3} at 31.2 °C (M2). Both materials are designed to provide good work and flow ability for the grouting of boreholes. This can be demonstrated with Marsh funnel flow times (1 L) of 47 s (M1) and 45 s (M2). Furthermore, the w/s, together with the composition of the sample (i.e., clay content, cement content, water absorption capacity), influences the degree of filtration. M2 has a significantly higher w/s of 0.8 than M1 with a w/s of 0.3. The results presented in the previous Chapter 5.3.2.1 highlight that M2 shows a higher water reduction than M1 (Figure 5-2c).

Overall, the subsurface properties support the explanation of filtration processes, resulting in the variation of the material properties. We expect the conditions of this study site to represent an

extreme scenario with grouting in the vadose zone without groundwater. However, filtration processes can also occur below the groundwater table as long as the pressure in the suspension exceeds the groundwater pressure (e.g., Schlötzer, 1995) and the filter criterion by Terzaghi et al. (1996) is fulfilled.

5.3.3 In-situ results

5.3.3.1 Enhanced thermal response test (ETRT)

In-situ thermal conductivities are determined with an ETRT. Depth-specific evaluation is shown in Figure 5-5 for three distinct evaluation times. The in-situ results are compared to the results of the field samples for the grouting material and soil.

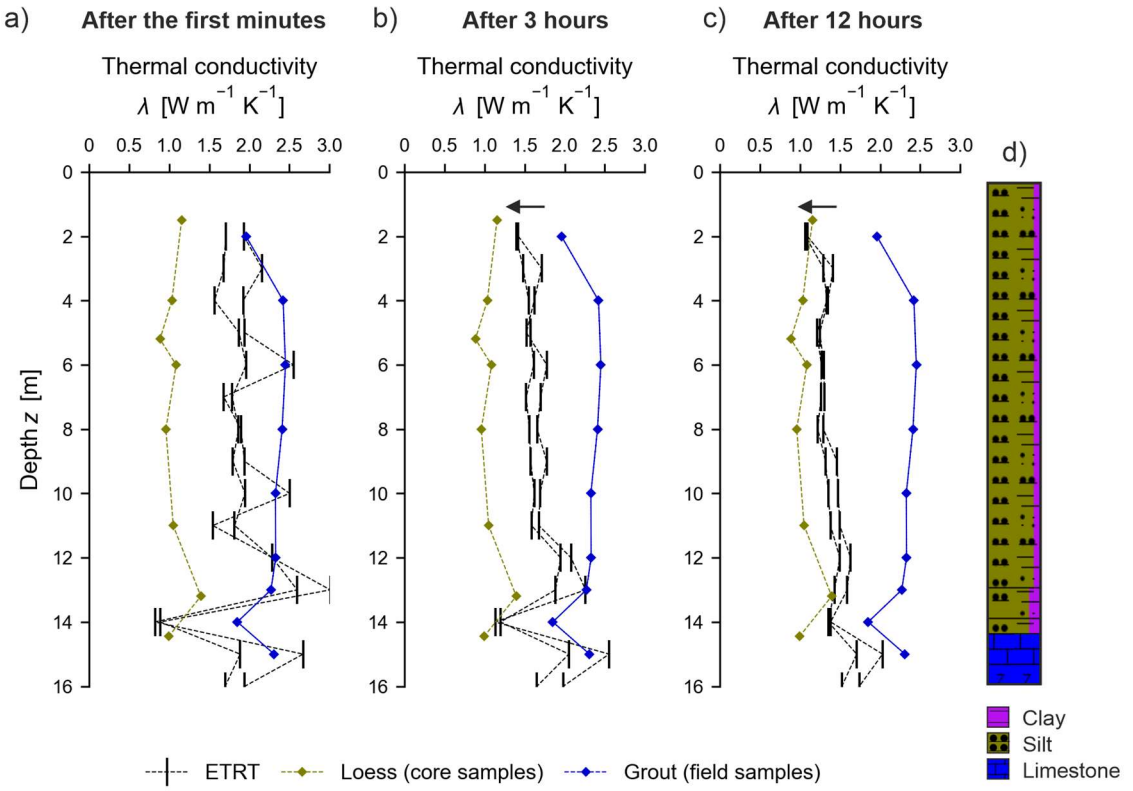

Figure 5-5: Depth-specific thermal conductivities evaluated for a) the time when the heat signal is expected to reach the borehole wall, b) 3 h, c) 12 h, compared to laboratory-derived thermal conductivities of field samples and d) to the borehole profile.

In Figure 5-5, from left to right, increasing evaluation times are considered. Figure 5-5a shows the evaluation of the first 5 to 50 min of heating time. Under the theoretical consideration that the temperature increase at the beginning of the ETRT is mainly influenced by the grouting material within the borehole, grout thermal conductivities are most likely assessed during this period. An average thermal conductivity of 1.9 W m^{-1} K^{-1} is evaluated and, thus, is lower than that of the field samples. At most depths, the in-situ thermal conductivities slightly scatter around 2.0 W m^{-1} K^{-1}. However, significantly lower thermal conductivities < 1 W m^{-1} K^{-1} are evaluated at 14 m bgl. The thermal conductivities are separately presented for the two shanks of

the hybrid cable. At some depths, thermal conductivities highly vary between the two shanks, which indicates a higher uncertainty of the results. Especially at 11 and 13 m bgl, the difference between the two values is high, with 29 % and 34 %.

Figure 5-5b shows the evaluation after 3 h of heating when the temperature increase is expected to be a mixed signal of the borehole and the subsurface. Since the grouting material has a higher thermal conductivity than the surrounding loess, the thermal conductivities decrease with increasing evaluation time (Figure 5-5a to b). The average thermal conductivity is calculated to be 1.7 W m^{-1} K^{-1}. The results already reflect the lower in-situ thermal conductivities of the soil at about 5 m bgl and the higher value at about 13 m bgl, which are measured from the core samples.

Figure 5-5c presents the evaluation from 3 – 12 h of heating when the temperature increase should be predominately influenced by the subsurface material. An average thermal conductivity of 1.4 W m^{-1} K^{-1} is evaluated, which is still higher than the thermal conductivity of the core samples.

To illustrate the evolution of the temperature increase with time, the temperature increase is plotted against the natural logarithm of the heating time in Figure 5-6. The temperature data is stacked for the depths 2 to 12 m bgl, as according to the results from Figure 5-2 and Figure 5-5c a homogeneous loess layer can be defined. Moreover, by stacking the data, the uncertainty of the temperature measurement is reduced.

By plotting the results on a logarithmic scale, the temperature increase shows significant break points in the data, which can indicate a change of material with different thermal conductivity (Riegger et al., 2012; Zhang et al., 2020). The different phases of heating the BHE system can easily be distinguished. The temperature shows a strong first increase due to the heating of the hybrid cable material (Figure 5-6a). Then, a weaker increase due to the high thermal conductivity of the borehole is observed (Figure 5-6b). A transition zone with increasing influence of the thermal properties of the loess can be distinguished (Figure 5-6c). At later heating times, the temperature increase is stronger than at the beginning of the test and is predominately influenced by soil properties (Figure 5-6d).

Additionally, the iterative thermal conductivity evaluation (Figure 5-6 in grey) is illustrated for a starting time of 5 min and a starting time of 3 h. The blue-shaded area highlights the stable thermal conductivity of about 1.9 W m^{-1} K^{-1} evaluated for the borehole. Afterwards, a gradual decrease of the thermal conductivity can be observed. The iterative evaluation also highlights the importance of the starting time when evaluating an ETRT, as a stable thermal conductivity value for the subsoil cannot be established within the 12 h of the test when selecting an early starting time. The olive-shaded area represents a stable thermal conductivity of about 1.1 to 1.2 W m^{-1} K^{-1} that is obtained with a starting time of 3 h, thereby reducing the influence of the borehole. The late-time evaluation (3 – 12 h) is in excellent agreement with the laboratory measurements. The thermal conductivity of the loess is evaluated to 1.1 W m^{-1} K^{-1} (laboratory 1.1 W m^{-1} K^{-1}). The thermal conductivity of the borehole is evaluated to 1.9 W m^{-1} K^{-1}. Hence, it is lower than the thermal conductivity of the field samples.

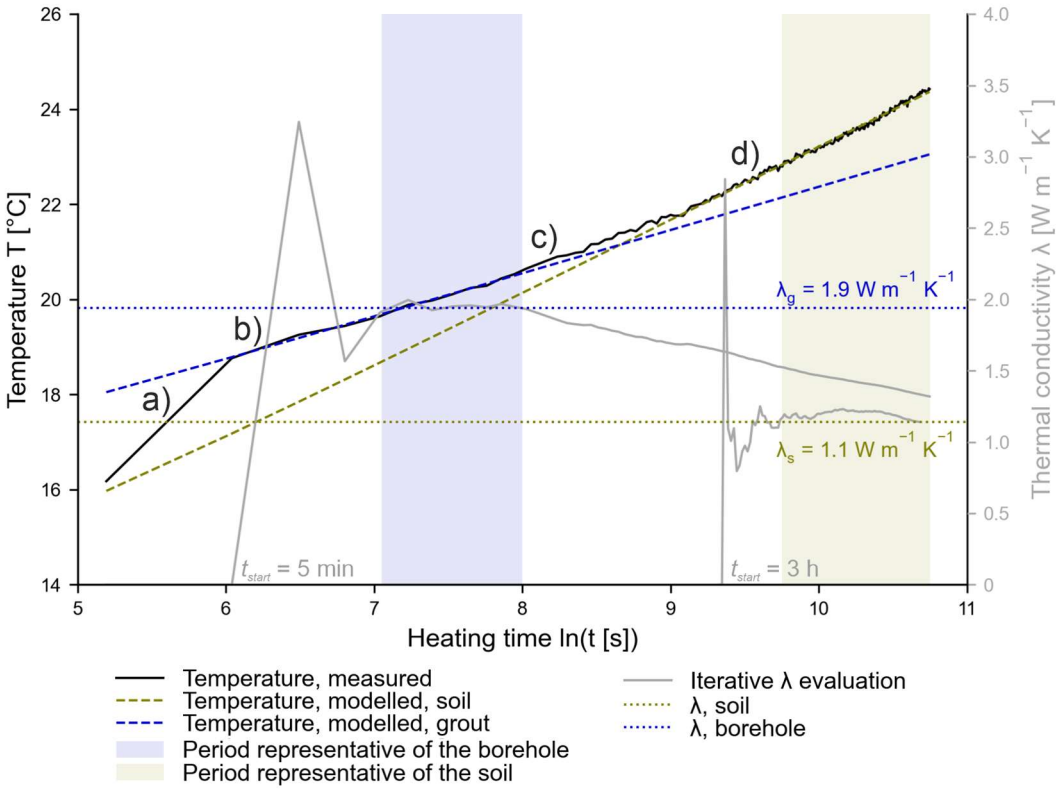

Figure 5-6: Evaluation of the short-time ETRT for stacked data (2 – 12 m bgl), illustrating the different phases of the temperature increase due to a) the heating cable, b) the borehole, c) increasing influence of the soil, d) soil-dominated.

5.3.3.2 Discussion

Several challenges in analysing the in-situ thermal conductivities of the grouting material can explain the discrepancy between the results of the different methods. Figure 5-7 highlights the challenges attributed to the borehole itself. The borehole consists of the grouting material, the water-filled BHE pipes, and the measurement technique, such as hybrid cables and cables for temperature and pressure sensors. By illustrating the positions of the BHE pipes and the hybrid cables at depths of 2 to 15 m bgl, Figure 5-7 also demonstrates that the geometry within the borehole is not symmetric at all. The position of the pipes changes significantly within 1 to 2 m. Prediction of the trajectory of the pipes is hardly possible. Moreover, the borehole represents a system with holes and contact failures, which can be observed in Figure 5-7 at depths 13 and 14 m bgl. In comparison, the thermal conductivities of field samples are measured from material samples without defects or cracks, and ensuring a good contact surface. Thus, the comparison between in-situ measurement and field samples is expected to contain these uncertainties, as the measured temperature signal represents a mixed signal of the entire borehole system. This can explain lower in-situ thermal conductivities evaluated for the grouting material.

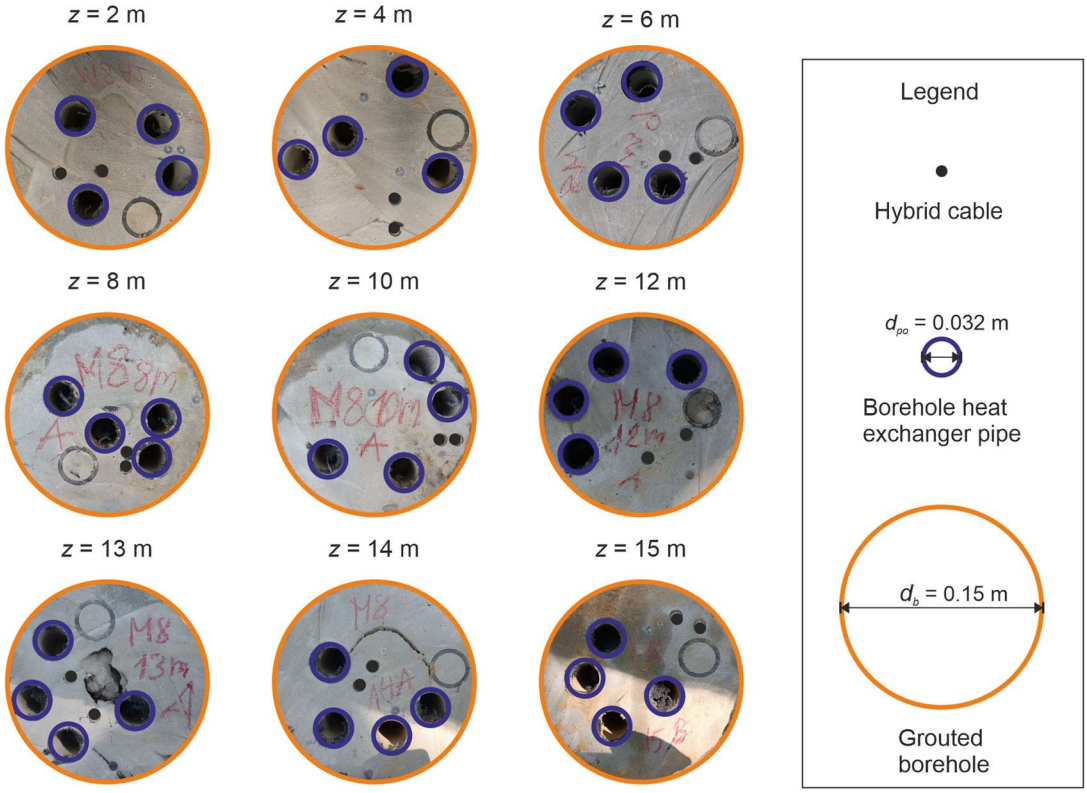

Figure 5-7: Position of the BHE pipes and the hybrid cables within borehole B1 for specific depths z collected from the grouted borehole pillar (Figure 5-1e).

Furthermore, several assumptions are made when evaluating the short-time ETRT. As shown in Figure 5-7, the position of the hybrid cable is not in the centre of the borehole but changes with depth. The distance of the hybrid cable from the borehole centre varies between 12 and 64 mm. The distance between the two shanks of the hybrid cable varies between 11 and 35 mm. When the hybrid cable is close to the borehole wall, the temperature signal quickly becomes a mixed response signal of the grout and the soil. When the distance between the hybrid cables itself is high, the difference in the evaluated values of both shanks can become high. Moreover, the specific heat load during the first minutes of the test can be inaccurate, as the heat signal of the two hybrid cables in one depth overlaps only after a few minutes. If the distance between the hybrid cable itself is high, the specific heat load can be overestimated. This issue was also shown by Riegger et al. (2012). They highlighted a successive overlay of the two heat loads of both shanks of the cable after the initial heating period of the cable. They concluded that the position of the hybrid cable has a relevant influence on the evaluation of the thermal conductivity of the grouting material and can result in an error of 13 to 14 %.

Additionally, when evaluating the early-time data of the ETRT, only a limited number of data points are analysed, which again increases the uncertainty of the estimate. This uncertainty can be reduced by evaluating homogeneous layers instead of each meter of the hybrid cable, as demonstrated in Figure 5-6. Furthermore, the time interval of the DTS measurement can be reduced to generate a higher number of data points. However, as a smaller time interval increases the uncertainty of the DTS measurement, a balance must be found.

In summary, the ETRT has proven effective for in-situ estimation of the thermal conductivity of the borehole. Observed differences between field samples and in-situ measurements are primarily attributed to the distinct analytical approaches for material versus borehole system.

5.4 Conclusion

This study sets out to examine the properties of grouting materials in the field. By comparing laboratory samples manufactured in the laboratory at defined conditions, field samples collected during the excavation of grouted BHEs, and in-situ measurements, the following conclusions can be made:

(1) The field samples of two different grouting materials show higher thermal conductivities by 13 % (w/s = 0.3) and 35 % (w/s = 0.8) than laboratory samples.
(2) This increase can be explained by filtration in the natural soil during the curing process of the grouting materials.
(3) Comparison to in-situ grout thermal conductivities show lower values by 17 % than the field samples. In-situ thermal conductivities are evaluated to an average of 1.9 W m^{-1} K^{-1}, whereas for field samples an average of 2.3 W m^{-1} K^{-1} is analysed. Uncertainties about the short time ETRT are attributed to the geometry of the borehole, the trajectory of the BHE pipes and the position of the hybrid cable.

The findings of this study provide further insights into the properties of grouting materials in the field, which contribute to the reliability of the simulation and design of GSHP systems. However, the findings are limited to the evaluated study site where filtration is the dominant process. Hence, further research should investigate the properties of grouting materials in different subsurface materials, where other processes, such as penetration and advection, are also considered.

5.5 Acknowledgements

The authors would like to thank the company Hans G. Hauri KG Mineralstoffwerke for providing the study site at the edge of their quarry and for their support in the deconstruction process. The provision of the grouting materials by Hans G. Hauri KG Mineralstoffwerke and Schwenk Zement KG is gratefully acknowledged. The authors would also like to thank Tom Brand from Solites for his support during the field deconstruction process; Madeline Dantin and Lucas Homann for their help with the laboratory experiments, as well as Dr. Ruth Haas Nüesch and Stephan Gehlsen for providing the particle size analysis data.

6 Synthesis

6.1 Summary

The reliable determination of the thermal properties of BHE systems is essential to sustainably and efficiently design these systems. Hence, this thesis contributes to understanding and improving the methods used to analyse the thermal properties. Furthermore, generalisations and overall relationships are established from site-specific challenges and material-specific properties, and further insights into the crucial influencing factors and processes are provided.

The four presented studies each address the issue with a different focus. The different methods are evaluated for different materials and scales within the BHE system, i.e., field and laboratory. While Studies 1 and 2 examine the properties of the subsurface, Studies 3 and 4 focus on the grouting material. The limitations of the different methods are discussed, and advancements in the methods are demonstrated. Furthermore, the comparability and transferability between the different methods and scales are critically examined. As a result, Figure 6-1 provides recommendations for a best practice approach derived from the findings of the four studies. Additionally, the contributions and novelty of this thesis are visualised by highlighting if a method was improved or developed (+) or if the suitability of an existing method was demonstrated (✓). This overview provides help for understanding and selecting the appropriate method. More concrete details and specifics on procedures and the application of the methods are described in the corresponding studies and are briefly summarised here.

Study 1 investigates the ETRT as an in-situ measurement method to evaluate depth-specific effective thermal conductivities and Darcy velocities. Therefore, an ETRT is critically examined at a challenging study site with high groundwater flow (> 0.2 m d^{-1}). The results demonstrate that the appropriate specific heat load is highly dependent on the heat transport properties of the study site. High Darcy velocities (> 0.6 m d^{-1}) can make a higher specific heat load necessary to ensure a sufficient temperature increase ($\Delta T > 0.6$ K). However, as there is a danger of overheating for the part of the cable installed outside of the BHE when applying a higher specific heat load, it is necessary to prevent overheating. Moreover, an improved evaluation procedure of the ETRT is introduced to adjust the specific heat load over time and along the heating cable, which can easily be integrated into the evaluation procedure using the theory of temperature-dependent resistances. Furthermore, the MILS model is highlighted as the recommended model to evaluate the Darcy flow with an ETRT. However, estimation and evaluation of layers of high groundwater flow is possible by using the ILS model and Péclet number analysis. Concluding, Study 1 provides valuable information on the planning and evaluation of ETRTs.

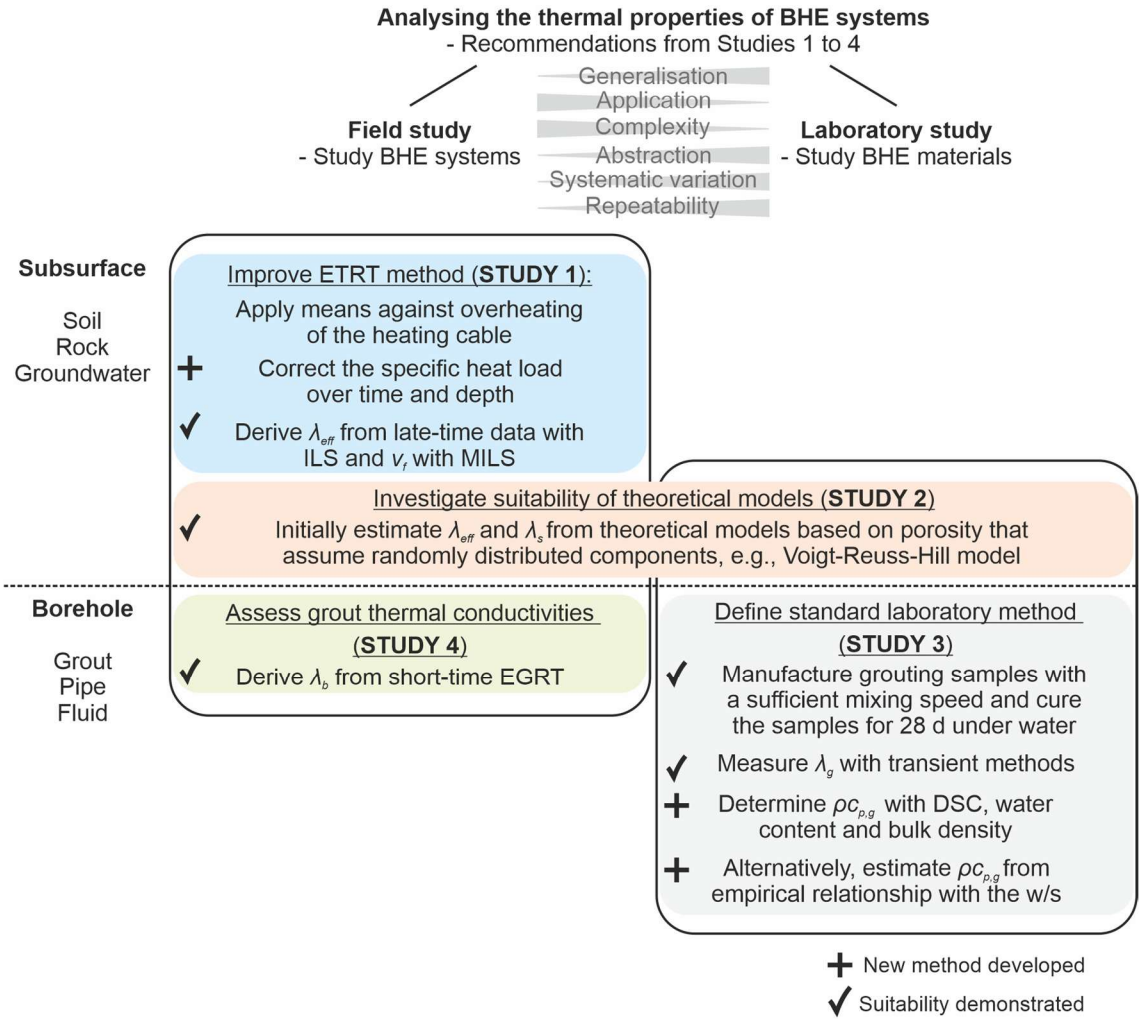

Figure 6-1: Analysing the thermal properties of BHE systems (soil and rock thermal conductivity λ_s, grout thermal conductivity λ_g, effective thermal conductivity λ_{eff}, borehole thermal conductivity λ_b, grout volumetric heat capacity $\rho c_{p,g}$, Darcy velocity v_f), recommendations from Studies 1 – 4.

Study 2 investigates the suitability of thermal conductivity models as an alternative method to estimate the effective thermal conductivity of Triassic sandstones. Therefore, the thermal conductivity of Bundsandstein sandstones is calculated with theoretical models, verified with laboratory measurements and compared to the corresponding effective thermal conductivity analysed with an ETRT. By analysing a total of 156 core samples, a group of theoretical models is identified to estimate the thermal conductivities of Triassic sandstones at laboratory and field scale within an accuracy of 0.7 – 0.8 W m^{-1} K^{-1}. Theoretical models that assume randomly distributed components (e.g., geometric mean, Voigt-Reuss-Hill model, statistical spatial distribution mean, Hashin-Shtrikman average) show the best agreement. However, their accuracy is limited by uncertainties in determining the matrix thermal conductivity and model assumptions. The significance of the estimation regarding the characterisation of a study site is further limited by analysing a representative sample size and number, and to study sites with negligible

groundwater flow. Concluding, Study 2 identifies suitable models to provide an initial estimation of the thermal conductivities of Triassic sandstones.

Study 3 demonstrates the variety of methods and procedures reported in the literature to analyse the thermal properties of grouting materials. It investigates the comparability of the different analysis methods by systematically evaluating the influence of the measurement methods and the sample preparation on determining the thermal conductivity and the volumetric heat capacity. An analysis procedure is recommended based on the findings. This includes the sample being manufactured at a high mixing speed and curing the samples under water for 28 d at room temperature. Transient measurement methods are recommended for thermal conductivity measurement. The DSC is the most precise method to measure the specific heat capacity of dried and ground samples. Subsequently, volumetric heat capacity can be calculated using the water content and wet bulk density. Moreover, an alternative estimation procedure of volumetric heat capacity is empirically derived that can be applied with the information available at a construction site. Concluding, Study 3 develops a standardised procedure to analyse the thermal properties of grouting materials.

Study 4 examines the properties of grouting materials at in-situ conditions. In a large-scale field experiment, two grouted BHEs are excavated up to a depth of 15 m to collect field samples of the grouting material. The thermal properties of the samples are compared to the results of a short-time ETRT where the ILS model is applied to evaluate the thermal conductivity of the borehole from the short-time temperature response. Uncertainties about the geometry of the borehole, the trajectory of the BHE pipes and the position of the hybrid cable explain lower in-situ thermal conductivities from ETRT (17 %). Concluding, Study 4 verifies the short-time ETRT method for analysing the thermal conductivity of the borehole.

Aside from the specific research questions of the four individual studies, some additional concluding remarks are drawn from the findings of Studies 1, 2 and 4 from applying the ETRT at three different study sites, each representing its own characteristic properties (i.e., different geology, different hydrogeological conditions, varying heterogeneity of the subsurface and the thermal properties):

- The depth-specific thermal conductivity evaluation from ETRTs can provide valuable information on the heterogeneity of the subsurface. Variations in the thermal properties of different geologic layers can be detected. Furthermore, zones of higher groundwater flow can be identified, as demonstrated in Study 1. This information helps identify subsurface layers with efficient heat transport, which can reduce the borehole length.
- The iterative evaluation of ETRT data can provide additional information on the properties of the subsurface and should be regularly integrated into the evaluation procedure of ETRTs. All three studies demonstrate the benefits of this approach. The iteratively evaluated effective thermal conductivities can serve as a criterion for stable test conditions and validity of the applied evaluation model, as discussed in Study 1 and Study 2 about groundwater flow. Moreover, they can indicate material changes, as discussed in Study 4 about the grout thermal conductivities.
- Site-specific characteristics must be considered when conducting ETRTs since they influence the setup and the evaluation procedure (e.g., evaluation model). The

appropriate specific heat load and test time depend on the thermal properties at the study site. Knowledge of the geologic and hydrogeologic conditions is crucial to approximate these properties reasonably.

Results from ETRT cannot readily be generalised. However, they provide valuable information on the applicability of BHE systems. On the other hand, laboratory results cannot directly be transferred to the field scale due to different measurement techniques, sample sizes and in-situ processes that cannot be depicted in the laboratory. The sampling, manufacture and storage of the samples is crucial for a representative laboratory analysis. Thus, all approaches and methods complement each other.

By combining different approaches, this thesis provides new insights into the concepts and processes that influence the thermal properties of BHE systems:

- **Study 1** establishes empirical relationships that describe the increase of the effective thermal conductivity determined with the ETRT due to groundwater flow.
- **Study 2** examines the influence of the porosity, pore geometry and pore structure on the thermal conductivity of Triassic sandstones and identifies models that approximate these relationships.
- **Study 3** analyses the influence of the w/s on the properties of grouting materials and establishes empirical relationships that can be used for estimating the volumetric heat capacity.
- **Study 4** provides new insights into the properties of grouting materials in the field from a unique study site. The study evaluates higher thermal conductivities for field samples than for laboratory samples (13 % and 35 %). This difference is explained by filtration in the natural soil during the curing process of the grouting materials. The role of filtration processes on the properties of grouting materials for BHE systems is better understood.

6.2 Perspectives and Outlook

The outcomes of this thesis improve the reliability of material specifications and support the interpretation of field experiments. Thereby, the thesis contributes to the reliability of the simulation and design of GSHP systems. This can increase public acceptance of the technology and give decision-makers the courage to decide about renewable energy sources. Beyond the findings presented in this thesis, there is still potential to optimise the methods to analyse the thermal properties of BHE systems further. Moreover, in the course of this thesis, additional research questions arose, which are briefly introduced in the following paragraph.

Suggestions to further improve the investigated methods were proposed within the presented studies:

(1) Study 1 showed that **actions against overheating of the heating cable** are necessary when applying the ETRT. Hence, in Study 4, the heating cable was covered with soil material to improve the heat transfer at the surface. However, it was only partially suc-

cessful as parts of the cable remained uncovered. Thus, further studies should be conducted to investigate different methods to reduce the overheating of the cable. One possibility could be to use heating cable sections instead of one continuous heating cable by working with varying cable cross sections as proposed by Vélez Márquez et al. (2018). Another possibility could be using a self-regulating heating cable to allow equal temperature development, as tested by Seibertz et al. (2016). However, the accurate determination of the specific heat load is a crucial aspect.

(2) Analytical models are limited when dealing with groundwater flow, as demonstrated in Study 1. Combining **numerical heat transport models** and field tests or large-scale laboratory experiments under **controlled groundwater flow velocities**, as in Del Val et al. (2021) or Wagner et al. (2014) could improve the analyses and the understanding of the heat transport processes.

(3) Study 1 evaluated **hydraulic conductivities** with the ETRT based on the MILS model as described in Wagner et al. (2014). An in-depth comparison of this method with other methods, such as pumping tests or flowmeter, permeameter and sieve analyses, would benefit the reliability of the method.

(4) A first step towards a standardised approach for analysing the thermal properties of grouting materials was taken in Study 3 by deriving a recommended laboratory procedure. The findings of this study could contribute to **establishing official standards**, such as DIN standards or VDI guidelines.

(5) Study 3 proposed an **estimation of grout volumetric heat capacities** based on the relationship between w/s and water content. Verification of the estimation with additional grouting materials is necessary.

In addition, other promising methods to analyse the thermal properties of BHE systems should be investigated:

(6) Study 2 demonstrated that theoretical models can derive thermal conductivities from porosities but sample size and number limit the accuracy of the estimation. One alternative for extensive laboratory analyses could be the application of **porosity borehole logs**, such as nuclear magnetic resonance (NMR) or Gamma-Gamma (Bayuk et al., 2011; Demongodin et al., 1991; Jorand et al., 2015; Meshalkin et al., 2020; Nasr et al., 2018). To test the method, a comparison of estimated thermal conductivities from porosity logs and effective thermal conductivities from ETRT at a study site with heterogeneous geology and negligible groundwater flow is needed.

(7) In this thesis, thermal conductivities are evaluated in the field and laboratory. Volumetric heat capacities, however, are only analysed in the laboratory. The oscillatory thermal response test (OTRT) was proposed as a method to derive **volumetric heat capacities in situ** (Giordano et al., 2021; Lamarche et al., 2024; Langevin et al., 2022). However, further research to test and implement the OTRT is needed.

(8) One drawback of the ETRT is that **borehole thermal resistance** cannot be determined directly with this test. It has to be analysed with other methods, such as the multipole method or numerical models (Hellström, 1991; Lamarche et al., 2010), therefore making assumptions on the geometry within the borehole. Using BHE trajectory tools and combining the results with ETRT and DTRT experiments, the validity of these assump-

tions could be investigated, and the analysis of borehole thermal resistance could be improved.

Moreover, the following research questions could be studied to improve our understanding of the relationships and processes that influence the thermal properties of BHE systems:

(9) Study 1 illustrated how **Darcy velocities can increase the effective thermal conductivities** as reported in different studies (Figure 2-6). However, general relationships between these properties cannot be derived from the limited data available, which includes varying TRT methods and evaluation procedures. Additional data combining ETRT and core sample analyses at various hydrogeological conditions could improve the estimation and, thereby, facilitate the design of GSHP systems.

(10) Study 2 indicated that **pore structure and connectivity significantly impact thermal conductivity** (Figure 3-4). By using high resolution microscopy and 3-dimensional modelling software, relationships and models based on pore contacts and pore structure could be developed.

(11) Study 4 highlighted the **influence of the subsurface on the properties of grouting materials**. However, the findings are limited to one study site and two grouting materials. To generalise findings and improve our understanding of the processes and the impact on the thermal performance, varying subsurface conditions and their influence on the properties of grouting materials must be considered. One possibility could be to study different grouting materials in large-scale laboratory experiments at defined subsurface conditions.

Finally, fundamental research and application always depend on the available data. New data can be generated by conducting experiments. However, we would highly benefit from implementing open geodatabases since experiments are exhaustive and expensive. With regard to analysing the thermal properties of BHE systems, the data could include thermal properties, densities and porosities of rocks, soils and grouting materials from laboratory measurements, temperature-time data and effective thermal conductivities from TRT or ETRT experiments and groundwater flow velocities. For example, Galgaro et al. (2021) developed the first Italian TRT database with data from more than 100 TRTs. Furthermore, a database of the thermal properties of commercially available grouting materials in Germany is planned to be built during the QEWSplus project (qewsplus.de).

Appendices

Appendix Study 1

This Appendix refers to Study 1 (Chapter 2). The content was published in the journal Geothermal Energy as a supporting information and is available online at: https://link.springer.com/article/10.1186/s40517-023-00278-y#Sec19

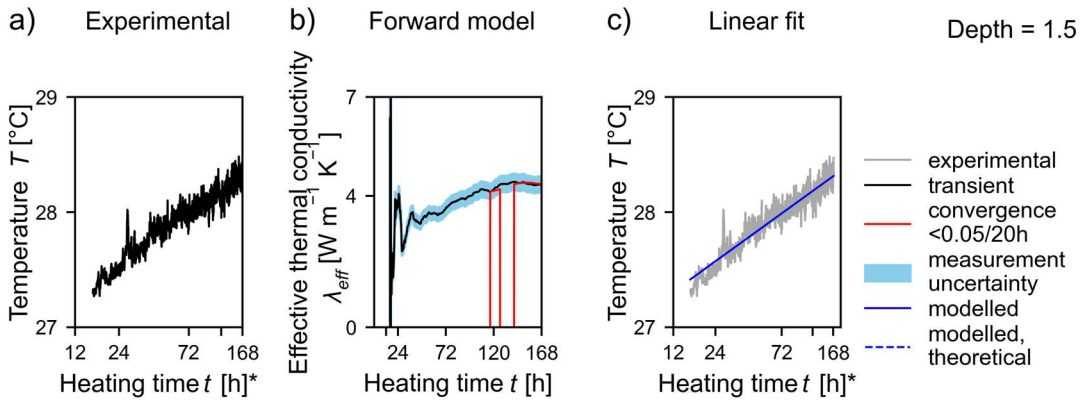

Figure A1- 1: Evaluation of the effective thermal conductivities (λ_{eff}) for the depth interval of 1.5 m.

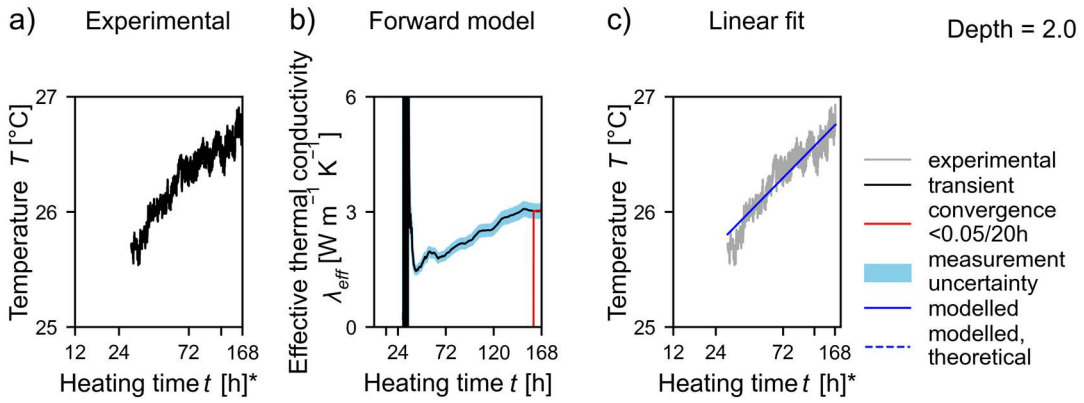

Figure A1- 2: Evaluation of the effective thermal conductivities (λ_{eff}) for the depth interval of 2.0 m.

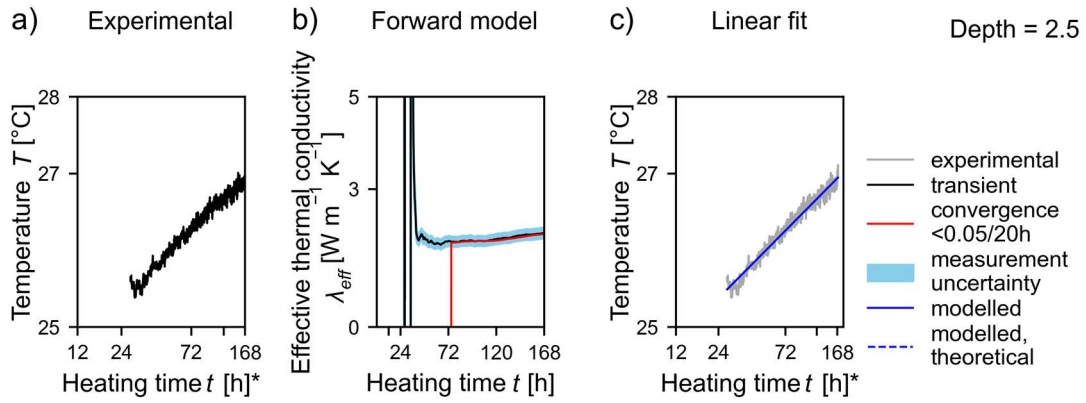

Figure A1- 3: Evaluation of the effective thermal conductivities (λ_{eff}) for the depth interval of 2.5 m.

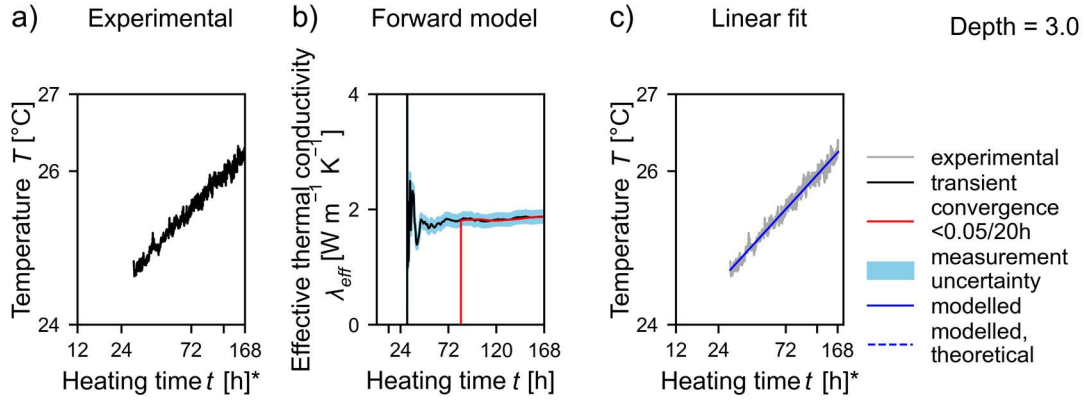

Figure A1- 4: Evaluation of the effective thermal conductivities (λ_{eff}) for the depth interval of 3.0 m.

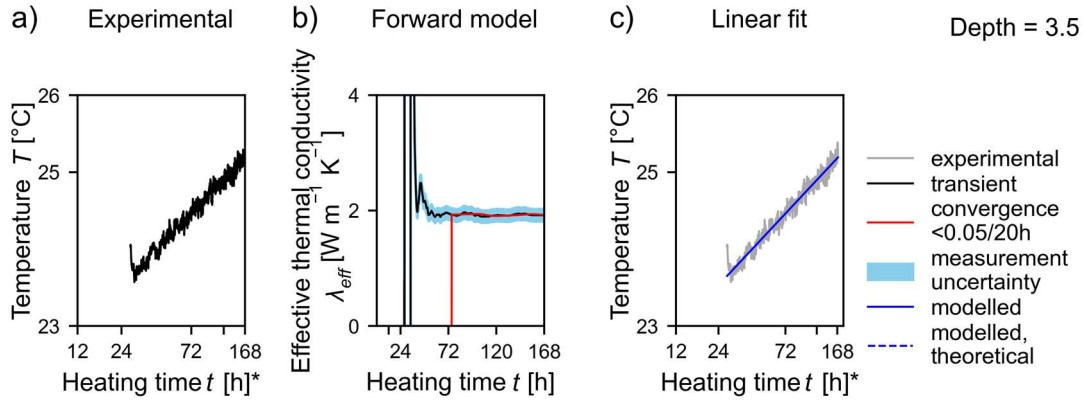

Figure A1- 5: Evaluation of the effective thermal conductivities (λ_{eff}) for the depth interval of 3.5 m.

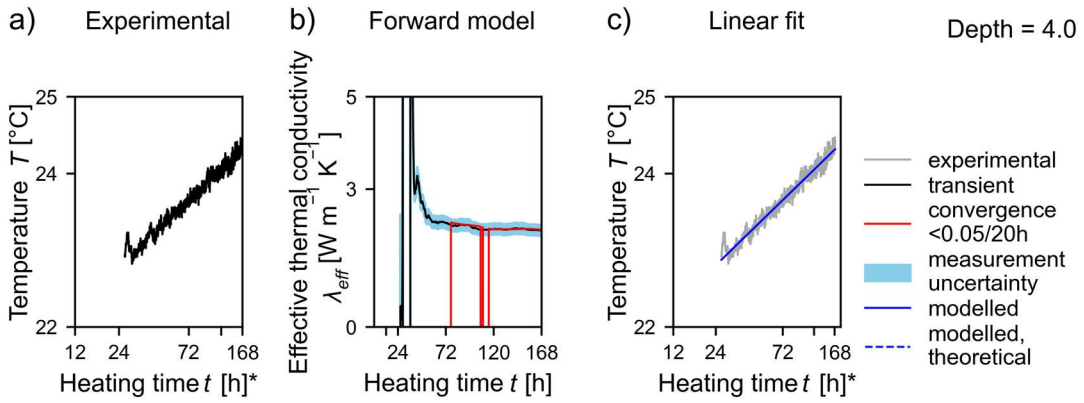

Figure A1- 6: Evaluation of the effective thermal conductivities (λ_{eff}) for the depth interval of 4.0 m.

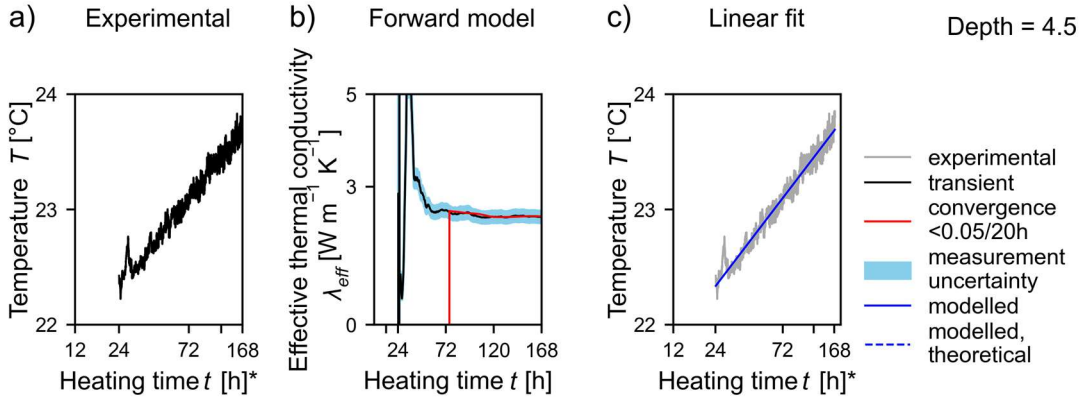

Figure A1- 7: Evaluation of the effective thermal conductivities (λ_{eff}) for the depth interval of 4.5 m.

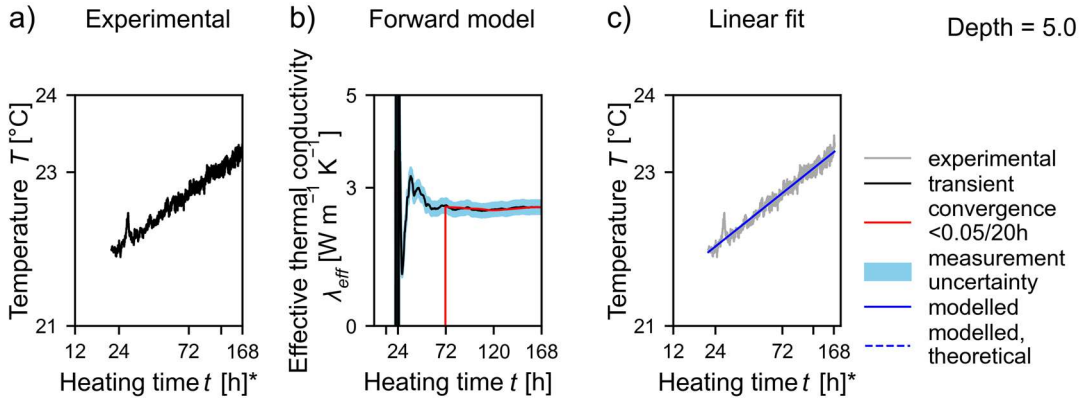

Figure A1- 8: Evaluation of the effective thermal conductivities (λ_{eff}) for the depth interval of 5.0 m.

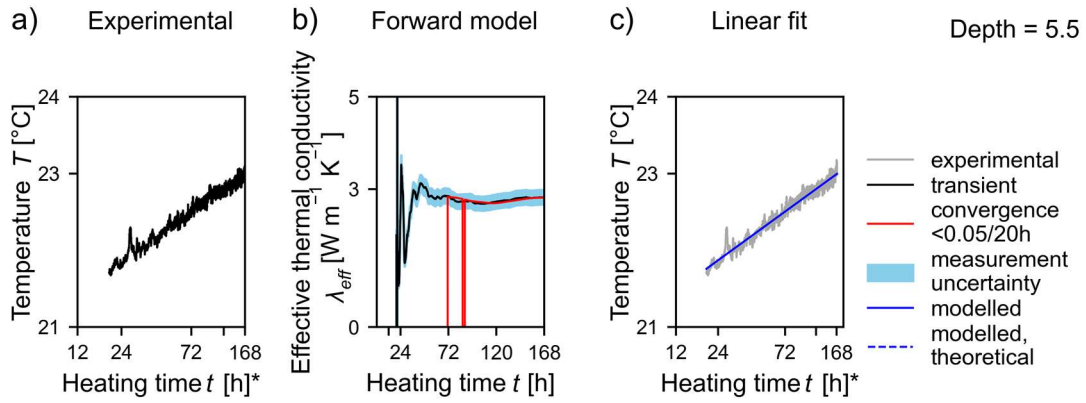

Figure A1- 9: Evaluation of the effective thermal conductivities (λ_{eff}) for the depth interval of 5.5 m.

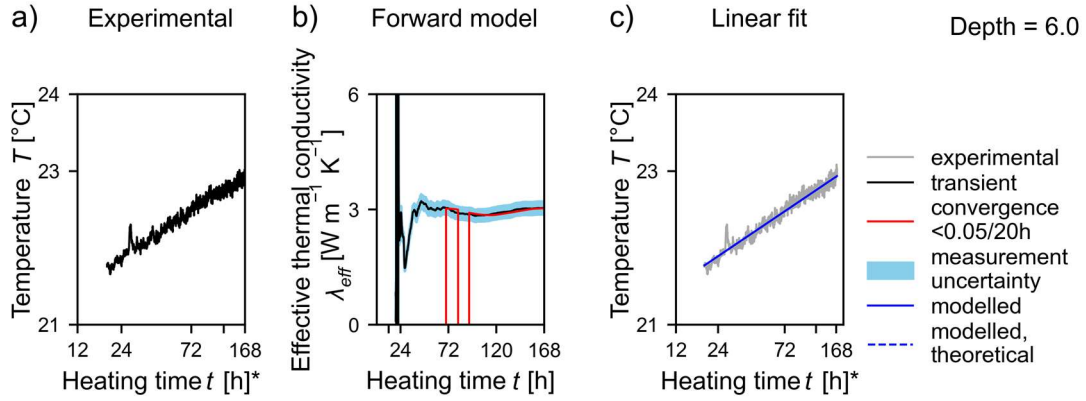

Figure A1- 10: Evaluation of the effective thermal conductivities (λ_{eff}) for the depth interval of 6.0 m.

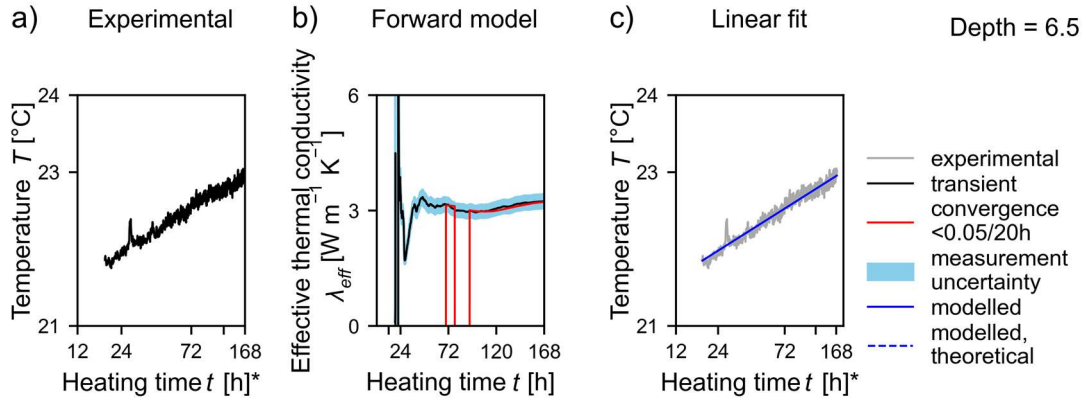

Figure A1- 11: Evaluation of the effective thermal conductivities (λ_{eff}) for the depth interval of 6.5 m.

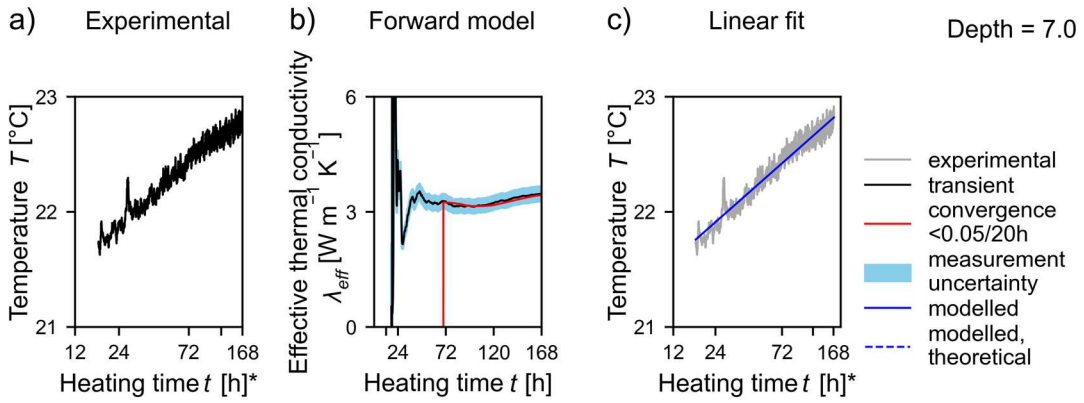

Figure A1- 12: Evaluation of the effective thermal conductivities (λ_{eff}) for the depth interval of 7.0 m.

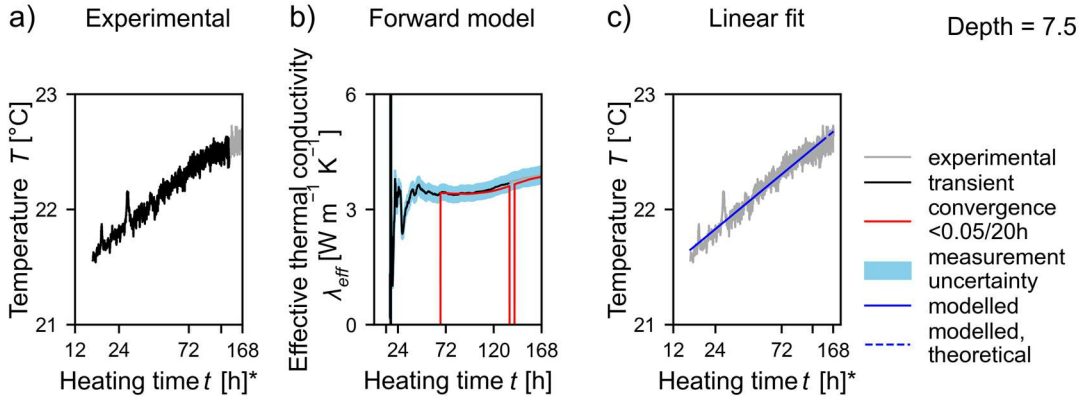

Figure A1- 13: Evaluation of the effective thermal conductivities (λ_{eff}) for the depth interval of 7.5 m.

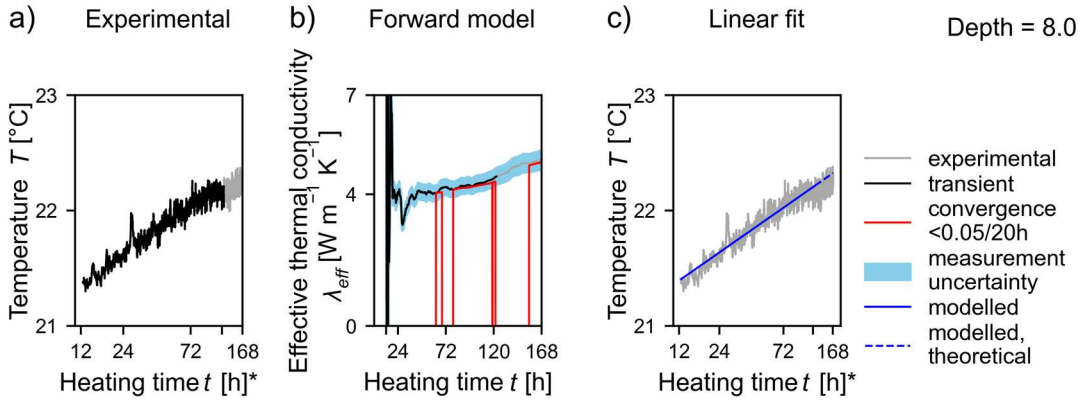

Figure A1- 14: Evaluation of the effective thermal conductivities (λ_{eff}) for the depth interval of 8.0 m.

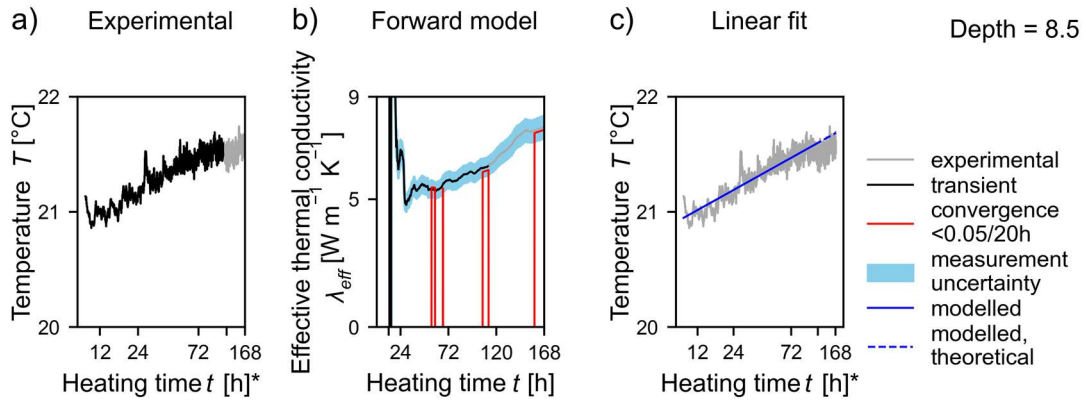

Figure A1- 15: Evaluation of the effective thermal conductivities (λ_{eff}) for the depth interval of 8.5 m.

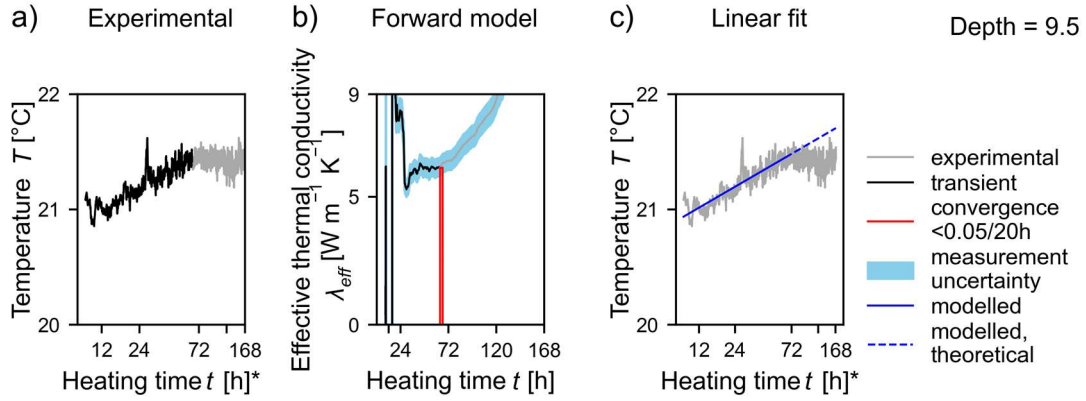

Figure A1- 16: Evaluation of the effective thermal conductivities (λ_{eff}) for the depth interval of 9.0 m.

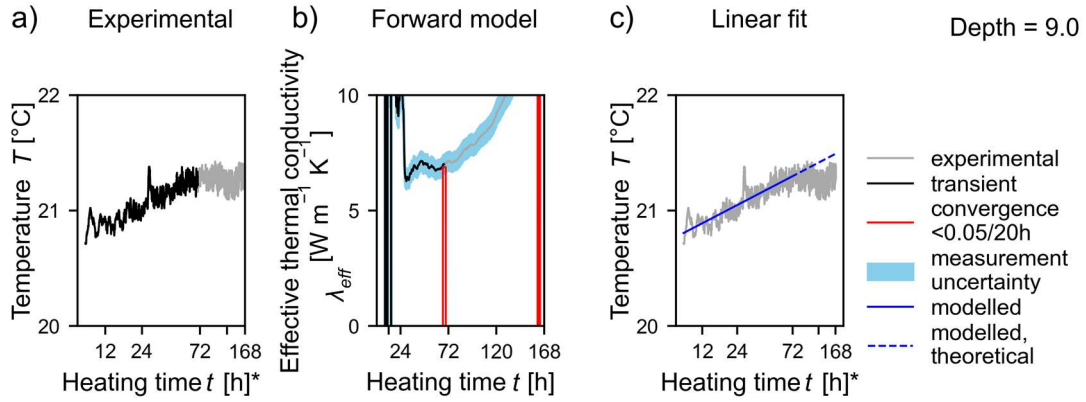

Figure A1- 17: Evaluation of the effective thermal conductivities (λ_{eff}) for the depth interval of 9.5 m.

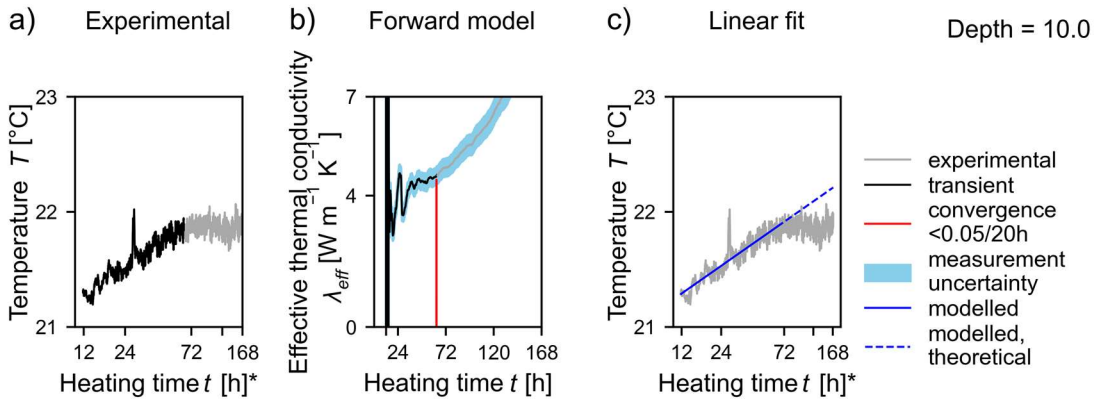

Figure A1- 18: Evaluation of the effective thermal conductivities (λ_{eff}) for the depth interval of 10.0 m.

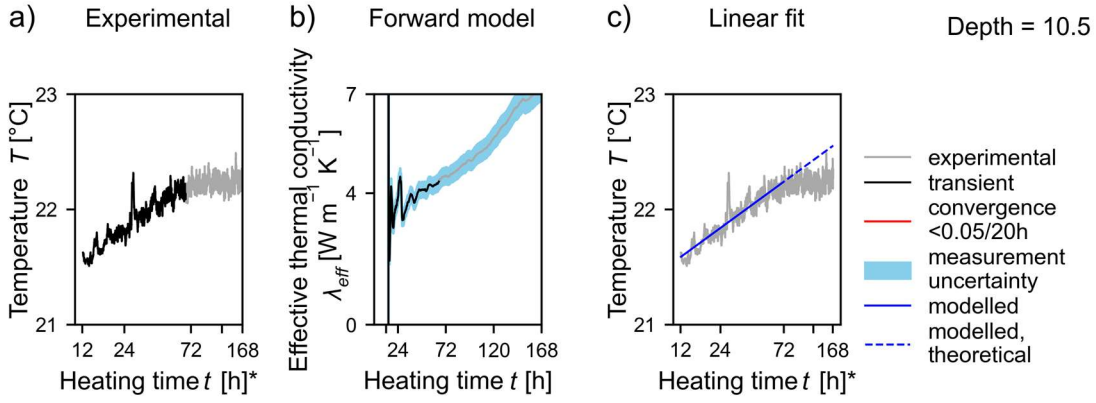

Figure A1- 19: Evaluation of the effective thermal conductivities (λ_{eff}) for the depth interval of 10.5 m.

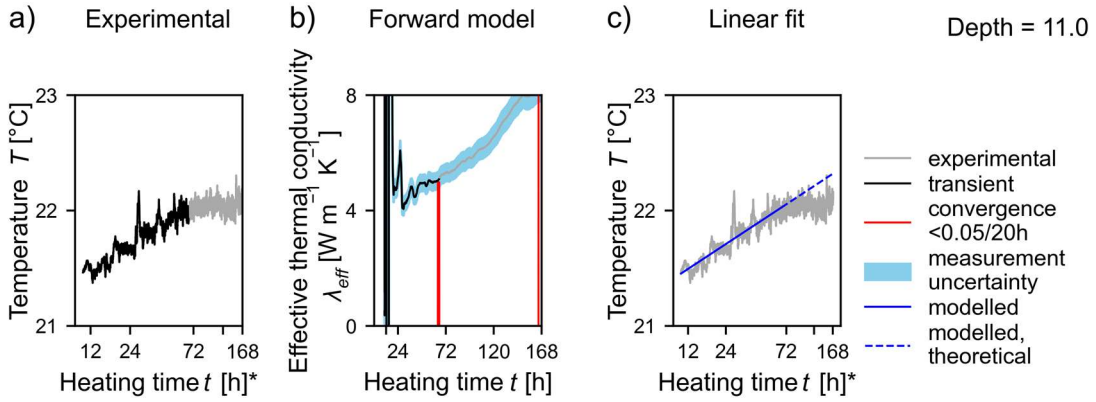

Figure A1- 20: Evaluation of the effective thermal conductivities (λ_{eff}) for the depth interval of 11.0 m.

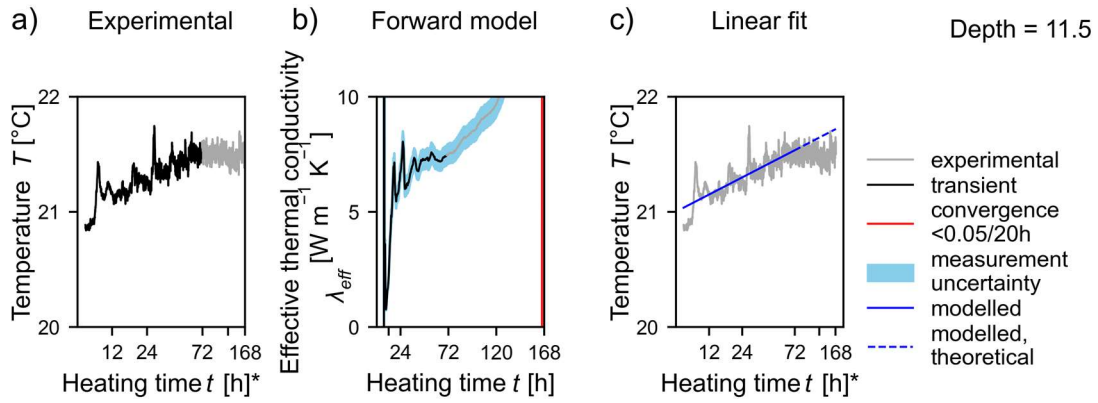

Figure A1- 21: Evaluation of the effective thermal conductivities (λ_{eff}) for the depth interval of 11.5 m.

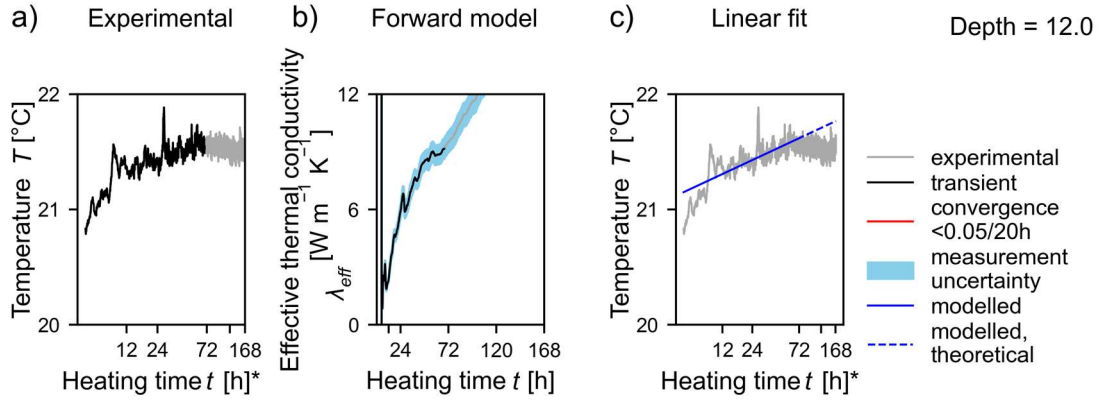

Figure A1- 22: Evaluation of the effective thermal conductivities (λ_{eff}) for the depth interval of 12.0 m.

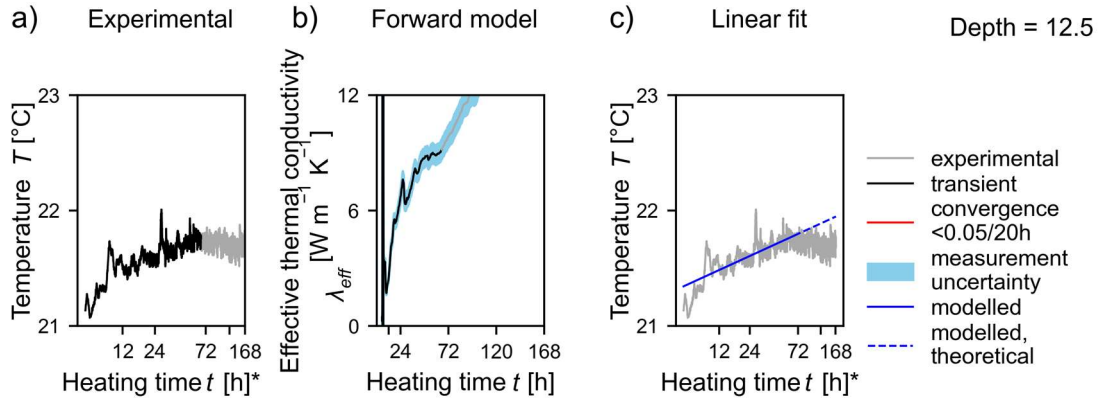

Figure A1- 23: Evaluation of the effective thermal conductivities (λ_{eff}) for the depth interval of 12.5 m.

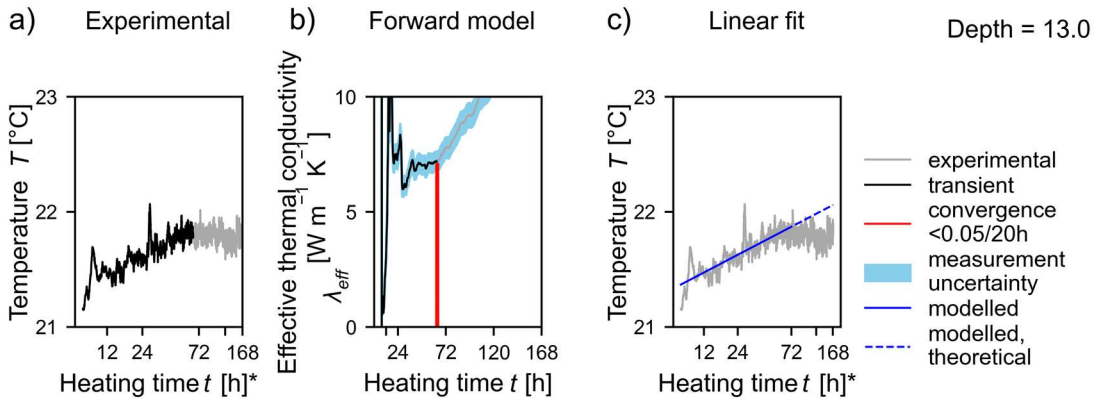

Figure A1- 24: Evaluation of the effective thermal conductivities (λ_{eff}) for the depth interval of 13.0 m.

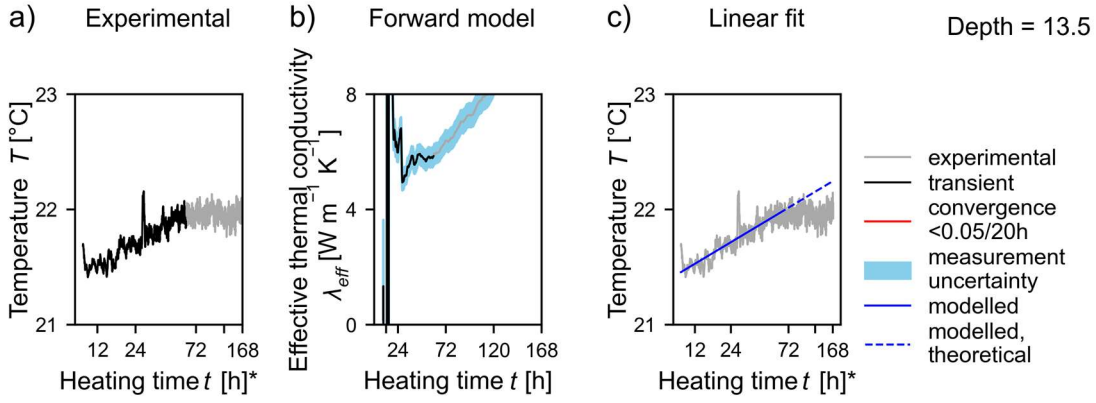

Figure A1- 25: Evaluation of the effective thermal conductivities (λ_{eff}) for the depth interval of 13.5 m.

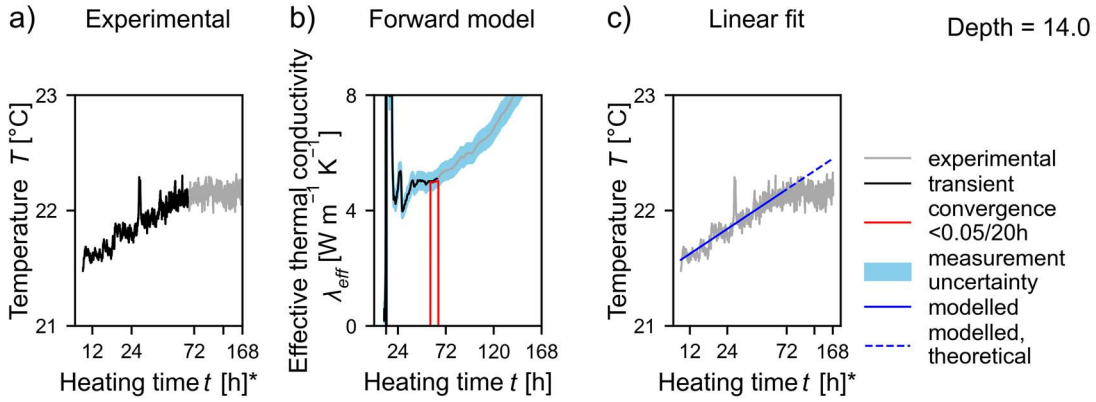

Figure A1- 26: Evaluation of the effective thermal conductivities (λ_{eff}) for the depth interval of 14.0 m.

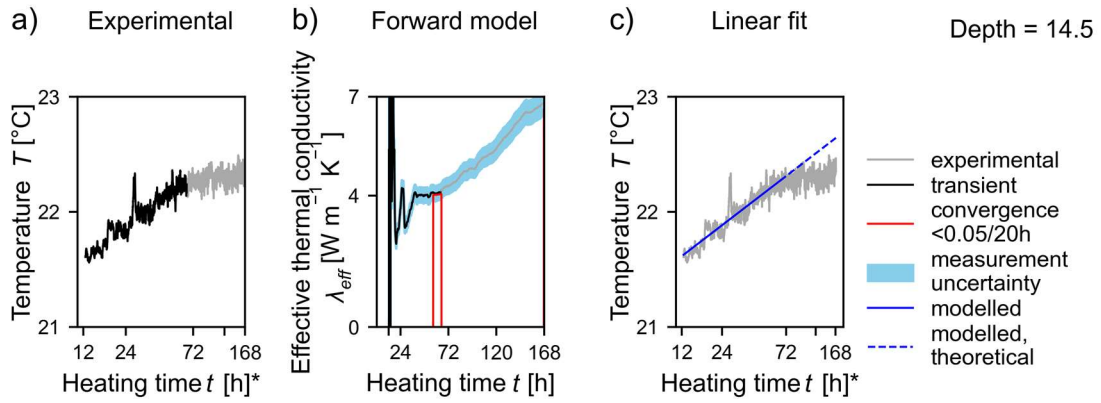

Figure A1- 27: Evaluation of the effective thermal conductivities (λ_{eff}) for the depth interval of 14.5 m.

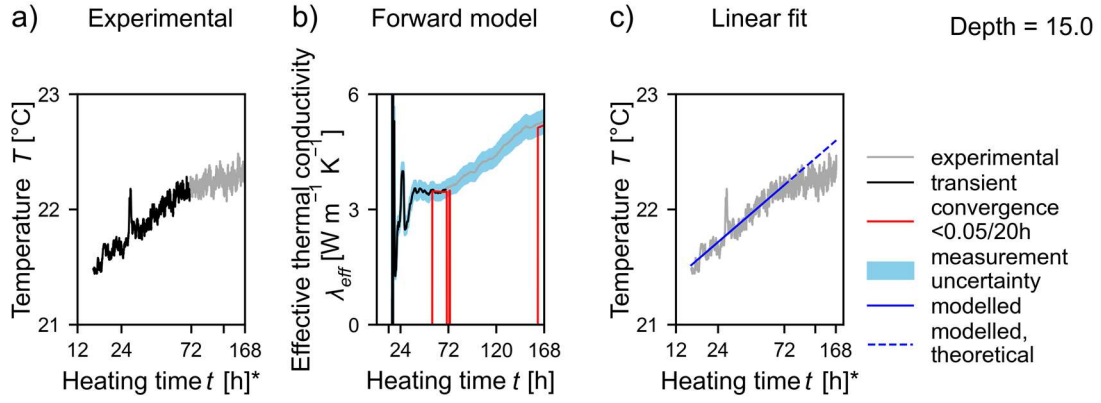

Figure A1- 28: Evaluation of the effective thermal conductivities (λ_{eff}) for the depth interval of 15.0 m.

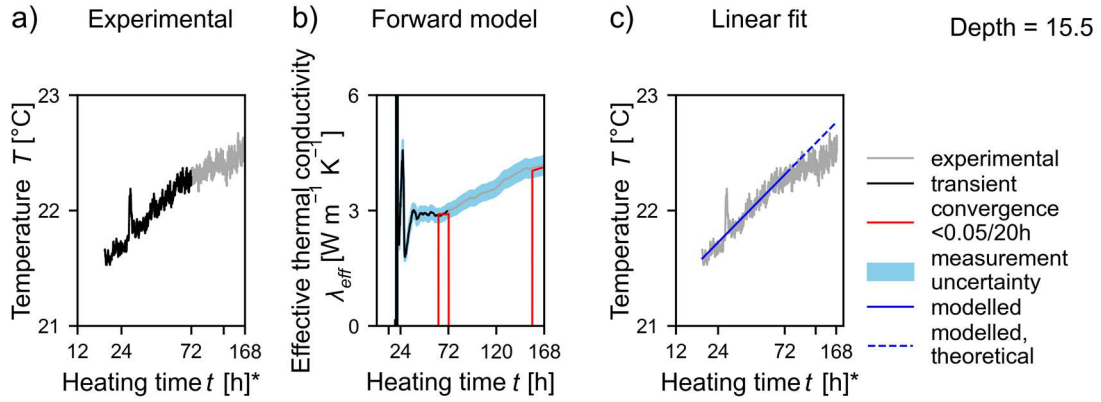

Figure A1- 29: Evaluation of the effective thermal conductivities (λ_{eff}) for the depth interval of 15.5 m.

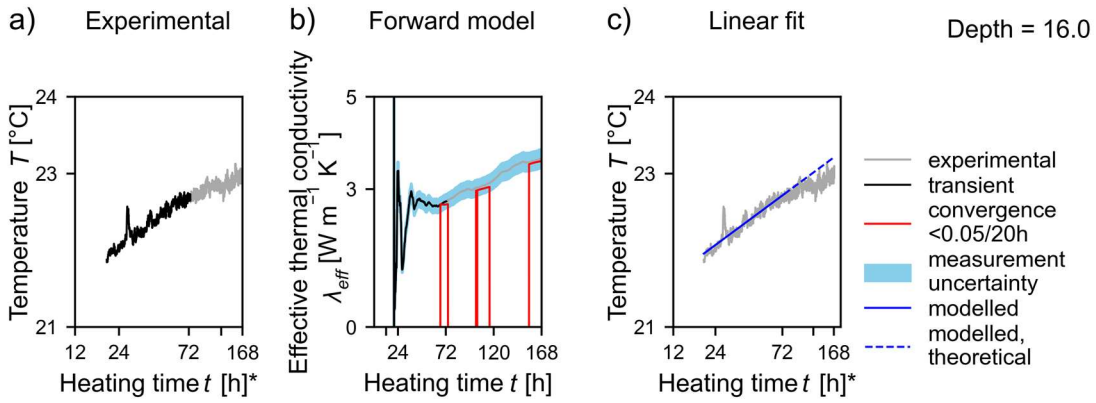

Figure A1- 30: Evaluation of the effective thermal conductivities (λ_{eff}) for the depth interval of 16.0 m.

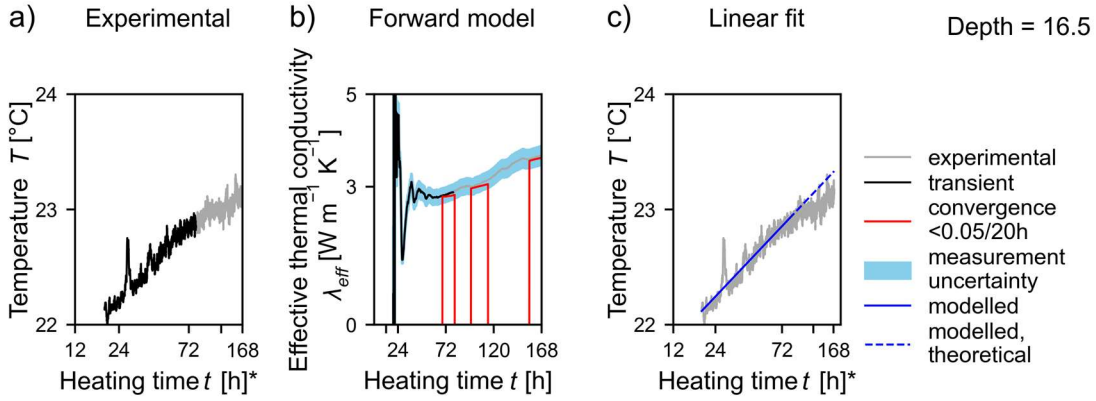

Figure A1- 31: Evaluation of the effective thermal conductivities (λ_{eff}) for the depth interval of 16.5 m.

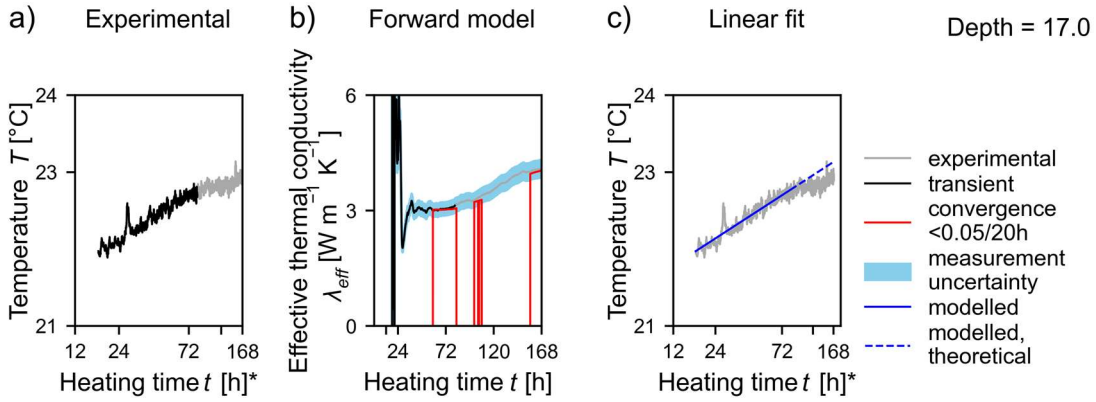

Figure A1- 32: Evaluation of the effective thermal conductivities (λ_{eff}) for the depth interval of 17.0 m.

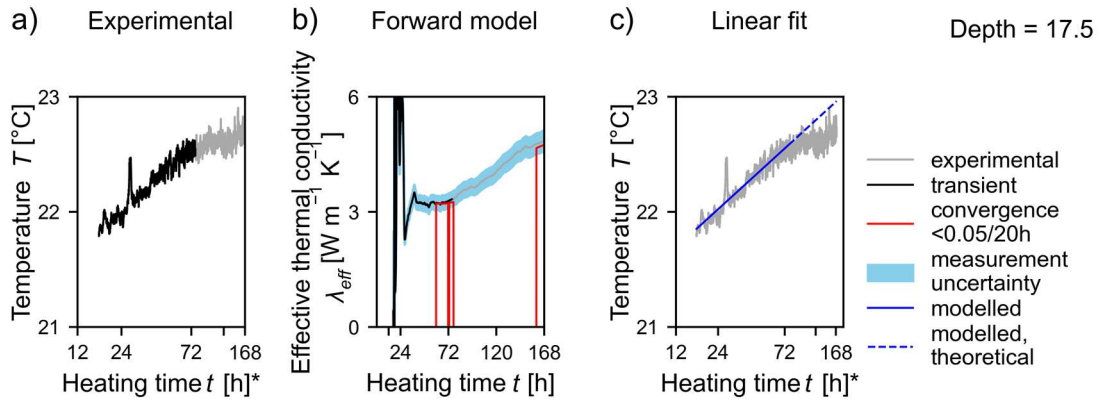

Figure A1- 33: Evaluation of the effective thermal conductivities (λ_{eff}) for the depth interval of 17.5 m.

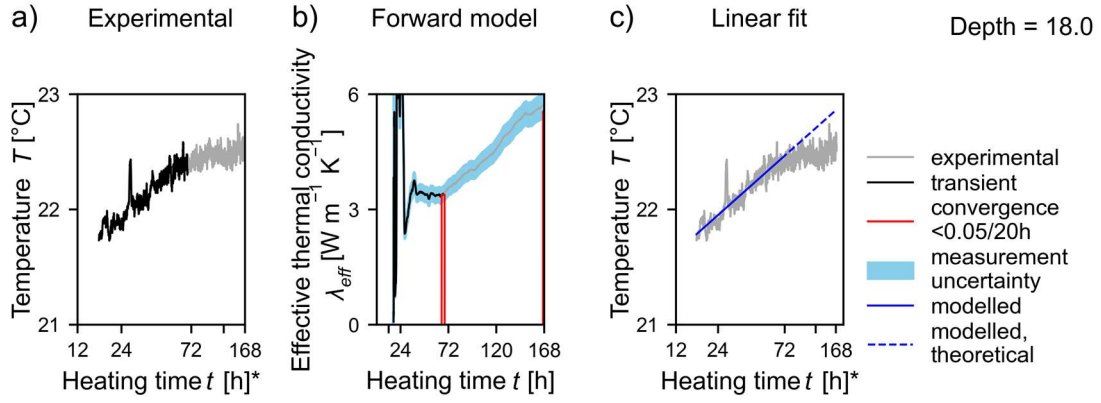

Figure A1- 34: Evaluation of the effective thermal conductivities (λ_{eff}) for the depth interval of 18.0 m.

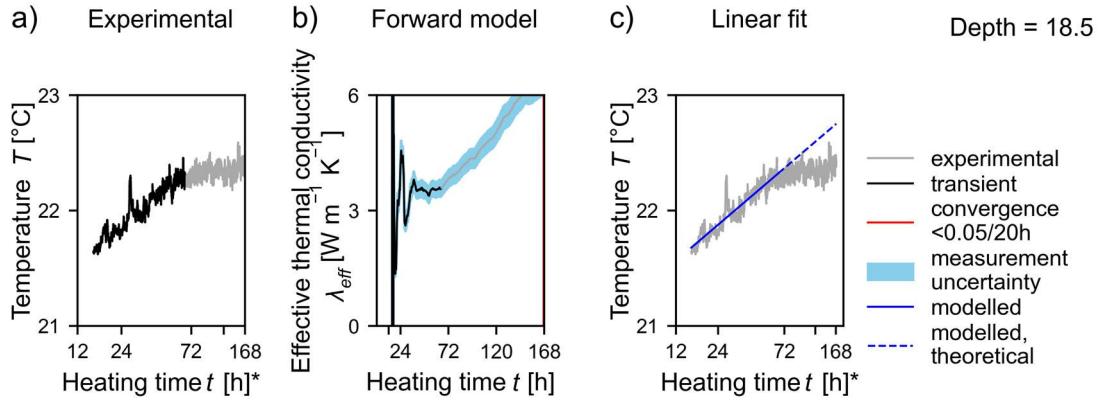

Figure A1- 35: Evaluation of the effective thermal conductivities (λ_{eff}) for the depth interval of 18.5 m.

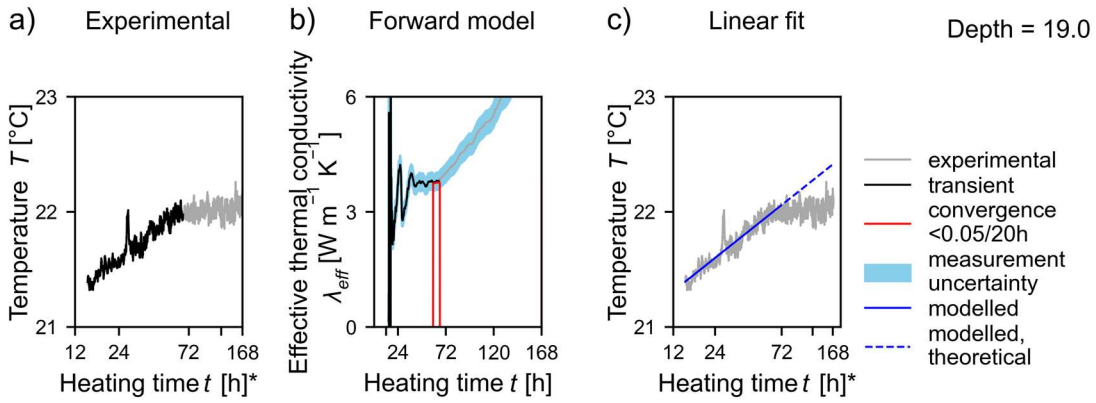

Figure A1- 36: Evaluation of the effective thermal conductivities (λ_{eff}) for the depth interval of 19.0 m.

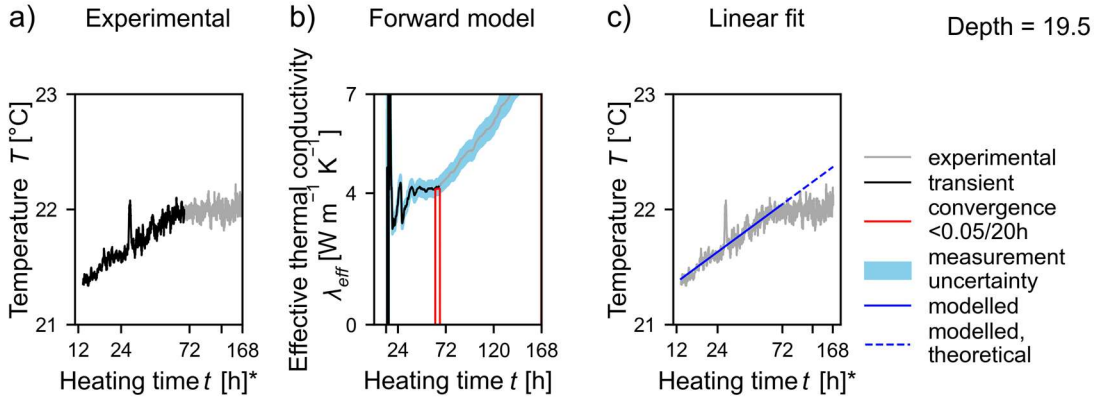

Figure A1- 37: Evaluation of the effective thermal conductivities (λ_{eff}) for the depth interval of 19.5 m.

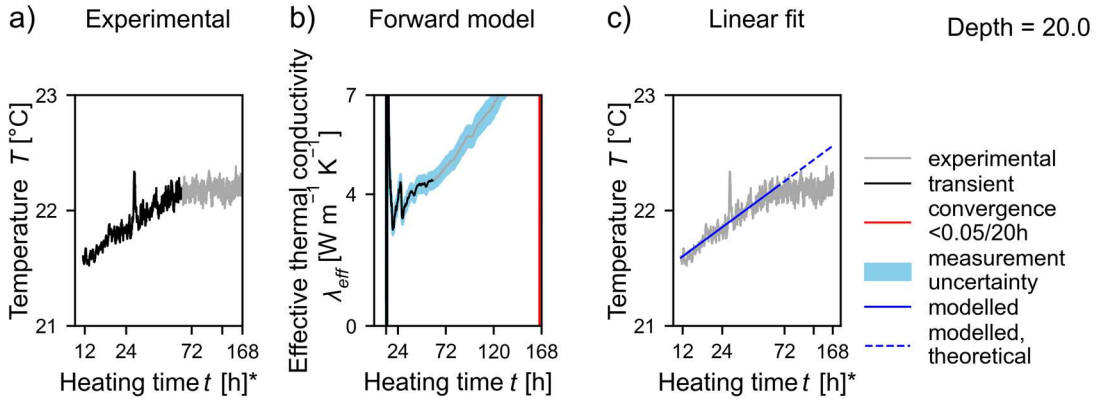

Figure A1- 38: Evaluation of the effective thermal conductivities (λ_{eff}) for the depth interval of 20.0 m.

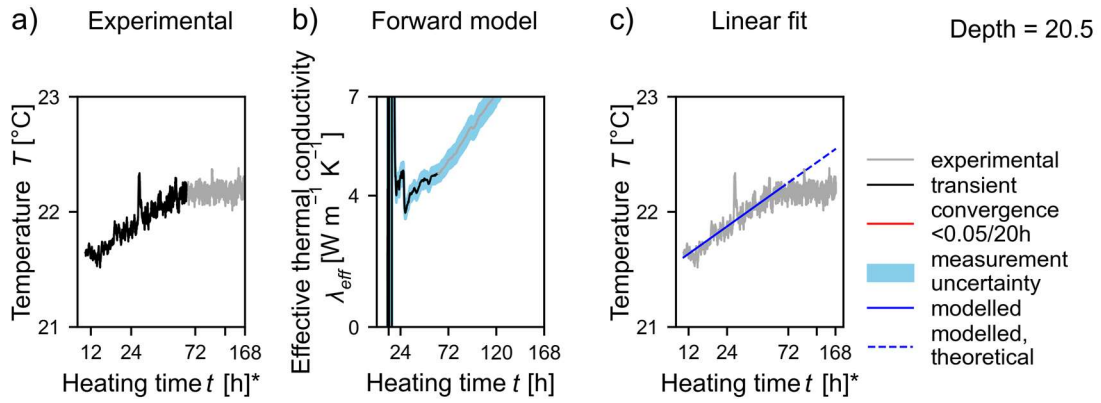

Figure A1- 39: Evaluation of the effective thermal conductivities (λ_{eff}) for the depth interval of 20.5 m.

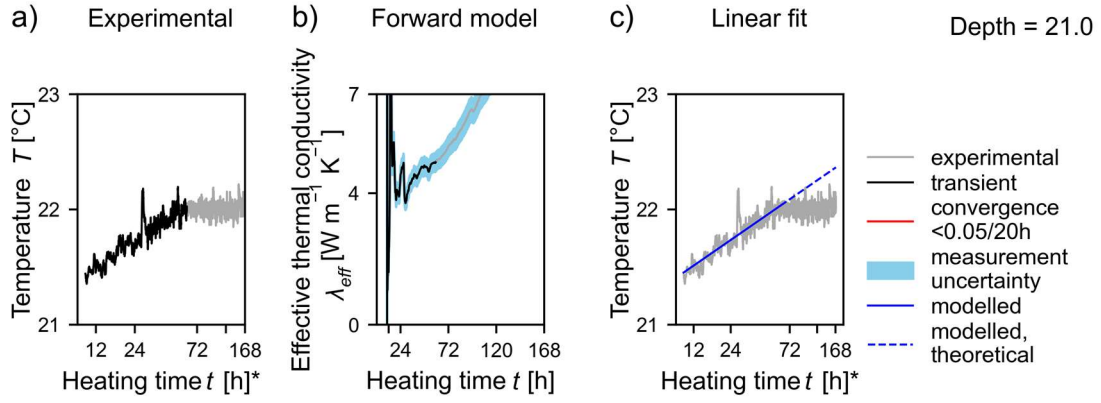

Figure A1- 40: Evaluation of the effective thermal conductivities (λ_{eff}) for the depth interval of 21.0 m.

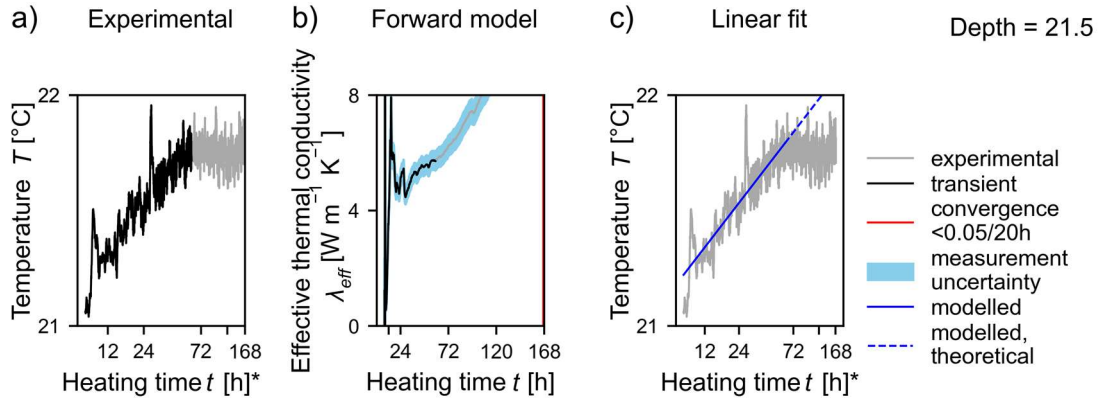

Figure A1- 41: Evaluation of the effective thermal conductivities (λ_{eff}) for the depth interval of 21.5 m.

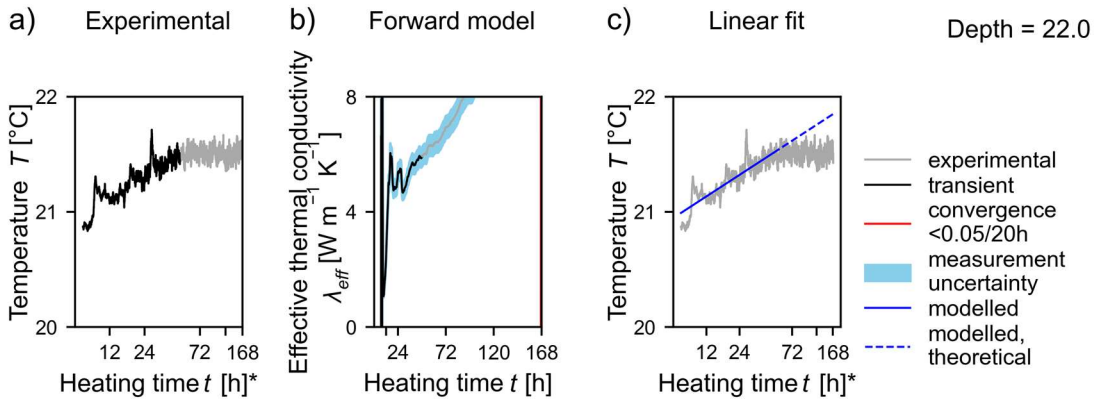

Figure A1- 42: Evaluation of the effective thermal conductivities (λ_{eff}) for the depth interval of 22.0 m.

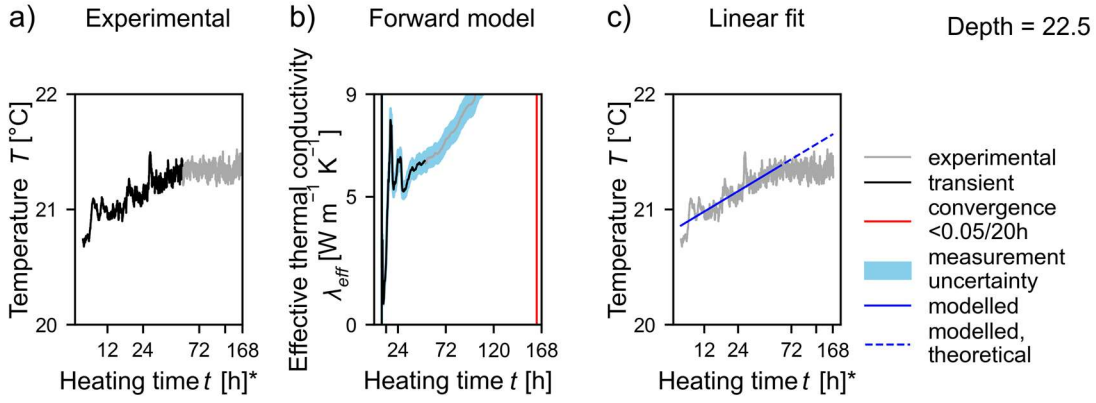

Figure A1- 43: Evaluation of the effective thermal conductivities (λ_{eff}) for the depth interval of 22.5 m.

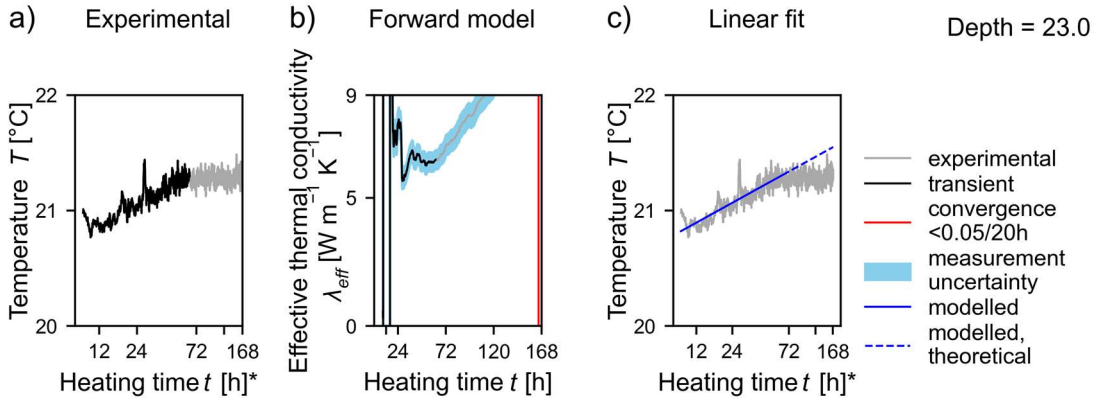

Figure A1- 44: Evaluation of the effective thermal conductivities (λ_{eff}) for the depth interval of 23.0 m.

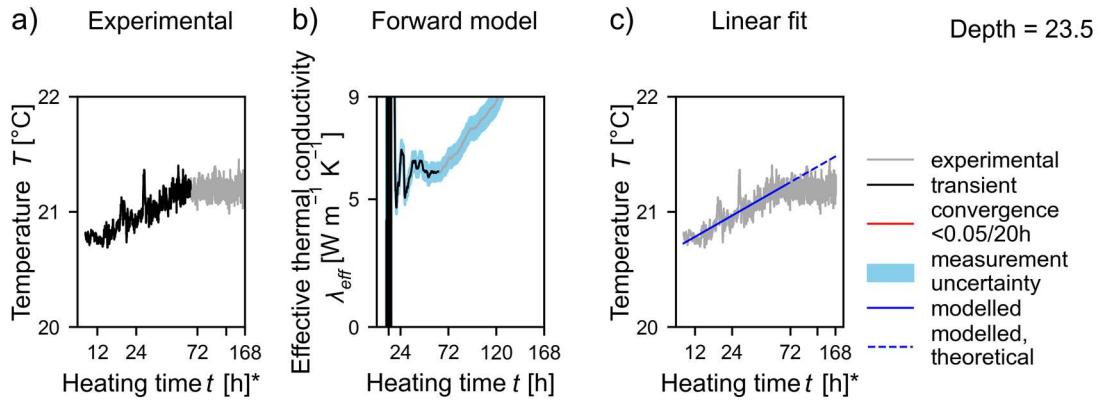

Figure A1- 45: Evaluation of the effective thermal conductivities (λ_{eff}) for the depth interval of 23.5 m.

Appendix Study 2

This Appendix refers to Study 2 (Chapter 3). The content was submitted to the journal Geothermal Energy as a supporting information.

Table A2- 1: Experimentally determined properties of the Triassic sandstones with the minimum (Min), arithmetic mean (Mean), median, maximum (Max), standard deviation (s [W m^{-1} K^{-1}]) and number of analysed samples.

		Min	Mean	Median	Max	s	Number
Effective thermal conductivity λ_{eff}	[W m^{-1} K^{-1}]	2.3	4.7	5.0	6.1	0.9	101
Saturated thermal conductivity λ_{sat}	[W m^{-1} K^{-1}]	2.7	4.6	4.6	6.4	0.6	141
Dry thermal conductivity λ_{dry}	[W m^{-1} K^{-1}]	1.4	2.5	2.4	3.9	0.5	147
Wet bulk density ρ_b	[g cm^{-3}]	2.15	2.46	2.45	2.68	0.08	156
Dry bulk density ρ_d	[g cm^{-3}]	1.80	2.32	2.31	2.63	0.11	156
Solid density ρ_s	[g cm^{-3}]	2.62	2.68	2.67	2.81	0.03	156
Water content w	[%]	2.0	5.8	5.7	19.4	2	156
Open porosity ϕ_{open}	[%]	5.6	13.2	13.4	23.6	3.3	155
Total porosity ϕ	[%]	2.0	12.9	13.2	18.8	3.2	115
Quartz content	[%]	82	87	86	95	4	10
Feldspar content	[%]	2.5	7.1	7.8	12.0	2.8	10
Lithic fragment content	[%]	3.5	6.5	6.5	10.0	2.3	10
Clay content	[%]	1.5	3.2	3.1	5.0	1.4	10
Carbonate content CO_3	[%]	0.1	4.6	0.4	55.5	10.8	147
Permeability K	[mD]	1.2	28.0	3.2	368.1	62.1	154
Average pore diameter d_{pore}	[µm]	0.01	0.14	0.09	1.04	0.18	143
Inner pore surface A_{pore}	[m^2 g^{-1}]	0.06	2.75	2.45	8.45	1.7	142

Table A2- 2: Statistics of the estimated thermal conductivities (λ_{est} [W m^{-1} K^{-1}]) applying the different theoretical models with the minimum (Min), arithmetic mean (Mean), maximum (Max), standard deviation (s [W m^{-1} K^{-1}]) and the root mean square error (RMSE).

	Min	Max	Mean	s	RMSE
Arithmetic mean	5.4	6.5	6.1	0.2	1.6
Harmonic mean	2.0	4.3	2.9	0.4	1.8
Geometric mean	3.9	6.0	5.0	0.4	0.8
Voigt-Reuss-Hill model	3.7	5.4	4.5	0.3	0.7
Statistical spatial distribution mean	3.3	5.3	4.2	0.4	0.8
Hashin-Shtrikman upper bound	5.0	6.4	5.8	0.3	1.4
Hashin-Shtrikman lower bound	3.2	5.6	4.4	0.4	0.7
Hashin-Shtrikman average	4.1	6.0	5.1	0.3	0.8
de Vries, $g_1 = 0.75$	3.8	5.9	4.9	0.4	0.8
Weighted geometric mean, $f = 0.65$	4.7	6.3	5.6	0.3	1.2
Sugawara and Yoshizawa, $n_c = 2$	4.0	6.0	5.1	0.4	0.8
Sugawara and Yoshizawa, $n_c = 2.5$	3.8	5.9	4.9	0.4	0.8
El Sayed	2.7	3.2	3.0	0.1	1.7
Nabawy-Géraud	2.8	4.4	3.8	0.4	1.1

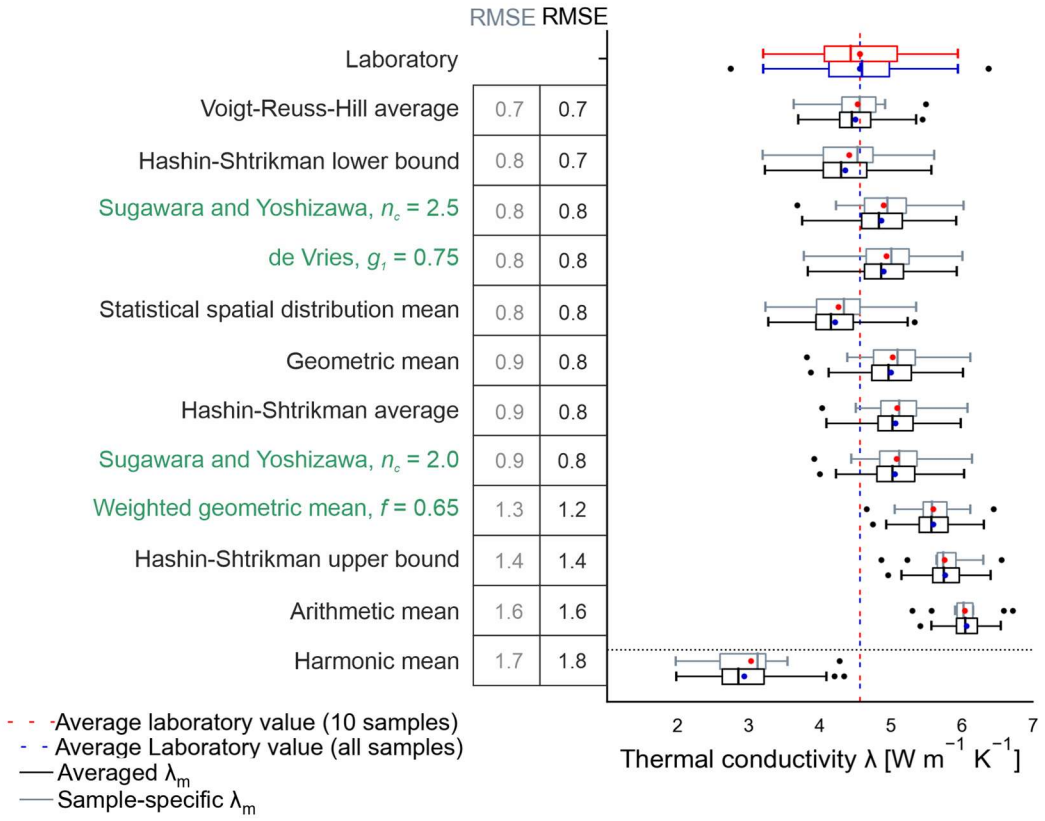

Figure A2- 1: Estimated thermal conductivities from theoretical models, comparing the approach using an average matrix thermal conductivity (λ_m) with using the sample-specific matrix thermal conductivities.

Table A2- 3: Error in estimated thermal conductivities, comparing the approach using an average matrix thermal conductivity with using the sample-specific matrix thermal conductivities for the ten samples with known mineralogy.

	Mean error [%]	Maximum error [%]
Voigt-Reuss-Hill average	2.5	4.8
Hashin-Shtrikman lower bound	2.1	4.1
Sugawara and Yoshizawa, n_c = 2.5	3.1	5.8
de Vries, g_1=0.75	2.5	4.8
Statistical spatial distribution mean	2.2	4.2
Geometric mean	2.8	5.3
Hashin-Shtrikman average	2.7	5.1
Sugawara and Yoshizawa, n_c = 2	3.1	5.8
Weighted geometric mean, f = 0.65	2.9	5.6
Hashin Shtrikman upper bound	3.1	5.9
Arithmetic mean	3.1	5.9
Harmonic mean	1.3	2.4

Appendix Study 3

This Appendix refers to Study 3 (Chapter 4). The content was published in the journal Geothermal Energy as a supporting information and is available online at: https://link.springer.com/article/10.1186/s40517-024-00316-3

Table A3- 1: Measurement methods applied for the determination of thermal conductivity λ of grouting materials.

Method		Literature	Specifications
Steady state		Alrtimi et al. (2013)	Own setup, source between two samples, saturated and dry samples
		Delaleux et al. (2012)	No information on the manufacturer (own setup?), Fourier's gradient, saturated sample
		Extremera-Jiménez et al. (2021)	Guarded heat flow meter FOX-50 (TA Instruments), ISO 8302
		Jobmann and Buntebarth (2009)	No information on the manufacturer (own setup?), divided bar
		Song et al. (2019)	TC3200 Thermal Conductivity Instrument, 3 – 5 % error, (probably) dry samples
		Wang et al. (2020)	Guarded hot plate, TPMBE-300 thermal conductivity meter
Transient hot wire	Needle probe	Blázquez et al. (2017)	KD2-PRO analyzer, needle probe, sensor RK-1, Decagon devices
		Do et al. (2018), Do et al. (2017)	Own setup, needle probe, ASTM D5334, (partly) saturated samples
		Erol and François (2014), Erol and François (2013)	Hukseflux company, needle probe TP02, (partly) saturated
		Kim et al. (2017), Kim and Oh (2019)	KD2 PRO (Decagon Manufacturing Co., Ltd., Pullman, WA, USA), TR-1 (single needle), SH-1 (dual needle), 10 % accuracy, improved contact with grease, saturated and dry samples
		Dinh et al. (2020), Kim et al. (2020)	Own setup, ASTM D5334, (partly) saturated samples
		Li et al. (2019)	Needle probe: K-type thermocouple (WRN-130, ZUHUJIANG, China), own setup
		Indacoechea-Vega et al. (2018), Pascual-Muñoz et al. (2018)	Hukseflux TPSYS02, ASTM 5334-08, saturated samples
		Shafigh et al. (2020)	KD2-PRO analyser using a TR1 needle
	Surface probe	Allan (1997)	Shotherm QTM-D2 Thermal Conductivity Meter, surface probe, saturated samples
		Frąc et al. (2021)	Isomet 2104, surface probe, saturated and dry samples
		Kim et al.(2016), Kim et al. (2015), Kim and Oh (2020)	Quick Thermal Conductivity Meter QTM500, Kyoto Electronics Manufacturing Co.), PD-11 surface probe, 3 % reproducibility, 5 % accuracy, saturated and dry samples
		Lee et al. (2010), Park et al. (2011)	QTM-500 thermal conductivity meter (Kyoto Electronics), PD-12 probe, 3 % reproducibility, saturated samples
		Riegger et al. (2016)	Isomet 2104, surface probe, saturated samples
		Viccaro (2018)	Heat Flow Meter Shotherm QTM Showa Denko, 2 % reproducibility, UNI EN 12664:2002
Transient plane source		Bentz (2007)	HotDisk Thermal Constants Analyser, 2 % reproducibility, (partly) saturated samples
		Berktas et al. (2020)	HotDisk Thermal Constants Analyser, TPS 2500S, (partly) saturated samples
		Borinaga-Treviño et al. (2013)	TCi C-Therm thermal conductivity tester, improved contact with measurement oil, dry samples
		Delaleux et al. (2012)	No information on the manufacturer (own setup?), (partly) saturated samples
		Dong et al. (2022)	Unsteady thermal conductivity tester, Harbin Institute of Technology
		Yang et al. (2024)	DRE-2C type thermal conductivity tester, 5 % accuracy
		Zhao et al. (2024)	TPS instrument (TPS 500)
		Zhou et al. (2018)	Thermal Conductivity Meter (TCi)

Table A3- 2: Measurement methods applied for the determination of specific heat capacity c_p and volumetric heat capacity ρc_p of grouting materials and other cementitious materials.

Method	Literature	Specifications
Transient hot wire	Frąc et al. (2021)	Isomet 2104, surface probe, saturated and dry samples, measurement of the volumetric heat capacity
	Kim et al. (2017), Kim and Oh (2019)	KD2 PRO (Decagon Manufacturing Co., Ltd., Pullman, WA, USA), SH-1 (dual needle), 10 % accuracy, improved contact with grease, saturated and dry samples, measurement of ρc_p and thermal diffusivity α
Transient plane source	Bentz (2007)	HotDisk, c_p-module with gold cell, (partly) saturated sample
	Zhou et al. (2018)	Thermal Conductivity Meter (TCi), measurement of ρc_p
Calorimetry	Extremera-Jiménez et al. (2021)	ASTM D4611, dry sample, law of mixtures
	Liu et al. (2022)	DSC, Q2000, TA Instruments, USA, functional cement paste for geothermal-coal synergetic mining, heat range: 20-80 °C
	Schutter and Taerwe (1995)	DSC, hardening cement paste
	Shafigh et al. (2020)	DSC, law of mixtures, (sand, cement for the application as building material, dry samples, 20 – 50 °C)
	Xu and Chung (2000)	DSC, Perkin-Elmer Differential Scanning Calorimeter (Norwalk, CT, USA) (DSC-7), (cement-sand-mixtures for the application as building material)

Table A3- 3: Sample preparation procedures applied for the analysis of thermal conductivity λ and volumetric heat capacity ρc_p of grouting materials.

	Literature	Mixing device	Mixing routine
Mixing method	Allan (1997)	Dependent on sample size: capacity blender, Hobart planetary mixer (1 L); air-driven grout paddle mixer, ChemGrout CG- 55OP (129 L); air-driven colloidal grout mixer, ChemGrout CG620 (227 L)	5 min (with paddle mixer); 30 – 60 s (colloidal grout mixer)
	Bentz (2007)	High-speed blender	Several minutes and temperature-controlled
	Berktas et al. (2020)	High-share dispersion system from VMA Getzmann	No information provided
	Dong et al. (2022)	No information provided	Mix and stir for 10 min
	Frąc et al. (2021)	No information provided	PN-EN 196-1:2006, 120 s
	Indacoechea-Vega et al. (2018)	750 W mortar mixer with variable speed	No information provided
	Mascarin et al. (2022)	IKA mixer	2 steps of about 1.5 min, EN 196–1, increasing rotation speed up to 385 rpm, then manually remixing with a rubber spatula, at T = 20 °C, 65 % RH
	Mendes et al. (2019)	Mortar mixer	1 min low speed, 30 s high speed
	Pascual-Muñoz et al. (2018)	1500 W mortar mixer	Speed regulation
	Song et al. (2019)	No information provided	Starting at a low speed of 4000 ± 200 rpm, cement was added in 15 s, rotated at a high speed of 12 000 ± 500 rpm for 35 s
	Viccaro (2018)	Colloidal grout mixer	UNI EN 196-1:2016
	Xu and Chung (2000)	Rotary mixer with a flat beater	No further information (“all ingredi-ents were mixed”)
	Zhao et al. (2024)	High-speed hand mixer	at 600 rpm

	Literature	Storage condition	Hydration time
Storage conditions	Allan (1997)	Samples sealed to prevent evaporation, demoulded after 24 h, placed in a water bath	14 d
	Alrtimi et al. (2013)	No information provided	> 14 d
	Bentz (2007)	Saturated (small volume of distilled water on top) or sealed conditions, at 20 °C	8 h, 1, 2, 3, 8, 15 and 28 d
	Berktas et al. (2020)	In climate chamber at 100 % RH and 20 °C	7 d
	Blázquez et al. (2017)	Dry (?) and harden	28 d
	Borinaga-Treviño et al. (2013)	At ambient temperature for 24 h – 2 d, demolition of moulds, submerged in water at 20 °C	14 d
	Dong et al. (2022)	Remove mould aft 24 h, cure in water	28 d
	Erol and François (2014)	80 % RH, at 20 °C	10 and 30 d
	Frąc et al. (2021)	24 h in moulds, then immerse in water at 22 °C	28 d
	Indacoechea-Vega et al. (2018), Pascual-Muñoz et al. (2018)	48 h at ambient conditions, removal of moulds, immersed in water at 20 °C	28 d
	Kim e al. (2017), Kim et al. (2016), Kim and Oh (2020)	Ambient conditions, dried in the oven, saturated by placing in water for 2 – 5 d	28 d
	Mendes et al. (2019)	Demoulded after 24 h, in a moist chamber at 25 °C and 90 % RH	28 d
	Park et al. (2011)	Wet conditions	continuously for 14 d
	Riegger et al. (2016)	100 % RH, ambient conditions	7, 14, 21, 28 d
	Shafigh et al. (2020)	Removed from moulds after 24 h, in normal water at 23 °C	28 d
	Song et al. (2019)	In 8040D10 HTHP consistometer (Chandler Engineering Company, L.L.C) for 8 h, at T = 60 °C, p = 20 MPa	No information provided (> 8 h)
	Viccaro (2018)	Drying (?) at 20 °C, 95 – 99 % RH	28 d
	Xu and Chung (2000)	Demoulding after 24 h, in the air at room temperature and 100 % RH	28 d
	Zhao et al. (2024)	Demould after 1 d, cure in lab environment at 23 ± 2 °C, 45 ± 10 % RH	28 d

Table A3- 4: List of the applied methods and the corresponding sample conditions.

Material	Conditions					Applied methods		
	Mixing speed [rpm]	Curing condition	t [d]	w [%]	S_r [%]	Thermal conductivity	Specific heat capacity	Volumetric heat capacity
Measurement method								
M1	2000	Under water	28	73.0	101	THW, TPS	DSC	THW, TPS, DSC + calculation
M2	2000	Under water	282	69.8	102	THW, TPS	DSC	THW, TPS, DSC + calculation
M3	2000	Under water	28	29.2	100	THW, TPS	DSC	THW, TPS, DSC + calculation
M4	2000	Under water	28	58.3	99	THW, TPS	DSC	THW, TPS, DSC + calculation
M5	2000	Under water	28	30.8	99	THW, TPS	DSC	THW, TPS, DSC + calculation
M6	2000	Under water	28	52.9	101	THW, TPS	DSC	THW, TPS, DSC + calculation
M7	2000	Under water	28	39.1	101	THW, TPS	DSC	THW, TPS, DSC + calculation
Mixing speed								
M1	650	Under water	28	72.0	100	TPS	DSC	DSC + calculation
M2	650	Under water	28	71.9	100	TPS	DSC	DSC + calculation
M3	650	Under water	28	29.7	99	TPS	DSC	DSC + calculation
M5	650	Under water	28	32.2	100	TPS	DSC	DSC + calculation
Curing condition								
M1	2000	Air-moist	28	70.2	98	TPS	DSC	DSC + calculation
M2	2000	Air-moist	28	69.2	99	TPS	DSC	DSC + calculation
M3	2000	Air-moist	28	26.4	94	TPS	DSC	DSC + calculation
M4	2000	Air-moist	28	55.3	-	TPS	DSC	-
Hydration time								
M1	2000	Under water	9	-	-	TPS	-	-
M1	2000	Under water	14	71.9	-	TPS	DSC	-
M1	2000	Under water	21	70.9	-	TPS	-	-
M1	2000	Under water	28	71.4	-	TPS	DSC	-
M1	2000	Under water	56	71.4	-	TPS	DSC	-
M1	2000	Under water	112	73.5	102	TPS	DSC	DSC + calculation
M1	2000	Under water	182	-	-	TPS	DSC	-
M1	2000	Under water	273	73.8	-	TPS	DSC	-
M1	2000	Under water	365	73.0	103	TPS	DSC	DSC + calculation
M2	2000	Under water	9	-	-	TPS	-	-
M2	2000	Under water	14	73.1	-	TPS	DSC	-
M2	2000	Under water	21	72.7	-	TPS	-	-
M2	2000	Under water	28	73.7	-	TPS	DSC	-
M2	2000	Under water	56	73.8	-	TPS	DSC	-
M2	2000	Under water	112	69.7	100	TPS	DSC	DSC + calculation
M2	2000	Under water	182	-	-	TPS	DSC	DSC + calculation
M2	2000	Under water	273	73.3	-	TPS	DSC	-
M2	2000	Under water	365	72.3	100	TPS	DSC	DSC + calculation
M3	2000	Under water	7	-	-	TPS	-	-
M3	2000	Under water	14	-	-	TPS	DSC	-
M3	2000	Under water	21	-	-	TPS	-	-
M3	2000	Under water	28	26.4	94	TPS	DSC	DSC + calculation
M3	2000	Under water	56	28.8	-	TPS	DSC	-
M3	2000	Under water	112	29.0	-	-	DSC	-
M3	2000	Under water	182	28.3	98	-	DSC	DSC + calculation
M3	2000	Under water	272	29.2	-	-	DSC	-
M3	2000	Under water	365	29.4	-	-	DSC	-
M4	2000	Under water	9	-	-	TPS	-	-
M4	2000	Under water	14	57.6	-	TPS	DSC	-
M4	2000	Under water	21	58.5	-	TPS	-	-
M4	2000	Under water	28	55.3	-	TPS	DSC	-
M4	2000	Under water	56	56.3	-	TPS	DSC	-
M4	2000	Under water	112	57.8	101	TPS	DSC	DSC + calculation
M4	2000	Under water	182	-	-	TPS	DSC	-
M4	2000	Under water	273	57.9	-	TPS	DSC	-
M4	2000	Under water	365	57.7	102	TPS	DSC	DSC + calculation

Transient hot wire (THW), transient plane source (TPS), differential scanning calorimetry (DSC)

Table A3- 5: Determination of measurement uncertainties based on the recommendations of the *Guide to the Expression of Uncertainty in Measurement* (ISO IEC 98-3, 2008).

Property	Method	Uncertainty type A	Uncertainty type B
Density of suspension	Mud balance	Reading accuracy [a] 0.01 g cm^{-1}	Single measurement
Wet bulk density	Immersion weighing	Accuracy of scale [b] 0.001 g	Standard deviation, incl. Student-t (2 – 3 measurements)
Water content	Gravimetry	Accuracy of scale [b] 0.001 g	Standard deviation, incl. Student-t (2 – 3 measurements)
Thermal conductivity	THW	Accuracy [c] 10 %	Standard deviation, incl. Student-t (4 – 8 measurements)
Thermal conductivity	TPS	Accuracy [d] 2 %	Standard deviation, incl. Student-t (3 – 5 measurements)
Volumetric heat capacity	THW	Accuracy [c] 15 % + 0.001 MJ m^{-3} K^{-1}	Standard deviation, incl. Student-t (4 – 8 measurements)
Volumetric heat capacity	TPS	Accuracy [d] 7 %	Standard deviation, incl. Student-t (3 – 5 measurements)
Specific heat capacity (dry samples, $c_{p,d}$)	DSC	Calibration [e] 1.5 % Integration, base-line [e] 3 % Mass of sample [f] 0.1 % Thermal contact [e] 0.2 %	Standard deviation, incl. Student-t (5 measurements)
Specific heat capacity (wet samples, $c_{p,f}$)	DSC, Water content	Equation 4-4	
Volumetric heat capacity	DSC, Water content, Wet bulk density	Equation 4-6	

[a] own estimate, [b] manufacturer value (Denver SI603, Sartorius AG, Germany), [c] manufacturer value (ISOMET 2104, Applied Precision Ltd., Slovakia), [d] manufacturer value (HotDisk TPS1500, C3 Prozess- und Analysentechnik, Germany), [e] Mettler Toledo (2016), [f] manufacturer value (Cubis II MCE 125P, Sartorius AG, Germany)

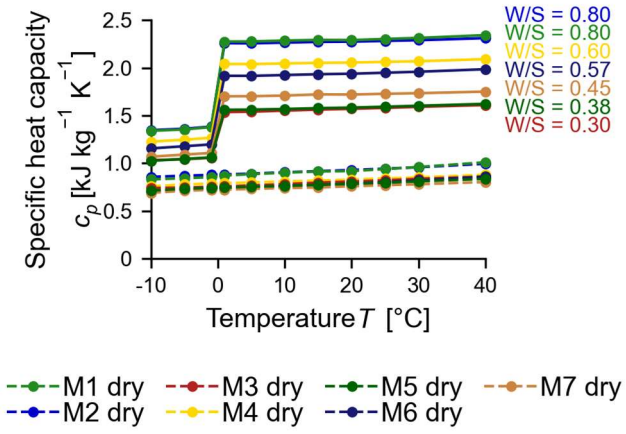

Figure A3- 1: Temperature dependence of the specific heat capacity using the differential scanning calorimetry (DSC) method. Sample preparation: Mixed at 2000 rpm, stored under water and hydration time of 28 d.

References

Abdulagatova, Z., Abdulagatov, I.M., Emirov, V.N., 2009. Effect of temperature and pressure on the thermal conductivity of sandstone. International Journal of Rock Mechanics and Mining Sciences 46, 1055–1071. https://doi.org/10.1016/j.ijrmms.2009.04.011

Abuel-Naga, Hossam.M., Bergado, Dennes.T., Bouazza, A., Pender, Michael.J., 2009. Thermal conductivity of soft Bangkok clay from laboratory and field measurements. Engineering Geology 105, 211–219. https://doi.org/10.1016/j.enggeo.2009.02.008

Acuña, J., 2013. Distributed thermal response tests – New insights on U-pipe and coaxial heat exchangers in groundwater-filled boreholes (Dissertation). KTH Royal Institute of Technology, Stockholm.

Acuña, J., Palm, B., 2010. A novel coaxial borehole heat exchanger: Description and first distributed thermal response test measurements, in: Proceedings World Geothermal Congress 2010. Presented at the World Geothermal Congress, 25-29 April 2010, Bali, Indonesia.

Adam, T., 2006. Ein Modell zur Beschreibung der Hydratation von Beton in Abhängigkeit vom Feuchtegehalt (Dissertation). Technical University of Darmstadt, Darmstadt.

Adebayo, P., Beragama Jathunge, C., Darbandi, A., Fry, N., Shor, R., Mohamad, A., Wemhöner, C., Mwesigye, A., 2024. Development, modeling, and optimization of ground source heat pump systems for cold climates: A comprehensive review. Energy and Buildings 320, 114646. https://doi.org/10.1016/j.enbuild.2024.114646

AGEB, 2024. Energieverbrauch in Deutschland im Jahr 2023. Arbeitsgemeinschaft Energiebilanzen e. V.

Aïtcin, P.-C., 2016. Portland cement, in: Science and Technology of Concrete Admixtures. Elsevier, pp. 27–51. https://doi.org/10.1016/B978-0-08-100693-1.00003-5

Albers, A., Huttenloch, P., Zorn, R., Steger, H., Blum, P., 2024a. Determination of thermal properties of grouting materials for borehole heat exchangers (BHE). Geotherm Energy 12, 36. https://doi.org/10.1186/s40517-024-00316-3

Albers, A., Steger, H., Zorn, R., Blum, P., 2024b. Evaluating an enhanced thermal response test (ETRT) with high groundwater flow. Geotherm Energy 12, 1. https://doi.org/10.1186/s40517-023-00278-y

Albert, K., Franz, C., Koenigsdorff, R., Zosseder, K., 2017. Inverse estimation of rock thermal conductivity based on numerical microscale modeling from sandstone thin sections. Engineering Geology 231, 1–8. https://doi.org/10.1016/j.enggeo.2017.10.010

Allan, M., 1997. Thermal conductivity of cementitious grouts for geothermal heat pumps, FY Progress Report. BNL 65129. New York: Brookhaven National Laboratory.

Allan, M., Kavanaugh, S., 1999. Thermal conductivity of cementitious grouts and impact on heat exchanger length design for ground source heat pumps. HVAC&R Res. 5, 85–96. https://doi.org/10.1080/10789669.1999.10391226

Alrtimi, A.A., Rouainia, M., Manning, D.A.C., 2013. Thermal enhancement of PFA-based grout for geothermal heat exchangers. Applied Thermal Engineering 54, 559–564. https://doi.org/10.1016/j.applthermaleng.2013.02.011

Angelotti, A., Ly, F., Zille, A., 2018. On the applicability of the moving line source theory to thermal response test under groundwater flow: Considerations from real case studies. Geothermal Energy 6. https://doi.org/10.1186/s40517-018-0098-z

Antelmi, M., Alberti, L., Angelotti, A., Curnis, S., Zille, A., Colombo, L., 2020. Thermal and hydrogeological aquifers characterization by coupling depth-resolved thermal response

test with moving line source analysis. Energy Conversion and Management 225. https://doi.org/10.1016/j.enconman.2020.113400
ASTM International, 2023. ASTM D5334-22a: Standard test method for determination of thermal conductivity of soil and soft rock by thermal needle probe procedure.
ASTM International, 2016. ASTM D 4611: Standard test method for specific heat of rock and soil.
Bakker, M., Caljé, R., Schaars, F., van der Made, K., Haas, S., 2015. An active heat tracer experiment to determine groundwater velocities using fiber optic cables installed with direct push equipment. Water Resources Research 51, 2760–2772. https://doi.org/10.1002/2014WR016632
Banks, E.W., Shanafield, M.A., Cook, P.G., 2014. Induced temperature gradients to examine groundwater flowpaths in open boreholes. Groundwater 52, 943–51. https://doi.org/10.1111/gwat.12157
Bayer, P., Saner, D., Bolay, S., Rybach, L., Blum, P., 2012. Greenhouse gas emission savings of ground source heat pump systems in Europe: A review. Renewable and Sustainable Energy Reviews 16, 1256–1267. https://doi.org/10.1016/j.rser.2011.09.027
Bayuk, I., Popov, Y., Parshin, A., 2011. A new powerful tool for interpreting and predicting in reservoir geophysics: Theoretical modeling as applied to laboratory measurements of thermal properties, in: Proceedings of the International Symposium of the Society of Core Analysts. Presented at the International Symposium of the Society of Core Analysts, 18-21 September, 2011.
Bense, V.F., Read, T., Bour, O., Le Borgne, T., Coleman, T., Krause, S., Chalari, A., Mondanos, M., Ciocca, F., Selker, J.S., 2016. Distributed temperature sensing as a downhole tool in hydrogeology. Water Resources Research 52, 9259–9273. https://doi.org/10.1002/2016WR018869
Bentz, D.P., 2007. Transient plane source measurements of the thermal properties of hydrating cement pastes. Mater Struct 40, 1073–1080. https://doi.org/10.1617/s11527-006-9206-9
Berktas, I., Nejad Ghafar, A., Fontana, P., Caputcu, A., Menceloglu, Y., Saner Okan, B., 2020. Synergistic effect of expanded graphite-silane functionalized silica as a hybrid additive in improving the thermal conductivity of cementitious grouts with controllable water uptake. Energies 13, 3561. https://doi.org/10.3390/en13143561
Bertermann, D., Suft, O., 2024. Determination of the temperature development in a borehole heat exchanger field using distributed temperature sensing. Energies 17, 4697. https://doi.org/10.3390/en17184697
Blázquez, C.S., Martín, A.F., Nieto, I.M., García, P.C., Sánchez Pérez, L.S., González-Aguilera, D., 2017. Analysis and study of different grouting materials in vertical geothermal closed-loop systems. Renewable Energy 114, 1189–1200. https://doi.org/10.1016/j.renene.2017.08.011
Blum, P., Campillo, G., Münch, W., Kölbel, T., 2010. CO2 savings of ground source heat pump systems – A regional analysis. Renewable Energy 35, 122–127. https://doi.org/10.1016/j.renene.2009.03.034
Borinaga-Treviño, R., Pascual-Muñoz, P., Castro-Fresno, D., Del Coz-Díaz, J.J., 2013. Study of different grouting materials used in vertical geothermal closed-loop heat exchangers. Applied Thermal Engineering 50, 159–167. https://doi.org/10.1016/j.applthermaleng.2012.05.029
Bozzoli, F., Pagliarini, G., Rainieri, S., Schiavi, L., 2011. Estimation of soil and grout thermal properties through a TSPEP (two-step parameter estimation procedure) applied to TRT (thermal response test) data. Energy 36, 839–846. https://doi.org/10.1016/j.energy.2010.12.031
Bucci, A., Prevot, A.B., Buoso, S., De Luca, D.A., Lasagna, M., Malandrino, M., Maurino, V., 2018. Impacts of borehole heat exchangers (BHEs) on groundwater quality: the role of

heat-carrier fluid and borehole grouting. Environ Earth Sci 77, 175. https://doi.org/10.1007/s12665-018-7375-9

Bullard, J.W., Jennings, H.M., Livingston, R.A., Nonat, A., Scherer, G.W., Schweitzer, J.S., Scrivener, K.L., Thomas, J.J., 2011. Mechanisms of cement hydration. Cement and Concrete Research 41, 1208–1223. https://doi.org/10.1016/j.cemconres.2010.09.011

Bundes-Klimaschutzgesetz (KSG), 2019.

Bundesverband Deutsche Wärmepumpe, 2023. Rekordabsatz: Wärmepumpenbranche beweist Leistungsfähigkeit trotz unsicherer Aussichten (press release).

Busch, K.-F., Luckner, L., 1973. Geohydraulik, 2. ed. Deutscher Verlag für Grundstoffindustrie, Leipzig.

Bussmann, G., Bracke, R., Eicker, T., Wittig, V., Tuente, H., Gueldenhaupt, J., Groenig, L., Kiel, F., Maeggi, F., Montag, B., 2015. GeoStar – A scalable borehole heat exchanger plant for growing district heating systems and restricted urban areas, in: Proceedings World Geothermal Congress 2015.

Carslaw, H.S., Jaeger, J.C., 1959. Conduction of Heat in Solids, 2nd ed. Oxford Science Publications, Oxford.

Chiasson, A., Rees, S.J., Spitler, J.D., 2000. A preliminary assessment of the effects of groundwater flow on closed-loop ground-source heat pump systems. ASHRAE Transactions 380–393.

Ciocca, F., Lunati, I., van de Giesen, N., Parlange, M.B., 2012. Heated optical fiber for distributed soil-moisture measurements: A lysimeter experiment. Vadose Zone Journal 11. https://doi.org/10.2136/vzj2011.0199

Clauser, C., 2006. 8 Geothermal Energy, in: Heinloth, K. (Ed.), Landolt-Börnstein, Group VIII Advanced Materials and Technologies, Volume 3C: (Renewable Energy). Springer-Verlag Berlin Heidelberg.

Clauser, C., Huenges, E., 1995. Thermal Conductivity of Rocks and Minerals, in: Rock Physics and Phase Relations, A Handbook of Physical Constants. American Geophysical Union, Washington.

Coleman, T.I., Parker, B.L., Maldaner, C.H., Mondanos, M.J., 2015. Groundwater flow characterization in a fractured bedrock aquifer using active DTS tests in sealed boreholes. Journal of Hydrology 528, 449–462. https://doi.org/10.1016/j.jhydrol.2015.06.061

Colombero, C., Comina, C., Guiliani, A., Mandrone, G., 2016. Ultrasonic equipment aimed to detect grouting homogeneity in geothermal heat exchangers.

Dalla Santa, G., Pasquier, P., Schenato, L., Galgaro, A., 2022. Repeated ETRTs in a complex stratified geological setting: High-resolution thermal conductivity identification by multiple linear regression. Journal of Geotechnical and Geoenvironmental Engineering 148. https://doi.org/10.1061/(ASCE)GT.1943-5606.0002724

De Vries, D.A., 1963. Thermal properties of soils, in: Physics of Plant Environment. North-Holland Publishing Co., Amsterdam, pp. 210–235.

Del Val, L., Carrera, J., Pool, M., Martínez, L., Casanovas, C., Bour, O., Folch, A., 2021. Heat dissipation test with fiber-optic distributed temperature sensing to estimate groundwater flux. Water Resources Research 57. https://doi.org/10.1029/2020WR027228

Delaleux, F., Py, X., Olives, R., Dominguez, A., 2012. Enhancement of geothermal borehole heat exchangers performances by improvement of bentonite grouts conductivity. Applied Thermal Engineering 33–34, 92–99. https://doi.org/10.1016/j.applthermaleng.2011.09.017

Demongodin, L., Pinoteau, B., Vasseur, G., Gable, R., 1991. Thermal conductivity and well logs: A case study in the Paris basin. Geophysical Journal InternationalGeophys. J. Int. 105, 675–691. https://doi.org/10.1111/j.1365-246X.1991.tb00805.x

Des Tombe, B.F., Bakker, M., Smits, F., Schaars, F., van der Made, K., 2019. Estimation of the variation in specific discharge over large depth using distributed temperature sensing (DTS) measurements of the heat pulse response. Water Resources Research 55, 811–826. https://doi.org/10.1029/2018WR024171

Desmedt, J., van Bael, J., Hoes, H., Robeyn, N., 2012. Experimental performance of borehole heat exchangers and grouting materials for ground source heat pumps. Int. J. Energy Res. 36, 1238–1246. https://doi.org/10.1002/er.1898

Deutsche Norm, 2022a. DIN EN ISO 17892-1, Geotechnical investigation and testing - Laboratory testing of soil - Part 1: Determination of water content (ISO 17892-1:2014 + Amd 1:2022); German version EN ISO 17892-1:2014 + A1:2022. https://dx.doi.org/10.31030/3364115

Deutsche Norm, 2022b. DIN EN ISO 22007-2:2022-09, Plastics - Determination of thermal conductivity and thermal diffusivity - Part 2: Transient plane heat source (hot disc) method (ISO 22007-2:2022); German version EN ISO 22007-2:2022. https://dx.doi.org/10.31030/3340784

Deutsche Norm, 2022c. DIN ISO 13320:2022-12, Particle size analysis - Laser diffraction methods (ISO 13320:2020). https://dx.doi.org/10.31030/3384453

Deutsche Norm, 2021. DIN EN ISO 11357-4, Plastics - Differential scanning calorimetry (DSC) - Part 4: Determination of specific heat capacity (ISO 11357-4:2021); German version EN ISO 11357-4:2021. https://dx.doi.org/10.31030/3215266

Deutsche Norm, 2019. DIN ISO 15901-1, Evaluation of pore size distribution and porosity of solid materials by mercury porosimetry and gas adsorption - Part 1: Mercury porosimetry (ISO 15901-1:2016). https://dx.doi.org/10.31030/3031674

Deutsche Norm, 2016a. DIN EN 196-1: Methods of testing cement - Part 1: Determination of strength; German version EN 196-1:2016. https://dx.doi.org/10.31030/2482416

Deutsche Norm, 2016b. DIN ISO 17892-3, Geotechnical investigation and testing - Laboratory testing of soil - Part 3: Determination of particle density (ISO 17892-3:2015, Corrected version 2015-12-15); German version EN ISO 17892-3:2015. https://dx.doi.org/10.31030/2337616

Deutsche Norm, 2015. DIN EN ISO 17892-2, Geotechnical investigation and testing - Laboratory testing of soil - Part 2: Determination of bulk density (ISO 17892-2:2014); German version EN ISO 17892-2:2014. https://dx.doi.org/10.31030/2159676

Deutsche Norm, 2014. DIN 4127, Earthworks and foundation engineering - Test methods for supporting fluids used in the construction of diaphragm walls and their constituent products. https://dx.doi.org/10.31030/2066555

Deutsche Norm, 2011. DIN 18129, Soil, investigation and testing - Determination of lime content. https://dx.doi.org/10.31030/1801168

Deutsche Norm, 2007. DIN EN 1936, Natural stone test method - Determination of real density and apparent density, and of total and open porosity; German version EN 1936:2006. https://dx.doi.org/10.31030/9831981

Diao, N., Li, Q., Fang, Z., 2004. Heat transfer in ground heat exchangers with groundwater advection. International Journal of Thermal Sciences 43, 1203–1211. https://doi.org/10.1016/j.ijthermalsci.2004.04.009

Dils, J., De Schutter, G., Boel, V., 2012. Influence of mixing procedure and mixer type on fresh and hardened properties of concrete: a review. Mater Struct 45, 1673–1683. https://doi.org/10.1617/s11527-012-9864-8

Dinh, B.H., Kim, Y., Kang, G., 2020. Thermal conductivity of steelmaking slag-based controlled low-strength materials over entire range of degree of saturation: A study for ground source heat pump systems. Geothermics 88, 101910. https://doi.org/10.1016/j.geothermics.2020.101910

Do, T.M., Kang, G., Kim, Y., 2018. Thermal conductivity of controlled low strength material (CLSM) under various degrees of saturation using a modified pressure plate extractor apparatus – A case study for geothermal systems. Applied Thermal Engineering 143, 607–613. https://doi.org/10.1016/j.applthermaleng.2018.07.116

Do, T.M., Kim, Y., Dang, M.Q., 2017. Influence of curing conditions on engineering properties of controlled low strength material made with cementless binder. KSCE J Civ Eng 21, 1774–1782. https://doi.org/10.1007/s12205-016-0731-y

Domenico, P.A., Schwartz, F.W., 1990. Physical and chemical hydrogeology. John Wiley & Sons, Inc.

Domes, X., 2015. Cement grouting during installation of ground anchors in non-cohesive soils (Dissertation). Norwegian University of Science and Technology Faculty of Engineering Science and Technology Department of Civil and Transport Engineering, Trondheim.

Domes, X., Benz, T., 2015. Untersuchungen zur Zementfiltration während der Herstellung von Verpressankern in nichtbindigen Böden. Bautechnik 92, 605–616. https://doi.org/10.1002/bate.201500048

Dong, S., Liu, G., Zhan, T., Yao, Y., Ni, L., 2022. Performance study of cement-based grouts based on testing and thermal conductivity modeling for ground-source heat pumps. Energy and Buildings 272, 112351. https://doi.org/10.1016/j.enbuild.2022.112351

Eklund, D., Stille, H., 2008. Penetrability due to filtration tendency of cement-based grouts. Tunnelling and Underground Space Technology 23, 389–398. https://doi.org/10.1016/j.tust.2007.06.011

El Sayed, A.M.A., 2011. Thermophysical study of sandstone reservoir rocks. Journal of Petroleum Science and Engineering 76, 138–147. https://doi.org/10.1016/j.petrol.2011.01.001

Erol, S., François, B., 2014. Efficiency of various grouting materials for borehole heat exchangers. Applied Thermal Engineering 70, 788–799. https://doi.org/10.1016/j.applthermaleng.2014.05.034

Erol, S., François, B., 2013. Thermal, hydraulic and mechanical performances of enhanced grouting materials for borehole heat exchanger, in: Musso, G. (Ed.), Coupled Phenomena in Environmental Geotechnics. CRC Press, pp. 491–499. https://doi.org/10.1201/b15004-64

Extremera-Jiménez, A.J., Eliche-Quesada, D., Guitérrez-Montes, C., Cruz-Peragón1, F., 2021. Experimental work over borehole filling material to reinforce characterization and model validation of Ground Heat Exchangers. REPQJ 19, 109–114. https://doi.org/10.24084/repqj19.227

Ferguson, G., 2015. Screening for heat transport by groundwater in closed geothermal systems. Groundwater 53, 503–6. https://doi.org/10.1111/gwat.12162

Fleuchaus, P., Blum, P., 2017. Damage event analysis of vertical ground source heat pump systems in Germany. Geotherm Energy 5. https://doi.org/10.1186/s40517-017-0067-y

Frąc, M., Szudek, W., Szołdra, P., Pichór, W., 2021. Grouts with highly thermally conductive binder for low-temperature geothermal applications. Construction and Building Materials 295, 123680. https://doi.org/10.1016/j.conbuildmat.2021.123680

Franz, C., Schulze, M., 2016. Bestimmung thermischer Eigenschaften der Gesteine des Unteren und Mittleren Buntsandsteins. Grundwasser 21, 47–58. https://doi.org/10.1007/s00767-015-0316-6

Freifeld, B.M., Finsterle, S., Onstott, T.C., Toole, P., Pratt, L.M., 2008. Ground surface temperature reconstructions: Using in situ estimates for thermal conductivity acquired with a fiber-optic distributed thermal perturbation sensor. Geophysical Research Letters 35. https://doi.org/10.1029/2008GL034762

Fuchs, S., Schütz, F., Förster, H.-J., Förster, A., 2013. Evaluation of common mixing models for calculating bulk thermal conductivity of sedimentary rocks: Correction charts and new conversion equations. Geothermics 47, 40–52. https://doi.org/10.1016/j.geothermics.2013.02.002

Fujii, H., Okubo, H., Itoi, R., 2006. Thermal response tests using optical fiber thermometers, in: Geothermal Resources Council Transactions - GRC 2006 Annual Meeting. Presented at the EventGRC 2006 Annual Meeting: Geothermal Resources-Securing Our Energy Future, pp. 545–551.

Galgaro, A., Dalla Santa, G., Zarrella, A., 2021. First Italian TRT database and significance of the geological setting evaluation in borehole heat exchanger sizing. Geothermics 94, 102098. https://doi.org/10.1016/j.geothermics.2021.102098

Galgaro, A., Pasquier, P., Schenato, L., Cultrera, M., Santa, G.D., 2018. Soil thermal conductivity from early TRT logs using an active hybrid optic fibre system, in: IGSHPA Research Track. Presented at the International Ground Source Heat Pump Association, pp. 1–9. https://doi.org/10.22488/okstate.18.000023

Gehlin, S., 2002. Thermal response test: Method Development and evaluation (Dissertation). Luleå University of Technology, Luleå.

Giordano, N., Lamarche, L., Raymond, J., 2021. Evaluation of subsurface heat capacity through oscillatory thermal response tests. Energies 14, 5791. https://doi.org/10.3390/en14185791

Greif, S., 2023. Räumlich hoch aufgelöste Analyse des technischen Potenzials von Wärmepumpen zur dezentralen Wärmeversorgung der Wohngebäude in Deutschland (Dissertation). Technical University of Munich, Munich.

Günther, D., 2010. Der Schwarzwald und seine Umgebung: Geologie, Mineralogie, Bergbau, Umwelt und Geotourismus. Bornträger Stuttgart, Stuttgart.

Gustafsson, S.E., 1991. Transient plane source techniques for thermal conductivity and thermal diffusivity measurements of solid materials. Review of Scientific Instruments 62, 797–804. https://doi.org/10.1063/1.1142087

Hacker, V., Sumereder, C., 2020. Electrical engineering: Fundamentals, De Gruyter Textbook. De Gruyter Oldenbourg, München; Wien. https://doi.org/10.1515/9783110521115

Haffen, S., Géraud, Y., Rosener, M., Diraison, M., 2017. Thermal conductivity and porosity maps for different materials: A combined case study of granite and sandstone. Geothermics 66, 143–150. https://doi.org/10.1016/j.geothermics.2016.12.005

Haines, P.J. (Ed.), 2002. Principles of thermal analysis and calorimetry. Royal Society of Chemistry, Cambridge.

Hakala, P., Vallin, S., Arola, T., Martinkauppi, I., 2022. Novel use of the enhanced thermal response test in crystalline bedrock. Renewable Energy 182, 467–482. https://doi.org/10.1016/j.renene.2021.10.020

Han, C., Yu, X., 2016. Sensitivity analysis of a vertical geothermal heat pump system. Applied Energy 170, 148–160. https://doi.org/10.1016/j.apenergy.2016.02.085

Hartog, A., Gamble, G., 1991. Photonic distributed sensing. Physics World 4. https://doi.org/10.1088/2058-7058/4/3/30

Hashin, Z., Shtrikman, S., 1963. A variational approach to the theory of the elastic behaviour of multiphase materials. Journal of the Mechanics and Physics of Solids 11, 127–140. https://doi.org/10.1016/0022-5096(63)90060-7

Heidinger, P., Dornstädter, J., Fabritius, A., Wahl, G., Welter, M., Zurek, 2004. EGRT - Enhanced Geothermal Response Tests, in: Die Neue Rolle Der Geothermie, Tagungsband GTV. Presented at the 5. Symposium Erdgekoppelte Wärmepumpen, Landau.

Heidinger, P., Fabritius, A., 2017. Faseroptische Temperaturmessungen - zur Detektierung der Hinterfüllungsqualität: Schlussbericht mit UpDate zu Drittmessungen in Deutschland (Final report No. E1712- 01P). Swiss Federal Office of Energy SFOE, Karlsruhe.

Hellström, G., 1991. Ground heat storage: Thermal analyses of duct storage systems (Dissertation). Lund University, Lund.

Heske, C., Kohlsch, O., Dornstädter, J., Heidinger, P., 2011. Der Enhanced-Geothermal-Response-Test als Auslegungsgrundlage und Optimierungstool. bbr Sonderheft.

Hill, R., 1952. The elastic behaviour of a crystalline aggregate. Proc. Phys. Soc. A 65, 349–354. https://doi.org/10.1088/0370-1298/65/5/307

Höhne, G.W.H., Hemminger, W.F., Flammersheim, H.J. (eds.), 2003. Differential Scanning Calorimetry, 2nd ed. Springer Berlin Heidelberg.

Huber, H., 2013. Experimentelle und numerische Untersuchungen zum Wärmetransportverhalten oberflächennaher, durchströmter Böden (Dissertation). Technical University of Darmstadt, Darmstadt.

Huber, H., Arslan, U., Sass, I., 2014. Zum Einfluss der Filtergeschwindigkeit des Grundwassers auf die effektive Wärmeleitfähigkeit. Grundwasser 19, 173–179. https://doi.org/10.1007/s00767-014-0263-7

IEA ECES, 2020. Quality management in design, construction and operation of borehole systems,. IEA Technology Collaboration Programme on Energy Conservation through Energy Storage (IEA ECES).

Indacoechea-Vega, I., Pascual-Muñoz, P., Castro-Fresno, D., Zamora-Barraza, D., 2018. Durability of geothermal grouting materials considering extreme loads. Construction and Building Materials 162, 732–739. https://doi.org/10.1016/j.conbuildmat.2017.12.072

Ingersoll, L., Plass, H., 1948. Theory of the ground pipe heat source for the heat pump. Heating, Piping & Air Conditioning 20, 119–122.

ISO IEC 98-3, 2008. Uncertainty of measurement — Part 3: Guide to the expression of uncertainty in measurement (GUM:1995).

Javadi, H., Mousavi Ajarostaghi, S., Rosen, M., Pourfallah, M., 2018. A comprehensive review of backfill materials and their effects on ground heat exchanger performance. Sustainability 10, 4486. https://doi.org/10.3390/su10124486

Javadi, H., Urchueguía, J.F., Badenes, B., Mateo, M.Á., Nejad Ghafar, A., Chaudhari, O.A., Zirgulis, G., Lemus, L.G., 2022. Laboratory and numerical study on innovative grouting materials applicable to borehole heat exchangers (BHE) and borehole thermal energy storage (BTES) systems. Renewable Energy 194, 788–804. https://doi.org/10.1016/j.renene.2022.05.152

Jia, G.S., Ma, Z.D., Xia, Z.H., Wang, J.W., Zhang, Y.P., Jin, L.W., 2022. Influence of groundwater flow on the ground heat exchanger performance and ground temperature distributions: A comprehensive review of analytical, numerical and experimental studies. Geothermics 100, 102342. https://doi.org/10.1016/j.geothermics.2021.102342

Jia, G.S., Tao, Z.Y., Meng, X.Z., Ma, C.F., Chai, J.C., Jin, L.W., 2019. Review of effective thermal conductivity models of rock-soil for geothermal energy applications. Geothermics 77, 1–11. https://doi.org/10.1016/j.geothermics.2018.08.001

Jobmann, M., Buntebarth, G., 2009. Influence of graphite and quartz addition on the thermo–physical properties of bentonite for sealing heat-generating radioactive waste. Applied Clay Science 44, 206–210. https://doi.org/10.1016/j.clay.2009.01.016

Jorand, R., Clauser, C., Marquart, G., Pechnig, R., 2015. Statistically reliable petrophysical properties of potential reservoir rocks for geothermal energy use and their relation to lithostratigraphy and rock composition: The NE Rhenish Massif and the Lower Rhine Embayment (Germany). Geothermics 53, 413–428. https://doi.org/10.1016/j.geothermics.2014.08.008

Kämmlein, M., Stollhofen, H., 2019. Pore-fluid-dependent controls of matrix and bulk thermal conductivity of mineralogically heterogeneous sandstones. Geotherm Energy 7. https://doi.org/10.1186/s40517-019-0129-4

Katsura, T., Nagano, K., Takeda, S., Shimakura, K., 2006. Heat transfer experiment in the ground with groundwater advection, in: The IEA 10th Energy Conservation Thermal Energy Storage Conference. Presented at the Thermal Energy Storage Conference, New Jersey, USA.

Kim, D., Kim, G., Baek, H., 2016. Thermal conductivities under unsaturated condition and mechanical properties of cement-based grout for vertical ground-heat exchangers in Korea—A case study. Energy and Buildings 122, 34–41. https://doi.org/10.1016/j.enbuild.2016.02.047

Kim, D., Kim, G., Baek, H., 2015. Relationship between thermal conductivity and soil–water characteristic curve of pure bentonite-based grout. International Journal of Heat and Mass Transfer 84, 1049–1055. https://doi.org/10.1016/j.ijheatmasstransfer.2015.01.091

Kim, D., Oh, S., 2020. Measurement and comparison of thermal conductivity of porous materials using box, dual-needle, and single-needle probe methods-A case study. International Communications in Heat and Mass Transfer 118, 104815. https://doi.org/10.1016/j.icheatmasstransfer.2020.104815

Kim, D., Oh, S., 2019. Relationship between the thermal properties and degree of saturation of cementitious grouts used in vertical borehole heat exchangers. Energy and Buildings 201, 1–9. https://doi.org/10.1016/j.enbuild.2019.07.017

Kim, Daehoon, Kim, G., Kim, Donghui, Baek, H., 2017. Experimental and numerical investigation of thermal properties of cement-based grouts used for vertical ground heat exchanger. Renewable Energy 112, 260–267. https://doi.org/10.1016/j.renene.2017.05.045

Kim, Y., Dinh, B.H., Do, T.M., Kang, G., 2020. Development of thermally enhanced controlled low-strength material incorporating different types of steel-making slag for ground-source heat pump system. Renewable Energy 150, 116–127. https://doi.org/10.1016/j.renene.2019.12.129

Kuchling, H., 2014. Taschenbuch der Physik, 21. ed. Carl Hanser verlag GmbH & Co. KG, München.

Kurdowski, W., 2014. Cement and concrete chemistry. New York; Springer, Dordrecht.

Lafhaj, Z., Goueygou, M., Djerbi, A., Kaczmarek, M., 2006. Correlation between porosity, permeability and ultrasonic parameters of mortar with variable water / cement ratio and water content. Cement and Concrete Research 36, 625–633. https://doi.org/10.1016/j.cemconres.2005.11.009

Lamarche, L., Beauchamp, B., 2007. New solutions for the short-time analysis of geothermal vertical boreholes. International Journal of Heat and Mass Transfer 50, 1408–1419. https://doi.org/10.1016/j.ijheatmasstransfer.2006.09.007

Lamarche, L., Kajl, S., Beauchamp, B., 2010. A review of methods to evaluate borehole thermal resistances in geothermal heat-pump systems. Geothermics 39, 187–200. https://doi.org/10.1016/j.geothermics.2010.03.003

Lamarche, L., Raymond, J., Giordano, N., 2024. Oscillatory thermal response tests to estimate the ground thermal diffusivity. Applied Energy 353, 122078. https://doi.org/10.1016/j.apenergy.2023.122078

Langevin, H., Giordano, N., Raymond, J., Gosselin, L., 2022. Oscillatory thermal response test using heating cables: A novel method for in situ thermal property analysis. SSRN Journal. https://doi.org/10.2139/ssrn.4120037

Lee, C., Lee, K., Choi, H., Choi, H.-P., 2010. Characteristics of thermally-enhanced bentonite grouts for geothermal heat exchanger in South Korea. Sci. China Ser. E-Technol. Sci. 53, 123–128. https://doi.org/10.1007/s11431-009-0413-9

Lee, C., Park, M., Nguyen, T.-B., Sohn, B., Choi, J.M., Choi, H., 2012. Performance evaluation of closed-loop vertical ground heat exchangers by conducting in-situ thermal response tests. Renewable Energy 42, 77–83. https://doi.org/10.1016/j.renene.2011.09.013

Lehr, C., Sass, I., 2014. Thermo-optical parameter acquisition and characterization of geologic properties: A 400-m deep BHE in a karstic alpine marble aquifer. Environmental Earth Sciences 72, 1403–1419. https://doi.org/10.1007/s12665-014-3310-x

Li, M., Lai, A.C.K., 2015. Review of analytical models for heat transfer by vertical ground heat exchangers (GHEs): A perspective of time and space scales. Applied Energy 151, 178–191. https://doi.org/10.1016/j.apenergy.2015.04.070

Li, M., Zhang, L., Liu, G., 2019. Estimation of thermal properties of soil and backfilling material from thermal response tests (TRTs) for exploiting shallow geothermal energy: Sensitivity, identifiability, and uncertainty. Renewable Energy 132, 1263–1270. https://doi.org/10.1016/j.renene.2018.09.022

Liang, B., Chen, M., Orooji, Y., 2022. Effective parameters on the performance of ground heat exchangers: A review of latest advances. Geothermics 98, 102283. https://doi.org/10.1016/j.geothermics.2021.102283

Liu, H., Rodriguez-Dono, A., Zhang, J., Zhou, N., Wang, Y., Sun, Q., Zhang, L., 2022. A new method for exploiting mine geothermal energy by using functional cemented paste backfill material for phase change heat storage: Design and experimental study. Journal of Energy Storage 54, 105292. https://doi.org/10.1016/j.est.2022.105292

Liu, X., Zhang, G., Wu, R., Chen, P., Guo, J., Wan, J., 2024. Performance of thermally enhanced backfill material in vertical ground heat exchangers under continuous operation in a cooling season. Applied Thermal Engineering 257, 124442. https://doi.org/10.1016/j.applthermaleng.2024.124442

Lund, J.W., Toth, A.N., 2021. Direct utilization of geothermal energy 2020 worldwide review. Geothermics 90, 101915. https://doi.org/10.1016/j.geothermics.2020.101915

Luo, J., Rohn, J., Bayer, M., Priess, A., Xiang, W., 2014. Analysis on performance of borehole heat exchanger in a layered subsurface. Applied Energy 123, 55–65. https://doi.org/10.1016/j.apenergy.2014.02.044

Luo, J., Rohn, J., Xiang, W., Bayer, M., Priess, A., Wilkmann, L., Steger, H., Zorn, R., 2015. Experimental investigation of a borehole field by enhanced geothermal response test and numerical analysis of performance of the borehole heat exchangers. Energy 84, 473–484. https://doi.org/10.1016/j.energy.2015.03.013

Luo, J., Rohn, J., Xiang, W., Bertermann, D., Blum, P., 2016. A review of ground investigations for ground source heat pump (GSHP) systems. Energy and Buildings 117, 160–175. https://doi.org/10.1016/j.enbuild.2016.02.038

Ma, Y., Zhang, Yanjun, Cheng, Y., Zhang, Yu, Gao, X., Shan, K., 2022. A case study of field thermal response test and laboratory test cased on distributed optical fiber temperature sensor. Energies 15, 8101. https://doi.org/10.3390/en15218101

Maghrabie, H.M., Abdeltwab, M.M., Tawfik, M.H.M., 2023. Ground-source heat pumps (GSHPs): Materials, models, applications, and sustainability. Energy and Buildings 113560. https://doi.org/10.1016/j.enbuild.2023.113560

Mahmoud, M., Ramadan, M., Pullen, K., Abdelkareem, M.A., Wilberforce, T., Olabi, A.-G., Naher, S., 2021. A review of grout materials in geothermal energy applications. International Journal of Thermofluids 10, 100070. https://doi.org/10.1016/j.ijft.2021.100070

Maldaner, C.H., Munn, J.D., Coleman, T.I., Molson, J.W., Parker, B.L., 2019. Groundwater flow quantification in fractured rock coreholes using active distributed temperature sensing under natural gradient conditions. Water Resources Research 55, 3285–3306. https://doi.org/10.1029/2018WR024319

Marshall, A.K., 1972. The thermal properties of concrete. Building Science 7, 167–174. https://doi.org/10.1016/0007-3628(72)90022-9

Mascarin, L., Garbin, E., Di Sipio, E., Dalla Santa, G., Bertermann, D., Artioli, G., Bernardi, A., Galgaro, A., 2022. Selection of backfill grout for shallow geothermal systems: Materials investigation and thermo-physical analysis. Construction and Building Materials 318, 125832. https://doi.org/10.1016/j.conbuildmat.2021.125832

McKinley, J.D., Bolton, M.D., 1999. A geotechnical description of fresh cement grout - Filtration and consolidation behaviour. Magazine of Concrete Research 51.

Menberg, K., Steger, H., Zorn, R., Reuß, M., Pröll, M., Bayer, P., Blum, P., 2013. Bestimmung der Wärmeleitfähigkeit im Untergrund durch Labor- und Feldversuche und anhand theoretischer Modelle. Grundwasser 18, 103–116. https://doi.org/10.1007/s00767-012-0217-x

Mendes, J.C., Barreto, R.R., Paula, A.C.B., Da Elói, F.P.F., Brigolini, G.J., Peixoto, R.A.F., 2019. On the relationship between morphology and thermal conductivity of cement-based composites. Cement and Concrete Composites 104, 103365. https://doi.org/10.1016/j.cemconcomp.2019.103365

Meschede, D. (Ed.), 2015. Gerthsen Physik, 25. Auflage. ed, Springer-Lehrbuch. Springer Spektrum, Berlin; Heidelberg.

Meshalkin, Y., Shakirov, A., Popov, E., Koroteev, D., Gurbatova, I., 2020. Robust well-log based determination of rock thermal conductivity through machine learning. Geophysical Journal International 222, 978–988. https://doi.org/10.1093/gji/ggaa209

Mettler Toledo, 2016. Thermal analysis in practice, tips and hints - Introductory Handbook.

Midttomme, K., Roaldset, E., 1998. The effect of grain size on thermal conductivity of quartz sands and silts. Petroleum Geoscience 4, 165–172. https://doi.org/10.1144/petgeo.4.2.165

Minchio, F., Cesari, G., Pastore, C., Fossa, M., 2020. Experimental Hydration Temperature Increase in Borehole Heat Exchangers during Thermal Response Tests for Geothermal Heat Pump Design. Energies 13, 3461. https://doi.org/10.3390/en13133461

Molina-Giraldo, N., Bayer, P., Blum, P., 2011. Evaluating the influence of thermal dispersion on temperature plumes from geothermal systems using analytical solutions. International Journal of Thermal Sciences 50, 1223–1231. https://doi.org/10.1016/j.ijthermalsci.2011.02.004

Nabawy, B.S., Géraud, Y., 2016. Impacts of pore- and petro-fabrics, mineral composition and diagenetic history on the bulk thermal conductivity of sandstones. Journal of African Earth Sciences 115, 48–62. https://doi.org/10.1016/j.jafrearsci.2015.11.025

Nasr, M., Raymond, J., Malo, M., Gloaguen, E., 2018. Geothermal potential of the St. Lawrence Lowlands sedimentary basin from well log analysis. Geothermics 75, 68–80. https://doi.org/10.1016/j.geothermics.2018.04.004

Nian, Y.-L., Cheng, W.-L., 2018. Analytical g-function for vertical geothermal boreholes with effect of borehole heat capacity. Applied Thermal Engineering 140, 733–744. https://doi.org/10.1016/j.applthermaleng.2018.05.086

Ordonez-Miranda, J., Alvarado-Gil, J.J., 2012. Effect of the pore shape on the thermal conductivity of porous media. J Mater Sci 47, 6733–6740. https://doi.org/10.1007/s10853-012-6616-7

Pambou, C.H.K., Raymond, J., Lamarche, L., 2019. Improving thermal response tests with wireline temperature logs to evaluate ground thermal conductivity profiles and groundwater fluxes. Heat Mass Transfer 55, 1829–1843. https://doi.org/10.1007/s00231-018-2532-y

Park, M., Min, S., Lim, J., Choi, J.M., Choi, H., 2011. Applicability of cement-based grout for ground heat exchanger considering heating-cooling cycles. Sci. China Technol. Sci. 54, 1661–1667. https://doi.org/10.1007/s11431-011-4388-y

Pascual-Muñoz, P., Indacoechea-Vega, I., Zamora-Barraza, D., Castro-Fresno, D., 2018. Experimental analysis of enhanced cement-sand-based geothermal grouting materials. Construction and Building Materials 185, 481–488. https://doi.org/10.1016/j.conbuildmat.2018.07.076

Pasquier, P., 2015. Stochastic interpretation of thermal response test with TRT-SInterp. Computers & Geosciences 75, 73–87. https://doi.org/10.1016/j.cageo.2014.11.001

Pauselli, C., Gola, G., Ranalli, G., Mancinelli, P., Trippetta, F., Ballirano, P., Verdoya, M., 2021. Thermal conductivity of Triassic evaporites. Geophysical Journal International 227, 1715–1729. https://doi.org/10.1093/gji/ggab293

Pichugin, Z., Chekhonin, E., Popov, Y., Kalinina, M., Bayuk, I., Popov, E., Spasennykh, M., Savelev, E., Romushkevich, R., Rudakovskaya, S., 2022. Weighted geometric mean model for determining thermal conductivity of reservoir rocks: Current problems with applicability and the model modification. Geothermics 104, 102456. https://doi.org/10.1016/j.geothermics.2022.102456

Popov, Y., Beardsmore, G., Clauser, C., Roy, S., 2016. ISRM Suggested Methods for Determining Thermal Properties of Rocks from Laboratory Tests at Atmospheric Pressure. Rock Mech Rock Eng 49, 4179–4207. https://doi.org/10.1007/s00603-016-1070-5

Popov, Y.A., Semenov, V.G., Korostelev, V.M., Berezin, V.V., 1983. Noncontact Evaluation of thermal conductivity of rocks with the aid of a mobile heat source. Earth Physics 19.

Pribnow, D., Umsonst, T., 1993. Estimation of thermal conductivity from the mineral composition: Influence of fabric and anisotropy. Geophysical Research Letters 20, 2199–2202. https://doi.org/10.1029/93GL02135

Prinz, H., Strauß, R., 2018. Ingenieurgeologie. Springer Berlin Heidelberg, Berlin, Heidelberg. https://doi.org/10.1007/978-3-662-54710-6

Rainieri, S., Bozzilo, F., Pagliarini, G., 2011. Modeling approaches applied to the thermal response test: A critical review of the literature. HVAC&R Research 17, 977–990. https://doi.org/10.1080/10789669.2011.610282

Rashid, F.L., Dhaidan, N.S., Hussein, A.K., Al-Mousawi, F.N., Younis, O., 2023. Ground heat exchanger in different configuration: Review of recent advances and development. Geoenergy Science and Engineering 227, 211872. https://doi.org/10.1016/j.geoen.2023.211872

Raymond, J., Lamarche, L., Malo, M., 2015. Field demonstration of a first thermal response test with a low power source. Applied Energy 147, 30–39. https://doi.org/10.1016/j.apenergy.2015.01.117

Raymond, J., Robert, G., Therrien, R., Gosselin, L., 2010. A novel thermal response test using heating cables, in: Proceedings World Geothermal Congress 2010. Presented at the World Geothermal Congress 2010, Bali, Indonesia.

Raymond, J., Therrien, R., Gosselin, L., Lefebvre, R., 2011. A review of thermal response test analysis using pumping test concepts. Ground Water 49, 932–45. https://doi.org/10.1111/j.1745-6584.2010.00791.x

Read, T., Bour, O., Selker, J.S., Bense, V.F., Le Borgne, T., Hochreutener, R., Lavenant, N., 2014. Active-distributed temperature sensing to continuously quantify vertical flow in boreholes. Water Resources Research 50, 3706–3713. https://doi.org/10.1002/2014WR015273

Reuß, M., Koenigsdorff, R., Zorn, R., Kuckelkorn, J., Steger, H., Pröll, M., Feuerstein, Ph., 2012. Qualitätssicherung bei Erdwärmesonden und Erdreichkollektoren, Final report, Federal Ministry for Economic Affairs and Technology (FKZ: 0327453A).

Riegger, M., Heidinger, P., Lorinser, B., Stober, I., 2012. Auswerteverfahren zur Kontrolle der Verfüllqualität in Erdwärmesonden mit faseroptischen Temperaturmessungen. Grundwasser 17, 91–103. https://doi.org/10.1007/s00767-012-0192-2

Riegger, M., Rolker, J., Steger, H., Stober, I., Haist, M., Eckhardt, J.-D., Schlager, P., Zemann, M., Zorn, R., Huttenloch, P., 2016. Abschlussbericht zu dem Forschungsvorhaben EWS-tech: Weiterentwicklung der Erwärmesonden-Technologie.

Sakata, Y., Katsura, T., Nagano, K., 2020. Estimation of ground thermal conductivity through indicator kriging: Nation-scale application and vertical profile analysis in Japan. Geothermics 88, 101881. https://doi.org/10.1016/j.geothermics.2020.101881

Sakata, Y., Katsura, T., Serageldin, A.A., Nagano, K., Ooe, M., 2021. Evaluating Variability of Ground Thermal Conductivity within a Steep Site by History Matching Underground Distributed Temperatures from Thermal Response Tests. Energies 14, 1872. https://doi.org/10.3390/en14071872

Sanner, B., Hellström, G., Spitler, J., Gehlin, S., 2005. Thermal Response Test – Current Status and World-Wide Application, in: Proceedings World Geothermal Congress 2005. Presented at the World Geothermal Congress 2005, Antalya, Turkey.

Sayde, C., Buelga, J.B., Rodriguez-Sinobas, L., El Khoury, L., English, M., van de Giesen, N., Selker, J.S., 2014. Mapping variability of soil water content and flux across 1-1000 m scales using the Actively Heated Fiber Optic method. Water Resources Research 50, 7302–7317. https://doi.org/10.1002/2013WR014983

Schlötzer, C., 1995. Filtrationsverhalten von Dichtsuspensionen an flüssigkeitsgestützten Erdwänden (Dissertation). Universität Hannover, Hannover.

Schön, J.H., 2011. Physical properties of rocks: A workbook, Handbook of petroleum exploration and production. Elsevier.

Schüppler, S., Zorn, R., Steger, H., Blum, P., 2021. Wireless probes for measuring vertical temperature profiles in borehole heat exchangers (BHEs), in: EGU General Assembly 2021. https://doi.org/10.5194/egusphere-egu21-9948

Schutter, G., Taerwe, L., 1995. Specific heat and thermal diffusivity of hardening concrete. Magazine of Concrete Research 47, 203–208. https://doi.org/10.1680/macr.1995.47.172.203

Seibertz, K.S.O., Chirila, M.A., Bumberger, J., Dietrich, P., Vienken, T., 2016. Development of in-aquifer heat testing for high resolution subsurface thermal-storage capability characterisation. Journal of Hydrology 534, 113–123. https://doi.org/10.1016/j.jhydrol.2015.12.013

Selker, J.S., Thévenaz, L., Huwald, H., Mallet, A., Luxemburg, W., van de Giesen, N., Stejskal, M., Zeman, J., Westhoff, M., Parlange, M.B., 2006. Distributed fiber-optic temperature sensing for hydrologic systems. Water Resour. Res. 42. https://doi.org/10.1029/2006WR005326

Shafigh, P., Asadi, I., Akhiani, A.R., Mahyuddin, N.B., Hashemi, M., 2020. Thermal properties of cement mortar with different mix proportions. Mater. construcc. 70, 224. https://doi.org/10.3989/mc.2020.09219

Shen, Y., Wang, X., Wang, Y., Zhou, K., Zhang, J., Zhang, H., Li, J., 2021. Thermal conductivity models of sandstone: applicability evaluation and a newly proposed model. Heat Mass Transfer 57, 985–998. https://doi.org/10.1007/s00231-020-02995-7

Shirazi, A.S., Bernier, M., 2013. Thermal capacity effects in borehole ground heat exchangers. Energy and Buildings 67, 352–364. https://doi.org/10.1016/j.enbuild.2013.08.023

Signorelli, S., Bassetti, S., Pahud, D., Kohl, T., 2007. Numerical evaluation of thermal response tests. Geothermics 36, 141–166. https://doi.org/10.1016/j.geothermics.2006.10.006

Simon, N., Bour, O., 2022. An ADTS Toolbox for Automatically Interpreting Active Distributed Temperature Sensing Measurements. Ground Water. https://doi.org/10.1111/gwat.13172

Song, X., Zheng, R., Li, R., Li, G., Sun, B., Shi, Y., Wang, G., Zhou, S., 2019. Study on thermal conductivity of cement with thermal conductive materials in geothermal well. Geothermics 81, 1–11. https://doi.org/10.1016/j.geothermics.2019.04.001

Soyk, D., 2015. Diagenesis and reservoir quality of the Lower and Middle Buntsandstein (Lower Triassic), SW Germany (Dissertation). Naturwissenschaftlich-Mathematischen Gesamtfakultät der Ruprecht-Karls-Universität, Heidelberg.

Spitler, J.D., Gehlin, S.E.A., 2015. Thermal response testing for ground source heat pump systems—An historical review. Renewable and Sustainable Energy Reviews 50, 1125–1137. https://doi.org/10.1016/j.rser.2015.05.061

Stark, J., Wicht, B., 2013. Dauerhaftigkeit von Beton. Springer Berlin Heidelberg, Berlin, Heidelberg. https://doi.org/10.1007/978-3-642-35278-2

Stauffer, F., Bayer, P., Blum, P., Giraldo, N.M., Kinzelbach, W., 2014. Thermal Use of Shallow Groundwater. Taylor and Francis, Hoboken.

Stober, I., Bucher, K., 2020. Geothermie. Springer Berlin Heidelberg, Berlin, Heidelberg. https://doi.org/10.1007/978-3-662-60940-8

Sugawara, A., Yoshizawa, Y., 1962. An Experimental Investigation on the Thermal Conductivity of Consolidated Porous Materials. Journal of Applied Physics 33, 3135–3138. https://doi.org/10.1063/1.1728581

Sugawara, A., Yoshizawa, Y., 1961. An investigation on the thermal conductivity of porous materials and its application to porous rock. Australian Journal of Physics 14, 469–480. https://doi.org/10.1071/PH610469

Terzaghi, K., Peck, R.B., Mesri, G., 1996. Soil mechanics—A new chapter in engineering science., 3. ed. Wiley, New York.

Theophil, T., Reduth, Y., Mangold, D., 2023. Interaktion von ErdwärmesondenVerfüllbaustoffen mit dem Untergrund. bbr Sonderheft.

United Nations, 2015. Paris Agreement. UNFCCC secretariat for ease of reference.

Vélez Márquez, M., Raymond, J., Blessent, D., Philippe, M., Simon, N., Bour, O., Lamarche, L., 2018. Distributed thermal response tests using a heating Cable and fiber optic temperature sensing. Energies 11, 3059. https://doi.org/10.3390/en11113059

Verdoya, M., Pacetti, C., Chiozzi, P., Invernizzi, C., 2018. Thermophysical parameters from laboratory measurements and in-situ tests in borehole heat exchangers. Applied Thermal Engineering 144, 711–720. https://doi.org/10.1016/j.applthermaleng.2018.08.039

Verein Deutscher Ingenieure, 2020. VDI 4640 part 5, Thermal use of the underground, Thermal response test (TRT).

Verein Deutscher Ingenieure, 2019. VDI 4640, part 2: Thermal use of the underground, Ground source heat pump systems.

Verein Deutscher Ingenieure, 2010. VDI 4640, part 1: Thermal use of the underground, Fundamentals, approvals, environmental aspects.

Verein Deutscher Zementwerke e.V., 2002. Zement-Taschenbuch, 50th ed. Erkrath.

Viccaro, M., 2018. Doped bentonitic grouts for implementing performances of low-enthalpy geothermal systems. Geotherm Energy 6. https://doi.org/10.1186/s40517-018-0090-7

Vieira, A., Alberdi-Pagola, M., Christodoulides, P., Javed, S., Loveridge, F., Nguyen, F., Cecinato, F., Maranha, J., Florides, G., Prodan, I., van Lysebetten, G., Ramalho, E., Salciarini, D., Georgiev, A., Rosin-Paumier, S., Popov, R., Lenart, S., Erbs Poulsen, S., Radioti, G., 2017. Characterisation of ground thermal and thermo-mechanical behaviour for shallow geothermal energy applications. Energies 10, 2044. https://doi.org/10.3390/en10122044

Wagner, R., Clauser, C., 2005. Evaluating thermal response tests using parameter estimation for thermal conductivity and thermal capacity. J. Geophys. Eng. 2, 349–356. https://doi.org/10.1088/1742-2132/2/4/S08

Wagner, V., Bayer, P., Bisch, G., Kübert, M., Blum, P., 2014. Hydraulic characterization of aquifers by thermal response testing: Validation by large-scale tank and field experiments. Water Resour. Res. 50, 71–85. https://doi.org/10.1002/2013WR013939

Wagner, V., Blum, P., Kübert, M., Bayer, P., 2013. Analytical approach to groundwater-influenced thermal response tests of grouted borehole heat exchangers. Geothermics 46, 22–31. https://doi.org/10.1016/j.geothermics.2012.10.005

Wang, C., Fang, H., Wang, X., Lu, J., Sun, Y., 2022. Study on the influence of borehole heat capacity on deep coaxial borehole heat exchanger. Sustainability 14, 2043. https://doi.org/10.3390/su14042043

Wang, S., Jian, L., Shu, Z., Chen, S., Chen, L., 2020. A High Thermal Conductivity Cement for Geothermal Exploitation Application. Nat Resour Res 29, 3675–3687. https://doi.org/10.1007/s11053-020-09694-4

Wang, X., Zhang, H., Cui, L., Wang, J., Lee, C., Zhu, X., Dong, Y., 2024. Borehole thermal energy storage for building heating application: A review. Renewable and Sustainable Energy Reviews 203, 114772. https://doi.org/10.1016/j.rser.2024.114772

Wärmeplanungsgesetz, 2023.

Wilke, S., Menberg, K., Steger, H., Blum, P., 2020. Advanced thermal response tests: A review. Renewable and Sustainable Energy Reviews 119, 109575. https://doi.org/10.1016/j.rser.2019.109575

Witte, H.J.L., 2013. Error analysis of thermal response tests. Applied Energy 109, 302–311. https://doi.org/10.1016/j.apenergy.2012.11.060

Woodside, W., Messmer, J.H., 1961. Thermal Conductivity of Porous Media. I. Unconsolidated Sands. Journal of Applied Physics 32, 1688–1699. https://doi.org/10.1063/1.1728419

Xu, Y., Chung, D.D.L., 2000. Effect of sand addition on the specific heat and thermal conductivity of cement. Cement and Concrete Research 30, 59–61. https://doi.org/10.1016/S0008-8846(99)00206-9

Yang, H., Cui, P., Fang, Z., 2010. Vertical-borehole ground-coupled heat pumps: A review of models and systems. Applied Energy 87, 16–27. https://doi.org/10.1016/j.apenergy.2009.04.038

Yang, Y., Li, B., Che, L., Li, M., Luo, Y., Han, H., 2024. Calculation model and influence factors of thermal conductivity of composite cement-based materials for geothermal well. Geotherm Energy 12, 3. https://doi.org/10.1186/s40517-024-00282-w

Zhang, B., Gu, K., Shi, B., Liu, C., Bayer, P., Wei, G., Gong, X., Yang, L., 2020. Actively heated fiber optics based thermal response test: A field demonstration. Renewable and Sustainable Energy Reviews 134, 110336. https://doi.org/10.1016/j.rser.2020.110336

Zhang, C., Guo, Z., Liu, Y., Cong, X., Peng, D., 2014. A review on thermal response test of ground-coupled heat pump systems. Renewable and Sustainable Energy Reviews 40, 851–867. https://doi.org/10.1016/j.rser.2014.08.018

Zhang, C., Song, W., Liu, Y., Kong, X., Wang, Q., 2019. Effect of vertical ground temperature distribution on parameter estimation of in-situ thermal response test with unstable heat rate. Renewable Energy 136, 264–274. https://doi.org/10.1016/j.renene.2018.12.112

Zhang, C., Xu, C., Yu, X., Lu, J., Liu, Y., Sun, S., 2024. A multi-parameter estimation of layered rock-soil thermal properties of borehole heat exchanger in a stratified subsurface. Renewable Energy 121074. https://doi.org/10.1016/j.renene.2024.121074

Zhang, X., Han, Z., Ji, Q., Zhang, H., Li, X., 2021. Thermal response tests for the identification of soil thermal parameters: A review. Renewable Energy 173, 1123–1135. https://doi.org/10.1016/j.renene.2020.12.028

Zhao, D., Qian, X., Gu, X., Jajja, S.A., Yang, R., 2016. Measurement techniques for thermal conductivity and interfacial thermal conductance of bulk and thin film materials. Journal of Electronic Packaging 138. https://doi.org/10.1115/1.4034605

Zhao, J., Huang, G., Guo, Y., Feng, Z., Gupta, R., Liu, W.V., 2024. Development of a novel cement-based grout with enhanced thermal and sealing performance for borehole heat exchangers. Energy and Buildings 302, 113754. https://doi.org/10.1016/j.enbuild.2023.113754

Zhou, Y., Zhang, Y., Xu, Y., 2018. Influence of grout thermal properties on heat-transfer performance of ground source heat exchangers. Science and Technology for the Built Environment 24, 461–469. https://doi.org/10.1080/23744731.2017.1402645

Zubair, S.M., Chaudhry, M.A., 1996. Temperature solutions due to time-dependent moving-line-heat sources. Heat and Mass Transfer 31, 185–189. https://doi.org/10.1007/s002310050044

Acknowledgements

Of course, this thesis would not have been possible except for the incredible support of so many wonderful people. I want to express my deepest gratitude towards everyone who accompanied me on my way and highlight some in particular:

First and foremost, Prof. Dr. Philipp Blum. I am very grateful for your supervision during my time as a PhD student in your institute with an open door and open mind attitude. Thank you for your guidance which helped me shape my research into publications.

Prof. Dr. Javier Urchueguía Schölzel from the Department of Applied Physics at the Polytechnical University Valencia. Thank you for kindly accepting to be my co-examiner. Also, Prof. Dr. Nico Goldscheider and Prof. Dr. Frank Schilling from the Institute of Applied Geosciences at KIT. Thank you for being part of my PhD committee.

Dr. Hagen Steger. I would never have been able to complete the experiments without your help. I enjoyed learning from your expertise, but also our talks about music and life during the long car trips. I guess, the *money* was not *for nothing*.

Dr. Petra Huttenloch from the European Institute for Energy Research (EIFER). It was exceptionally easy to work with you. I loved to share all the brilliant and stupid thoughts on our projects with you.

Dr. Roman Zorn from EIFER. You are always a treasure box of knowledge and ideas. I gratefully acknowledge how you fired these at me, as often as I wished for a recorder to capture everything.

Lucas Homann, my student assistant. Thank you for your help with the laboratory experiments, while never complaining about all the repetitions. Also, Felix Voss and Madeline Dantin from EIFER. I enjoyed sharing the laboratory with you and highly appreciate your help with the experiments.

Prof. Dr. Katsunori Nagano from the Graduate School of Engineering, Hokkaido University. Thank you for inviting me to your institute and giving me the chance to learn from your working group and broaden my perspective. Also, Dr. Hongzhi Li and Dr. Ahmed A. Serageldin. Thank you for all your help and your open ear during my stay at Hokudai.

My academic family, all my colleagues and friends from Engineering Geology, Hydrogeology and EIFER. You created and maintained an atmosphere where I could always count on you. You have made the process feel a lot less like a solo mission. Special props go out to Dr. Fabien Glatting and Dr. Ruben Stemmle. Thank you for your help in finalising this thesis.

Nicole Suteu. Thank you for your help with the paperworks and all official matters.

The Federal Ministry of Economy Affairs and Climate Action. Thank you for funding my position through the project QEWSplus. Also, the Federal Ministry of Education and Research for funding my position through the project SpeicherCity.

All the QEWSplus project partners. I really enjoyed our project meetings and the open and friendly atmosphere when working together. Thank you for sharing your knowledge with me.

The Graduate School for Environment and Climate (GRACE), and especially Dr.-Ing. Andreas Schenk and Dipl.-Min. Diana Lieber. Thank you for funding my research stay at Hokudai, but also for your guidance during my time as a PhD student.

And last but not least, my family and friends. You knew when not to ask for progress and when to celebrate even the smallest achievements. Thank you for always being understanding and supportive.

Declaration of authorship

Study 1 (Chapter 2)

Albers, A., Steger, H., Zorn, R., Blum, P., 2024. Evaluating an enhanced thermal response test (ETRT) with high groundwater flow. Geothermal Energy 12:1. https://doi.org/10.1186/s40517-023-00278-y

Anna Albers (AA), Hagen Steger (HS) and Philipp Blum (PB) developed the methodology and study design. AA, HS and Roman Zorn (RZ) carried out the ETRT. AA executed the data analysis and prepared the first draft. All authors read and approved the final manuscript.

Study 2 (Chapter 3)

Albers, A., Glatting, F., Menberg, K., Steger, H., Fliegauf, C., Schindler, L., Wilke, S., Zorn, R., Blum, P. Depth-specific thermal conductivities of Triassic sandstones, Geothermal Energy (under review)

AA, Fabien Glatting (FG), Kathrin Menberg (KM) and PB developed the methodology and study design. AA, HS and RZ carried out the ETRT. HS, Christina Fliegauf (CF), Linda Schindler (LS) and Sascha Wilke (SW) conducted the laboratory experiments. AA, FG and CF executed the data analyses. AA, FG and CF created the figures. AA and FG prepared the first draft. All authors read and approved the final manuscript.

Study 3 (Chapter 4)

Albers, A., Huttenloch, P., Zorn, R., Steger, H., Blum, P., 2024. Determination of thermal properties of grouting materials for borehole heat exchangers (BHE). Geothermal Energy 12:36. https://doi.org/10.1186/s40517-024-00316-3

AA, Petra Huttenloch (PH) and HS developed the methodology and study design. AA and PH conducted the laboratory analyses and data evaluation. AA created the figures. RZ and HS acquired the funding. PB provided supervision. AA prepared the first draft. All authors read and approved the final manuscript.

Study 4 (Chapter 5)

Albers, A., Huttenloch, P., Reduth, Y., Zorn, R., Steger, H., Blum, P. In-situ thermal properties of grouting materials in borehole heat exchangers. Geothermal Energy (under review)

AA, PH, HS and RZ developed the methodology and study design. AA and PH conducted the laboratory analyses. AA and RZ evaluated the data. Yannick Reduth (YR), AA and HS deconstructed the BHE. AA, RZ and HS carried out the ETRT. HS and RZ acquired the funding. HS, RZ and YR handled the project administration. PB provided supervision. AA created the figures and prepared the first draft. All authors reviewed and approved the final manuscript.